Cosmological Stochastic Backgrounds of Gravitational Waves

Chiara Caprini

Cosmological Stochastic Backgrounds of Gravitational Waves

Chiara Caprini

Laboratoire Astroparticule et Cosmologie
CNRS UMR 7164
Université Paris VII Diderot

Mémoire d'Habilitation à Diriger des Recherches
- 2018 -

Présentation et synthèse du mémoire

Mes intérêts de recherche couvrent différent sujets entre les domaines de la cosmologie et des ondes gravitationnelles, comme les signaux d'ondes gravitationnelles provenant de l'univers primordial, l'utilisation des ondes gravitationnelles émises par les binaires compactes pour tester l'expansion de l'univers, mais aussi la physique du fond diffus cosmologique, les champs magnétiques cosmologiques, la turbulence dans le plasma primordial, l'énergie noire et les champs scalaires en cosmologie.

Au cours du temps, les aspects plus étroitement reliés aux ondes gravitationnelles ont pris un place importante dans ma recherche, en particulier dans le contexte des études préparatoires à l'interféromètre spatial LISA. Ceci a été dû principalement au fait que, en fin 2013, je suis devenue coordinatrice du Groupe de Travail de Cosmologie au sein du Consortium LISA, ce qui m'a donné la possibilité de suivre de près le développement du cas scientifique de LISA, et d'avoir une idée claire des arguments qu'il était nécessaire approfondir dans ce contexte.

L'approbation de LISA par l'ESA en début 2017, favorisée par le succès de LISA Pathfinder et par le cadre heureux de la première détection directe des ondes gravitationnelles par aLIGO et aVirgo, a ultérieurement renforcé ma conviction que la cosmologie avec les ondes gravitationnelles est un sujet important et d'actualité, auquel il vaut la peine de dédier sa propre recherche. La récente détection coïncidente des ondes gravitationnelles et électromagnétiques émises par la collision des deux étoiles à neutrons a démontré le potentiel des ondes gravitationnelles pour la cosmologie: elle a permis une nouvelle mesure de la constante de Hubble, et de contraindre la vitesse des ondes gravitationnelles (et par conséquent certaines théories de la gravitation modifiée très importantes pour la cosmologie).

Devant décider le sujet de ce mémoire, et les travaux à y intégrer, il m'a semblé donc naturel de choisir comme thématique les ondes gravitationnelles en tant que observable cosmologique. Parmi les sujets sur lesquels j'ai travaillé, deux possibilités s'ouvraient concernant cette thématique: soit les tests cosmologiques par moyen de l'observation des ondes gravitationnelles émises par le binaires compactes [1–5], soit les fonds stochastiques d'ondes gravitationnelles générés dans l'univers primordial [6–14]. Ayant récemment écrit une revue sur ce dernier sujet, en collaboration avec Daniel Figueroa [15], j'ai opté pour la deuxième possibilité. Une bonne partie de ce mémoire est extraite donc de la revue, mais en ce qui

concerne les sources d'ondes gravitationnelles qui y sont traités, j'ai sélectionné premièrement celle sur laquelle j'ai travaillé le plus par le passé: les transitions de phase cosmologiques de premier ordre.

Le mémoire est structuré comme suit. Le chapitre 2 définit les ondes gravitationnelles dans l'univers en expansion, et le chapitre 3 introduit et motive les fonds stochastiques d'ondes gravitationnelles d'origine cosmologique. Le chapitre 4 présente les limites supérieures à ces fonds stochastiques, et les détecteurs d'ondes gravitationnelles opérationnels et futurs. Le chapitre 5 adresse le spectre de modes tensoriels produit lors de l'inflation *slow roll*, et son évolution depuis la fin de l'inflation jusqu'à maintenant.

Le chapitre 6 est la partie la plus importante de ce mémoire, et traite du fond stochastique d'ondes gravitationnelles produit par les transitions de phase de premier ordre. La première partie du chapitre est de nouveau extraite de la revue, et résume les caractéristiques principales du signal. La deuxième partie inclut quatre publications sélectionnées parmi mes travaux. La première publication est une analyse du signal produit par la turbulence magnétohydrodynamique qui survient après la transition de phase [9]. Les trois autres sont de caractère plus observationnels. Elles étudient la détection du signal issu de différentes transitions de phase, qui ont lieu à différents échelles d'énergie dans l'univers primordial, par différents détecteurs d'ondes gravitationnelles. En particulier, la section 6.3 traite de LISA et, par conséquent, des transitions de phase autour et au delà de l'échelle éléctrofaible [12]. La section 6.4 analyse par contre les Pulsar Timing Arrays, et donc la transition de phase QCD [10]. Finalement la section 6.5 examine le Cosmic Explorer et des transitions de phase hypothétiques à très haute température, autour de 10^6 GeV [14]. J'ai choisi ces publications parce que elle montrent le potentiel que ont les détecteurs d'ondes gravitationnelles de tester l'univers à des échelles d'énergie très diversifiées, et qui ne sont pas accessibles par d'autre observables cosmologiques basées sur l'émission électromagnétique.

Chaque chapitre, et chaque section qui inclut une publication, sont dotés d'un préambule pour en faciliter la lecture. Les préambules expliquent le contexte, résument les principaux résultat, et présentent les développements et mes projets futurs concernant la thématique, s'il y en a. J'ai joint mon CV à la fin du mémoire.

Contents

Chapter 1

Introduction

The first detection of gravitational waves (GWs) by the LIGO/Virgo collaboration on Sept. 2015 [16], has happily ended 50 years of experimental effort towards a direct detection of GWs. At the same time, it has proven the existence of a quite unexpected source, binary systems with fairly massive stellar-origin black holes. It was a first hint of the great potential of GW detection for the exploration and understanding of the universe: further detections by the aLIGO interferometer first, and by the aLIGO and aVirgo network starting from summer 2017, have subsequently fully revealed this potential [17–20]. The implications of these detections concern not only the discovery of new astrophysical objects, but extend also to powerful tests of fundamental physics and cosmology. Several aspects of General Relativity (GR) can be probed, such as for example the speed of propagation and polarisation of GWs. The first detection of the coalescence of two neutron stars, accompanied by the coincident detection of the same event in various electromagnetic bands [21, 22], has strongly constrained the GW propagation speed $|c_T - 1| \leq 5 \cdot 10^{-16}$. Focussing on cosmology this has, for example, important consequences for modified gravity scenarios candidates to explain the current acceleration of the universe, see e.g. [23–26], and [27, 28] for early works. Moreover, this observation has provided a measurement of the Hubble rate today [29], though not precise enough yet to help solving the tension between Cosmic Microwave Background (CMB) [30] and local universe measurements [31]. The measurement of the Hubble rate will however improve consistently as new GW signals will be detected in the upcoming years.

The discovery potential of GW observations also concerns the cosmology of the early universe. On general grounds, due to the weakness of gravity, GWs are decoupled from the

rest of matter and radiation components in the universe, upon production: comparing the rate of interaction of GWs with the Hubble rate, one gets qualitatively [32]

$$\frac{\Gamma(T)}{H(T)} \sim \frac{G^2\,T^5}{T^2/M_{Pl}} = \left(\frac{T}{M_{Pl}}\right)^3 , \tag{1.1}$$

where M_{Pl} denotes the Planck mass, $G = 1/M_{Pl}^2$ the Newton constant, $H(T) \sim T^2/M_{Pl}$ the Hubble rate in the radiation dominated era, and we have assumed a weak interaction with rate $\Gamma(T) = n\,\sigma\,v$, with the number density of particles $n \sim T^3$, cross-section $\sigma \sim G^2T^2$ and $v \sim 1$. This estimate shows that the GW interaction rate is smaller than the Hubble parameter, essentially at any temperature in the universe $T < M_{Pl}$ for which our present knowledge about gravitation holds. In other words, GWs propagate freely in the early universe, immediately after they are generated. This means that GWs carry unique information about the processes that produced them, and therefore about the state of the universe at epochs and energy scales unreachable by any other means. The energy scales that GWs can probe extend beyond the reach of presently available observational probes of the universe, mostly based on electromagnetic emission. Furthermore, GWs can provide information on particle physics, in a complementary way to the Large Hadron Collider or future particle colliders. Mechanisms generating GWs in the early universe are typically based on theories beyond the Standard Model of particle physics. They can occur within a broad range of energies, from the QCD scale $\sim \mathcal{O}(10^2)$ MeV, all the way up to the inflationary scale, bounded as $E_{\rm inf} \lesssim 10^{16}$ GeV.

The potential of GW detection to improve our knowledge of the early universe, is in principle comparable to the one of the CMB detection at its dawn, which marked the beginning of modern cosmology. Still, the GW signals must have sufficient amplitude to be captured by current and future GW detectors. In general, this requires the production of a substantial amount of tensor metric fluctuations. Fortunately, there are a number of well motivated mechanisms that can generate cosmological GW backgrounds within the reach of some GW experiments. Furthermore, the number of present and planned GW detectors is increasing, and presently include: the network of terrestrial interferometers, currently composed by aLIGO and aVirgo, but to be complemented by KAGRA in the near future, and subsequently by LIGO India; the space-based interferometer LISA, which has been accepted by the European Space Agency with a predicted launch date around 2034; and Pulsar Tim-

ing Arrays, which in the future will reach an extreme sensitivity with the Square Kilometre Array.

In the following, we first present some generalities on GW signals from the early universe, and then focus on two processes that can generate a stochastic GW background: after having briefly overviewed standard slow roll inflation, we thoroughly discuss the main topic of this dissertation, first order phase transitions (PTs) in the early universe. The manuscript is organised as follows. In chapter 2 we provide a definition of GWs, initially on a flat space-time, and then focussing on the relevant case of a Friedmann-Lemaître-Robertson-Walker (FLRW) background, together with some noteworthy solutions of the GW equation of motion. In chapter 3, after discussing why any GW background produced in the early universe is of stochastic nature, we present a general characterization of a statistically homogeneous and isotropic stochastic gravitational wave background (SGWB). In chapter 4 we review the present constraints on SGWBs, and discuss some of the characteristics of current and future GW detectors. In chapter 5 we discuss the irreducible SGWB arising from quantum vacuum fluctuations in standard inflation, and its evolution until today. Finally, chapter 6 is dedicated to first order phase transitions beyond the standard model of particle physics, both related and unrelated to the electroweak symmetry breaking.

Notations. Throughout the manuscript, unless otherwise specified, we use units $c = \hbar = 1$. We will use interchangeably the Newton constant G, the full Planck mass $M_{Pl} \simeq 1.22 \cdot 10^{19}$ GeV, or the reduced Planck mass $m_{Pl} \simeq 2.44 \cdot 10^{18}$ GeV, related through $M_{Pl}^2 = 8\pi m_{Pl}^2 = 1/G$. Latin indices are reserved for spatial dimensions $i, j, k, ... = 1, 2, 3$, and Greek indices for space-time dimensions $\mu, \nu, \alpha, \beta, ... = 0, 1, 2, 3$. We assume the Einstein convention so that repeated indices are interpreted as a sum over their values. We use a flat FLRW metric $ds^2 = -dt^2 + a^2(t)\,\delta_{ij}\,dx^i dx^j = a^2(\eta)(d\eta^2 + \delta_{ij}\,dx^i dx^j)$, where t denotes physical time, and η (alternatively τ in some sections) denotes the conformal time. Comoving momenta are presented by k, the physical Hubble rate is denoted by H, and the conformal Hubble rate by $\mathcal{H}$. The critical density today is

$$\rho_c^0 = \frac{3H_0^2}{8\pi G}\,, \tag{1.2}$$

and, unless otherwise specified, cosmological parameters are fixed to the CMB values given in [30]. Our Fourier convention is given in section 2.4.

Chapter 2

Definition of gravitational waves

This chapter, taken from the review [15], presents the definition of GWs. We first discuss the case of 'linearized gravity' in Sect. 2.1, defining GWs as metric perturbations in globally-vacuum asymptotically flat space-times. A more general definition is given in Sect. 2.2, including the case when sources are present, by decomposing the metric perturbation into scalar-vector-tensor components. We identify the GWs with the only gauge-invariant radiative part of the metric perturbation. After a discussion on the notion of GWs in arbitrary space-times (Sect. 2.3), we focus on the cosmological context, introducing the GW equation of motion in an expanding FLRW universe, and discussing some of its solutions in vacuum (Sect. 2.4). The GW evolution in the presence of a generic source is postponed to Sect. 3, after we have introduced the statistical characterization of cosmological SGWBs.

The main aim of this chapter is to present the framework necessary to define GWs in a FLRW background. This definition is not completely straightforward, and it is possible because of the symmetries of the FLRW space-time, namely homogeneity and isotropy. We also derive here two solutions of the GW equation of motion, for sub- and super-horizon modes, that will be useful for the rest of the dissertation.

2.1 Linearized theory in vacuum: the transverse-traceless gauge

A natural approach to introduce gravitational waves (GWs) is that of 'linearised gravity', by which one considers a small perturbation over a fixed Minkowski background

$\eta_{\mu\nu} \equiv \text{diag}(-1,+1,+1,+1)$,

$$g_{\mu\nu}(x) = \eta_{\mu\nu} + h_{\mu\nu}(x)\,, \qquad |h_{\mu\nu}(x)| \ll 1\,. \tag{2.1}$$

The condition $|h_{\mu\nu}(x)| \ll 1$ implies that one is allowing for *a*) only weak gravitational fields, and *b*) a restricted set of coordinate systems where Eq. (2.1) holds. General Relativity (GR) is invariant under general coordinate transformations $x^\mu \longrightarrow x'^\mu(x)$, under which the metric tensor transforms as $g'_{\mu\nu}(x') = \frac{\partial x^\alpha}{\partial x'^\mu}\frac{\partial x^\beta}{\partial x'^\nu} g_{\alpha\beta}(x)$. This implies that, under general infinitesimal coordinate transformations $x'^\mu \longrightarrow x^\mu + \xi^\mu$, with $\xi^\mu(x)$ an arbitrary infinitesimal vector field, the metric perturbation transforms as

$$h'_{\mu\nu}(x') = h_{\mu\nu}(x) - \partial_\mu \xi_\nu - \partial_\nu \xi_\mu\,. \tag{2.2}$$

In order to preserve the functional form of Eq. (2.1) in the new system of coordinates, i.e. $g'_{\mu\nu}(x') = \eta_{\mu\nu} + h'_{\mu\nu}(x')$, $|h'_{\mu\nu}(x')| \ll 1$, we require $|\partial_\alpha \xi_\beta| \lesssim |h_{\alpha\beta}|$. Therefore, only slowly varying infinitesimal coordinate transformations are a symmetry of the linearised theory[1].

The affine connection (Christoffel symbols) to linear order in the tensor perturbation is

$$\Gamma^\alpha{}_{\mu\nu} \equiv \frac{1}{2} g^{\alpha\beta}(\partial_\nu g_{\beta\mu} + \partial_\mu g_{\alpha\nu} - \partial_\beta g_{\mu\nu}) = \frac{1}{2}(\partial_\nu h^\alpha{}_\mu + \partial_\mu h^\alpha{}_\nu - \partial^\alpha h_{\mu\nu}) + \mathcal{O}(h_{**}^2)\,. \tag{2.3}$$

Using this expression we can write, also to linear order, the Riemann tensor, Ricci tensor and Ricci scalar, as

$$R^\alpha{}_{\mu\nu\beta} = \partial_\nu \Gamma^\alpha{}_{\mu\beta} - \partial_\beta \Gamma^\alpha{}_{\mu\nu} = \frac{1}{2}(\partial_\mu\partial_\nu h^\alpha{}_\beta + \partial_\beta\partial^\alpha h_{\nu\mu} - \partial_\nu\partial^\alpha h_{\mu\beta} - \partial_\beta\partial_\mu h^\alpha_\nu)\,, \tag{2.4}$$

$$R_{\mu\nu} \equiv R^\alpha{}_{\mu\alpha\nu} = \frac{1}{2}(\partial_\nu\partial_\alpha h^\alpha_\mu + \partial_\mu\partial^\alpha h_{\nu\alpha} - \partial_\mu\partial_\nu h - \Box h_{\mu\nu})\,, \tag{2.5}$$

$$R = R^\mu{}_\mu = (\partial^\alpha\partial_\beta h_\alpha^\beta - \Box h)\,, \tag{2.6}$$

where $h \equiv h^\alpha{}_\alpha$ is the trace of the metric perturbation, and $\Box \equiv \partial_\alpha\partial^\alpha$. From these expressions

[1] Notice that under a Lorentz transformation $x'_\mu = \Lambda_\mu{}^\nu x_\nu$, $g'_{\mu\nu}(x') = \Lambda_\mu{}^\alpha \Lambda_\nu{}^\beta g_{\alpha\beta}(x)$, preservation of Eq. (2.1) requires $|\Lambda_\mu{}^\alpha \Lambda_\nu{}^\beta h_{\alpha\beta}(x)| \ll 1$, so that it remains true that $|h'_{\mu\nu}(x')| \ll 1$. Rotations do not spoil the condition $|h_{\mu\nu}(x)| \ll 1$, but boosts could, and therefore must be restricted to those that do not spoil such condition. As $h_{\mu\nu}(x)$ is invariant under constant displacements $x'^\mu \longrightarrow x^\mu + a^\mu$, linearised gravity Eq. (2.1) is also invariant under Poincaré transformations.

we can construct the Einstein tensor, again to first order in the metric perturbation, as

$$\begin{aligned} G_{\mu\nu} &\equiv R_{\mu\nu} - \frac{1}{2}\eta_{\mu\nu}R = \frac{1}{2}(\partial_\nu\partial_\alpha h^\alpha_\mu + \partial_\mu\partial^\alpha h_{\nu\alpha} - \partial_\mu\partial_\nu h - \Box h_{\mu\nu} - \eta_{\mu\nu}\partial^\alpha\partial_\beta h_\alpha^{\ \beta} + \eta_{\mu\nu}\Box h) \\ &= \frac{1}{2}(\partial_\alpha\partial_\nu \bar{h}^\alpha_{\ \mu} + \partial^\alpha\partial_\mu\bar{h}_{\nu\alpha} - \Box\bar{h}_{\mu\nu} - \eta_{\mu\nu}\partial_\alpha\partial^\beta\bar{h}^\alpha_{\ \beta})\,, \end{aligned} \tag{2.7}$$

where in the last line, for convenience, we have introduced a new metric perturbation

$$\bar{h}_{\mu\nu} \equiv h_{\mu\nu} - \frac{1}{2}\eta_{\mu\nu}\,h\,. \tag{2.8}$$

As the trace of $\bar{h}_{\mu\nu}$ has opposite sign to that of $h_{\mu\nu}$, $\bar{h} = -h$, $\bar{h}_{\mu\nu}$ is referred to as the trace-reversed metric perturbation. Writing $G_{\mu\nu}$ in terms of $\bar{h}_{\mu\nu}$ has the advantage that it eliminates the trace.

The expression of $G_{\mu\nu}$ in Eq. (2.7) can be further simplified, by exploiting the invariance of the linearised theory under slowly varying infinitesimal coordinate transformations. Under $x'^\mu \longrightarrow x^\mu + \xi^\mu$, the metric perturbation $h_{\mu\nu}$ changes as in Eq. (2.2), whereas the trace-reversed perturbation transforms as

$$\bar{h}'_{\mu\nu}(x') = \bar{h}_{\mu\nu}(x) + \xi_{\mu\nu}(x)\,, \quad \xi_{\mu\nu}(x) \equiv \eta_{\mu\nu}\partial_\alpha\xi^\alpha - \partial_\mu\xi_\nu - \partial_\nu\xi_\mu\,. \tag{2.9}$$

In light of the expression of $G_{\mu\nu}$ in terms of $\bar{h}_{\alpha\beta}$, it seems convenient to make a coordinate transformation such that the metric perturbation verifies

$$\partial^\mu\bar{h}_{\mu\nu}(x) = 0\,. \tag{2.10}$$

We now demonstrate that this gauge choice, known as the Lorentz gauge, is always possible. Let us start with an arbitrary perturbation $\bar{h}_{\mu\nu}$ for which $\partial^\mu\bar{h}_{\mu\nu} \neq 0$. The Lorentz gauge condition, using Eq. (2.9), transforms as

$$\partial'^\mu\bar{h}'_{\mu\nu}(x') = \partial^\mu\bar{h}_{\mu\nu}(x) - \Box\xi_\nu\,, \tag{2.11}$$

so that we can always demand that $\partial'^\mu\bar{h}'_{\mu\nu}(x') = 0$, as long as

$$\Box\xi_\nu = f_\nu(x)\,, \qquad f_\nu(x) \equiv \partial^\mu\bar{h}_{\mu\nu}(x)\,. \tag{2.12}$$

One can always find solutions to the above Eq. (2.12), because the d'Alembertian operator $\Box$ is invertible. Therefore, one is free to exploit the invariance of the linearised theory under infinitesimal coordinate transformations, in order to pick the Lorentz gauge.

The advantage of expressing $G_{\mu\nu}$ in terms of the trace-reverse metric, becomes now manifest. Restricting the coordinate systems to those verifying the Lorentz-gauge condition Eq. (2.10), leads to a very simple expression for the Einstein tensor,

$$G^{(\mathrm{L})}_{\mu\nu} = -\frac{1}{2}\Box\bar{h}_{\mu\nu}\,, \tag{2.13}$$

where $^{(\mathrm{L})}$ refers to the Lorentz gauge. One can always write $G_{\mu\nu}$ as in Eq. (2.13), as long as one restricts oneself to the set of Lorentz coordinate systems verifying Eq. (2.10). The amount of gauge freedom in Lorentz coordinate systems is of course reduced, compared to the full freedom in linearized gravity under general infinitesimal coordinate transformations given by Eqs. (2.2), (2.9). Once $\bar{h}_{\mu\nu}$ verifies $\partial^\mu\bar{h}_{\mu\nu}(x) = 0$, we can always make a further infinitesimal coordinate transformation $x'^\mu \longrightarrow x^\mu + \xi^\mu$, so that the new metric perturbation $\bar{h}'_{\mu\nu}$ still verifies $\partial'^\mu\bar{h}'_{\mu\nu}(x') = 0$, as long as Eq. (2.12) is satisfied with $f_\nu(x) = 0$. The gauge freedom within Lorentz coordinate systems amounts therefore, to an infinitesimal vector displacement characterized by four functions $\xi_\nu(x)$, which are not fully free, but rather restricted to satisfy the source-less wave equation[2] $\Box\xi_\nu = 0$.

In the Lorentz gauge, linearized Einstein gravity reduces therefore to the equation

$$\Box\bar{h}_{\mu\nu} = -\frac{2}{m_p^2}T_{\mu\nu}\,, \tag{2.14}$$

which is nothing else but a wave equation with a source. The general homogeneous solution to the wave equation, based on the superposition of the linearly independent solutions, can be written as

$$\bar{h}_{\mu\nu}(x) = \int d^3k\ (\bar{h}_{\mu\nu}(\mathbf{k})e^{ikx} + \bar{h}^*_{\mu\nu}(\mathbf{k})e^{-ikx})\,, \quad \text{with}\ \ k^\mu\bar{h}_{\mu\nu} = 0\,, \tag{2.15}$$

where $kx \equiv k^\mu x_\mu = -\omega(|\mathbf{k}|)t + \mathbf{k}\cdot\mathbf{x}$, $\omega(|\mathbf{k}|) = |\mathbf{k}|$, and $\bar{h}_{\mu\nu}(\mathbf{k})$, are functions that depend solely on the wave vector $\mathbf{k}$. The latter are not free, but must satisfy $k^\mu\bar{h}_{\mu\nu} = 0$, as it follows from

[2] Alternatively, the gauge freedom in Lorentz coordinate systems, amounts to 8 free functions depending on the 3 spatial coordinates, determining the initial data hyper-surface.

Eq. (2.10). The solution Eq. (2.15) characterizes completely a gravitational wave background $h_{\mu\nu}(x) \equiv \bar{h}_{\mu\nu}(x) - \frac{1}{2}\eta_{\mu\nu}\bar{h}(x)$, at every space-time point $x = (\mathbf{x}, t)$. In light of Eqs. (2.14) and (2.15), it becomes clear why, in fact, we speak of gravitational waves.

As the Lorentz gauge Eq. (2.10) represents 4 constraints over the trace-reverse metric perturbation $\bar{h}_{\mu\nu}$, one might be tempted to conclude that there are in total $10 - 4 = 6$ radiative degrees of freedom verifying Eq. (2.14), and hence propagating at the speed of light. However, this is not the case: as discussed above, fixing the Lorentz gauge does not saturate completely the gauge freedom. In fact, from Eq. (2.9), we see that the trace-reversed metric changes under infinitesimal coordinate transformations, as $\bar{h}_{\mu\nu} \longrightarrow \bar{h}_{\mu\nu} + \xi_{\mu\nu}$, with $\xi_{\mu\nu} \equiv \eta_{\mu\nu}\partial^{\alpha}\xi_{\alpha} - \partial_{\mu}\xi_{\nu} - \partial_{\nu}\xi_{\mu}$. Once in a Lorentz frame $\partial^{\mu}\bar{h}_{\mu\nu} = 0$, to remain in a Lorentz frame after applying a new infinitesimal coordinate transformation, requires that $\Box\xi_{\mu} = 0$. From this we observe that also $\Box\xi_{\mu\nu} = 0$ is verified.

We now restrict to globally-vacuum spatially flat space-times, where the first condition implies $T_{\mu\nu}(x) = 0$ at every point and time, and the second conditions requires $h_{\mu\nu}(x) \longrightarrow 0$ as $|\mathbf{x}| \longrightarrow \infty$ (the case where a source is present is treated in the next section). It follows then, that the wave equation is invariant under Lorentz preserving infinitesimal coordinate transformations[3], as $\Box'\bar{h}'_{\mu\nu} = \Box(\bar{h}_{\mu\nu} + \xi_{\mu\nu}) = \Box\bar{h}_{\mu\nu} = 0$. In light of this, we can consider taking 4 infinitesimal vector displacements ξ_{μ} (appropriately chosen so that $\Box\xi_{\mu} = \Box\xi_{\mu\nu} = 0$ is verified), and use them to impose 4 conditions over a newly (Lorentz-gauge preserving) transformed metric perturbation $\bar{h}'_{\mu\nu}(x') = \bar{h}_{\mu\nu}(x) + \xi_{\mu\nu}(x)$, hence eliminating 4 degrees of freedom. In other words, out of the seemingly 6 degrees of freedom that verify the wave equation Eq. (2.14), we realize that, in reality, only two independent degrees of freedom are present. These are the truly physical propagating degrees of freedom, as any new Lorentz-gauge preserving coordinate transformation $\bar{h}_{\mu\nu} \longrightarrow \bar{h}_{\mu\nu} + \xi_{\mu\nu}$, with $\Box\xi_{\mu} = \Box\xi_{\mu\nu} = 0$, would not reduce further the number of independent degrees of freedom below 2.

Under these circumstances, one can exploit the residual gauge freedom to eliminate directly components of the metric perturbation. For instance, using Eq. (2.9), we can make the trace and the spatial-temporal components to vanish, $\bar{h} = \bar{h}_{0i} = 0$. This implies that we do not need to differentiate any more between trace-reversed and normal perturbations, as

[3]The box operator $\Box$ also changes under a coordinate transformation, $\Box' = \eta^{\mu\nu}\frac{\partial}{\partial x'^{\mu}}\frac{\partial}{\partial x'^{\nu}} = \eta^{\mu\nu}[(\delta^{\alpha}_{\mu} - \frac{\partial\xi^{\alpha}}{\partial x^{\mu}})\frac{\partial}{\partial x^{\alpha}}]\,[(\delta^{\beta}_{\nu} - \frac{\partial\xi^{\beta}}{\partial x^{\nu}})\frac{\partial}{\partial x^{\beta}}] = \eta^{\mu\nu}\frac{\partial}{\partial x^{\mu}}\frac{\partial}{\partial x^{\nu}} + \mathcal{O}(\partial\xi) = \Box + \mathcal{O}(\partial\xi)$. As $\mathcal{O}(|\partial\xi|) \lesssim \mathcal{O}(|h_{**}|)$, then $\Box' = \Box + \mathcal{O}(|h_{**}|)$, and hence $\Box' h_{\mu\nu} = \Box h_{\mu\nu} + \mathcal{O}(h^2_{**})$.

they become equal $\bar{h}_{\mu\nu} = h_{\mu\nu}$. From the Lorentz condition we obtain that $\dot{h}_{00} = -\partial_i h_{i0} = 0$, and hence that the temporal-temporal component is only a function of the spatial coordinates $h_{00} = V(\mathbf{x})$. This time independent term corresponds in fact to the static part of the gravitational interaction, i.e. to the Newtonian potential. As GWs are only concerned with the time-dependent part of the gravitational interaction, we may very well set $h_{00} = 0$. So in summary, we have specialized the gauge to

$$h_{\mu 0} = 0\,, \qquad h = h^{i}{}_{i} = 0\,, \qquad \partial_i h_{ij} = 0\,, \tag{2.16}$$

where the last condition follows from the Lorentz condition Eq. (2.10). This is known as the transverse-traceless (TT) gauge. The counting of the degrees of freedom in the TT gauge becomes now more clear than before, as after having eliminated all temporal components $h_{\mu 0} = 0$, we are left with 6 degrees of freedom in the spatial components h_{ij}. Out of these 6 degrees of freedom, 3 are further eliminated from the 3 transversality condition(s) $\partial_i h_{ij} = 0$, and 1 more degree of freedom is eliminated from the trace-less condition $h = h^{i}{}_{i} = 0$. Hence, we obtain that there are, finally, only $6 - 3 - 1 = 2$ degrees of freedom surviving. Once the TT gauge Eq. (2.16) is adopted, gauge freedom is saturated.

The TT gauge is therefore particularly convenient as it fixes completely the gauge freedom, so that the metric perturbation contains only the physical radiative degrees of freedom. This can be seen particularly clearly by considering a plane wave propagating in direction $\hat{n} = \mathbf{k}/|\mathbf{k}|$. Due to the transversality condition $\partial_i h_{ij} = 0$, we see that the tensor components parallel to the direction of propagation vanish, as $\hat{n}_i h_{ij} = 0$. Without loss of generality, we can fix $\hat{z} = \hat{n}$, so that only h_{11}, h_{12}, h_{21} and h_{22} are non-zero in such system of reference. As we also require the metric perturbation to be trace-less and symmetric, then we are left only with 2 independent components, which we call $h_\times \equiv h_{12} = h_{21}$ and $h_+ \equiv h_{11} = -h_{22}$. We find that the perturbed line element, due to the passing of a GW, is thus given by

$$ds^2 = -dt^2 + dz^2 + (1 + h_+)dx^2 + (1 - h_+)dy^2 + 2h_\times dxdy\,, \tag{2.17}$$

where it is manifest that there are only 2 degrees of freedom, $h_\times$ and h_+.

Furthermore, in a globally vacuum space-time, all non-zero components of the Riemann

tensor can be obtained from R_{i0j0}, which in the TT gauge reads

$$R_{i0j0} = -\frac{1}{2}\ddot{h}_{ij}\,. \tag{2.18}$$

This simple relation between the Riemann tensor and metric perturbations in the TT-gauge, makes particularly simple the study of the response of a detector when a GW passes through it. We refer the reader to the elaborated discussion on this in section 1.3 of [33].

2.2 Linearized theory in matter: scalar-vector-tensor decomposition

We ended the previous section considering linearised gravity over a Minkowski background ($g_{\mu\nu} = \eta_{\mu\nu} + h_{\mu\nu}$), in asymptotically-flat ($h_{\mu\nu} \longrightarrow 0$ at infinity) and globally vacuum space-times (i.e. with null stress-energy tensor everywhere $T_{\mu\nu} = 0$). In this setting, we were able to demonstrate that GWs are characterised by only two physical degrees of freedom, h_+ and $h_\times$. However, this characteristic is a manifestation of the intrinsic nature of the gravitational interaction, mediated by the graviton, a spin-two massless field that has only two independent helicity states (see e.g. chapter 2 of [33]). The TT gauge, that can only be picked in vacuum, clearly exhibits the fact that GWs are characterised by only two physical degrees of freedom, corresponding to two polarisation states. However, this must be true in general, not only in globally vacuum space-times. In this section we develop a formalism that renders this fact manifest.

We thus maintain, in the following, the conditions of linearised gravity over a Minkowski background ($g_{\mu\nu} = \eta_{\mu\nu} + h_{\mu\nu}$, $|h_{\mu\nu}| \ll 1$), but consider the more realistic situation where a non-vanishing stress-energy tensor is present, $T_{\mu\nu} \neq 0$. The rest of this section is based on [34] (see also [35]), which presents the flat space-time limit of Bardeen's cosmological gauge-invariant perturbation theory [36]. We follow standard notations in cosmology (that deviate somewhat from those of the previous section): the background metric is $\bar{g}_{\mu\nu} = \eta_{\mu\nu}$, and we denote the first order metric perturbation as $\delta g_{\mu\nu}$ (this corresponds to $h_{\mu\nu}$ in the previous section). The main difference with the cosmological setting of [36] is that our metric background is Minkowski, and hence the energy momentum tensor $T_{\mu\nu}$ at the background level, must vanish.

We begin by decomposing the metric perturbation and the energy-momentum tensor into irreducible parts with respect to 2-dimentional rotations around a vector,

$$\delta g_{00} = -2\phi\,, \tag{2.19}$$

$$\delta g_{0i} = \delta g_{i0} = (\partial_i B + S_i)\,, \tag{2.20}$$

$$\delta g_{ij} = \delta g_{ji} = -2\psi\delta_{ij} + (\partial_i\partial_j - \frac{1}{3}\delta_{ij}\nabla^2)E + \partial_i F_j + \partial_j F_i + h_{ij}\,, \tag{2.21}$$

and

$$T_{00} = \rho\,, \tag{2.22}$$

$$T_{0i} = T_{i0} = \partial_i u + u_i\,, \tag{2.23}$$

$$T_{ij} = T_{ji} = p\,\delta_{ij} + (\partial_i\partial_j - \frac{1}{3}\delta_{ij}\nabla^2)\sigma + \partial_i v_j + \partial_j v_i + \Pi_{ij}\,. \tag{2.24}$$

By construction, the above functions can be classified as scalars, vectors and tensors, according to how they transform under rotations,

	$\delta g_{\mu\nu}$	$T_{\mu\nu}$
Scalar(s)	ϕ, B, ψ, E	ρ, u, p, σ
Vector(s)	S_i, F_i	u_i, v_i
Tensor(s)	h_{ij}	Π_{ij}

In order not to overcount degrees of freedom, the vector and tensor parts must satisfy the following conditions

$$\partial_i S_i = 0 \text{ (1 constraint)}\,, \quad \partial_i F_i = 0 \text{ (1 constraint)}\,, \tag{2.25}$$

$$\partial_i h_{ij} = 0 \text{ (3 constraints)}\,, \quad h_{ii} = 0 \text{ (1 constraint)}\,. \tag{2.26}$$

and

$$\partial_i u_i = 0 \text{ (1 constraint)}\,, \quad \partial_i v_i = 0 \text{ (1 constraint)}\,, \tag{2.27}$$

$$\partial_i \Pi_{ij} = 0 \text{ (3 constraints)}\,, \quad \Pi_{ii} = 0 \text{ (1 constraint)}\,, \tag{2.28}$$

where we have implicitly assumed that all terms vanish $\rho, u, u_i, p, \sigma, v_i, \Pi_{ij} \longrightarrow 0$ at infinity. The total number of degrees of freedom is as follows. For the metric perturbation, the total

number of functions introduced in Eqs. (2.19)-(2.21) is 16 = 4 scalars (ϕ, B, ψ, E) + 6 vector components (S_i, F_i) + 6 tensor components of the 3×3 symmetric tensor h_{ij}. The total number of constraints in Eqs. (2.25), (2.26) is 6, so the number of independent functions in the decomposition defined by Eqs. (2.19)-(2.21) is $10 = 16 - 6$, as expected for a 4×4 symmetric tensor. Analogous consistent counting follows for the energy-momentum tensor, decomposed in Eqs. (2.22)-(2.24), and subject to the constraint equations (2.27), (2.28).

Given our assumptions about metric perturbations over a flat background $\eta_{\mu\nu}$, and asymptotic flatness $\delta g_{\mu\nu} \longrightarrow 0$, the decomposition of the metric perturbation into scalar, vector and tensor pieces, defined by Eqs. (2.19)-(2.21), is actually unique. Given a metric perturbation $\delta g_{\mu\nu}$, one can always solve unequivocally for ϕ, B, ψ, E, S_i, F_i and h_{ij}, as a function of $\delta g_{\mu\nu}$. Similarly, the decomposition of the energy-momentum tensor by Eqs. (2.22)-(2.24) is also unique.

All functions introduced so far (scalars, vectors and tensors) are assumed to be arbitrary functions of space-time coordinates and, in general, they are not independent from each other. For instance, from the conservation of the stress-energy tensor $\partial^\mu T_{\mu\nu} = 0$, it follows that the functions introduced in Eqs. (2.22)-(2.24), must satisfy

$$\nabla^2 u = \dot{\rho} \quad (1 \text{ constraint}), \tag{2.29}$$

$$\nabla^2 \sigma = \frac{3}{2}(\dot{u} - p) \quad (1 \text{ constraint}), \tag{2.30}$$

$$\nabla^2 v_i = 2\dot{u}_i \quad (2 \text{ constraints}). \tag{2.31}$$

Therefore, considering these 4 extra constraints, in the case of the energy-momentum tensor, out of the 10 seemingly independent functions $\rho, u, u_i, p, \sigma, v_i, \Pi_{ij}$, there are in reality only $6 = 10 - 4$ independent degrees of freedom. For instance ρ, u_i, p, Π_{ij} can be set arbitrarily, whereas the remaining functions u, σ, v_i can be derived from the latter, by solving the system of Eqs. (2.29)-(2.31).

Similarly, from the conservation of the Einstein tensor $\partial^\mu G_{\mu\nu} = 0$ (which amounts to 4 constraints), it follows that out of the 10 metric functions ϕ, B, S_i, ψ, E, F_i, h_{ij} in the metric decomposition Eqs. (2.19)-(2.21), only $6 = 10 - 4$ functions are truly independent degrees of freedom. The relation among metric components is however more complicated than in the case of the stress-energy tensor components Eqs. (2.29)-(2.31), as it is the metric

perturbation $\delta g_{\mu\nu}$ (and not the Einstein tensor $G_{\mu\nu}$), that we have decomposed into scalar, vector, and tensor parts. In order to reduce the number of independent degrees of freedom in Eqs. (2.19)-(2.21) from 10 to 6, it is more practical to exploit the invariance of linearised gravity, under arbitrary infinitesimal coordinate transformations $x_\mu \longrightarrow x_\mu + \xi_\mu$. Following the logic of the metric decomposition in Eqs. (2.19)-(2.21), let us first express an arbitrary infinitesimal 4-vector displacement as

$$\xi_\mu = (\xi_0, \xi_i) \equiv (d_0, \partial_i d + d_i) \qquad \text{with} \;\; \partial_i d_i = 0\,, \tag{2.32}$$

where d, d_0, d_i are general functions of the space-time coordinates $(t, \mathbf{x})$. As the metric perturbation transforms under an arbitrary infinitesimal diffeomorphism as $\delta g_{\mu\nu} \longrightarrow \delta g_{\mu\nu} - \partial_\mu \xi_\nu - \partial_\nu \xi_\mu$, see Eq. (2.2), one obtains that scalar parts of the metric perturbation in Eqs. (2.19)-(2.21), transform as

$$\phi \longrightarrow \phi - \dot{d}_0\,, \qquad\qquad B \longrightarrow B - d_0 - \dot{d}\,, \tag{2.33}$$

$$\psi \longrightarrow \psi + \frac{1}{3}\nabla^2 d\,, \qquad E \longrightarrow E - 2d\,, \tag{2.34}$$

the vector parts as

$$S_i \longrightarrow S_i - \dot{d}_i\,, \qquad\qquad F_i \longrightarrow \quad F_i - 2d_i\,, \tag{2.35}$$

and the tensor part as

$$h_{ij} \longrightarrow h_{ij}\,. \tag{2.36}$$

The 2 degrees of freedom encoded in the tensor perturbation h_{ij} are therefore gauge invariant, i.e. independent of the system of coordinates (as long as we preserve the infinitesimal condition $|\delta g_{\mu\nu}| \ll 1$). Since we know that there should be only 6 $(= 10-4)$ physical degrees of freedom, it must be possible to reduce the above scalar and vector perturbations (8 functions) to only 4 $(= 6 - 2)$ degrees of freedom. In light of Eqs. (2.33), (2.34) and (2.35), one can build new

scalar and vector perturbations

$$\Phi \equiv -\phi + \dot{B} - \frac{1}{2}\ddot{E}\,, \tag{2.37}$$

$$\Theta \equiv -2\psi - \frac{1}{3}\nabla^2 E\,, \tag{2.38}$$

$$\Sigma_i \equiv S_i - \frac{1}{2}\dot{F}_i\,, \qquad \text{with} \;\; \partial_i \Sigma_i = 0\,, \tag{2.39}$$

which are directly invariant under arbitrary infinitesimal coordinate transformations.

Note that for the energy momentum tensor, we did not need to perform a coordinate transformation to exhibit the gauge-invariant independent degrees of freedom, as we just did for the metric perturbations: they followed simply after imposing energy-momentum conservation, see discussion after Eqs. (2.29)-(2.31). This is a consequence of the fact that, in our approach, the energy momentum tensor must be zero in the background, because of the assumption of linearisation around Minkowski. In fact, the first-order perturbation of a generic tensor $T_{\mu\nu} = \bar{T}_{\mu\nu} + \delta T_{\mu\nu}$ transforms under an infinitesimal coordinate transformation as $\delta T_{\mu\nu} \longrightarrow \delta T_{\mu\nu} + L_\xi \bar{T}_{\mu\nu}$, where $L_\xi \bar{T}_{\mu\nu}$ denotes the Lie derivative of the background component $\bar{T}_{\mu\nu}$, along the vector field ξ_μ (which reduces to Eq. (2.2) in flat spacetime and for the metric tensor). Therefore, a tensor with $\bar{T}_{\mu\nu} = 0$ is automatically gauge invariant, i.e. it is invariant under arbitrary infinitesimal coordinate transformations. This is the so-called Stewart Walker lemma [37, 38].

As the set of variables Φ, Θ, Σ_i and h_{ij} are gauge invariant, and all together represent in total 6 degrees of freedom ($= 1\ (\Phi) + 1\ (\Theta) + 2\ (\Sigma_i) + 2\ (h_{ij})$), we are certain that these variables represent the truly physical degrees of freedom of the metric. It must be possible therefore, to express the Einstein equations as a function exclusively of these variables. As a matter of fact, the Einstein tensor can be written purely in terms of such gauge invariant quantities, as

$$G_{00} = -\nabla^2 \Theta\,, \tag{2.40}$$

$$G_{0i} = -\frac{1}{2}\nabla^2 \Sigma_i - \partial_i \dot{\Theta}\,, \tag{2.41}$$

$$G_{ij} = -\frac{1}{2}\Box h_{ij} - \partial_{(i}\dot{\Sigma}_{j)} - \frac{1}{2}\partial_i\partial_j\left(2\Phi + \Theta\right) + \delta_{ij}\left[\frac{1}{2}\nabla^2\left(2\Phi + \Theta\right) - \ddot{\Theta}\right]. \tag{2.42}$$

Introducing now Eqs. (2.40)-(2.42) in the left hand side of the Einstein Equations $G_{\mu\nu} =$

$\frac{1}{m_p^2}T_{\mu\nu}$, and Eqs. (2.22)-(2.24) in the right hand side, one finds, with the help of Eqs. (2.29)-(2.31), that

$$\begin{aligned} \nabla^2\Theta &= -\tfrac{1}{m_p^2}\rho\,, \qquad & \nabla^2\Phi &= \tfrac{1}{2m_p^2}\left(\rho + 3p - 3\dot{u}\right)\,, \\ \nabla^2\Sigma_i &= -\tfrac{2}{m_p^2}u_i\,, \qquad & \Box h_{ij} &= -\tfrac{2}{m_p^2}\Pi_{ij}\,. \end{aligned} \tag{2.43}$$

It appears that only the tensor part of the metric h_{ij} obeys a wave equation. The other variables Θ, Φ and Σ_i, obey Poisson-like equations. Indeed, in a globally vacuum space-time, the above equations reduce to five Laplace equations and a wave equation,

$$\begin{aligned} \nabla^2\Theta &= 0\,, \qquad & \nabla^2\Phi &= 0\,, \\ \nabla^2\Sigma_i &= 0\,, \qquad & \Box h_{ij} &= 0\,. \end{aligned} \tag{2.44}$$

This demonstrates explicitly that, among the gauge-invariant degrees of freedom of the metric perturbation Θ, Φ, Σ_i and h_{ij}, only the tensor part h_{ij} (which has two independent components) represents radiative degrees of freedom that can propagate in vacuum.

The above statement is actually independent of the system of reference, as long as the metric perturbation remains as such, i.e. a perturbation $|\delta g_{\mu\nu}| \ll 1$. In Sect. 2.1 we found that the invariance under infinitesimal coordinate transformations of the linearised theory, allows to saturate the gauge freedom once one reduces the metric perturbations to only 2 degrees of freedom, in the transverse-traceless gauge and in vacuum. However, identifying correctly the truly gauge invariant and radiative degrees of freedom is not just a matter of a gauge choice. In some gauges, as e.g. the Lorentz one, it is possible to have all metric components satisfying a wave equation, but this is only a 'gauge artefact', arising due to the choice of coordinates. Such gauge choices, although useful for calculations, may mistakenly led to identify pure gauge modes with truly physical gravitational radiation.

To summarise, in general, a metric perturbation $\delta g_{\mu\nu}$ contains: *i*) gauge spurious degrees of freedom, *ii*) physical but non-radiative degrees of freedom, and *iii*) physical radiative degrees of freedom. In the previous section we have found that, using infinitesimal coordinate transformations, one can arrive to the result that only two physical radiative degrees of freedom are relevant. However, due to the presence of the physical non-radiative degrees of freedom, these cannot be made explicit, unless in vacuum: it is not possible in general to

write the metric perturbation in the TT gauge, since usually we cannot eliminate the temporal components of the stress-energy tensor that do not vanish $T_{00},\ T_{0i} \neq 0$. Nonetheless, here we have demonstrated that the linearised metric perturbation can be split up uniquely into scalar, vector and tensor parts, as in Eqs. (2.19)-(2.21). This decomposition contains all type of degrees of freedom $i) - iii)$. From Einstein equations it appears clearly that the physical radiative degrees of freedom correspond only to the tensor piece of the metric perturbation, i.e. to the piece that satisfies a wave equation and verifies the TT gauge conditions (often referred to as the TT piece), irrespective of the gauge choice. In vacuum, the TT-gauge happens to correspond to the set of coordinate systems where the whole metric perturbation reduces to the physical radiative degrees of freedom. In the presence of matter, there are instead four physical degrees of freedom on top of the TT ones. Yet, the latter are – unmistakably – the only physical degrees of freedom truly representing gravitational radiation, independently of the gauge choice, and/or the presence of matter.

2.3 Gravitational waves in a curved background

In section 2.1 we have presented the definition of GWs in the context of linearised gravity over a Minkowski background, in asymptotically-flat and globally vacuum space-times. In section 2.2 we have demonstrated that GWs can be unequivocally defined also dropping the assumption of globally-vacuum space-times. The next step is to drop the assumption of linearised theory over Minkowski, and tackle the definition of GWs over a curved background[4].

This step becomes indeed mandatory in order to define the GW energy momentum tensor [33, 34, 39]. In GR, every form of energy contributes to the curvature of space-time. In order to find expressions for the energy and momentum carried by GWs, one has to explore in which sense GWs are themselves a source of space-time curvature. However, this simple statement is enough to conclude that one needs to go beyond linearised theory over Minkowski: sticking to it, one excludes from the beginning the possibility of generating any form of curvature in the space-time, it being by definition flat. Furthermore, in the rest of this review we will be dealing with GWs generation processes operating in the early universe, and hence it is crucial that we determine how to define GWs over a FLRW background, which naturally corresponds to a curved background.

[4]We remind that in our treatment 'background' means 'everything except GWs'.

Going beyond linearised theory over Minkowski emerges as an outstanding necessity, but it is far from being a simple task. We need to generalize the theory to $g_{\mu\nu}(x) = \bar{g}_{\mu\nu}(x)+\delta g_{\mu\nu}(x)$, with $|\delta g_{\mu\nu}(x)| \ll |\bar{g}_{\mu\nu}(x)|$ and $\bar{g}_{\mu\nu}(x)$ a general metric. However, it is clear that in this setting it becomes non-obvious to define GWs, since it is non-trivial to distinguish the background from the fluctuation, as $\bar{g}_{\mu\nu}(x)$ can contain space- and time-dependent components, due for instance to space- and time-varying Newtonian fields. The only way to define fluctuations representing GWs in this context, is to exploit a possible separation of scales/frequencies: if the background $\bar{g}_{\mu\nu}(x)$ varies over a typical length-scale L_B (or its time variation is characterised by a typical frequency f_B), and the GWs have typical reduced wavelength $\lambda\!\!\!^{-} = \lambda/2\pi$ (or frequency $f = 1/\lambda$), one can distinguish the GWs from the background provided that $L_B \gg \lambda\!\!\!^{-}$ ($f_B \ll f$). In this case, the GWs can be viewed as small perturbations on a smooth background (from 'their' point of view), or rapidly varying perturbations over a slowly varying background.

Let us make this more explicit with two examples. We will properly introduce the case of the FLRW metric later on, but let us anticipate that in this case, it is easy to see that the typical space and time variations of the background today correspond to the Hubble factor, $L_B \sim 1/f_B \sim 1/(a_0 H_0)$ (here we refer to comoving quantities). For a GW production mechanism operating causally (i.e. within the causal horizon) at a given time t_* in the radiation or matter dominated eras, the typical wave-lengths/frequencies of the GW signal today would correspond to $\lambda = 1/f \leq 1/\mathcal{H}(t_*)$. Since the universe is expanding it holds that $\mathcal{H}(t_*) \gg a_0 H_0$, and therefore it is clear that the above conditions (in terms of length-scales and in terms of frequencies) are satisfied in this case. This is an anticipation of the fact that GWs can indeed be well defined in a cosmological context.

In the case of GWs arriving on Earth, e.g. from a compact binary coalescence, the situation is more complicated. Earth-based GW detectors have the best sensitivity to GWs for frequencies around $f \sim 100 - 1000$ Hz, corresponding to $\lambda\!\!\!^{-} \sim 500 - 50$ km: on these length scales, the Newtonian gravitational field of the Earth does have spatial variations, rendering it impossible to distinguish it from GWs solely based on the condition $L_B \gg \lambda\!\!\!^{-}$. Moreover, its amplitude is much bigger than the GW one, $\delta g_{00}^N \sim 10^{-9} \gg \delta g_{ij}^{\rm GW} \sim 10^{-21}$. On the other hand, the Earth gravitational field is almost static in the frequency window in which terrestrial interferometers operate: it varies mostly on typical frequencies $f_B \lesssim 0.1$ Hz. Therefore,

Earth-based interferometers can indeed perform GW measurements (as proven recently!), and distinguish GWs from the background, based on the condition $f_B \ll f$: i.e. by maximizing their sensitivity in a frequency window which is clean from the time varying Newtonian gravitational field, Earthquakes and other seismic motions.

Let us then start from the principle that GWs can be defined within the approximation that their wave-length (frequency) is much smaller (bigger) than the length (inverse time-scale) characterising the background space-time over which the waves are propagating. The method to implement this definition on a practical level, is to perform averages of physical quantities over a length-scale ℓ (time-scale τ) such that $\lambda\!\!\!^{-} \ll \ell \ll L_B$ $(1/f \ll \tau \ll 1/f_B)$. For proper covariant definitions of the averaging procedure, see [40].

Since an averaging is involved, it becomes clear that, in order to proceed consistently in the definition of GWs, it is necessary to go to second order in the expansion of the metric perturbation $|\delta g_{\mu\nu}| \ll 1$. Averaging the first order contribution in fact gives zero, because of the oscillatory nature of the waves. So we need to look for the contribution of GWs to the background curvature, but linear quantities in $\delta g_{\mu\nu}$ cannot influence the background, as they average to zero. On the other hand, the averaging of a second order quantity can mix two short wavelength (high frequency) modes, in such a way, that in total they contribute a long wavelength (low frequency) mode, as commonly experienced in convolutions. Therefore, second order quantities in $\delta g_{\mu\nu}$ can give rise to the corrections to the background metric at scales larger than the GW wavelength. A particularly relevant point, that will help to clarify these ideas, is the definition GW energy momentum tensor, which we discuss next.

For a full analysis of perturbation theory over a generic background to second order in $|\delta g_{\mu\nu}| \ll 1$, we refer the reader to the excellent treatments of Refs. [33, 34, 39]. Here, we only present the two main results that will be useful for us in the review: the definition of the GW energy momentum tensor, and the equation for the propagation of GWs on a curved background. Concerning the first point, the analysis of the Einstein equations at second order, shows that the effective energy momentum tensor of GWs is obtained by averaging the second order Ricci tensor. Denoting the metric perturbation as $h_{\mu\nu} = \delta g_{\mu\nu}$ and generalizing the trace-reserve metric perturbation definition as $\bar{h}_{\mu\nu} = h_{\mu\nu} - \frac{1}{2}\bar{g}_{\mu\nu}\bar{g}^{\alpha\beta}h_{\alpha\beta}$ (where $\bar{g}_{\mu\nu}$ is the background metric), the result reads, in the Lorentz gauge $\nabla^{\mu}\bar{h}_{\mu\nu} = 0$ and once all spurious

gauge modes have been removed, as

$$T^{\rm GW}{}_{\mu\nu} = \frac{\langle \nabla_\mu h_{\alpha\beta} \nabla_\nu h^{\alpha\beta} \rangle}{32\pi\, G}\,, \tag{2.45}$$

where ∇ denotes the covariant derivative with respect the background space-time, and $\langle ... \rangle$ an average over ℓ and/or τ. The above GW energy momentum tensor must be inserted in the right hand side of the background Einstein equations, as any other form of matter. It contributes to the background space-time curvature as a term of order $\mathcal{O}(h^2/\lambda\!\!\!^{-2})$, which must satisfy $h^2/\lambda\!\!\!^{-2} \lesssim 1/L_B^2$, where the $<$ sign applies if the background already contains a contribution from another (dominant) source of space-time curvature, whereas the $\simeq$ sign applies if the only contribution is due to the GWs. The consistency of the second order treatment is then manifest, since one has $|h_{\mu\nu}| \lesssim \lambda\!\!\!^{-}/L_B$: the definition of GWs in the limit $\lambda\!\!\!^{-}/L_B \ll 1$ implies, therefore, that these are small perturbations, $|h_{\mu\nu}| \ll 1$. From Eq. (2.45) we see that the energy density of GWs becomes the well known expression

$$\rho_{\rm GW} = T^{00}_{\rm GW} = \frac{\langle \dot{h}_{ij}\, \dot{h}^{ij} \rangle}{32\pi\, G}\,, \tag{2.46}$$

where we have written it in the TT gauge. Following the results presented in sections 2.1 and 2.2, TT gauge can be chosen either far away from the sources where one is almost in vacuum, in which case $\dot{h}_{ij}$ denotes the derivative with respect to the time variable of Minkowski metric; or in curved space-time, for example in FLRW, in which case $\dot{h}_{ij}$ denotes the derivative with respect to physical time, leading to Eq. (3.13). Note that, for FLRW at first order in perturbation theory, $\nabla_0 h_{ij} = \dot{h}_{ij}$.

To analyse the propagation of GWs on a curved background, one the other hand, one does not need to go to second order in the $h_{\mu\nu}$ expansion. The Einstein equations at first order, in the case of the expansion around a flat background, led to the propagation equation in (2.43). In the case of a curved background, this generalises to (see e.g. [41–44])

$$\begin{aligned} -\tfrac{1}{2}\Box \bar{h}_{\mu\nu} + \quad & R^{\lambda}{}_{\mu\nu}{}^{\sigma} \bar{h}_{\lambda\sigma} + \nabla_{(\nu} \nabla^\sigma \bar{h}_{\mu)\sigma} - \frac{1}{2} \bar{g}_{\mu\nu} \nabla^\alpha \nabla^\beta \bar{h}_{\alpha\beta} + \\ & + R^{\alpha\beta} \left[\frac{1}{2} \bar{g}_{\mu\nu} \bar{h}_{\alpha\beta} - \frac{1}{2} \bar{h}_{\mu\nu} \bar{g}_{\alpha\beta} + \bar{g}_{\beta(\mu} \bar{h}_{\nu)\alpha} \right] = 8\pi\, G\, \delta T_{\mu\nu}\,, \end{aligned} \tag{2.47}$$

where round parentheses in a subscript denote symmetrisation, $\bar{h}_{\mu\nu}$ is the trace reversed

metric perturbation, $\Box$, ∇, the Riemann and the Ricci tensors are defined with respect the background $\bar{g}_{\mu\nu}$. We have decomposed the matter energy momentum tensor as $T_{\mu\nu} = \bar{T}_{\mu\nu} + \delta T_{\mu\nu}$, where $\bar{T}_{\mu\nu}$ is the background contribution, sourcing the background curvature of $\bar{g}_{\mu\nu}$, while $\delta T_{\mu\nu}$ is the first order contribution, that can act as source of GWs. Note that we have written the above equation without fixing the gauge choice and in presence of a generic matter source, as in this way it can be directly adapted to the FRLW case. The above equation is most commonly written in vacuum and in the Lorentz gauge $\nabla^{\alpha}\bar{h}_{\alpha\beta} = 0$, where it takes the simpler form [34]

$$\Box\bar{h}_{\mu\nu} - 2R^{\lambda}{}_{\mu\nu}{}^{\sigma}\bar{h}_{\lambda\sigma} = 0\,. \tag{2.48}$$

In the limit $L_B \gg \lambda\!\!\!^{-}$, the couplings to the background due to the $\Box$ term and the term proportional to the background Riemann tensor, have the effect of imprinting gradual changes on the properties of the GWs, e.g. in their amplitude and polarisations. This can be analysed by solving the above equation in the geometric optics limit $L_B \gg \lambda\!\!\!^{-}$, with the result that GWs propagate along null geodesics of the space-time background, with parallel-transported polarisation, orthogonal to the rays, see e.g. [33] for a discussion about this. Furthermore, one of the consequences of the geometric optics limit is a conservation law, that represents, in the quantum language, the conservation of the number of gravitons.

In chapter 5 we will present an example of a situation, namely inflation, where the conservation of gravitons does not hold. During inflation one has that the GWs (sub-Hubble tensor metric perturbations) gradually exit the Hubble scale, breaking the condition $L_B \gg \lambda\!\!\!^{-}$. When this occurs, the dynamics of the GWs is strongly coupled to the dynamics of the background, and the graviton number is no longer conserved. We will explain this in detail in chapter 5. The important point to remark here is that, even though in that case $L_B \simeq \lambda\!\!\!^{-}$, one can still distinguish the background from the metric fluctuations (albeit the tensor modes become GWs only after they have crossed back inside the Hubble scale) because of the particular symmetries of the FLRW space-time.

All of this finally brings us to the definition of GWs in the particular case when the background space-time is the FLRW metric. It is a remarkable case in which the splitting of the metric into a curved background component plus linear perturbations can be

uniquely defined, even in the regime[5] $L_B \simeq \lambda$. The reason are the symmetries of the FLRW background, experimentally well verified by CMB observations [45]: the hyper-surfaces of constant time are homogeneous and isotropic. Therefore, there is no possible ambiguity between what pertains to $\bar{g}_{\mu\nu}(x)$ and what to $h_{\mu\nu}(x)$. Furthermore, because of homogeneity and isotropy, two-index tensors can be irreducibly decomposed on these hyper-surfaces under spatial translations (harmonic analysis) and rotations. One can therefore perform the same decomposition carried on in section 2.2, but on a time-evolving background. A general perturbation of the metric can be decomposed into scalar, vector and tensor modes, according to the way they transform under spatial rotations in the background space-time. For derivations of this decomposition in the case of a FLRW background, see e.g. [36, 38, 46, 47].

As already mentioned in section 2.2, the main difference with the flat space-time case is the presence of a non-zero energy momentum tensor at the background level, which has to satisfy the symmetries of the FLRW space (admitted cases are for example an unperturbed perfect fluid or a scalar field that depends on time only). Consequently, in cosmological perturbation theory one has to build a set of gauge-invariant variables also for the components of the energy momentum tensor, which we did not need to do in section 2.2. Moreover, in cosmological perturbation theory, it is customary to also expand the metric perturbations into eigenfunctions of the Laplacian (i.e. in Forurier modes), which represent irreducible components under translations. Other than this, the two analyses proceed in a very similar way.

In the context of cosmological perturbation theory one also finds that the two degrees of freedom of the tensor modes of the metric perturbations, h_{ij}, are the only radiative modes[6], and therefore correspond to GWs: scalar and vector modes cannot propagate in vacuum. The symmetries of the FLRW background imply that h_{ij} vanishes in the background: it is therefore gauge-invariant at first order by the Stewart Walker lemma (c.f. section 2.2). Scalar, vector and tensor modes are decoupled from each other at linear order in perturbation theory [38]. GWs may then be represented by the tensor spatial perturbations h_{ij} $(i, j = 1, 2, 3)$ of

[5] Another example are e.g. static space-times.

[6] Note that, in this context, one also finds a wave-like equation for the scalar Bardeen potential, which in the case of adiabatic perturbations of a perfect fluid and zero spatial curvature reads $\ddot{\Phi} + 3\mathcal{H}(1 + c_s^2)\dot{\Phi} + [\mathcal{H}^2(1 + 3c_s^2) - \mathcal{H}^2(1 + 3w) + k^2 c_s^2]\Phi = 0$, where w is the background fluid equation of state, and c_s its sound speed. However, these are sound waves and represent the perturbations in the matter-radiation fluid, coupled to the metric. They do not exist if the background fluid is not present, and their modes cannot propagate in vacuum: they have therefore an entirely different nature than the tensor mode.

the FLRW metric

$$ds^2 = -dt^2 + a^2(t)\,(\delta_{ij} + h_{ij})\,dx^i dx^j \tag{2.49}$$

with

$$\partial_i h_{ij} = h_{ii} = 0\,. \tag{2.50}$$

Since h_{ij} is symmetric, the transverse and traceless conditions (2.50), leaves only two independent degrees of freedom, which correspond to the two GW polarizations. For most practical purposes there is no need to go beyond linear order in perturbations theory.

2.4 Propagation of gravitational waves in expanding backgrounds

In this section we analyse the propagation of GWs in a cosmological context, and provide some useful definitions. The GW equation of motion is given by the Einstein equations linearized to first order in h_{ij}, over a FLRW background. It can be deduced from Eq. (2.47), by specifying the FLRW connection, Riemann and Ricci tensors, and keeping only the TT piece h_{ij} of the metric perturbation. This leads to

$$\ddot{h}_{ij}(\mathbf{x},t) + 3\,H\,\dot{h}_{ij}(\mathbf{x},t) - \frac{\nabla^2}{a^2}\,h_{ij}(\mathbf{x},t) = 16\pi G\,\Pi_{ij}^{TT}(\mathbf{x},t)\,, \tag{2.51}$$

where $\nabla^2 = \partial_i\,\partial_i$ is the Laplacian associated to the comoving coordinates x^i in (2.49), a dot denotes derivative with respect to t, $H = \dot{a}/a$ is the Hubble rate, and Π_{ij}^{TT} is the transverse and traceless part of the anisotropic stress. The anisotropic stress is given by

$$a^2\,\Pi_{ij} = T_{ij} - p\,a^2\,(\delta_{ij} + h_{ij})\,, \tag{2.52}$$

where T_{ij} denotes the spatial components of the energy-momentum tensor of the source, and p is the background pressure. In the RHS of Eq. (2.52), the term in $p\,\delta_{ij}$ is a pure trace that does not contribute to Π_{ij}^{TT}, while the term in $p\,h_{ij}$ cancels out with an identical term of opposite sign that emerges in the derivation of Eq. (2.51).

The transverse and traceless part of a tensor is most easily extracted in Fourier space.

Consider the spatial Fourier transform

$$\Pi_{ij}(\mathbf{x},t) = \int \frac{d^3\mathbf{k}}{(2\pi)^3}\,\Pi_{ij}(\mathbf{k},t)\,e^{-i\mathbf{k}\cdot\mathbf{x}}\,. \tag{2.53}$$

The transverse and traceless part of a symmetric tensor is then given by the projection (see e.g. Ref. [39])

$$\Pi_{ij}^{\rm TT}(\mathbf{k}) = \mathcal{O}_{ij,lm}(\hat{\mathbf{k}})\,\Pi_{lm}(\mathbf{k}) = \left[P_{il}(\hat{\mathbf{k}})\,P_{jm}(\hat{\mathbf{k}}) - \frac{1}{2}\,P_{ij}(\hat{\mathbf{k}})\,P_{lm}(\hat{\mathbf{k}})\right]\Pi_{lm}(\mathbf{k})\,, \tag{2.54}$$

with

$$P_{ij}(\hat{\mathbf{k}}) = \delta_{ij} - \hat{k}_i\,\hat{k}_j\,, \tag{2.55}$$

where $\hat{\mathbf{k}} = \mathbf{k}/k$ is the unit vector in the $\mathbf{k}$ direction. The operators P_{ij} are projectors on the subspace orthogonal to $\mathbf{k}$, satisfying $P_{ij}k_i = 0$ and $P_{ij}\,P_{jl} = P_{il}$. From this it follows directly that $k_i\,\Pi_{ij}^{\rm TT} = \Pi_{ii}^{\rm TT} = 0$.

The transverse and traceless perturbation h_{ij} can be decomposed into the two polarization states $r = +, \times$, as

$$h_{ij}(\mathbf{x},t) = \sum_{r=+,\times}\int \frac{d^3\mathbf{k}}{(2\pi)^3}\,h_r(\mathbf{k},t)\,,e^{-i\mathbf{k}\cdot\mathbf{x}}\,e_{ij}^r(\hat{\mathbf{k}}) \tag{2.56}$$

where the two polarisation tensors $e_{ij}^r(\hat{\mathbf{k}})$ can be taken to be real and to satisfy $e_{ij}^r(-\hat{\mathbf{k}}) = e_{ij}^r(\hat{\mathbf{k}})$. The condition for h_{ij} to be real is then $h_r^*(\mathbf{k},t) = h_r(-\mathbf{k},t)$. The two polarisation tensors depend only on the unit vector $\hat{\mathbf{k}}$ and are symmetric ($e_{ij}^r = e_{ji}^r$), transverse ($\hat{k}_i\,e_{ij}^r = 0$) and traceless ($e_{ii}^r = 0$). They can be written as

$$\begin{aligned} e_{ij}^+(\hat{\mathbf{k}}) &= \hat{m}_i\,\hat{m}_j - \hat{n}_i\,\hat{n}_j\,, \\ e_{ij}^\times(\hat{\mathbf{k}}) &= \hat{m}_i\,\hat{n}_j + \hat{n}_i\,\hat{m}_j\,, \end{aligned} \tag{2.57}$$

where $\hat{\mathbf{m}}$ and $\hat{\mathbf{n}}$ are two unit vectors that are orthogonal to $\hat{\mathbf{k}}$, and well as to each other. We

then have the orthonormal and completeness relations

$$e^r_{ij}(\hat{\mathbf{k}})\, e^{r'}_{ij}(\hat{\mathbf{k}}) = 2\,\delta_{rr'}\,, \tag{2.58}$$

$$\sum_{r=+,\times} e^r_{ij}(\hat{\mathbf{k}})\, e^r_{lm}(\hat{\mathbf{k}}) = P_{il}\,P_{jm} + P_{im}\,P_{jl} - P_{ij}\,P_{lm}\,, \tag{2.59}$$

where the projectors P_{ij} are defined in Eq. (2.55), and can be written alternatively as $P_{ij} = \hat{m}_i\,\hat{m}_j + \hat{n}_i\,\hat{n}_j$.

The space-time behavior of GWs is determined by Eq. (2.51), with solutions depending on the particular source considered. Most examples of cosmological sources last only for a finite amount of time, and become eventually negligible. In linearised GR, once the source has stopped operating, GWs propagate freely through the FLRW space-time. It is therefore useful to derive the corresponding free solutions of Eq. (2.51), particularly in the two regimes of interest in a cosmological setting: for wavelengths smaller and larger than the Hubble radius.

It is convenient to work with conformal time $d\eta = dt/a(t)$, so that the metric (2.49) reads

$$ds^2 = a^2(\eta)\,\left[-d\eta^2 + (\delta_{ij} + h_{ij})\,dx^i dx^j\right]\,. \tag{2.60}$$

Defining

$$H_{ij}(\mathbf{k},\eta) = a\,h_{ij}(\mathbf{k},\eta)\,, \tag{2.61}$$

Eq. (2.51) in Fourier space becomes

$$H''_{ij}(\mathbf{k},\eta) + \left(k^2 - \frac{a''}{a}\right)\,H_{ij}(\mathbf{k},\eta) = 16\pi G\,a^3\,\Pi^{TT}_{ij}(\mathbf{k},\eta)\,, \tag{2.62}$$

where primes denote derivatives with respect to η, and $k = |\mathbf{k}|$ is the comoving wave-number. Restricting ourselves to the case where the source is absent, $\Pi^{TT}_{ij}(\mathbf{x},t) = 0$ (the solution in the presence of a generic stochastic source is deferred to section 3.4), we are interested in solving the time-dependence of the Fourier amplitudes $h_r(\mathbf{k},\eta)$ in Eq. (2.56). These can be easily obtained from the equation

$$H''_r(\mathbf{k},\eta) + \left(k^2 - \frac{a''}{a}\right)\,H_r(\mathbf{k},\eta) = 0\,, \tag{2.63}$$

where we have set the source to zero, and defined $H_r(\mathbf{k},\eta) = a\, h_r(\mathbf{k},\eta)$. Let us focus on a generic scale factor with power law behaviour $a(\eta) = a_n \eta^n$, which covers the cases of radiation ($n = 1$) and matter ($n = 2$) domination, as well as of de Sitter inflation ($n = -1$), (see e.g. [38]). The general solution is

$$h_r(\mathbf{k},\eta) = \frac{A_r(\mathbf{k})}{a(\eta)} \eta\, j_{n-1}(k\eta) + \frac{B_r(\mathbf{k})}{a(\eta)} \eta\, y_{n-1}(k\eta)\,, \tag{2.64}$$

where $j_n(x), y_n(x)$ are the spherical Bessel functions, and $A_r(\mathbf{k})$ and $B_r(\mathbf{k})$ are dimensional constants, to be established from the initial conditions.

Somewhat more explicit solutions can be obtained using the fact that, for a power law scale factor, $a''/a \propto \mathcal{H}^2$, where $\mathcal{H} = a'/a$ is the comoving Hubble factor. One can therefore solve approximately Eq. (2.63) in the limits of super-Hubble ($k \ll \mathcal{H}$) and sub-Hubble ($k \gg \mathcal{H}$) scales, which simply correspond to the solutions one obtains taking the limits $k\eta \ll 1$ and $k\eta \gg 1$ in Eq. (2.64).

For sub-Hubble scales, one neglects the term a''/a with respect the term k^2, in Eq. (2.63), and the solution becomes

$$h_r(\mathbf{k},\eta) = \frac{A_r(\mathbf{k})}{a(\eta)}\, e^{ik\eta} + \frac{B_r(\mathbf{k})}{a(\eta)}\, e^{-ik\eta}\,, \qquad \text{for } k \gg \mathcal{H}\,. \tag{2.65}$$

Again, $A_r(\mathbf{k})$ and $B_r(\mathbf{k})$ are dimensional constants [of different dimension than in Eq. (2.64)], to be established from the initial conditions. For $h_{ij}(\mathbf{x},\eta)$ to be real, they must satisfy the conditions $A_r(-\mathbf{k}) = B_r^*(\mathbf{k})$ and $B_r(-\mathbf{k}) = A_r^*(\mathbf{k})$. With the above solution for sub-Hubble modes, Eq. (2.56) reduces to a superposition of plane waves with wave-vectors $\mathbf{k}$, and amplitude decaying as $1/a(\eta)$,

$$h_{ij}(\mathbf{x},\eta) = \frac{1}{a(\eta)} \sum_{r=+,\times} \int \frac{d^3\mathbf{k}}{(2\pi)^3}\, e_{ij}^r(\hat{\mathbf{k}}) [A_r(\mathbf{k}) e^{ik\eta - i\mathbf{k}\cdot\mathbf{x}} + \text{c.c.}] = \tag{2.66}$$

$$= \frac{1}{a(\eta)} \sum_{r=+,\times} \int \frac{d^3\mathbf{k}}{(2\pi)^3}\, e_{ij}^r(\hat{\mathbf{k}}) [B_r(\mathbf{k}) e^{-ik\eta - i\mathbf{k}\cdot\mathbf{x}} + \text{c.c.}]\,, \tag{2.67}$$

where c.c. stands for complex conjugate. These formulas will be useful at the end of subsection 3.2.

To solve Eq. (2.63) for super-Hubble scales, one neglects instead the term k^2 in Eq. (2.63),

and then one obtains

$$h_r(\mathbf{k},\eta) = A_r(\mathbf{k}) + B_r(\mathbf{k}) \int^{\eta} \frac{d\eta'}{a^2(\eta')} \quad \text{for } k \ll \mathcal{H}\,, \tag{2.68}$$

where the first term in the RHS is constant in time, and the second one decays with the expansion of the universe (again, $A_r(\mathbf{k})$ and $B_r(\mathbf{k})$ are arbitrary constants). As it will be discussed in chapter 5, Eq. (2.68) applies, in particular, to the super-Hubble modes generated from quantum fluctuations of the tensor metric perturbation during inflation. In that case, the decaying mode in Eq. (2.68) becomes quickly negligible due to the quasi-exponential expansion of the universe, so that $h_r(\mathbf{k},\eta)$ is constant in time, for modes outside the Hubble radius. These tensor perturbations eventually re-enter the Hubble radius during the post-inflationary evolution, and then become standard GWs, behaving as in Eq. (2.65).

Note that, in a radiation-dominated universe, the term a''/a vanishes identically, therefore strictly speaking one cannot perform the approximation based on neglecting k^2 vs a''/a. The super-Hubble solution in that case, is simply Eq. (2.65) in the limit $k\eta \ll 1$, which also reduces to a decaying and a constant mode.

Chapter 3

Cosmological (ergo stochastic) gravitational wave backgrounds

In this chapter, taken from the review [15], we introduce general aspects of cosmological backgrounds of GWs. We review the reasons why GW signals generated by cosmological sources are expected to have a stochastic character (section 3.1), and we present how to characterize the spectrum of such SGWB (section 3.2). Furthermore, we discuss the evolution of a cosmological SGWB from the time of its production until the present epoch, as it redshifts with the expansion of the universe (section 3.3). Finally, we present a derivation of the GW spectrum by a generic stochastic source (section 3.4).

The most important message of this chapter is that the characteristic frequency ranges of GW detectors allow to probe the presence of GWs sources at very early epochs of the universe's evolution, far before Nucleosynthesis (BBN), the earliest observational window on the thermal universe (see figure 3.1). Between inflation at say 10^{15} GeV (probed via the CMB, c.f. section 4.2), and BBN at 0.1 MeV (c.f. section 4.1), there can be a wide range of energy scales inaccessible by observables based on electromagnetic radiation, since photons are tightly coupled. On the other hand, GWs propagate freely in the early universe, providing, at least in principle, observational access to these energy scales.

3.1 Stochastic nature of cosmological backgrounds

Early universe sources typically lead to the production of stochastic backgrounds of GWs today. This means that the amplitude of the tensor perturbation $h_{ij}(\mathbf{x}, \eta)$ in Eq. (2.56) is a random variable, which can be characterised only statistically, by means of ensemble averages. In principle, to perform an ensemble average, many copies of the system should be available; obviously in the case under analysis this does not happen, as there is only one observable universe. What is customarily done in cosmology is to invoke the ergodic hypothesis, equating the ensemble average with either spatial and/or temporal averages. This implies that, by observing today large enough regions of the Universe, or a given region for long enough time, one has access to many realisations of the system. Two conditions must be met for this to hold. The first one is that the universe is almost homogeneous and isotropic, so that the 'initial conditions' of the GW generating process are the same (even if only in a statistical sense) at every point in space. The second one is that a GW source fulfils causality, and operates at a time when the typical size of a region of causal contact in the universe was smaller than the causal horizon today[1]. Under these conditions, the GW signal from the early universe takes the form of a stochastic background and one can invoke the ergodic theorem to study its properties. Before showing in further detail why GWs from the early universe must be viewed as a stochastic field, let us remark that, under the ergodic hypothesis, the average over length- and/or time-scales introduced in section 2.3, necessary to define GWs, can be identified with the ensemble average needed to characterise the statistical properties of the GW signal.

Because of causality, a cosmological GW source acting at a given time in the early universe, cannot produce a signal correlated at length/time scales larger than the cosmological horizon at that time. Denoting with a subscript p the time of production, the (physical) correlation scale of the emitted GWs, must satisfy $\ell_p \leq H_p^{-1}$, while the GW signal can be correlated at best on a time scale $\Delta t_p \leq H_p^{-1}$. Here we have set the inverse Hubble factor H_p^{-1} as the cosmological horizon, which is a good approximation for most of the cosmological evolution (except for inflation, a case that we discuss below). Since at the present time we have access to much larger length/time scales than today's redshifted scale associated to H_p^{-1}, the

[1]Inflation does not verify this condition but still provides a SGWB: we discuss this case later on in the chapter.

GW signal in the universe today is composed by the superposition of many signals, that are uncorrelated in time and space. The number of independent signals can be actually obtained, knowing the evolution of the universe and depending on the time of GW production.

We start by comparing the size of the horizon today H_0^{-1} with the correlation length scale redshifted to today $\ell_p^0 = \ell_p(a_0/a_p)$ (for simplicity, we focus for now on the length-scale only and analyse the case of time-scales later on). This gives

$$\frac{\ell_p^0}{H_0^{-1}} = \frac{\ell_p}{H_0^{-1}}\frac{a_0}{a_p} \leq \frac{H_p^{-1}}{H_0^{-1}}\frac{a_0}{a_p} = \frac{a_0/a_p}{\sqrt{\Omega_{\rm mat}(z_p) + \Omega_{\rm rad}(z_p) + \Omega_\Lambda}}\,, \tag{3.1}$$

where in the third equality z denotes the redshift, and we have inserted one of the Friedmann equations in its form $H(z) = H_0\sqrt{\Omega_{\rm mat}(z) + \Omega_{\rm rad}(z) + \Omega_\Lambda}$, where $H_0 = 100\,h\,{\rm km\,sec^{-1}\,Mpc^{-1}}$ is the Hubble constant today and $\Omega_*(z) = \rho_*(z)/\rho_c^0$, with $\rho_c^0 = 3H_0^2/(8\pi G)$ the critical energy density today, $\rho_*(z)$ denoting the energy densities associated with radiation $\rho_{\rm rad}(z)$, matter $\rho_{\rm mat}(z)$, and the cosmological constant $\rho_\Lambda \equiv \Lambda/(8\pi G)$.

Since we are interested in sources operating far in the radiation era, the term proportional to $\Omega_{\rm rad}(z)$ dominates. In order to rewrite Eq. (3.1), we first need to make a short digression. It is an excellent approximation to treat the expansion of the universe as adiabatic, so that it is governed until today by the conservation of entropy per comoving volume[2] [38],

$$g_S(T)\,T^3\,a^3(t) = \text{constant} \tag{3.2}$$

where T is the photon temperature at time t, and g_S is the effective number of entropic degrees of freedom at that time [48]. As the universe cools down, g_S decreases when some species become non-relativistic. When this occurs, they release their entropy to the species that are still in thermal equilibrium, causing the temperature to decrease as $T \propto a^{-1}\,g_S^{-1/3}$, i.e. slower than the usual $T \propto a^{-1}$. The amount the universe has expanded between GW production at a temperature T_p, and today, is then characterized by the ratio

$$\frac{a_0}{a_p} = \left(\frac{g_S(T_p)}{g_S(T_0)}\right)^{1/3}\left(\frac{T_p}{T_0}\right) \simeq 1.25\times 10^{13}\left(\frac{g_S(T_p)}{100}\right)^{1/3}\left(\frac{T_p}{\rm GeV}\right)\,, \tag{3.3}$$

where we have used $T_0 \simeq 2.35\times 10^{-13}$ GeV for the photon temperature today [49]

[2]The total entropy of the universe is very large and dominated by the relativistic species: extra entropy production due to known decoupling processes is sub-dominant with respect to the total entropy.

and $g_S(T_0) \simeq 3.91$ for the Standard Model degrees of freedom with three light neutrino species [48]. Note that $g_S(T_0)$ must be evaluated in this calculation as if the neutrinos were still relativistic today. This is because they decouple from the thermal plasma when they are relativistic (at $T \sim$ MeV, while $m_\nu < 2$ eV [49]) and do not release their entropy to the photons when they later become non-relativistic. In the Standard Model, the last decrease of g_S occurs when electrons and positrons become non-relativistic (at $T \sim m_e \simeq 0.5$ MeV), and the photon temperature evolves simply as $T \propto a^{-1}$ afterwards. In the radiation era, the total energy density is given by [48]

$$\rho_{\rm rad} = \frac{\pi^2}{30}\, g_*(T)\, T^4\,, \tag{3.4}$$

where $g_*(T)$ is the effective number of relativistic degrees of freedom at temperature T. Combining Eqs. (3.3) and (3.4), one obtains

$$\Omega_{\rm rad}(T) = \Omega^0_{\rm rad} \left(\frac{g_S(T_0)}{g_S(T)}\right)^{4/3} \left(\frac{g_*(T)}{g_*(T_0)}\right) \left(\frac{a_0}{a}\right)^4\,, \tag{3.5}$$

where $\Omega^0_{\rm rad} = h^{-2}\, 2.47 \times 10^{-5}$ is the radiation energy density today, and $g_*(T_0) = 2$ (the photons). Note that for numerical estimates we take $h = 0.67$ [50]. Saturating inequality (3.1), i.e. setting $\ell_p \equiv H_p^{-1}$, and keeping only the dominant term during the radiation era, Eqs. (3.3) and (3.5) lead to (in the last equality we set $g_*(T_p) = g_S(T_p)$ for $T_p > 0.1$ MeV [48])

$$\begin{aligned} \frac{\ell^0_p}{H_0^{-1}} &\simeq \frac{a_0/a_p}{\sqrt{\Omega_{\rm rad}(T_p)}} = \frac{1}{\sqrt{\Omega_{\rm rad}}} \left(\frac{g_S(T_p)}{g_S(T_0)}\right)^{1/3} \sqrt{\frac{g_*(T_0)}{g_*(T_p)}}\, \frac{T_0}{T_p} \\ &\simeq 1.3 \times 10^{-11} \left(\frac{100}{g_*(T_p)}\right)^{1/6} \left(\frac{\rm GeV}{T_p}\right)\,, \end{aligned} \tag{3.6}$$

which clearly shows that the correlation scale today of a GW signal from the early universe is tiny comparable to the present Hubble scale.

The number of uncorrelated regions from which we are receiving today independent GW signals, can be found from calculating the angle Θ_p subtending the size ℓ_p at z_p:

$$\Theta_p = \frac{\ell_p}{d_A(z_p)}\,, \tag{3.7}$$

where $d_A(z_p)$ is the angular diameter distance

$$d_A(z_p) = \frac{1}{H_0(1+z_p)} \int_0^{z_p} \frac{dz'}{\sqrt{\Omega_{\rm mat}(z') + \Omega_{\rm rad}(z') + \Omega_\Lambda}} \,. \tag{3.8}$$

In total, today one has access to $\sim d_A(z_p)^2/\ell_p^2 = \Theta_p^{-2}$ uncorrelated regions. Let us consider, as an example of a GW source, the electroweak (EW) phase transition at $T_{\rm EW} \sim \mathcal{O}(10^2)$ GeV, for which we can take $g_S(T_{\rm EW}) \sim 100$. The redshifted scale today corresponding to the horizon scale at the EW phase transition is $(a_0/a_{\rm EW})H_{\rm EW}^{-1} \simeq 2.7 \times 10^{-4}$ pc. Inserting $h^2\Omega_{\rm mat} = 0.12$ and $\Omega_\Lambda = 1 - \Omega_{\rm mat}$ in Eq. (3.8), from Eq. (3.7) one gets $\Theta_{\rm EW} \simeq 2 \times 10^{-12}$ deg, meaning that the GW signal (as received today on Earth) due to a causal process operating at the EW epoch, is composed by the superposition of independent signals emitted by at least $\sim 10^{24}$ uncorrelated regions (even more, if the inequality $\ell_{\rm EW} \leq H_{\rm EW}^{-1}$ is not saturated)[3]. This indicates that the GW signal can only be described statistically. Thus, a GW signal from the early universe cannot possibly be resolved beyond its stochastic nature. In order to resolve individual realizations of the signal, a GW detector should have an angular resolution as good as Θ_p. However, as shown for the example of a GW signal produced at the time of the EW transition, $\Theta_{\rm EW}$ corresponds to a tiny resolution unreachable by any realistic GW detector.

It appears therefore entirely justified to consider the GW signal from sources operating in the early universe as a stochastic background. Furthermore, since any signal is composed by the superposition of sources operating in regions that are not in causal contact during the GW generation, but in which the same physical process is taking place, it is justified to invoke the ergodic hypothesis, and assume that a spatial average corresponds to an ensemble average.

In fact, the above considerations apply even to much lower energy scales than the one of the EW transition. For instance, at the epoch of photon decoupling, at redshift $z_{\rm dec} \simeq 1090$, we have $\Theta_{\rm dec} \simeq 0.9$ deg. For the sake of the exercise, let us postulate the existence of a stochastic background with a high enough amplitude so that a future GW detector could observe it, say with an angular resolution of about 10 deg. The redshift at which the

[3]It is important to note that, even though these regions are not in causal contact, and hence are uncorrelated, the phase transition is happening everywhere at the same time, because the temperature is the same everywhere, as the the universe is homogeneous and isotropic. Inflation is the leading mechanism to provide the right initial conditions for this to happen, see Sect. 5.

background should have been generated, in order to be correlated on an angular scale of 10 deg, should be, according to Eq. (3.7), $z_p \simeq 17$. Consequently, the property of stochasticity holds for any GW signal sourced until well into the matter dominated era.

One may ask whether the signal could be resolved in time, instead of in terms of its characteristic length-scale. The correlation time-scale of the GW signal is again given by $\Delta t_p \leq H_p^{-1}$. Saturating the inequality, for the EW phase transition at $T_{\rm EW} \sim 100$ GeV, one finds a time interval today $\Delta t^{(0)}_{\rm EW} \simeq 8$ hours, while for the QCD phase transition at $T_{\rm QCD} \sim 200$ MeV, it is $\Delta t^{(0)}_{\rm QCD} \simeq 9$ months. The correlation time of primordial sources looks therefore reasonable from a point of view of observational time. However, to resolve the signal, one would need a detector capable of pointing in the same direction within the above calculated angular size Θ_p, for a time interval corresponding to $\Delta t^{(0)}_p$. This is clearly not possible, again because of the limited resolution of GW detectors.

Note that the above arguments remain valid also for causal GW sources that are not localised in time at a given moment t_p, but are continuously operating during several Hubble times. The paradigmatic example of this are topological defects (see e.g. section 9 of [15]). For example, a network of cosmic strings emits GWs continuously, all the way since the epoch of the phase transition that produced it, until today. The GW signal in this case is the sum of two components. One is the irreducible component, given by GWs that are produced around the horizon at each time t, by the anisotropic stress of the network. The second contribution is the superposition of the emission of GWs from sub-horizon cosmic string loops, at each time t. The GW signal from these two components is a stochastic background, contributed by the superposition of the many horizons that at every moment, fit (redshifted) within today's horizon. Therefore, if we observe it today, it cannot be resolved beyond its stochastic nature, for the same reasons discussed above. The main difference between this continuously sourced background and the one arising from a source localised at a time t_p, is that the former extends over many frequencies, precisely due to the source operating during many Hubble times [15].

On the other hand, during inflation the causal horizon grows exponentially [38], and the above arguments do not apply. In this case, the reason why the inflationary GW signal is a stochastic background, resides in the intrinsic quantum nature of the generating process. As we will see in detail in section 5, the source of this GW background are quantum vacuum fluctuations of the metric during inflation. The tensor metric perturbations are therefore

random variables with random phases. They become effectively classical, as the universe expands and the wave-numbers of the fluctuations become larger than the Hubble scale during inflation, leading to very large occupation numbers, see discussion e.g. in [51] and [52, 53]. This quantum-to-classical transition renders the metric perturbation, of quantum origin, equivalent to a stochastic variable after Hubble crossing. The perturbations re-enter progressively the Hubble radius during the radiation and matter dominated eras, leading to a GW signal which is intrinsically stochastic.

In general, the stochastic GW background from sources in the early universe is assumed to be *statistically homogeneous and isotropic*, *unpolarised* and *Gaussian*. The reasons behind these assumptions are easily understood, as we will explain next (for a thorough discussion see also [51]).

Statistical homogeneity and isotropy is inherited from the same property of the FLRW universe, be it during inflation or afterwards during the thermal era. It implies that the two-point spatial correlation function satisfies

$$\langle h_{ij}(\mathbf{x},\eta_1)\, h_{lm}(\mathbf{y},\eta_2)\rangle = \xi_{ijlm}(|\mathbf{x}-\mathbf{y}|,\eta_1,\eta_2)\,, \tag{3.9}$$

where $h_{ij}(\mathbf{x},\eta_1)$ is the tensor perturbation of Eq. (2.60), and $\langle ...\rangle$ denotes the ensemble average (that becomes an average over volume/time under the ergodic hypothesis). In the case presented before about a phase transition operating during the radiation dominated era for example, even though the GW signal is given by the superposition of the signals emitted from many uncorrelated regions, the (statistical) homogeneity and isotropy of the universe causes these regions to have, essentially, the same characteristics, e.g. the temperature and particle densities. Therefore the phase transition happens everywhere in the universe at the same time and with the same outcome, so that the produced GW background is statistically homogeneous and isotropic. The same holds for the irreducible GW background generated during inflation, because the tensor metric perturbations representing the GWs, are generated over the homogeneous and isotropic FLRW background.

The GW cosmological backgrounds are assumed typically to be unpolarised, as a consequence of the absence of a significant source of parity violation in the universe. If the process sourcing the GWs is based on interactions that are symmetric under parity, the

outcome is a GW background for which the two polarisations $+$, $\times$, are uncorrelated. In terms of the Fourier amplitudes of Eq. (2.56), this means $\langle h_+(\mathbf{k},\eta)h_\times(\mathbf{k},\eta)\rangle = 0$. The connection with the parity symmetry is made more explicit by introducing the helicity basis $\epsilon_i^{\pm}(\hat{\mathbf{k}}) = (\hat{\mathbf{m}} \pm i\,\hat{\mathbf{n}})_i/\sqrt{2}$, where $\hat{\mathbf{m}}$, $\hat{\mathbf{n}}$ are the unit vectors used in Eq. (2.57). Out of the usual $e_{ij}^{+,\times}$ polarisation tensors defined in Eq. (2.57), one can construct a basis for the transverse-traceless tensor space representing the two independent helicity states ± 2: $e_{ij}^{\pm 2} = (e_{ij}^{+} \pm i\, e_{ij}^{\times})/2$. The basis transforms as $e_{ij}'^{\pm 2} = e^{\pm 2i\theta} e_{ij}^{\pm 2}$ under rotation by an angle θ around the $\hat{\mathbf{k}}$ axis (see e.g. [54, 55]). An arbitrary symmetric rank two transverse-traceless tensor is in general a mixture of both helicity states, and can be expressed as a linear combination in this basis, $h_{ij} = h_{+2}\, e_{ij}^{+2} + h_{-2}\, e_{ij}^{-2}$. Using these definitions, one can easily derive that $\langle h_{+2}(\mathbf{k},\eta)h_{+2}(\mathbf{k},\eta) - h_{-2}(\mathbf{k},\eta)h_{-2}(\mathbf{k},\eta)\rangle = \langle h_+(\mathbf{k},\eta)h_\times(\mathbf{k},\eta)\rangle = 0$, where the last equality holds if the background is unpolarised (see e.g. [56]). The absence of a net polarisation is therefore equivalent to the condition that the two independent helicity modes are produced, on the average, with the same amplitude, i.e. with identical expectation values. If this is not the case, the GW background can be chiral and must arise from some parity-violating source (see e.g. section 6.1.2 in [15]).

Gaussianity also follows straightforwardly in most cases of GW backgrounds formed by the emission of many uncorrelated regions. As discussed above, since the signal is composed by a large number of sources that were independent at the moment of the GW emission, by the central limit theorem one can expect the outcome signal given by the superposition of all independent signals, to have a Gaussian distribution [51]. Gaussianity also applies in the case of the irreducible background generated during inflation, again because of the quantum nature of this background: in the simplest scenarios, the tensor metric perturbation can be quantised as a free field, and hence with Gaussian probability distribution for the amplitudes[4].

Note that, although the properties of statistical homogeneity and isotropy, gaussianity, and absence of net polarisation, are satisfied to a good approximation for most cosmological sources, there can be exceptions. For example, a certain level of large-scale anisotropy in the universe is allowed by present CMB constraints [45]. A typical example of GW source from the early universe, leading to a statistically anisotropic GW background, is the excitation of

[4] In reality, there is always a small degree of deviation from gaussianity in the inflationary perturbations, as they are created over a dynamical quasi-de Sitter background that also evolves (even if slowly) during inflation [57]. In practice, the amount of non-gaussianity is 'slow-roll suppressed'.

a gauge field during inflation (although this has been studied mainly for the scalar mode, see e.g. [58–60]). The GW background generated by gauge field dynamics during inflation is also non-Gaussian, since the GW source is quadratic in the fields [61], and it can be polarised if the interaction between the gauge field and the inflaton is parity-breaking [62, 63] (in this case the inflaton is a pseudo-scalar).

3.2 Characterization of a stochastic gravitational wave background

In the following we introduce different quantities that are used to characterize the power spectrum of a stochastic GW background. The Fourier amplitudes $h_r(\mathbf{k},\eta)$ of Eq. (2.56) are considered to be random variables. For a statistically homogeneous and isotropic, unpolarised and Gaussian GW background, their power spectrum can be written as

$$\langle h_r(\mathbf{k},\eta)\, h_p^*(\mathbf{q},\eta)\rangle = \frac{8\pi^5}{k^3}\,\delta^{(3)}(\mathbf{k}-\mathbf{q})\,\delta_{rp}\,h_c^2(k,\eta)\,, \tag{3.10}$$

where h_c is dimensionless, real and depends only on the time η and the comoving wave-number $k = |\mathbf{k}|$. The delta function in $\mathbf{k}$, $\mathbf{q}$, and the fact that h_c does not depend on the direction $\hat{\mathbf{k}}$, are consequences of statistical homogeneity and isotropy; the delta function in the polarisation states r, p is a consequence of the absence of a net polarisation, and gaussianity implies that the above expectation value contains all the relevant information on the statistical distribution of the random variables $h_r(\mathbf{k},\eta)$. We do not need to investigate therefore higher-point correlation functions, as for a Gaussian field even-point correlation functions can be rewritten in as powers of $h_c^2(k,\eta)$, while odd-point correlations are vanishing. The factor $8\pi^5$ in Eq. (3.10) has been chosen so that Eqs. (2.56) and (2.58) give

$$\langle h_{ij}(\mathbf{x},\eta)\, h_{ij}(\mathbf{x},\eta)\rangle = 2\int_0^{+\infty}\frac{dk}{k}\,h_c^2(k,\eta)\,, \tag{3.11}$$

where the factor 2 in the RHS is a convention motivated by the fact that the LHS involves contributions from two independent polarizations (we adopt here the same convention as [32,33], while the one adopted in [64] differs by a factor 2). It appears from the above equation that $h_c(k,\eta)$ represents a characteristic GW amplitude per logarithmic wave-number interval

and per polarization state, at a time η.

As discussed at the beginning of subsection 3.1, for free waves at sub-Hubble scales (those detectable today), the average in the LHS of Eq. (3.10) can be taken both as a volume average over sufficiently large regions compared to the GW wavelengths, and a time average over several periods of oscillation (i.e. the average under which GWs can be defined, following what presented in section 2.3). The time behaviour of the GW Fourier amplitudes for sub-Hubble modes is given by Eq. (2.65). Inserting this solution into Eq. (3.10), and keeping in mind that the presence of the delta function imposes $k = q$, one can average out the terms that are oscillatory in time, and find

$$\langle h_r(\mathbf{k},\eta)\, h_p^*(\mathbf{q},\eta)\rangle = \frac{1}{a^2(\eta)}[\langle A_r(\mathbf{k})\, A_p^*(\mathbf{q})\rangle + \langle B_r(\mathbf{k})\, B_p^*(\mathbf{q})\rangle]\,. \tag{3.12}$$

The above equation, together with Eq. (3.10), shows that for free waves inside the Hubble radius, $h_c(k,\eta) \propto 1/a(\eta)$ after the oscillatory terms are averaged out.

Besides h_c, a quantity of prime interest to characterize a stochastic GW background, is the spectrum of GW energy density per logarithmic wave-number interval, $d\rho_{\rm GW}/d\log k$. The energy density in GWs is given by the 00-component of the energy-momentum tensor, see Eq. (2.46)

$$\rho_{\rm GW} \,=\, \frac{\langle \dot{h}_{ij}(\mathbf{x},t)\, \dot{h}_{ij}(\mathbf{x},t)\rangle}{32\pi G} \,=\, \frac{\langle h'_{ij}(\mathbf{x},\eta)\, h'_{ij}(\mathbf{x},\eta)\rangle}{32\pi G\, a^2(\eta)} \,=\, \int_0^{+\infty} \frac{dk}{k}\, \frac{d\rho_{\rm GW}}{d\log k}\,, \tag{3.13}$$

where in the second equality we have converted the derivatives with respect to the physical time t into derivatives with respect to the conformal time η, while the third equality defines $d\rho_{\rm GW}/d\log k$. Again, we have seen from the discussion in subsection 2.3 (c.f. also what presented in [33,39]) that, even for a deterministic GW signal, the energy-momentum tensor of GWs cannot be localized inside a volume smaller than the GW typical wavelength, but can only be defined by performing an average over volume and/or time (over several wavelengths and/or frequencies for its Fourier components). For a stochastic background generated in the early universe, invoking the ergodic hypothesis, the average performed in Eq. (3.13) corresponds to the usual ensemble average of Eq. (3.10).

An expression for the GW energy density power spectrum $d\rho_{\rm GW}/d\log k$ valid for free waves inside the Hubble radius, can be found from Eq. (3.13), inserting the time behaviour

of the GW Fourier modes given by Eq. (2.65). The first step is to postulate that the same structure of Eq. (3.10) holds for the power spectrum of the conformal time derivatives of the Fourier modes $h_r(\mathbf{k},\eta)$,

$$\langle h_r'(\mathbf{k},\eta)\, h_p'^{\,*}(\mathbf{q},\eta)\rangle = \frac{8\pi^5}{k^3}\,\delta^{(3)}(\mathbf{k}-\mathbf{q})\,\delta_{rp}\,h_c'^{\,2}(k,\eta)\,, \tag{3.14}$$

where we have defined a new characteristic amplitude $h_c'^{\,2}(k,\eta)$, analogous to $h_c^2(k,\eta)$. One then substitutes solution (2.65) in the above equation. Again, because of the delta function imposing $k=q$, it is straightforward to average out the terms that oscillate in time (as we did to derive Eq. (3.12)). Besides, one can neglect the $\mathcal{H}^2$ term arising due to the conformal time derivative of (2.65), with respect to the term k^2, since in the case under analysis, $k \gg \mathcal{H}$. One then finds a simple relation among the amplitudes:

$$h_c'^{\,2}(k,\eta) \simeq k^2\, h_c^2(k,\eta)\,. \tag{3.15}$$

With this identity, one can evaluate Eq. (3.13) with the help of Eqs. (2.56), (2.58) and (3.14), to find

$$\frac{d\rho_{\rm GW}}{d\log k} = \frac{k^2\, h_c^2(k,\eta)}{16\pi G\, a^2(\eta)}\,. \tag{3.16}$$

Furthermore, we have seen before that $h_c(k,\eta) \propto 1/a(\eta)$ for sub-Hubble modes. Thus, as expected for massless degrees of freedom, the GW energy density is diluted as radiation with the expansion of the universe, $\rho_{\rm GW} \propto a^{-4}$.

In order to make connection with observations, it is necessary to evaluate the GW background today in terms of the present-day physical frequency $f = k/(2\pi\, a_0)$, corresponding to the comoving wave-number k redshifted to today (we remind that a subscript "0" indicates a quantity evaluated at the present time). The characteristic GW amplitude per logarithmic frequency interval today, is then given by

$$h_c(f) = h_c(k,\eta_0)\,, \tag{3.17}$$

which corresponds to the definition given in Ref. [32]. A stochastic background is often

characterized also by its spectral density

$$S_h(f) = \frac{h_c^2(f)}{2f}\,, \tag{3.18}$$

which has dimension Hz^{-1}. This quantity is directly comparable to the noise in a detector, parametrised by $S_n(f)$. We will use the spectral density in section 4.4, when discussing the sensitivity of interferometric experiments to stochastic backgrounds.

The spectrum of GW energy density per logarithmic frequency interval, can be conveniently normalized as

$$\Omega_{\rm GW}(f) = \frac{1}{\rho_c}\,\frac{d\rho_{\rm GW}}{d\log f}\,, \tag{3.19}$$

where $\rho_c = 3H^2/(8\pi G)$ is the critical energy density at time t. The quantity traditionally considered by cosmologists is $h^2\,\Omega_{\rm GW}^{(0)}$, because it is independent of the observational uncertainty on the value of H_0. Eqs. (3.16 - 3.18) with $f = k/(2\pi\,a_0)$ give (note the factor two difference with respect to e.g. [64])

$$\Omega_{\rm GW}^{(0)}(f) = \frac{4\pi^2}{3H_0^2}\,f^3\,S_h(f)\,. \tag{3.20}$$

Inserting H_0, in terms of the dimensionless amplitude $h_c = \sqrt{2f\,S_h}$, we have

$$S_h(f) = 7.98\times10^{-37}\,\left(\frac{\mathrm{Hz}}{f}\right)^3\,h^2\,\Omega_{\rm GW}(f)\,\frac{1}{\mathrm{Hz}}\,, \tag{3.21}$$

$$h_c(f) = 1.26\times10^{-18}\,\left(\frac{\mathrm{Hz}}{f}\right)\,\sqrt{h^2\,\Omega_{\rm GW}(f)}\,. \tag{3.22}$$

It is important to notice that, when performing a GW direct detection experiment, the expansion of the universe is completely negligible on the time scales of interest (with the exception of very particular cases, see e.g. [3]). This allows us to make the connection between the quantities introduced above, in particular expansion (2.56), and the expansion of $h_{ij}(\mathbf{x},t)$ often used in the literature, for example in Refs. [32, 33, 64]:

$$h_{ij}(\mathbf{x},t) = \sum_{r=+,\times}\int_{-\infty}^{+\infty} df\,\int d^2\hat{\mathbf{k}}\;\bar{h}_r(f,\hat{\mathbf{k}})\,e^{i\,2\pi\,f(t-\hat{\mathbf{k}}\cdot\mathbf{x})}\,e^r_{ij}(\hat{\mathbf{k}})\,, \tag{3.23}$$

where the integration over negative frequencies is obtained via the definition $\bar{h}_r(-f,\hat{\mathbf{k}}) \equiv$

$\bar{h}_r^*(f,\hat{\mathbf{k}})$ that is necessary for $h_{ij}(\mathbf{x},t)$ to be real. To connect the above equation to expansion (2.56), the starting point is (2.66) for sub-Hubble GWs, those of interest for detectors. The scale factor must be fixed to the scale factor today, while neglecting the expansion of the universe means that it is possible to perform a time Fourier Transform: the time in the exponentials of (2.66) becomes therefore the Fourier conjugate variable to the frequency f. One can then rewrite Eq. (2.66) in terms of frequency via the change of variable $d^3\mathbf{k} = (2\pi\, a_0)^3\, f^2\, df\, d\hat{\mathbf{k}}$, and extend to negative frequencies by identifying $A_r(-f,\hat{\mathbf{k}}) \equiv A_r^*(f,\hat{\mathbf{k}})$, to get

$$h_{ij}(\mathbf{x},t) = a_0^2 \sum_{r=+,\times} \int_{-\infty}^{+\infty} f^2\, df \int d^2\hat{\mathbf{k}}\, A_r(f,\hat{\mathbf{k}})\, e^{i\,2\pi\, f(t-\hat{\mathbf{k}}\cdot\mathbf{x})}\, e_{ij}^r(\hat{\mathbf{k}})\,. \tag{3.24}$$

If the expansion of the universe can be neglected, Eq. (2.66) becomes therefore equivalent to Eq. (3.23), provided one identifies $\bar{h}_r(f,\hat{\mathbf{k}}) = a_0^2\, f^2\, A_r(f,\hat{\mathbf{k}})$ (the same can be done with $B_r(f,\hat{\mathbf{k}})$).

At this point, the usual expression for the power spectrum of the Fourier amplitudes $\bar{h}_r(f,\hat{\mathbf{k}})$, given in Refs. [32, 33, 64], and defining the power spectral density, can be easily recovered. First of all, one needs to observe that Eq. (3.12) can also be written as (by using Eq. (2.67))

$$\langle h_r(\mathbf{k},\eta)\, h_p^*(\mathbf{q},\eta)\rangle = \frac{2}{a^2(\eta)} \langle A_r(\mathbf{k})\, A_p^*(\mathbf{q})\rangle\,. \tag{3.25}$$

One obtains therefore

$$\begin{aligned} \langle \bar{h}_r(f,\hat{\mathbf{k}}) \bar{h}_p^*(g,\hat{\mathbf{q}})\rangle &= a_0^4\, f^2\, g^2 \langle A_r(\mathbf{k})\, A_p^*(\mathbf{q})\rangle = \\ &= \frac{1}{8\pi}\, \delta(f-g)\, \delta^{(2)}(\hat{\mathbf{k}}-\hat{\mathbf{q}})\, \delta_{rp}\, S_h(f)\,, \end{aligned} \tag{3.26}$$

where the second equality has been obtained inserting Eq. (3.10), changing variable to $f = k/(2\pi\, a_0)$ and using definition (3.18). From the above equation, one can appreciate that the definition of the spectral density given in [32, 33, 64] is equivalent to the one of Eq. (3.10).

3.3 Propagation of gravitational waves through cosmic history

As already mentioned, the weakness of the gravitational interaction guarantees that GWs are decoupled from the rest of the universe since the Planck scale. Furthermore, because of the symmetries of FLRW space-time, for most practical purposes there is no need to go beyond

linear order in perturbation theory (c.f. Eq. (2.49)). For these reasons, one can neglect both interactions with ordinary matter and self-interactions, and assume that sub-Hubble GWs propagate freely once they have been produced (or once they re-enter the Hubble radius, in the case of an inflationary produced signal). Consequently Eq. (2.65) applies for sub-Hubble modes as soon as the GW source has stopped operating. As demonstrated in the section above, in this case the GW energy density spectrum redshifts with the expansion of the universe, but it retains its initial shape. In fact, the GW energy density is diluted as radiation, $\rho_{\rm GW} \propto a^{-4}$, while the GW physical wave-numbers evolve simply as k/a. Normalizing the GW energy density at the time of production to the total energy density in the universe at that time ρ_p (the subscript p indicates that a quantity is evaluated at the time of GW production), the GW spectrum today is given by

$$h^2\,\Omega_{\rm GW}(k) = \frac{h^2}{\rho_c}\left(\frac{a_p}{a_0}\right)^4 \rho_p \left(\frac{1}{\rho}\frac{d\rho_{\rm GW}}{d{\rm log}k}\right)_p \qquad \text{for } k \gg \mathcal{H}\,. \tag{3.27}$$

Furthermore, normalizing the physical wave-number at the time of GW production to the Hubble rate at that time,

$$x_k = \frac{k/a_p}{H_p} \tag{3.28}$$

the corresponding GW frequency today is given by

$$f = \frac{1}{2\pi}\frac{k}{a_0} = \frac{x_k}{2\pi}\frac{a_p}{a_0}\,H_p\,. \tag{3.29}$$

As discussed in section 3.1, the GW signal from a source operating at some time t_p in the early universe cannot be correlated on length/time scales larger than H_p^{-1}. In general, the typical correlation scale shows up as a peak (or a feature) in the power spectrum: consequently, we expect the GW energy density spectrum to be peaked at a characteristic wave-number smaller than the Hubble radius at the time of production of the GWs, i.e. we expect its characteristic wave-number to be $k/a_p \geq H_p$. Thus, although the value x_k in Eq. (3.28) for the peak of the spectrum depends on the particular source under consideration, we can conclude that it certainly satisfies $x_k \geq 1$. Examples of such short-lasting sources include first-order phase transitions (discussed in Chapter 6) and preheating after inflation (see e.g. section 7 of [15]). Other sources like e.g. cosmic strings, on the other hand, produce GWs continually during a

long period of time. In this case the source is active for a large range of values of $a_p\,H_p$ in Eq. (3.29), and the resulting GW spectrum today covers a wide frequency range. Similarly, the GW spectrum produced by inflation is very broad because $a_p\,H_p$ varies exponentially during (de Sitter) inflation. Note also that, if a source produces GWs continually during the radiation era with an energy density $\rho_{\rm GW}$ that remains a constant fraction of the total energy density ρ at the time of production, then the resulting spectrum (3.27) is approximately flat because $a_p^4\,\rho_p$ is approximatively constant during the radiation era (up to variations of the number of relativistic species discussed in section 3.1). This is in fact a typical situation for long-lasting sources (including inflation for modes that re-enter the Hubble radius during the radiation era, as we will see in section 5).

For GWs produced during the radiation era, Eqs. (3.27) and (3.29) can be rewritten with the help of (3.3) and (3.4) to give the present-day GW amplitude and GW frequency in terms of the temperature T_p at the time of production:

$$h^2\,\Omega_{\rm GW} = 1.6\times10^{-5}\,\left(\frac{100}{g_*(T_p)}\right)^{1/3}\,\left(\frac{1}{\rho}\,\frac{d\rho_{\rm GW}}{d\log k}\right)_p \tag{3.30}$$

and

$$f = 2.6\times10^{-8}\,{\rm Hz}\;\;x_k\,\left(\frac{g_*(T_p)}{100}\right)^{1/6}\,\frac{T_p}{\rm GeV} \tag{3.31}$$

where we have used $H^2 = 8\pi G\rho/3$ and again $g_*(T_p) = g_S(T_p)$ for $T_p \gtrsim$ MeV [48].

Eq. (3.29), and its analogue in the radiation era Eq. (3.31), provide an interesting connection between the frequency of the GW today and the epoch in the early universe when a GW source was operating. The precise value of x_k can only be determined within a specific GW generation process; however, since $x_k \geq 1$, one can still find, through these equations, the lowest possible frequency emitted by a process operating at a given time in the universe parametrised by T_p. Therefore, it is possible to associate to a given GW detection experiment, operating in a given frequency range, the epochs in the early universe during which a source should have been active to produce GWs detectable by that experiment. This is shown in Fig. 3.1 for several GW detectors (for details, see section 4.4): $1\,{\rm Hz} \lesssim f \lesssim 10^3\,{\rm Hz}$ for ground-based interferometers, $10^{-5}\,{\rm Hz} \lesssim f \lesssim 0.1\,{\rm Hz}$ for LISA, $3\times10^{-9}\,{\rm Hz} \lesssim f \lesssim 10^{-6}\,{\rm Hz}$ for Pulsar Timing Arrays, and $3.4\times10^{-19}\,{\rm Hz} \lesssim f \lesssim 7\times10^{-18}\,{\rm Hz}$ for the CMB. In this last case, the observable frequency window corresponds respectively to the Horizon today and at

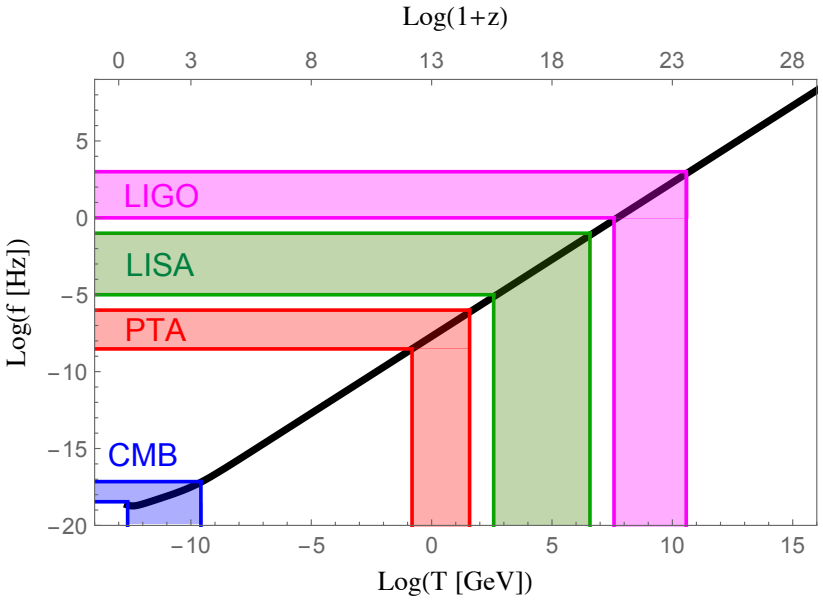

Figure 3.1: Black line: the characteristic GW frequency of Eq. (3.29) with $x_k = 1$ as a function of temperature (the corresponding redshift is shown above). Shaded regions: the frequency ranges detectable by several GW experiments, from right to left respectively $1\,\mathrm{Hz} \lesssim f \lesssim 10^3\,\mathrm{Hz}$ for ground-based interferometers, $10^{-5}\,\mathrm{Hz} \lesssim f \lesssim 0.1\,\mathrm{Hz}$ for LISA, $3\times10^{-9}\,\mathrm{Hz} \lesssim f \lesssim 10^{-6}\,\mathrm{Hz}$ for Pulsar Timing Arrays, and $3.4\times10^{-19}\,\mathrm{Hz} \lesssim f \lesssim 7\times10^{-18}\,\mathrm{Hz}$ for the CMB.

the epoch of photon decoupling, c.f. section 4.2: $H_0/(2\pi) \leq f \leq H_{\rm dec}\,(a_0/a_{\rm dec})/(2\pi)$, with $T_{\rm dec} \simeq 0.26$ eV. Note that Eq. (3.31) does not hold in the case of the CMB, which extends beyond the radiation era, while Eq. (3.29) is generically valid. Fig. 3.1 illustrates how GW experiments have the potential to probe well separated energy scales and cosmological epochs that are not directly accessible by any other mean, since the universe was opaque to photons at that time. Other cosmological probes like e.g. Large Scale Structure, the CMB and Big Bang Nucleosynthesis (BBN) can probe temperatures $T_p \lesssim 1$ MeV, or the inflationary epoch for what concerns CMB anisotropies and polarisation. On the other hand, GW experiments have in principle access to a wide range of energy scales beyond 1 MeV.

3.4 Gravitational wave spectrum by a generic stochastic source

In section 2.4 we have presented the free solutions for the GW Fourier modes $h_r(\mathbf{k},\eta)$ at sub- and super-horizon scales. Here we derive the amplitude of the Fourier modes and the energy density power spectrum Eq. (3.16) in the presence of a generic stochastic source of

GW acting during the radiation or matter dominated eras[5].

The tensor anisotropic stress sourcing the GWs can be decomposed, analogously to h_{ij}, in two polarisation states (here and in the following we omit the superscript TT for brevity):

$$\Pi_{ij}(\mathbf{x},t) = \sum_{r=+,\times} \int \frac{d^3\mathbf{k}}{(2\pi)^3}\, \Pi_r(\mathbf{k},t)\, e^{-i\mathbf{k}\cdot\mathbf{x}}\, e^r_{ij}(\hat{\mathbf{k}})\,. \tag{3.32}$$

For the reasons put forward in section 3.1, it is enough to describe the source stochastically. Though there are exceptions, here we assume that the properties of statistical homogeneity and isotropy, gaussianity and the absence of a preferred polarisation, apply for the GW source as well, as assumed for the GW spectrum (c.f. section 3.1). The power spectrum of the Fourier components of the tensor anisotropic stress can therefore be written as

$$\langle \Pi_r(\mathbf{k},\eta)\, \Pi^*_p(\mathbf{q},\zeta)\rangle = \frac{(2\pi)^3}{4}\, \delta^{(3)}(\mathbf{k}-\mathbf{q})\, \delta_{rp}\, \Pi(k,\eta,\zeta)\,. \tag{3.33}$$

Note the chosen the normalisation, and that we have written the correlator at unequal times for future convenience.

In terms of the Fourier amplitudes of $H_{ij} = a\, h_{ij}$, the evolution equation (2.62) reads

$$H_r''(\mathbf{k},\eta) + \left(k^2 - \frac{a''}{a}\right) H_r(\mathbf{k},\eta) = 16\pi G\, a^3\, \Pi_r(\mathbf{k},\eta)\,. \tag{3.34}$$

In the radiation dominated era with $a(\eta) = a_*\eta$, and in terms of the dimensionless variable $x = k\eta$, the above equation becomes simply

$$\frac{d^2 H_r^{\rm rad}(\mathbf{k},x)}{dx^2} + H_r^{\rm rad}(\mathbf{k},x) = \frac{16\pi G a_*^3}{k^5}\, x^3\, \Pi_r(\mathbf{k},x)\,, \tag{3.35}$$

which has $\{\sin x, \cos x\}$ as homogeneous solutions and $\mathcal{G}(x,y) = \sin(x-y)$ as the Green function associated to the differential operator in the LHS of Eq. (3.35). Let us suppose that the source starts operating at a time $x_{\rm in} = k\eta_{\rm in}$ and stops operating at $x_{\rm fin} = k\eta_{\rm fin}$, with $\eta_{\rm fin}$ still well into the radiation dominated era. While the source is active $x < x_{\rm fin}$, one has

[5] The solution for a source that acts continuously through the radiation-matter transition requires numerical integration and goes beyond the illustrative purposes of this section.

therefore (assuming vanishing initial conditions)

$$H_r^{\rm rad}(\mathbf{k}, x < x_{\rm fin}) = \frac{16\pi G a_*^3}{k^5} \int_{x_{\rm in}}^{x} dy\, y^3\, \sin(x-y)\, \Pi_r(\mathbf{k}, y)\,. \tag{3.36}$$

We are interested in the GW spectrum today: we need therefore the solution at $x_0 = k\eta_0 \gg x_{\rm fin}$. For this, one has to match (3.36) with the homogeneous solution

$$H_r^{\rm rad}(\mathbf{k}, x > x_{\rm fin}) = A_r^{\rm rad}(\mathbf{k}) \cos x + B_r^{\rm rad}(\mathbf{k}) \sin x \tag{3.37}$$

and its first derivative, to find the matching coefficients $A_r^{\rm rad}, B_r^{\rm rad}$. This procedure leads to

$$A_r^{\rm rad}(\mathbf{k}) = \frac{16\pi G a_*^3}{k^5} \int_{x_{\rm in}}^{x_{\rm fin}} dy\, y^3\, \sin(-y)\, \Pi_r(\mathbf{k}, y), \tag{3.38}$$

$$B_r^{\rm rad}(\mathbf{k}) = \frac{16\pi G a_*^3}{k^5} \int_{x_{\rm in}}^{x_{\rm fin}} dy\, y^3\, \cos(y)\, \Pi_r(\mathbf{k}, y). \tag{3.39}$$

One can now apply Eq. (3.12) together with Eq. (3.10) and Eq. (3.33) to find the power spectrum amplitude today due to a GW source acting in the radiation era:

$$h_c^2(k, \eta_0)|_{\rm rad} = 64\, \frac{G^2}{a_0^2}\, \frac{a_*^6}{k^7} \int_{x_{\rm in}}^{x_{\rm fin}} dy\, y^3 \int_{x_{\rm in}}^{x_{\rm fin}} dz\, z^3\, \cos(y-z)\, \Pi(k, y, z)\,. \tag{3.40}$$

It is now straightforward to get the energy density power spectrum by applying Eq. (3.16):

$$\left.\frac{d\rho_{\rm GW}}{d\log k}(k, \eta_0)\right|_{\rm rad} = \\ = \frac{4}{\pi}\, \frac{G}{a_0^4}\, k^3 \int_{\eta_{\rm in}}^{\eta_{\rm fin}} d\eta\, a^3(\eta) \int_{\eta_{\rm in}}^{\eta_{\rm fin}} d\zeta\, a^3(\zeta)\, \cos[k(\eta-\zeta)]\, \Pi(k, \eta, \zeta)\,, \tag{3.41}$$

where we have rewritten the integrals in terms of conformal time. The above equation represents the energy density power spectrum for a generic stochastic source operating during the radiation dominated era.

If the source is operating during the matter dominated era with $a(\eta) = a_* \eta^2$, the solution of the GW equation

$$\frac{d^2 H_r^{\rm mat}(\mathbf{k}, x)}{dx^2} + \left(1 - \frac{2}{x^2}\right) H_r^{\rm mat}(\mathbf{k}, x) = \frac{16\pi G a_*^3}{k^8}\, x^6\, \Pi_r(\mathbf{k}, x)\,, \tag{3.42}$$

after the source has ceased acting becomes

$$H_r^{\rm mat}(\mathbf{k}, x > x_{\rm fin}) = A_r^{\rm mat}(\mathbf{k}) \left(\frac{\cos x}{x} + \sin x\right) + B_r^{\rm mat}(\mathbf{k}) \left(\frac{\sin x}{x} - \cos x\right) , \tag{3.43}$$

with matching coefficients

$$A_r^{\rm mat}(\mathbf{k}) = \frac{16\pi G a_*^3}{k^8} \int_{x_{\rm in}}^{x_{\rm fin}} dy\, y^5 \left[y\cos y - \sin(y)\right] \Pi_r(\mathbf{k}, y), \tag{3.44}$$

$$B_r^{\rm mat}(\mathbf{k}) = \frac{16\pi G a_*^3}{k^8} \int_{x_{\rm in}}^{x_{\rm fin}} dy\, y^5 \left[\cos y + y\sin y\right] \Pi_r(\mathbf{k}, y). \tag{3.45}$$

Note that, since we are interested in wave-numbers satisfying $x_0 \gg 1$, the terms proportional to x_0^{-1} are sub-dominant and can be dropped in Eq. (3.43), which then takes the same form as the sub-Hubble solution Eq. (2.65). We can adopt the same procedure as for the radiation case and find the GW energy density power spectrum for a source operating during the matter era:

$$\left.\frac{d\rho_{\rm GW}}{d\log k}(k, \eta_0)\right|_{\rm mat} = \frac{4}{\pi}\frac{G}{a_0^4} k\, a_* \int_{\eta_{\rm in}}^{\eta_{\rm fin}} d\eta\, a^{5/2}(\eta) \int_{\eta_{\rm in}}^{\eta_{\rm fin}} d\zeta\, a^{5/2}(\zeta)\, \Pi(k, \eta, \zeta) \times\left[(1 + k^2\eta\zeta)\cos(k(\eta - \zeta)) + (k\eta - k\zeta)\sin(k(\eta - \zeta))\right]. \tag{3.46}$$

Chapter 4

Bounds and detectors

This chapter, taken from the review [15], describes the present observational constraints on stochastic backgrounds of GWs (Sects. 4.1-4.3), and the basic features of current and future GW detectors (Sect. 4.4). In Section 4.1 we discuss how BBN and the CMB can be used to set upper bounds on the total energy density of a cosmological SGWB. In section 4.2 we discuss the imprint of a SGWB on the CMB temperature and polarisation anisotropies. We present the current upper bound on the SGWB spectrum at CMB scales, as inferred from current CMB measurements. In section 4.3 we review the ability of pulsar timing arrays (PTA) to probe the SGWB, and discuss the present and future upper bounds that can be placed using this technique. In section 4.4 we turn to the direct detection of a SGWB via interferometers. We review the basic principles of the SGWB detection using interferometry, and briefly survey the present and future Earth- and space-based detectors.

The main message of this chapter is conveyed by figures 4.1 and 4.2, which show some of the observational upper bounds on the energy density of a SGWB of primordial origin, together with the sensitivity of current and future GW detectors. From these figures one infers the amplitude and frequency ranges that are still unexplored, where generation mechanisms in the early universe may have operated.

4.1 Constraints on the gravitational wave background energy density

As discussed in Section 3, the energy density of a GW background decays with the expansion of the universe as relativistic degrees of freedom, i.e. $\rho_{\rm GW} \propto a^{-4}$. This means that a GW background acts as an additional radiation field in the universe[1], contributing to the background expansion rate as

$$H^2(a) = H_0^2 \left[\left(\frac{\rho_{\rm GW}^0}{\rho_c^0} + \Omega_{\rm rad}^0 \right) \left(\frac{a_0}{a} \right)^4 + \Omega_{\rm mat}^0 \left(\frac{a_0}{a} \right)^3 + \Omega_\Lambda^0 \right] . \tag{4.1}$$

Any observable capable of probing the background evolution of the universe (and hence its energy content), has therefore the potential ability to constrain the integrated GW energy density $\rho_{\rm GW}/\rho_c = (\rho_{\rm GW}^0/\rho_c^0)(H_0/H(a))^2(a_0/a)^4$ present in that moment. In particular, two events that yield a very precise measurement of the expansion rate of the universe are Big Bang Nucleosynthesis (BBN), and the process of photon decoupling leading to the CMB. An upper bound on the energy density of a GW background present at the time of BBN or at CMB decoupling, can therefore be derived from the constraint on the amount of radiation tolerated at those cosmic epochs (when the Universe had a temperature of $T_{\rm BBN} \sim 0.1$ MeV and $T_{\rm CMB} \sim 0.3$ eV, respectively). Using Eq. (3.3), and Eq. (3.4) for the photon component $\rho_\gamma(T) = (\pi^2/15)\, T^4$, we can write

$$\left(\frac{h^2 \rho_{\rm GW}}{\rho_c} \right)_0 = h^2 \Omega_\gamma^0 \left(\frac{g_S(T_0)}{g_S(T)} \right)^{4/3} \frac{\rho_{\rm GW}(T)}{\rho_\gamma(T)} , \tag{4.2}$$

where $h^2\Omega_\gamma^0 = 2.47 \times 10^{-5}$ is the density parameter of photons today. The GW energy density $\rho_{\rm GW}(T)$ must not exceed the limits on the abundance of radiation during BBN and CMB decoupling. A constraint on the presence of 'extra' radiation is usually expressed in terms of an effective number of neutrino species N_ν, as follows. The radiation energy density in the universe is given by Eq. (3.4)

$$\rho_{\rm rad} = \frac{\pi^2}{30} g_*(T) T^4 \equiv \frac{\pi^2}{30} \left[\sum_b g_{*b} \left(\frac{T_b}{T} \right)^4 + \frac{7}{8} \sum_f g_{*f} \left(\frac{T_f}{T} \right)^4 \right] T^4 , \tag{4.3}$$

[1] Here we implicitly assume that the characteristic wavelengths of the GW background are well inside the horizon.

where we have made explicit the contributions to $g_*(T)$: the sum $\sum_b$ is over bosonic species and the sum $\sum_f$ over fermionic species. Before electron-positron annihilation, at $T \sim$ MeV, the total number of relativistic degrees of freedom was

$$g_*(T = \text{MeV}) = 2 + \frac{7}{8}\,(4 + 2\,N_\nu) \tag{4.4}$$

where the first term is due to the photons (with two helicity states), the second one is due to the electrons and positrons (with two helicity states each), and the last term is due to the N_ν species of neutrinos and anti-neutrinos (with one helicity state each). In the Standard Model, $N_\nu = 3$. From Eqs. (4.3) and (4.4), we see that an extra amount of radiation can be put in the form of ΔN_ν extra neutrino species as

$$\Delta\rho_{\rm rad} = \frac{\pi^2}{30}\,\frac{7}{4}\,\Delta N_\nu\,T^4\,. \tag{4.5}$$

Thus, an upper bound on any extra radiation component in addition to those of the Standard Model, can be seen as an upper bound on ΔN_ν. Since the energy density in GW must satisfy $\rho_{\rm GW}(T) \leq \Delta\rho_{\rm rad}(T)$, one has

$$\left(\frac{\rho_{\rm GW}}{\rho_\gamma}\right)_{T=\text{MeV}} \leq \frac{7}{8}\,\Delta N_\nu\,. \tag{4.6}$$

Inserting the above equation into (4.2), one finds a constraint on the GW energy density redshifted to today in terms of the number of extra neutrino species,

$$\left(\frac{h^2\rho_{\rm GW}}{\rho_c}\right)_0 \leq h^2\Omega_\gamma^0\left(\frac{g_S(T_0)}{g_S(T)}\right)^{4/3}\frac{7}{8}\,\Delta N_\nu = 5.6\times10^{-6}\Delta N_\nu\,, \tag{4.7}$$

where we have inserted $h^2\Omega_\gamma^0 = 2.47\times10^{-5}$, $g_S(T = \text{MeV}) = 10.75$ and $g_S(T_0) \simeq 3.91$ [48], see discussion below Eq. (3.3).

Before proceeding to discuss how BBN and CMB can limit ΔN_ν, let us note that the bound in Eq. (4.7) is often quoted in terms of $N_{\rm eff}$, the effective number of neutrino species present in the thermal bath after e^+e^- annihilation. In the Standard Model $N_{\rm eff} = 3.046$, differing slightly from $N_\nu = 3$ simply due to the fact that neutrinos are not yet completely decoupled when e^+e^- annihilation takes place, and hence they are partially 'reheated' along with the rest of the plasma [65]. Instead of normalising (4.6) at $T =$ MeV we can choose a

temperature below e^+e^- annihilation. In this case we have to use

$$g_*(T < T_{e^+e^-}) = 2 + \frac{7}{4} N_{\rm eff} \left(\frac{4}{11}\right)^{4/3} , \tag{4.8}$$

since, after the photons have been reheated by e^+e^- annihilation, the temperature of the neutrinos satisfies $T_\nu = (4/11)^{1/3} T$. Carrying on the same procedure as before, leads to

$$\left(\frac{h^2\rho_{\rm GW}}{\rho_c}\right)_0 \leq h^2\Omega_\gamma^0 \, \frac{7}{8} \left(\frac{4}{11}\right)^{4/3} \Delta N_{\rm eff} = 5.6 \times 10^{-6} \, \Delta N_{\rm eff} \, , \tag{4.9}$$

equivalent to Eq. (4.7).

The above bound applies on the integrated energy density, defined in Eq. (3.19), as

$$\left(\frac{h^2\rho_{\rm GW}}{\rho_c}\right)_0 = \int \frac{df}{f} \, h^2 \, \Omega_{\rm GW}(f) \, . \tag{4.10}$$

Except in the extreme case of a GW spectrum with a very narrow peak of width $\Delta f \ll f$, the above bound can be interpreted as a bound on the amplitude of a GW spectrum, $h^2 \, \Omega_{\rm GW}(f) \lesssim 5.6 \times 10^{-6} \Delta N_\nu$, over a wide frequency range. This of course only applies to GWs with characteristic wavelength well inside the horizon at the time (or slightly before) when the constraint on ΔN_ν is established; otherwise, if the wavelength is super-horizon, the tensor mode does not propagate as a wave and hence it cannot affect the expansion rate of the universe. As shown in section 3, the comoving scale entering the horizon at time t_p is $k = H_p \, a_p$, corresponding to a frequency $f = (H_p/2\pi)(a_p/a_0)$. Furthermore, the bounds in Eq. (4.7) (equivalently (4.9)) obviously applies only to GW backgrounds produced before the physical mechanism (BBN or CMB decoupling) considered to infer the constraint on N_ν ($N_{\rm eff}$), takes place.

Let us now turn to actual constraints on N_ν ($N_{\rm eff}$). We first discuss BBN, which can be used to place an upper limit on N_ν through the predictions of the primordial abundances of light elements. For a review, see e.g. Ref. [66]. BBN successfully predicts the primordial abundances of ^{2}H (Deuterium), ^{3}He, ^{4}He, in very good agreement with measurements from the CMB and astrophysical observations[2] [69]. In particular, the abundance of ^{4}He is very sensitive to the expansion rate $H(T)$ at the beginning of BBN ($T \sim$ MeV), and therefore to

[2]The predictions for ^{6}Li and ^{7}Li are in contrast with observations [67, 68], and this remains an open problem today.

the total amount of radiation at that time, including a possible GW background (Eq. 4.1). The expansion rate in fact controls the relative abundance of neutrons and protons n_n/n_p. At $T \gtrsim$ MeV, neutrons and protons are kept in thermal equilibrium by weak processes like $p + e^- \leftrightarrow n + \nu_e$, simply thanks to their interaction rate $\Gamma_{\rm weak} \sim G_F^2\, T^5$, which is larger than the expansion rate $H(T)$. However, as T decreases, the interaction rate falls below $H(T)$, and the interactions freeze-out at the temperature $T_f \simeq 0.7$ MeV, for which $\Gamma_{\rm weak}(T_f) = H(T_f)$. The neutron-to-proton ratio then freezes at the value $n_n/n_p \sim e^{-Q/T_f}$, where $Q = m_n - m_p$ is the difference between the neutron and proton masses, whereas the exponential (Boltzmann) suppression comes from the fact that the protons and neutrons are non-relativistic. Until the actual onset of BBN, n_n is reduced only by neutron decays. Even though T_f is smaller than the Deuterium biding energy (2.2 MeV), the huge amount of photons present in the early universe delays the Deuterium synthesis by photo-dissociation, until $T_N \simeq 0.1$ MeV, the temperature at which BBN truly starts: the Deuterium formation in fact initiates a chain of nuclear processes leading to heavy nuclei production, especially ^{4}He. Since practically all the available neutrons eventually form ^{4}He, its abundance depends directly on e^{-Q/T_f}, and on the baryon-to-photon ratio $\eta_B = n_B/n_\gamma = 6 \times 10^{-10}$ [30]. An extra radiation component parametrised by N_ν increases the Hubble rate, leading to a larger freeze-out temperature T_f, and therefore to more neutrons and hence to a larger abundance of ^{4}He.

The latest constraints on N_ν by BBN can be found in Ref. [69]. From ^{4}He measurements only, the constraint is $N_\nu < 4$, quite loose because of the strong degeneracy with the baryon to photon ratio η_B. This improves considerably if considered in combination with the Deuterium abundance, and quite strong bounds can be put on both N_ν and η_B. However, the best determination of both parameters is obtained adding the CMB data, as the latter yield a very good measurement of η_B. In particular Ref. [69] finds $N_\nu < 3.2$ at 95% confidence level. Eq. (4.7) then gives $(h^2\, \rho_{\rm GW}/\rho_c)_0 < 1.12 \times 10^{-6}$. As mentioned above, this constraint applies only to GW backgrounds produced before BBN, and not to stochastic backgrounds e.g. from astrophysical sources. Furthermore, it applies only to GWs that were inside the Hubble radius at the time of BBN, which corresponds to present-day frequencies $f \geq 1.5 \times 10^{-12}$ Hz (we have used Eq. (3.31) with $x_k = 1$ and $T = 0.1\,\mathrm{MeV}$).

The CMB constitutes as well a very precise measurement of the radiation energy density, and can be used therefore to infer an upper bound on extra radiation components

parametrised by N_ν, and in turn on the presence of a GW background. The effects that an extra radiation component can have on the CMB are multiple, see e.g. [70]. At the background level, it alters the redshift of matter-radiation equality and of photon decoupling: this leads to a change of all angular scales, shifting the position and amplitude of the CMB acoustic peaks, as well as of the baryon acoustic oscillations observed in galaxy catalogues; it also leads to less growth of the perturbations inside the Hubble radius, affecting the matter power spectrum. For a representation of the effects on the CMB, see Fig. 1 of [71].

The implications of this for GWs have been first analysed in Ref. [72], using a combined dataset including WMAP, ACBAR, CBI, VSA and BOOMERnaG for the CMB, and 2dF and SLOAN galaxy surveys and Lyman-α forest for the matter structure. Two cases were identified, depending on the initial conditions. In the first case, labelled as the 'adiabatic initial condition', the GW background is assumed to be alike a gas of free-streaming neutrinos, so that there are perturbations imprinted on its energy density, following the same distribution as all other components in the universe. The constraint in this case is $(h^2\,\rho_{\rm GW}/\rho_c)_0 \leq 3.9\times10^{-5}$. In the second case, labelled as the 'homogeneous initial condition', the GW background is not perturbed and the curvature perturbation is the one of the standard adiabatic case (therefore it would vanish in the limit of a universe made exclusively by GWs). We view this second option for initial conditions as more justified, since it applies to all known mechanisms of generation of a GW background[3] (from the irreducible GW background due to quantum fluctuations during inflation, to all active sources operating during or after inflation in the early Universe). In the case of homogeneous initial conditions, Ref. [72] finds a stronger bound as $(h^2\,\rho_{\rm GW}/\rho_c)_0 \leq 6.9\times10^{-6}$, since all degeneracy with the neutrino parameters (number of species, sum of the masses) is broken.

Note that this bound extends over a wider range of frequencies than the analogous one from the BBN one, as the frequency corresponding to the comoving scale entering the horizon during decoupling is $f = (H_{\rm dec}/2\pi)(a_{\rm dec}/a_0) \simeq 7\times10^{-18}$ Hz. More realistically, Ref. [72] considers that the the tensor modes will have to oscillate for a while, once inside the horizon, before they can be fully considered as GWs (and hence as a radiation component), in order

[3] In most circumstances the energy density of GWs is not perturbed at first order in cosmological perturbation theory, though there are exceptions as in certain cases of preheating, see [73, 74] for a discussion on this. Furthermore, GWs are not expected to be produced by the decay of the inflation field in the same manner as all other matter/radiation fields in the universe, so there is really no clear justification to assume they have the same adiabatic initial conditions that apply to neutrinos.

to provide the effect under analysis. Therefore Ref. [72] tentatively sets the lowest frequency for which the bound applies to $f > 10^{-15}$ Hz.

The analysis of [72] has been redone more recently by [71, 75]. In particular, the latests analysis of Ref. [75] uses Planck data, together with CMB lensing, Baryon Acoustic Oscillations and also Deuterium abundances, and finds a constraint that goes down to $(h^2\,\rho_{\rm GW}/\rho_c)_0 \leq 1.2 \times 10^{-6}$. Not surprisingly, this is comparable to what is obtained from the BBN analysis by [69], which also uses WMAP data to pin down the baryon to photon ratio η_B. However, Ref. [75] only analyses adiabatic initial conditions. From the results of Refs. [71, 72], one can infer that the gain obtained imposing homogeneous initial conditions, due to the breaking of degeneracies with neutrino parameters, is of a factor of a few, of the order of ~ 5. Using this, we can tentatively estimate the constraints that could be put by Planck and other actual cosmological data in the hypothesis of GW with homogeneous initial conditions, as $(h^2\,\rho_{\rm GW}/\rho_c)_0 \lesssim 2 \times 10^{-7}$.

The bounds presented above apply to any GW background produced before BBN or before CMB decoupling, as those we will discuss in the following sections. They are not relevant however for the irreducible background of GWs expected from inflation, that we will introduce in section 5.2. The inflationary background of GWs is in fact constrained much better (down to many orders of magnitude lower in amplitude) by another kind of constraint, formerly know as the 'COBE bound', which we describe in the next section[4].

4.2 Constraints from Cosmic Microwave Background anisotropies

As the CMB is our best probe of the homogeneity and isotropy of the universe, it can also be used to place constraints on the amplitude of metric perturbations over the FLRW metric, in particular in the presence of a SGWB[5]. A SGWB induces fluctuations in both the temperature and polarisation of the CMB, as GWs affect the space-time through which

[4] As we will see, the 'COBE' bound attains only lower frequencies (corresponding to CMB scales), but assuming the standard almost-scale invariant form of the inflationary spectrum (c.f. section 5), the corresponding bound on $h^2\,\rho_{\rm GW}/\rho_c$ at CMB scales can be extrapolated to much higher frequencies (corresponding to scales much smaller than the CMB scales).

[5] Let us recall here that tensor perturbations can only be properly interpreted as a background of GWs for modes well inside the horizon, see discussions in Sect. 2. The imprint of tensor perturbations on the CMB, similarly as in the case of scalar perturbations, is however due to both super- and sub-horizon modes at the CMB time. Thus, we should be really speaking about stochastic tensor modes, rather than of a stochastic background of GWs. We will nonetheless allow ourselves such abuse of language, as it is customary when discussing the effect of tensor perturbations on the CMB.

the photons propagate with their characteristic quadrupolar pattern. The measurement of the CMB temperature and polarization angular power spectra at large angular scales, can be used therefore to constrain the amplitude and spectral index of a SGWB at the very low frequencies $f = k/(2\pi a_0)$, comprised between the Hubble parameter today and the Hubble parameter at matter-radiation equality, i.e. $H_0 a_0 < k < H_{\rm eq} a_{\rm eq}$ (for a universe dominated by radiation and matter only, $H_{\rm eq} a_{\rm eq} = \sqrt{2}\, a_0\, H_0\, \Omega_{\rm mat}/\sqrt{\Omega_{\rm rad}}$, c.f. Eq. (5.43)).

In principle, the constraint that can be inferred from the measurement of CMB fluctuations holds irrespective of the origin of the stochastic GW background. In practice, however, it is only relevant for mechanisms capable of producing a GW spectrum with a non-negligible amplitude on scales around the Hubble scale at the epoch of CMB decoupling (both sub- and super-horizon scales). These mechanisms include an early epoch of accelerated expansion: inflation (chapter 5.2), or its alternatives like pre-big bang and ekpyrotic scenarios (see e.g. section 6.5 in [15]). They also include active seeds like cosmic defects, which continuously source metric perturbations around the horizon scale at every moment of cosmic evolution (treated e.g. in section 9 of [15]). On the contrary, typical GW generation mechanisms from the early Universe, operating for a short amount of time and within the causal horizon (e.g. a phase transition), cannot be probed well by the CMB fluctuations. As we will see in chapter 6, short-time mechanisms lead generically to a SGWB energy density spectrum scaling as $\Omega_{\rm GW}(k) \propto k^3$, on scales $k < H_{\rm in} a_{\rm in}$ larger than the size of the horizon at the time $\eta_{\rm in}$ of production. These mechanisms are typically operative after inflation but well before Nucleosynthesis. Their characteristic time and length scale, of the order of $1/(H_{\rm in} a_{\rm in})$ at most, is therefore much smaller than CMB scales, which span around the size of the horizon at photon decoupling $c_s(\eta_{\rm dec})/(H_{\rm dec} a_{\rm dec})$.

A stochastic background of GW induces temperature fluctuations in the CMB through the Sachs Wolfe effect [76, 77] as

$$\frac{\Delta T}{T} = -\int_i^f h'_{jl}(\mathbf{x}, \eta) n^j n^l d\lambda \,, \tag{4.11}$$

where λ is an affine parameter along the photon geodesic with tangent vector $\mathbf{n}$, $h'_{jl}(\mathbf{x}, \eta)$ is the time derivative of the tensor metric perturbation and i and f denote the initial (e.g. photon decoupling) and final (e.g. today) times. Note that the above temperature fluctuation,

due to presence of the tensor mode, has a quadrupolar pattern. Around the recombination time, photons perform Thomson scattering with the electrons of the primordial plasma. If the incident radiation on the electron is not isotropic, the resulting scattered light becomes polarised. Consequently, the quadrupole anisotropy in the photon distribution, due to the presence of tensor modes, induces a net polarisation in the Thomson-scattered photons. The polarization pattern is then maintained until today, as the photons travel freely since they performed their last scattering [78–80].

This polarisation signal in the CMB is generated only at last scattering, contrary to the temperature anisotropies sourced continuously up to today as in Eq. (4.11). Customarily, CMB polarisation is decomposed into two polarisation patterns that have the advantage of being independent of the reference frame: E and B polarisation modes. The E-mode is sourced by all scalar, vector and tensor metric perturbations, while the B-mode is only sourced by vector and tensor perturbations, but not by scalar perturbations. As in the dominant paradigm of the early Universe, inflation, vector perturbations died away during the accelerated expansion, a B-mode polarization represents a unique imprint of the presence of primordial inflationary GWs. Unfortunately, more important sources of B-polarisation than the primordial tensor perturbations are gravitational lensing and galactic foregrounds, such as galactic dust and synchrotron emission. This poses a serious challenge for CMB detectors aiming at measuring the tensor primordial spectrum. While lensing can be distinguished in the angular CMB spectrum by the characteristic shape it produces, and by the fact that it becomes important only at relatively high multipoles, distinguishing galactic foregrounds is more challenging[6]. Envisaged solutions are to measure several CMB frequencies (in order to distinguish the CMB black-body spectrum in frequency from the foreground spectra), ground-based observations of regions of the sky poorly contaminated by foreground emissions, and full-sky observations with space satellites.

The contribution of tensor modes to the CMB temperature and polarisation anisotropy angular power spectra today can be written in a very compact form using the formalism

[6] In 2014, BICEP2 announced the detection of B-mode polarization of primordial origin [81], before a joint analysis using Planck data proved that it was in reality polarised emission from galactic dust [82], see footnote in Sect. 5.2.

of [55],

$$C_{\ell,T}^{XY} = \frac{2}{\pi}\frac{1}{(2\ell+1)^2}\int dk\, k^2 [X_\ell^2(k,\eta_0)Y_\ell^{2*}(k,\eta_0) + X_\ell^{-2}(k,\eta_0)Y_\ell^{-2*}(k,\eta_0)] \tag{4.12}$$

where T stands for tensor, and X and Y can be, respectively, the temperature $\Theta_\ell^{\pm 2}$, or the polarization $E_\ell^{\pm 2}$ or $B_\ell^{\pm 2}$, anisotropies today. These are here expanded using the normal modes defined in Eqs. (10-11) of [55], which combine the angular dependence from the spherical harmonic decomposition (adopted since temperature and polarisation transform, respectively, as a scalar and a spin two field, on the surface of the sky) with the one of a plane wave decomposition (in terms of which the spatial dependence of the temperature and polarisation fields is expanded, and which accounts for the photon propagation after CMB decoupling). Note that, in the formalism of [55], tensors are expanded in the helicity basis (see Eq. (34) of [55], from which we borrow the normalisation, and also Sect. 3)

$$e_{ij}^{\pm 2} = -\sqrt{\frac{3}{8}}\,(\hat{m} \pm i\,\hat{n})_i \times (\hat{m} \pm i\,\hat{n})_j \tag{4.13}$$

where $\hat{m}$ and $\hat{n}$ are the unit vectors of Eq. (2.57). In terms of the usual polarisation tensors defined in section 3 one has $e_{ij}^{\pm 2} = -\sqrt{3/8}\,(e_{ij}^{+} \pm i\, e_{ij}^{\times})$. The coefficients of the tensor-induced temperature $\Theta_\ell^{\pm 2}$ and $E_\ell^{\pm 2}$, $B_\ell^{\pm 2}$ polarisation anisotropies today, are given by time integrals of the sources as [55]

$$\frac{\Theta_\ell^{\pm 2}(k,\eta_0)}{2\ell+1} = -\frac{2}{3}\int_0^{\eta_0} d\eta\, e^{-\tau}\,(h^{\pm 2}(k,\eta))' j_\ell^{(2\,2)}(k(\eta_0-\eta))\,, \tag{4.14}$$

$$\frac{E_\ell^{\pm 2}(k,\eta_0)}{2\ell+1} = -\frac{\sqrt{6}}{10}\int_0^{\eta_0} d\eta\, \tau' e^{-\tau}\,[\Theta_2^{\pm 2} - \sqrt{6}E_2^{\pm 2}]\,\epsilon_\ell^{\pm 2}(k(\eta_0-\eta))\,, \tag{4.15}$$

$$\frac{B_\ell^{\pm 2}(k,\eta_0)}{2\ell+1} = -\frac{\sqrt{6}}{10}\int_0^{\eta_0} d\eta\, \tau' e^{-\tau}\,[\Theta_2^{\pm 2} - \sqrt{6}E_2^{\pm 2}]\,\beta_\ell^{\pm 2}(k(\eta_0-\eta))\,, \tag{4.16}$$

where $\tau(\eta)$ is the optical depth between time η and today, whereas the radial functions $j_\ell^{(2\,2)}$, $\epsilon_\ell^{\pm 2}$ and $\beta_\ell^{\pm 2}$ represent how the total angular power is transferred into the ℓ modes, and can be found in Eqs. (15), (17), (18) of [55]. Eq. (4.14) follows directly from (4.11) and shows that the source of temperature anisotropy is the time derivative of the tensor perturbations. Moreover, the factor $e^{-\tau(\eta)}$ becomes non-zero only from the time of photon decoupling onwards, naturally selecting the period since the last scattering surface till today, as the time window

during which the source of temperature anisotropy is active. This is to be compared with Eqs. (4.15, 4.16), where on the contrary $\tau' e^{-\tau}$ is strongly peaked around decoupling time, indicating that CMB polarisation is generated only around this time. Moreover, Eqs. (4.15, 4.16) show that only the quadrupole $\ell = 2$ in the temperature anisotropy Θ_2^m and in the polarisation E_2^m can source the polarisation signal.

In the following we derive the temperature anisotropy angular spectrum, as a worked out example of the effect of tensor modes on the CMB fluctuations. For the initial tensor spectrum leading to the signal we want to evaluate, we consider the case of a super-horizon spectrum with constant amplitude A_T and spectral index n_T, c.f. Eq. (4.21). This leads to equations which are sufficiently simple to be tackled analytically, at least if one is looking for an approximate (but instructive) result. Furthermore, it is directly applicable to the case of inflation (c.f. section 5), even though it is in principle valid for any generation mechanism that produces such a spectrum on super-horizon scales.

In order to find the CMB temperature spectrum, one has to combine Eqs. (4.14) and (4.12). Using $j_\ell^{(2\,2)}(x) = \sqrt{3(\ell+2)!/(8(\ell-2)!)}\; j_\ell(x)/x^2$, this gives

$$\begin{aligned} C_{\ell,T}^{\Theta\Theta} \;\simeq\; & \frac{1}{3\pi}\frac{(\ell+2)!}{(\ell-2)!}\int dk\, k^2 \int_{\eta_{\rm dec}}^{\eta_0} d\zeta\, \frac{j_\ell(k(\eta_0-\zeta))}{k^2(\eta_0-\zeta)^2}\int_{\eta_{\rm dec}}^{\eta_0} d\xi\, \frac{j_\ell(k(\eta_0-\xi))}{k^2(\eta_0-\xi)^2} \\ & \times[(h^2(k,\zeta))'(h^{2*}(k,\xi))' + (h^{-2}(k,\zeta))'(h^{-2*}(k,\xi))']\,, \end{aligned} \tag{4.17}$$

where $\eta_{\rm dec}$ denotes the photon decoupling time, inserted as a lower bound of integration in order to account for the effect of the optical depth. The tensor perturbation $h^{\pm 2}(k,\eta)$ can be inferred from the non-decaying solution of the wave equation (2.63). Tensor perturbations contribute to the present CMB temperature fluctuations roughly from the decoupling time onwards. If the GW source operated for a finite period of time in the early universe and ceased to act before decoupling time, we have seen in section 3 that the homogeneous solution $h_r(k, \eta > \eta_{\rm dec})$ of equation (2.63) is a constant fixed by the initial conditions on super-horizon scales, while it oscillates and decays as a^{-1} once the mode has entered the horizon. We will re-derive and confirm this result in the context of slow roll inflation in section 5.2. As a consequence, the dominant contribution to the time integrals of Eq. (4.17) comes from modes that entered the horizon during the matter dominated era, since the amplitude of those that entered before has been further suppressed by the sub-horizon decay, giving a

negligible contribution. As we will derive in section 5.3, in the matter era the solution is particularly simple, c.f. Eq. (5.40):

$$h^{\pm 2}(x) = h^{\pm 2}_{\rm in}(k)\,\frac{3\,j_1(x)}{x} \tag{4.18}$$

$$(h^{\pm 2}(x))' = h^{\pm 2}_{\rm in}(k)\,\frac{-3\,k\,j_2(x)}{x} \tag{4.19}$$

where $x = k\eta$ and $h^{\pm 2}_{\rm in}(k)$ denotes the initial amplitude at super-horizon scales. To make contact with definitions in other sections (e.g. sections 3 and 5), we go from the helicity basis to the usual tensor basis, and define the initial GW spectrum (see e.g. equation (5.27)):

$$\begin{aligned}\left\langle h^{+2}_{\rm in}(k)h^{+2*}_{\rm in}(k) + h^{-2}_{\rm in}(k)h^{-2*}_{\rm in}(k)\right\rangle &= \frac{4}{3}\left\langle [h^{+}_{\rm in}(k)h^{+*}_{\rm in}(k) + h^{\times}_{\rm in}(k)h^{\times *}_{\rm in}(k)]\right\rangle \\ &= \frac{4}{3}\,\pi^2\frac{\mathcal{P}_h(k)}{k^3}\,.\end{aligned} \tag{4.20}$$

Because of the presence of the time integrals in (4.17), it is useful to normalise $\mathcal{P}_h(k)$ at the scale corresponding to the inverse comoving time today, $k_0 = 1/\eta_0$ (note however that this normalisation is completely arbitrary). Allowing for a generic spectral index, we write

$$\mathcal{P}_h(k) = A_T(k_0)\,(k\eta_0)^{n_T}\,. \tag{4.21}$$

In the inflationary case, the initial tensor spectrum is due to the amplification of vacuum metric fluctuations and it is given in Eq. (5.28) (see also Eq. (5.31)) at first order in slow roll. Going back to Eq. (4.17), and using Eq. (4.19), the CMB temperature spectrum becomes

$$\begin{aligned}C^{\Theta\Theta}_{\ell,T} &\simeq 4\pi\frac{(\ell+2)!}{(\ell-2)!}\int\frac{dk}{k}\,\mathcal{P}_h(k)\left[\int_{x_{\rm dec}}^{x_0} dx\,\frac{j_\ell(x_0-x)}{(x_0-x)^2}\frac{j_2(x)}{x}\right]^2 \\ &\simeq \frac{\sqrt{\pi}}{3}\,A_T(k_0)\,\frac{\ell(\ell+2)!}{(\ell-2)!}\,\frac{\Gamma\left[\frac{7-n_T}{2}\right]\Gamma\left[\ell+\frac{n_T}{2}\right]}{\Gamma\left[4-\frac{n_T}{2}\right]\Gamma\left[\ell+7-\frac{n_T}{2}\right]} \\ &\propto \ell^{n_T-2} \quad \text{for} \quad \ell \gg 1\,,\end{aligned} \tag{4.22}$$

where the approximated result in the second line has been evaluated using Eq. (B.5) of Ref. [56] for the integral in x, and then integrating exactly over k using (6.574.2) of Ref. [83]. The spectrum in Eq. (4.22) has been derived also e.g. in [38]. In the limit of big multipoles (small angular scales) $\ell \gg 1$, one recovers the usual shape for the CMB tensor angular

spectrum, where $\ell(\ell+1)C_\ell \propto const.$ for a scale invariant tensor spectrum $n_T = 0$ [38, 84]. However, in general, there is a dependence of the CMB spectrum on n_T as ℓ^{n_T-2}. Note that the latter result is valid only for $1 \ll \ell \lesssim 60$, as it is a quite crude estimation which does not take into account the decay of GW for modes that enter the horizon before matter-radiation equality, corresponding roughly to an angular scale of $\ell \simeq 60$ [38].

From Eq. (4.22) it appears that the measurement of the CMB spectrum at low multipoles can be used to infer a combined bound on the amplitude A_T and the spectral index n_T of a GW background (generated before decoupling) at super-horizon scales. Historically, in the GW literature, this constraint has been referred to as the 'COBE bound', since it was first established using the measurement of the CMB quadrupole $\ell = 2$ by the COBE satellite [85–89]. The bound was derived setting $n_T = 0$ and considering that the CMB temperature anisotropy at large angular scales was entirely due to the tensor mode. Today we know that this is not the case, and that the main contribution to the CMB anisotropy comes from scalar perturbations. In fact, the difference in the shape of the scalar and tensor temperature CMB spectra as a function of multipole ℓ allows to distinguish the two contributions.

For what concerns the latest results from the Planck satellite, Ref. [30] states that the strongest constraint on tensor modes still comes from the CMB temperature spectrum at $\ell < 100$ (the tensor mode contribution decays at higher multipoles), so that the addition of E-polarisation does not change the result significantly. Therefore, the precision of this constraint is limited by cosmic variance, and can only be improved by adding a direct measurement of B-polarisation. This has been done in [90], where the data of the BICEP2 and Keck Array B-polarisation detectors have been combined with the Planck data, yielding the strongest constraint to date on the amplitude of tensor modes, coming from CMB only. The bound is given in terms of the tensor to scalar ratio (see section 5.2 and in particular Eq. (5.35) for a definition) and reads (for the pivot scale $k_* = 0.05\,\mathrm{Mpc}^{-1}$) [30]

$$r_{0.05} = \frac{\mathcal{P}_h}{\mathcal{P}_\mathcal{R}} \leq 0.07 \qquad \text{at} \quad 95\% \text{ c.l.} \tag{4.23}$$

where $\mathcal{P}_\mathcal{R} \simeq 2 \cdot 10^{-9}$ denotes the primordial curvature power spectrum amplitude at the pivot scale $k_* = 0.05\,\mathrm{Mpc}^{-1}$, see Eq. (5.34).

Note that the above constraint is derived assuming a ΛCDM model, fixing the tensor

spectral index to zero, $n_T = 0$. Current CMB measurements do not have the ability to constrain n_T, since the measurement of r is still compatible with zero, and for low enough r, practically any value of n_T is acceptable. For this reason, the constraints on n_T depend on the chosen prior on r, as pointed our for example in [91]. This situation will change if, in the future, a positive detection of a non-zero tensor amplitude is obtained from primordial B-modes (see [91] for forecasts concerning a COrE-like mission [92] exclusively dedicated to B-mode polarisation). In the meanwhile, other observations like those from Pulsar Timing Arrays (PTA) (c.f. section 4.3), or from direct GW detection ground-based interferometers (c.f. section 4.4), can be used to place upper bounds on n_T in the case of blue tilted SGWB spectra, see e.g. Refs. [13, 91, 93, 94].

The GW energy density fraction today can be expressed in terms of the tensor to scalar ratio r and a generic spectral index n_T using Eq. (5.52) (c.f. section 5.3 and the discussion therein),

$$\Omega_{\rm GW}(f) = \frac{3}{128}\,\Omega_{\rm rad}\,r\,\mathcal{P}_{\mathcal{R}}\left(\frac{f}{f_*}\right)^{n_T}\left[\frac{1}{2}\left(\frac{f_{\rm eq}}{f}\right)^2+\frac{16}{9}\right], \tag{4.24}$$

where $f_* = k_*/(2\pi a_0)$ is the pivot frequency at which the primordial scalar amplitude is normalised, $k_* = 0.05\,\mathrm{Mpc}^{-1}$, and $f_{\rm eq} = H_0\,\Omega_{\rm mat}/(\pi\sqrt{2\,\Omega_{\rm rad}})$ is the frequency entering the horizon at matter-radiation equality, c.f. Eq. (5.43). The energy density spectrum of Eq. (4.24) is shown in Fig. 4.1 for r saturating the bound in Eq. (4.23) and two values of n_T: the red-tilted value predicted by slow roll inflation, corresponding to the consistency relation $n_T = -r/8$ (c.f. sec. 5.2 and in particular Eq. (5.37)), and a blue-tilted case with large index, $n_T = 0.15$. In this figure we also show the sensitivity of current and future GW detectors (which we will describe in Sect. 4.4) and the CMB bound derived in Eq. (4.23), which applies for $n_T = 0$. Note that, as discussed before, tensor modes decay once they enter the horizon; this determines the regime of validity of the CMB bound, namely frequencies which were outside the horizon at matter-radiation equality but are inside the horizon today: $3.4\cdot10^{-19} < f < 2.1\cdot10^{-17}$ Hz. For forecasts on the constraints that can be derived on the couple of parameters (n_T, r) by the combination of data from CMB temperature anisotropies and B-polarization, with direct bounds established by advanced LIGO/Virgo and PTA, and with indirect bounds described in section 4.1, we refer the reader for example to Fig. 2 of [93], see also [91, 94].

At last, it is worth mentioning another way to probe the presence of primordial tensor

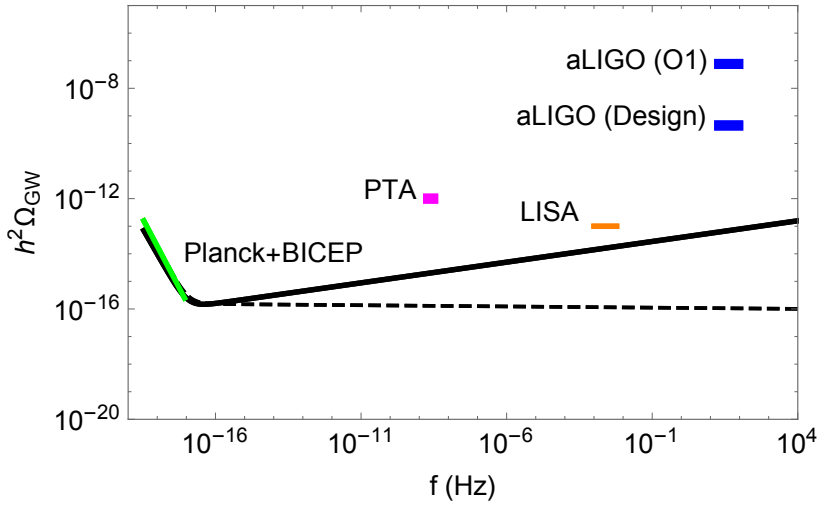

Figure 4.1: The power spectrum of Eq. (4.24) for $r = 0.07$ and $n_T = -r/8$ (black dashed line), and $n_T = 0.15$ (black solid line), together with the constraint given by Planck+BICEP2+Keck Array data given in Eq. (4.23), i.e. setting $r = 0.07$ and $n_T = 0$ (green solid line), and the reach of current and future GW detectors: PTA (magenta, solid), advanced LIGO at the first run and at design sensitivity (blue, solid) and LISA (orange, solid).

modes via the CMB, namely spectral distortions of the CMB black-body spectrum [95, 96]. These are tiny deviations of the CMB monopole from a perfect black-body, produced at redshift $z \lesssim 10^6$, when thermalisation processes like Compton scattering and Bremsstrahlung start to be less efficient. Spectral distortions can be due to several processes that cause energy injection in the photon distribution, both in the context of the standard cosmological model (recombination, the dissipation of primordial fluctuations, reionisation, structure formation...) and of its extensions (annihilation or decay of particles, primordial magnetic fields, primordial black holes, cosmic strings...). See [97, 98] for recent analyses, and references therein. The CMB spectral distortion due to the presence of primordial tensor modes is produced via Thomson scattering in a similar way to the one due to the dissipation of scalar perturbations, but the tensor anisotropic stress (shear viscosity) in the photon distribution, necessary to activate the dissipation process, is directly induced by the tensor modes instead of by photon free-streaming [95]. As a consequence, the dissipation occurs over a wider range of scales than those probed by Silk damping, as in the case of scalar modes. For the almost scale invariant tensor spectrum produced in slow roll inflationary scenarios, it has been shown that the amplitude of the distortion is very small, providing only a tiny correction to the signal expected from the dissipation of scalar perturbations [95, 96]. A more

important deviation from the CMB black-body can be induced if the tensor spectrum is very blue, say with $n_T \simeq 1$. In this case, the level of the distortion can become comparable to the one induced by scalar modes in the standard inflationary scenario [96].

4.3 Pulsar timing arrays

Pulsars are highly magnetized, rotating neutron stars, that emit a beam of electromagnetic radiation in the direction of their magnetic axis (which spins along with the rotation of the neutron star). It is the magnetic axis of the pulsar, which does not necessarily coincide with the rotational axis, that determines the direction of the electromagnetic beam. If the beam sweeps the line of sight between Earth and the pulsar, a regular train of radiation pulses is observed, similarly as when we observe a lighthouse from the distance. Pulsars are thus colloquially referred to as 'cosmic lighthouses'. The arrival times of the pulses are extremely regular and can be predicted very accurately over long times. Pulsars represent therefore very stable 'clocks' scattered around the sky, which allow for a variety of precise astronomical measurements. For instance, the first extra-solar planet was discovered around a pulsar [99], and the decrease of the orbital period of a binary system with a pulsar – the *Hulse-Taylor binary* – provided the first indirect evidence for the existence of GWs [100, 101]. As we will discuss in the following, pulsars can be used also as a direct probe of SGWBs, since the arrival times of the electromagnetic pulses experience a shift in the presence of a GW background.

The use of pulsars as a precise clock, rely on a technique known as 'pulsar timing', see e.g. Ref. [102] for a review. This basically involves two main steps: first, the beam profiles are analysed so that a 'time of arrival' (TOA) is assigned to each pulse. Secondly, the measured TOA's are compared to a theoretical modelling that incorporates many circumstances possibly affecting the signal, from the evolution of the pulsar's rotation, to the relative motion between the pulsar and Earth, the propagation of the pulses through the interstellar medium, etc. Parameters such as the pulsar's spin period, spin-down rate, proper motion, and others, are obtained from fits to the data. The difference between the best-fit model predictions and the measured TOA, for a given pulsar, is called 'timing residual'. Among the different pulsars, those with rotation periods of the order of a millisecond, have very small timing irregularities, and their TOA's can be measured with very high precision. Millisecond pulsars

are therefore particularly suited for the detection of GW backgrounds, as timing residuals varying by no more than few micro seconds over several years can be obtained for them, see e.g. Fig. 5 of Ref. [103].

The use of pulsar timing observations as a way to detects/constrain GWs was first studied by Sazhin [104] and Detweiler [105] and further developed in Refs. [106–109]. The very small timing residuals observed in various pulsars can be used to set upper bounds on the presence of a GW background between a given pulsar and Earth. The maximum sensitivity can be achieved for a GW background with power at frequencies of the order of the inverse total observation time T, typically[7] at $f \sim 10^{-9} - 10^{-8}$ Hz for $T \sim$ few years. For a timing residual varying by an amount of δt, a constraint on the characteristic amplitude of a stochastic GW background, typically of the order of $h_c \lesssim \delta t/T$ [see Eqs. (3.11,3.17)], can be obtained. Using this fact and e.g. $\delta t \sim$ few $\times 10^{-6}$ sec and $T \sim$ few years, Eq. (3.21) leads to a constraint $h^2\,\Omega_{\rm GW} \lesssim$ few $\times 10^{-8}$ at $f \sim 10^{-8}$ Hz. More precisely, using long-term observations of stable millisecond pulsars, Kaspi et al [103] obtained, for a flat spectrum of GW, an upper bound of $h^2\,\Omega_{\rm GW} < 6 \times 10^{-8}$ (at 95% confidence level) at $f \approx 4.5 \times 10^{-9}$ Hz. This was further improved to $h^2\,\Omega_{\rm GW} < 10^{-8}$ at $f \approx 4.5 \times 10^{-9}$ Hz in Ref. [110], and to $h^2\,\Omega_{\rm GW} < 2 \times 10^{-9}$ at $f \approx 2 \times 10^{-9}$ Hz in Ref. [111]. Note however that the statistical method used in the latter works has been criticized in the literature, see Refs. [112], [113].

The previous technique allows to establish strong upper bounds on the presence of a stochastic GW background in the Universe. However, since it is not possible to determine the exact origin of a given timing residual, the observation of an individual pulsar does not allow by itself, to actually detect a GW stochastic background. The timing residuals might be due to a number of reasons, not always under control, such as irregularities in the pulsar's rotation or in the terrestrial time standards. The effect of a stochastic GW background on the timing residuals of various pulsars, however, may be distinguished and isolated by looking for correlations among the different pulsars' residuals. This can be done by the so called 'pulsar timing arrays' (PTA), where timing observations are performed for many pulsars distributed over the sky. The presence of an isotropic stochastic background of GWs will induce a correlation between the timing residuals from different pulsars, depending only on the angular separation between the location of the pulsars in the sky. The GW induced

[7] The fitting procedure to a pulsar model described before removes the signal effect from GWs with frequencies much smaller than $\sim 1/T$.

frequency shifts in the arrival times of a train of pulses (from a given pulsar) depends on the GW amplitude along the path of the pulse,

$$\frac{\Delta\nu}{\nu} = -\frac{1}{2}\int_{\lambda_e}^{\lambda_r} d\lambda\, h'_{ij}(x(\lambda))\hat{\zeta}_i\hat{\zeta}_j\,, \tag{4.25}$$

where $\hat{\zeta}_i$ is the unit vector in the pulsar-Earth direction, and λ is the affine parameter parametrizing the spatial trajectory of the pulse [c.f. Eq. (4.11)]. The correlation between the frequency shifts of two pulsars comes from the Earth-contribution to each pulsar. Using the decomposition of a GW background given by Eq. (2.56), with e^r_{ij} the polarization tensors Eq. (2.57), the correlation can be written as [107]

$$\left\langle \frac{\Delta\nu}{\nu}(\hat{\boldsymbol{\zeta}})\,\frac{\Delta\nu}{\nu}(\hat{\boldsymbol{\xi}})\right\rangle \;\propto\; \sum_{r=+,\times}\int d^2\hat{\mathbf{k}}\,\frac{e^r_{ij}(\hat{\mathbf{k}})\,e^r_{kl}(\hat{\mathbf{k}})\,\hat{\zeta}_i\,\hat{\zeta}_j\,\hat{\xi}_k\,\hat{\xi}_l}{(1+\hat{k}_m\,\hat{\zeta}_m)\,(1+\hat{k}_n\,\hat{\xi}_n)} \tag{4.26}$$

$$\propto\; x\log x - \frac{x}{6} + \frac{1}{3} \quad \text{with} \quad x = \frac{1-\cos\theta}{2}\,, \tag{4.27}$$

where in the second line we have used the polarization tensor completeness relation Eq. (2.59), and defined the angle $\cos\theta = \hat{\zeta}_i\,\hat{\xi}_i$ between the unit vectors in the pulsar-Earth direction for each pulsar. The specific dependence on the angle θ exhibited by this correlation between frequency shifts, represents a characteristic and unique signature of the presence of a stochastic GW background in PTA observations.

There are various active PTA collaborations searching for GW backgrounds: the *Parkes Pulsar Timing Array* [114] (PPTA), the *European Pulsar Timing Array* [115] (EPTA) and the *North American Nanohertz Observatory for Gravitational Waves* [116] (NANOGrav). They have recently joint forces forming the *International Pulsar Timing Array* [117, 118] (IPTA). The current upper bounds on GW backgrounds obtained by these collaborations have been reported in Refs. [113], [119], [120], and [121]. In these works, a GW background is characterized by its amplitude $h_c(f)$ (see Eq. (3.21) for the relation to $\Omega_{\rm GW}(f)$), parametrized like

$$h_c(f) = A_\alpha\left(\frac{f}{\text{year}^{-1}}\right)^\alpha\,. \tag{4.28}$$

The upper limits obtained on A_α depend, in principle, on each chosen value for α. In particular $\alpha = -2/3$ (i.e. $\Omega_{\rm GW}(f) \propto f^{2/3}$) is expected in the case of the GW background from unresolved supermassive black hole binaries, whereas $\alpha = -1$ corresponds to a flat

spectrum $\Omega_{\rm GW}(f) \propto$ *const.*, and $\alpha = -7/6$ (i.e. $\Omega_{\rm GW}(f) \propto f^{-1/3}$) is a typical value expected for the GW background from cosmic strings. The upper bounds at the frequency where the sensitivity is best achieved, $f \sim 1/T$ (T here is the effective total observation time of the multiple pulsars), are approximately independent of the slope of the GW spectrum. The α-dependence of the upper limits on A_α comes about mostly because the chosen reference frequency $f = 1/\text{year}$ differs from $f \sim 1/T$, see Refs. [113], [119]. For instance, Jenet et al [113] obtained, for a range of values of α, an upper bound (95% confidence) $h^2\,\Omega_{\rm GW} < 2 \times 10^{-8}$ at $f = (8\,\text{years})^{-1} \simeq 4 \times 10^{-9}$ Hz, whereas Lentati et al [120] obtained $h^2\,\Omega_{\rm GW} < 1.2 \times 10^{-9}$, at $f = (18\,\text{years})^{-1} \simeq 2.4 \times 10^{-9}$ Hz. For $\alpha = -2/3$, the results yield $h^2\,\Omega_{\rm GW} < 3.1 \times 10^{-8}$ at $f \sim 3 \times 10^{-8}$ Hz (Demorest et al [119]) and $h^2\,\Omega_{\rm GW} < 1.1 \times 10^{-9}$ at $f \sim 2.4 \times 10^{-9}$ Hz (Lentati et al [120]). The PTA bounds on GW backgrounds are particularly constraining for cosmic strings. Furthermore, contrary to the BBN and CMB bounds discussed in Sect. 4.1, the PTA bound can be applied as well to stochastic backgrounds produced (way after BBN and photon decoupling) by unresolved astrophysical sources.

The sensitivity of PTA to SGWBs is expected to improve in the near future. There are good prospects for improving the timing precision, the total observation time, the number of observations and the number of millisecond pulsars that will be observed. The IPTA [117] is expected to reach a sensitivity of the order of $h^2\,\Omega_{\rm GW} \sim 10^{-11}$. In the longer term, the *Square Kilometer Array* (SKA) is expected to reach sensitivities, in the nHz frequency range, down to $h^2\,\Omega_{\rm GW} \sim 10^{-15}$ assuming 50 pulsars monitored every two weeks for 20 years [122]. Let us note however, that one of the most significant stochastic backgrounds of GWs in the PTA frequency range, is produced by super-massive black hole (SMBH) binaries that coalesce when galaxies merge [123–126]. Even though this astrophysical background has a characteristic frequency-dependence as $\Omega_{\rm GW} \propto f^{2/3}$ that distinguishes it from other backgrounds, it will 'hide' other cosmological backgrounds with smaller amplitude. The amplitude of the SMBH background depends on the galaxy merger rates during the cosmological evolution and on the typical SMBH masses. Given the current uncertainties on the astrophysical parameters characterizing these mergers, a conservative lower limit on this background can be obtained using the results from Refs. [126], [127],

$$h^2\,\Omega_{gw}^{SMBH} \lesssim 10^{-11}\left(\frac{f}{10^{-8}\,\text{Hz}}\right)^{2/3} \qquad \text{for} \qquad f \lesssim 10^{-8}\,\text{Hz}\,. \tag{4.29}$$

A cosmological background with a smaller amplitude than in Eq. (4.29) will thus be unlikely to be observable by PTA. Note also that the signal amplitude Eq. (4.29) is well within the reach of an experiment like SKA.

4.4 Gravitational wave interferometers

4.4.1 Principles of the detection of a stochastic background.

We present here a basic description of the principles of SGWB detection by GW interferometers, based mainly on [32]. We point the reader interested in a closer examination of this topic to the exhaustive treatments of Refs. [33, 64].

The detection of GWs consists in measuring the quadrupolar deformation of spacetime that they induce. This can be done through a resonating mechanical system (the first GW detectors were resonant massive bars, for an overview see [33]), but a much more efficient method is via a Michelson interferometer operating between freely suspended masses. In the idealized case of a linearly polarized wave hitting perpendicularly the interferometric system, with its polarization axes aligned with the arms in the proper detector frame as defined in [33], one arm contracts while the other expands. Therefore, the laser beams returning from each arm pick up a phase difference which changes in time following the passage of the wave, influencing the interferometric patterns: this is the principle of the GW detection via interferometers[8] (for a review, see e.g. [128]).

In the case of one interferometer with arms of equal length L in the x and y directions, the output of the detector due to the passing of a GW is the strain $h(t) = (\Delta L_x(t) - \Delta L_y(t))/L$. This scalar signal is related to the GW in the TT gauge as $h(t) = F_+ h_+(t) + F_\times h_\times(t)$, where $F_{+,\times}(\hat{\Omega}, \psi)$ are the detector pattern functions, which depend on the geometry of the system [32, 129]: the direction of arrival of the wave $\hat{\Omega}$, and the choice of axes with respect to which one defines the polarizations, represented by a rotation angle ψ in the plane orthogonal to $\hat{\Omega}$. The Fourier transform of the signal becomes then [32]

$$\tilde{h}(f) = \int d\hat{\Omega} \left[F_+(\hat{\Omega}, \psi) h_+(f, \hat{\Omega}) + F_\times(\hat{\Omega}, \psi) h_\times(f, \hat{\Omega}) \right]. \tag{4.30}$$

[8] As analysed in detail in [33], the interpretation of the physical effect a GW has on the experimental device differs for different coordinate choices: in the TT gauge for example, since the coordinates expand with the metric perturbation, the GWs affect the propagation of photons along the geodesic instead of affecting the masses position.

For an unpolarized stochastic background, there is no privileged choice of axes to define the polarizations, and the angle ψ effectively cancels from the final result. Furthermore, the average of the signal vanishes, while the second moment of the signal distribution can be written simply as [32]

$$\langle h^2(t)\rangle = F\int_0^\infty df\, S_h(f)\,, \qquad F = \int \frac{d\hat{\Omega}}{4\pi}\left[F_+^2(\hat{\Omega},\psi)+F_\times^2(\hat{\Omega},\psi)\right], \tag{4.31}$$

where $S_h(f)$ is the spectral density defined in Eq. (3.18), and the factor F is the average of the detector pattern functions over all directions of arrival of the waves. This factor quantifies the loss of sensitivity due to the fact that the GW background hits the detector isotropically, with respect to the sensitivity of the detector in the optimal direction: if α is the angle between the two arms, one has [32] $F = 2/5\sin^2\alpha$.

The total output of a detector is given by the GW signal plus the noise, $S(t) = h(t)+n(t)$. In the same way as done for the signal $h(t)$, one can define the noise spectral density $S_n(f)$ from the averaged squared noise:

$$\langle \tilde{n}^*(f)\tilde{n}(f')\rangle = \delta(f-f')\frac{S_n(f)}{2}\,, \qquad \langle n^2(t)\rangle = \int_0^\infty df\, S_n(f)\,. \tag{4.32}$$

The level of noise in the detector is given by the strain sensitivity $h_f = \sqrt{S_n(f)}$. In a single detector the SGWB manifests itself simply as an extra source of noise. This makes impossible to isolate the detector from the signal, in order to measure the actual detector noise, subtract it, and thereby distinguish the two components. Therefore, when a single detector is operating, a stochastic background can be measured if it overcomes the detector noise level (this is what happened e.g. with the measurement of the CMB black-body spectrum) or it is of comparable amplitude. Methods to distinguish the signal from the noise are, for example, a substantial difference between their spectral shapes, or the distinctive time modulation of an anisotropic signal due to the detector motion (as expected, for instance, in the case of the SGWB from galactic binaries visible by the space-based interferometer LISA [130]). Furthermore, a good knowledge of the noise can be achieved using null channels: particular combinations of the interferometer outputs to which the contribution of the signal is strongly suppressed [64]. Null channels allow to measure the noise spectral density directly from the detector output; the knowledge of the noise is then used to assess the presence of a SGWB in

the standard interferometric channels. However, the interferometer structure must be such as to allow the construction of a null channel: in the case of the triangular LISA configuration, for example, the null channel is the so called *symmetrised Sagnac* combination [131, 132]. Once the noise has been evaluated, the technique to dig out a signal buried in it is optimal Wiener filtering, often using a parametrized model for the signal. This has been demonstrated e.g. in the third Mock LISA Data Challenge [133]: a relatively loud isotropic stochastic background, with amplitude slightly below the LISA instrument noise (c.f. Fig. 4.2), had been buried in the simulated detector output, and the teams participating in the data analysis challenge were able to recover the presence of this signal and its spectral characteristics.

The minimal condition to observe the SGWB with a single interferometer can be defined then as $S_h(f) > S_n(f)/F$. In terms of the GW energy density parameter $\Omega_{\rm GW} = (4\pi^2/3H_0^2)\, f^3\, S_h(f)$ (c.f. Eq. (3.20)), this condition can be translated into a minimum value for detection assuming a signal to noise ratio of one, at a frequency f, and given the interferometer strain sensitivity $h_f(f)$ [33]:

$$h^2\Omega_{\rm GW}(f) \gtrsim \frac{10^{-2}}{F}\left(\frac{f}{100\,{\rm Hz}}\right)^3\left(\frac{h_f}{10^{-22}\,{\rm Hz}^{-1/2}}\right)^2 . \tag{4.33}$$

From the above equation it appears that, for the same noise level h_f, detectors with lower detection frequency window are more sensitive to a stochastic background.

Concerning currently operating detectors on Earth, for which Eq. (4.33) has been normalised, the predicted amplitude of both astrophysical and cosmological stochastic backgrounds is still below their sensitivity. On the other hand, as several detectors are present, this allows to adopt a more elaborated detection strategy, which consists in cross-correlating the output of two (or more) different detectors, exploiting the fact that different detectors have (in principle) independent noise. We present a brief description of this strategy, based on Refs. [32, 51]. The cross-correlation signal S_{12} is constructed multiplying the two detector outputs $S_1(t)$ and $S_2(t)$, and integrating over the observation time T with a filter function Q,

$$S_{12} = \int_{-T/2}^{T/2} dt \int_{-T/2}^{T/2} dt' S_1(t) S_2(t') Q(t-t') \, . \tag{4.34}$$

As we will see later, the filter function must be chosen to maximize the signal to noise ratio: it depends on the position and orientation of the detectors, on the features of their characteristic

noise, as well as on the spectrum of the stochastic background. However, since one considers that both the signal and the noise are stationary in time, it is reasonable to assume that the best choice for Q depends only on the time difference $t-t'$. Furthermore, $Q(t-t')$ is different from zero only for $|t-t'| \ll T$: it must fall off rapidly for time intervals which are larger than the light-travel distance between the two detectors, which is of the order of 10^{-2} sec if they are both on Earth. On the other hand, the integration time is typically of the order of one year: one can therefore Fourier transform Eq. (4.34) in the limit of large integration time T. Moreover, because the noise in each detector is uncorrelated with the other one, and with the GW strain, it turns out that the expected value of the cross-correlation of the detector outputs $S_i(t) = h_i(t) + n_i(t)$, obtained by taking the expectation value of Eq. (4.34), depends only on the GW stochastic background. Using Eq. (3.18) together with the response of the detector through the pattern functions, one finds finally [32]

$$\langle S_{12} \rangle = \frac{T}{2} \int_{-\infty}^{\infty} df\, S_h(f) \Gamma(f) \tilde{Q}(f)\,, \tag{4.35}$$

where $\tilde{Q}(f)$ denotes the Fourier transform of the filter function, and $\Gamma(f)$ is the overlap function. This latter characterizes the reduction in sensitivity to the GW background arising from the relative positions and orientations of the pair of detectors:

$$\Gamma(f) = \frac{1}{4\pi} \int d\hat{\Omega}\, [F_1^+ F_2^+ + F_1^\times F_2^\times] \exp\left[2\pi \mathrm{i} \hat{\Omega} \cdot \Delta \mathbf{x}\right]\,, \tag{4.36}$$

where $\Delta \mathbf{x}$ denotes the separation between the two detectors. In the case of two coincident interferometers, $\Delta \mathbf{x} = 0$ and $\Gamma(f) = F = 2/5$. The exponential phase factor in the definition of Γ is the phase shift arising from the time delay between the two detectors for radiation arriving along the direction $\hat{\Omega}$. As an example, the overlap function between the LIGO interferometers at Hanford and Livingston is shown in Ref. [134]. From the definition of $\langle S_{12} \rangle$, it appears that the expected signal grows linearly with the observation time. We will see that the r.m.s noise, on the other hand, grows only as $\sqrt{T}$: in principle, with enough observation time one can detect a GW stochastic background buried in any level of detector noise.

The form of the optimal filter function $\tilde{Q}(f)$ for a stochastic background search is the one that maximizes the signal to noise ratio. The noise in the detector is given by the

variation of S_{12} away from its mean value: $N = S_{12} - \langle S_{12}\rangle$. We are dealing with the case in which the noise is much higher than the gravitational strain signal, $n_i \gg h_i$, so that one can approximate $S_i \simeq n_i$. With the further condition that the noise is Gaussian and uncorrelated among the two detectors, one gets for the squared r.m.s. value of the expected noise [32]

$$\langle N^2\rangle = \langle S_{12}^2\rangle - \langle S_{12}\rangle^2 = \frac{T}{4}\int_{-\infty}^{\infty} df\, S_n^{(1)}(f)\, S_n^{(2)}(f)\, |\tilde{Q}(f)|^2\,, \tag{4.37}$$

where $S_n^{(i)}(f)$ denote the spectral noise densities in each detector. As anticipated, one sees that the r.m.s. noise grows as $\sqrt{T}$. The value of $\tilde{Q}(f)$ that maximizes the signal to noise ratio SNR $= \langle S_{12}\rangle/\sqrt{\langle N^2\rangle}$ is found by solving a variational problem and turns out to be [32]

$$\tilde{Q}(f) = c\,\frac{\Gamma(f)\, S_h(f)}{S_n^{(1)}(f) S_n^{(2)}(f)}\,, \tag{4.38}$$

with c a normalization constant. The optimal filter function depends then on the GW spectral density: in order to search for the signal, one has to perform the data analysis using several forms for the filter function. $\tilde{Q}(f)$ can be chosen either so as to match the theoretical predictions for the GW stochastic backgrounds, or assuming a simple power law behavior $S_h(f) \propto f^{\alpha}$, so as to generically model the frequency dependence of a stochastic background over the (often narrow) frequency range a detector. The value of the signal to noise ratio SNR using the optimal filter function for two interferometers is then given by

$$\mathrm{SNR} = \frac{\langle S_{12}\rangle}{\sqrt{\langle N^2\rangle}} = \left[2\,T\int_0^{\infty} df\,\frac{\Gamma^2(f)\, S_h^2(f)}{S_n^{(1)}(f) S_n^{(2)}(f)}\right]^{1/2}. \tag{4.39}$$

Starting from this expression for the signal to noise ratio, it is possible to estimate the gain in sensitivity due to the cross-correlation of two detectors with respect to the single detector case. Let us suppose that the integrand in the above equation is approximately constant over the frequency range of sensitivity of the detector, say $\Delta f \simeq 100$ Hz for a typical Earth-based interferometer. Setting SNR > 1, the GW spectral density must satisfy

$$S_h(f) > \frac{\sqrt{S_n^{(1)}(f) S_n^{(2)}(f)}}{\Gamma(f)\sqrt{2\,T\,\Delta f}}\,. \tag{4.40}$$

We assume the same noise spectral density in the two detectors, so that $\sqrt{S_n^{(1)}(f) S_n^{(2)}(f)} =$

$S_n(f) = h_f^2$, where h_f is the strain sensitivity. Moreover, we assume that the two detectors are coincident, and as a plausible observation time, we take $T \simeq 1$ year. Through the relationship between S_h and $\Omega_{\rm GW}$, we can then evaluate the minimum detectable value of $\Omega_{\rm GW}$ from an ideal two detector correlation $\Omega^{\rm 2d}_{\rm GW}(f)$, and compare it with the single detector case given in Eq. (4.33) labelled now as $\Omega^{\rm 1d}_{\rm GW}(f)$:

$$h^2\Omega^{\rm 2d}_{\rm GW}(f) \gtrsim 10^{-5}\ [h^2\Omega^{\rm 1d}_{\rm GW}(f)]\ \sqrt{\frac{1\,\text{year}}{T}}\ \sqrt{\frac{100\,\text{Hz}}{\Delta f}}\,. \tag{4.41}$$

The cross-correlation between two coincident detectors, with the same noise characteristics but fully uncorrelated noise, helps in the detection of a GW stochastic background by about five orders of magnitude. The minimum detectable value of $\Omega_{\rm GW}(f)$ for 1 year of integration time and assuming that everything can be treated as constant over a frequency range of about $\Delta f \simeq 100$ Hz becomes then [32]

$$h^2\Omega^{\rm 2d}_{\rm GW}(f) \simeq \frac{10^{-7}}{F}\left(\frac{f}{100\,\text{Hz}}\right)^3\left(\frac{h_f}{10^{-22}\,\text{Hz}^{-1/2}}\right)^2\,. \tag{4.42}$$

From the expression of the signal to noise ratio (4.39), it appears that the detectability of a SGWB improves with the integration time T and with the frequency span of the signal. In order to visualise this effect when plotting the sensitivity of GW detectors as a function of frequency, Ref. [134] proposes a method that holds for signals having a power law frequency dependence in the frequency band corresponding to the detector sensitivity. This consists in plotting the so-called Power Law-Integrated Curve, composed by the envelope of a set of power laws,

$$\Omega_{\rm PI} = \max_{\beta}\ \Omega_\beta\left(\frac{f}{f_*}\right)^\beta\,, \tag{4.43}$$

where f_* is a reference frequency and the amplitudes Ω_β are chosen such that they provide a given value for the SNR: converting the noise spectral density into an energy density using $S_n(f) = (3H_0^2/4\pi^2)\Omega_n(f)/f^3$, one defines

$$\Omega_\beta = \frac{\rm SNR}{\sqrt{2T}}\left[\int_{f_{\rm min}}^{f_{\rm max}} df\ \frac{(f/f_*)^{2\beta}}{\Omega_n^2(f)}\right]^{-1/2}\,, \tag{4.44}$$

where $f_{\rm min},\ f_{\rm max}$ denote the detector bandwidth. The meaning of the Power Law-Integrated

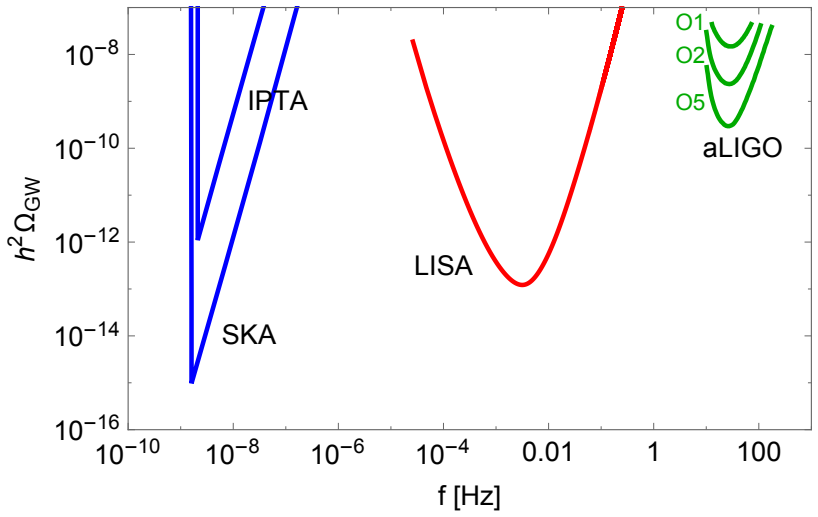

Figure 4.2: The Power Law-Integrated Curves of current and future GW detectors. From left to right: for PTA (blue) we show the predictions for the International Pulsar Timing array and for a network monitored by the SKA, taken from [122]; for LISA (red), we show the expected power law-integrated curve adapted from Ref. [130]; for Advanced LIGO/Virgo (green) we show the sensitivities given in [135] for the first (O1) and second (O2) runs, and at design sensitivity (O5).

Curve is that, a power-law background lying above it, is detectable with signal to noise ratio larger than the actual value of SNR chosen in Eq. (4.44).

Note that, since the bandwidths of current GW detectors are relatively small, it seems justified to construct a sensitivity curve which is meaningful for single power-law SGWBs. On the other hand, this method is going to become inadequate in the future, especially with space-based detectors such as LISA or with third generation Earth-based detectors such as the Einstein Telescope (c.f. next subsections). Depending on the generation model, there are several predictions for the spectral shape of a cosmological SGWB, which go beyond simple power laws [15]. Often, this constitutes the only handle one has to possibly distinguish the origin of the SGWB. Nevertheless, the Power Law-Integrated Curve remains the best currently available visualisation of the sensitivity of detectors to SGWB, and this is what we plot in Fig. 4.2 for PTA, LISA and several observation runs of advanced LIGO/Virgo.

4.4.2 Earth-based detectors.

The first generation of earth-based GW interferometers included four detectors: LIGO, Virgo, GEO 600 and TAMA. The **GEO 600** interferometer [136] is a 600-meter interferometer

located near Hannover (Germany), with best sensitivity of $h_f \sim 3 \cdot 10^{-22}$ Hz$^{-1/2}$ at about 700 Hz. The **TAMA** interferometer [137] has 300-meter arm, is located near Toyko (Japan), and was the first of the network to be operational: it reached its best sensitivity of $h_f \sim 1.5 \cdot 10^{-21}$ Hz$^{-1/2}$ at about 1 kHz. Both these interferometers have been important for testing several technical innovations needed for the second generation experiments. **LIGO (Laser Interferometer Gravitational-wave Observatory)** [138] consisted of three multi-kilometers interferometers, at two locations: H1 with 4 km arms and H2 with 2 km arms located at Hanford (Washington State), and L1 also with 4 km arm located in Livingston Parish (Louisiana). They have been operational since 2002. The **Virgo** interferometer [139], located near Pisa (Italy), has a 3km arm.

In general, for ground based detectors, the most important limitations to sensitivity result from the effects of seismic noise in the low frequency range (up to a few Hz), thermal noise associated with the test masses and their suspensions (up to a few hundreds Hz), and finally laser shot noise (from a few hundreds to 10^4 Hz). All these aspects have been improved in the upgrade that brought the initial devices to the **the second generation of GW detectors**, **Advanced LIGO** [140] and **Advanced Virgo** [141]. At the level of sensitivity reached by the first generation of Earth-based interferometers, there was no guaranteed source of detection. In 2015, the planned upgrade of LIGO into advanced LIGO was ready, with an improvement in sensitivity by about a factor of ten. This enhanced considerably the physics reach: the distance searched for detectable sources improves linearly with the strain sensitivity, so an order of magnitude in strain sensitivity means the ability to probe a thousand times more volume in the sky. This has guaranteed the first direct detection of GWs, announced in February 2016: the GW emission from the coalescence of two black holes with masses around $30\,M_\odot$ [16]. Since, the detection of other three black hole binary coalescences have been announced, performed by the Advanced LIGO interferometers only [17–19]. In the spring of 2017, Advanced Virgo was ready to join the search, and not much later the network of three detectors performed the first the common detection of another black hole binary coalescence [20], followed by the first detection of the merger of two neutron stars that, most remarkably, has been detected at the same time in various electromagnetic bands [21, 22].

Concerning stochastic backgrounds, so far there is no detection but only upper bounds.

The most recent one has been obtained with the data of the first Advanced LIGO run (without Advanced Virgo) in [142]. We have seen in Eq. (4.38) that the ideal filter function $\tilde{Q}(f)$ depends on the shape of the GW spectrum: Ref. [142] assumes then a power law template GW spectrum of the form $\Omega_{\rm GW}(f) = \Omega_\alpha (f/25\,{\rm Hz})^\alpha$. This procedure yields the 95% confidence upper limit $\Omega_{\alpha=0} < 1.7 \cdot 10^{-7}$. For other values of the power index α in the range between -5 and 5, the 95% upper limit varies between about $2 \cdot 10^{-7}$ and about $4 \cdot 10^{-10}$ (c.f. Figure 2 of Ref. [142]). These constraints are stronger than both the BBN (c.f. Section 4.1) and integrated CMB (c.f. Section 4.2) constraints in the above mentioned frequency range.

The next technological step is to use cryogenic mirrors, which is now being explored by the KAGRA collaboration. **KAGRA** [143] is a 3 km arm interferometer currently under construction, which besides using cooled mirrors to reduce the thermal vibrations, is placed underground in the Kamioka mine (Japan) to suppress also the seismic noise. KAGRA should join the network in the next years, and can be considered a path-finder for the third generation GW detectors to be placed underground. Furthermore, there is a planned advanced detector to be located in India (IndIGO) [144].

Since the second generation of Earth-based GW interferometers is expected to get to the lowest possible sensitivity given their technical structure, a conceptual design study for a **third generation detector, the Einstein Telescope (E.T.)**, has been funded by the European Framework Programme FP7 [145]. The third generation detector should be sensitive to a great variety of sources, at much larger distances and with higher signal to noise ratio than Advanced LIGO and Virgo. Via the implementation of new technologies, the aim is to provide a strain sensitivity about ten times better than second generation detectors (corresponding to scanning a thousand times larger volume of the universe), and to shift the minimal detectable frequency to approximately 1 Hz. Consequently, E.T. will allow to probe the stochastic background down to a level of $\Omega_{\rm GW} \sim 10^{-12}$ [146]. A proposed configuration [147, 148] is that of a 10-km arm triangular set of three Michelson interferometers, situated underground to significantly reduce seismic noise and allow for very long low frequency suspensions, with 500 W lasers using squeezed light to beat down quantum noise, and cryogenic test masses of 120 Kg kept at 20 K. The arms of the triangle, which has an opening angle of 60 degrees, are each used twice to form three co-located interferometers, which allows to measure both GW polarization states, and to use time delay interferometry:

a technique developed to suppress the noise in LISA (c.f. section 4.4.3), which consists in constructing virtual output signals by time shifting and linearly combining the actual interferometer output signals. As an example, one can construct the Sagnac observable [131], a combination of interferometric output signals that is insensitive to GW and can be used to firmly identify the instrument noise, improving greatly the performance of the instrument. Another proposed configuration for E.T. is the xylophone design [149, 150]: this is composed by a high-power, high-frequency interferometer (ET-HF), which employs powerful lasers to suppress the high-frequency photon shot noise, and a cryogenic low-power, low- frequency interferometer (ET-LF), with less powerful lasers reducing the thermal noise which would dominate at low frequency. The two interferometers would be co-located and with the same orientation, but only ET-LF would be situated underground. Compared to the single-interferometer design, the xylophone configuration improves the sensitivity by a factor of 2-10 in the frequency range 6-10 Hz.

4.4.3 Space-based detectors.

Earth-based interferometers, even situated underground, are limited by seismic noise and cannot probe frequencies smaller than about 1 Hz. It is possible to reach much lower frequencies placing interferometers in space: the principle is to put drag-free spacecrafts into orbit, and compare the distances between test masses in the spacecrafts using laser interferometry.

The most advanced and long-studied space-based project is **LISA (Laser Interferometer Space Antenna)**: it consists in an array of three drag-free spacecrafts at the vertices of an equilateral triangle of side-length $2.5 \cdot 10^9$ m, orbiting at a distance of 1 AU from the Sun on a Earth-like orbit, but 20 degrees behind the Earth and inclined at 60 degrees with respect to the ecliptic [130]. This configuration allows to probe the frequency band between 0.1 mHz and 0.1 Hz, which is expected to be richly populated by signals from sources such as galactic binaries of white dwarfs and neutron stars, stellar-origin black hole binaries, coalescing massive black hole binaries in the mass range $10^4 - 10^7\ M_\odot$, binaries formed by a massive black hole and a stellar-mass compact object, and a stochastic background generated by cosmological sources [130].

The key technology for LISA, namely the ability to keep the test masses in free-fall with extremely low residual acceleration, was successfully tested by the **LISA Pathfinder**

mission in 2016 [151]. This mission, consisting in one LISA arm reduced in one spaceship, has measured a differential acceleration among the two test masses that fully meets (and even overcomes, depending on the frequency range) the requirements for LISA. This has led the European Space Angency (ESA) to issue a call for mission concerning a GW observatory in space at the end of 2016, and in response to that call the LISA proposal has been accepted by ESA in spring 2017, in the configuration proposed in [130]. Currently, the planned launch date is 2034.

In the LISA configuration, the direct reflection of laser light like in standard Michelson interferometers, is not feasible due to the large distance between the spacecrafts. Therefore, each arm is composed of two laser beams: the first one is sent out from a spacecraft, and received by the other spacecraft; there, instead of begin reflected, it is phase locked to the second laser beam, which is then send back to the first spacecraft. The combination of the emitted and sent back lasers gives the information about the arm length. The same procedure is repeated in the adjacent arms, and with the information about the length of the three arms one then constructs the interferometry signal. LISA has therefore six masses and six laser links joining the three satellites (two in opposite directions for each side of the triangle): this three-interferometer configuration was chosen first of all since it provides redundancy against component failure. Moreover, it allows to use time delay interferometry, i.e. the use of virtual interferometric observables to effectively reduce the laser noise level [152], and it improves the capability to disentangle an isotropic cosmological (or astrophysical) background from the instrumental noise through Sagnac calibration [131]. As mentioned for the E.T., the symmetrized Sagnac observable is a combination of six interferometric signals that is much less sensitive to GWs at low frequencies than other combinations, and thus can be used to determine the instrumental noise level. Furthermore, concerning stochastic backgrounds, there is a considerable gain in moving to lower frequencies: the factor f^3 in Eq. (4.33) leads to an improvement in the minimum detectable value of $h^2\Omega_{\rm GW}$ at 1 mHz by fifteen orders of magnitude with respect to the minimum detectable value at 100 Hz, for the same instrument strain sensitivity h_f. Therefore, whereas going to space prevents the possibility of increasing the detection performance through cross-correlation with other detectors (as in the case of Earth-based interferometers), on the other hand it provides a mean to retrieve a very high sensitivity to a stochastic background just by the opportunity of reaching a lower frequency

range in the absence of seismic noise. LISA is expected to probe a SGWB down to a level of $h^2\Omega_{\rm GW} \sim 10^{-13}$ [130].

There are also concepts for two other space-based projects using optical interferometry, **DECIGO (DECi-hertz Interferometer Gravitational Wave Observatory)** [153, 154] and **BBO (Big Bang Observer)** [155, 156]. The proposed configuration for these two missions is quite similar: they consist of four LISA-like interferometers orbiting the Sun at 1 AU, two of which are co-located in a 'star of David' shape, while the other two are ahead and behind by an angle of $2\pi/3$ respectively, on the same orbit. The reason for this design is that it allows to measure with high-precision the stochastic background by cross-correlating the outputs of the two overlapping constellations; while the other two constellations are there to improve the angular resolution, which is useful for characterizing and removing the compact binary 'foreground' [157]. The angular position of the source is determined by exploiting the differences in the arrival times of the GW at the different constellations. Both missions are designed to probe the 0.1-10 Hz frequency band, where the stochastic background from white dwarf binaries is absent: the primary goal of these missions is in fact to reach a sensitivity of about [158, 159] $\Omega_{\rm GW} \gtrsim 10^{-17}$, in order to detect the primordial stochastic background from inflation (see Section 5). The dominant astrophysical foreground in this band is due to compact binaries of neutron stars and stellar-origin black holes; however, the concept missions are planned to be sufficiently sensitive to individually detect and subtract out every merging compact binary out to high redshift, thereby uncovering the primordial GW background. Note that this 'foreground removal', which in practice consists in the detection of hundreds of thousands of merging binaries, allows to use this kind of detectors also for doing precision cosmology [158] and tests of general relativity [160]. The BBO mission is a follow-up of LISA with the previously described constellation, with shorter arms of $5\cdot10^7$ m, and exploiting very powerful lasers of about 300W. On the other hand, the DECIGO mission, though sharing the same constellation, would have shorter arms of 10^6 m which form Fabry-Perot cavities, i.e. the lasers (of 10 W in this case) are reflected among the arms, and would be 2 to 3 times less sensitive than BBO.

There are also proposals for space-based missions using atom interferometry instead of optical interferometry, like **AGIS (Atomic Gravitational-wave Interferometric Sensor)** and the more recent proposal AGIS-LEO [161, 162]. The principle of such a GW measure-

ment is to combine the use of the atom interferometry with lasers traveling a long distance. The experiment is constructed such that it compares the phase shifts of two separate atom interferometers that are manipulated by the same laser. Typically, the separation between the two interferometers is of the order of 1000 km, therefore probing the frequency band $10^{-2} - 10$ Hz, with a strain sensitivity of the order of [163] $h \sim 10^{-18}$ Hz$^{-1/2}$.

Chapter 5

Gravitational wave background from inflation

In this chapter, taken from the review [15], we present the SGWB generated during slow-roll inflation by the rapid evolution of the universe background. In sections 5.1 and 5.2, we briefly overview single-field slow-roll inflation, and derive the tensor spectrum arising from the amplification of initial quantum fluctuations of the gravitational field. We define the spectrum main properties: amplitude, spectral index, gaussianity, polarisation. In section 5.3 we proceed to describe the principal processes that influence the time evolution of the tensor spectrum from the end of inflation until today, affecting its present-day amplitude. We first evaluate the transfer function in the case of a universe constituted of radiation and matter (sub-sect. 5.3.1), and then discuss the effects on the tensor spectrum in the context of a more complete picture, that includes: changes in the particle content during the radiation dominated epoch, the presence of a stiff component, late time acceleration, free streaming neutrinos (sub-sect. 5.3.2).

5.1 Generalities

The inflationary period, defined as an early phase of accelerated expansion, provides a natural solution to the shortcomings of the hot Big Bang framework [164–166], namely the horizon and flatness problems; see also Refs. [167–170] for early works. The major success of inflation is to provide a natural explanation for the physical origin of the primordial density pertur-

bations, required to start the process of structure formation in the Universe. Inflation leads naturally to the stretching of quantum fluctuations [171–175], which result parametrically amplified into classical density perturbations [176–178]. Later on, during the decelerated evolution of the universe following after the end of inflation, the perturbations re-enter the Hubble radius, providing the required 'seed' to trigger, via gravitational collapse, the formation of structures in the universe. The perturbations leave at the same time an imprint in the CMB, in the form of temperature and polarization anisotropies. The simplest models of inflation lead to a homogeneous and isotropic spatially flat universe, with adiabatic, Gaussian, and approximately scale-invariant density perturbations. These predictions have been spectacularly confirmed over the years by increasingly accurate observations of the CMB and of the large-scale structure in the universe.

During inflation any light field with a mass smaller than the the inflationary Hubble rate $m^2 \ll H^2$, experiences quantum fluctuations. Due to the accelerated expansion, initially small fluctuations with wavelength smaller than the inflationary Hubble radius, $k > aH$, result amplified and stretched to super-Hubble scales, $k < aH$. This affects, in particular, the tensor metric perturbations [179–182], as these correspond to massless fields. As we will show in detail, the resulting spectrum of tensor modes is quasi scale-invariant, spanning over a wide range of scales (from the Hubble scale at the end of inflation, to at least the Hubble scale today). When the tensor modes re-enter the Hubble radius during the post-inflationary era, they turn into a proper classical (yet stochastic) background of GWs, with a quasi scale-invariant spectrum. This background constitutes an irreducible emission of GWs expected from any inflationary model.

The irreducible background of GWs from inflation is expected to create a pattern of B-modes in the polarization of the CMB [183–186]. This major prediction from inflation remains however unverified, as to date this effect has not been observed[1]. If B-modes due to primordial tensors are eventually detected in the CMB, this will constitute a very strong evidence in favor of inflation[2]. Besides, a detection of primordial B-modes will provide a powerful tool

[1]Let us recall that on March 2014, the BICEP2 collaboration announced the detection of B-modes due to the irreducible background of GWs from inflation [81]. Even though the detection of B-modes was very real (later on confirmed by other experiments), unfortunately the interpretation of the signal as due to inflationary tensors was mistaken. An underestimation of the contribution to polarized light from dust in the interstelar medium [187–189], led the BICEP2 team to consider such dust contribution negligible as compared to the measured signal. It turned out that the signal was however only due to (or at least mostly dominated by) the dust contamination [82, 190].

[2]This will not be a definitive proof of inflation. It has been shown nonetheless, that other primordial

to discriminate between the (currently) many different inflationary models compatible with the data.

Many CMB polarization B-mode experiments are currently ongoing or under construction, aiming to detect or further constrain in the near future, the irreducible GW background from inflation, see Section 4.2. In light of present CMB constraints, we know that the amplitude of this background is too small to expect detecting it with current or planned direct detection GW observatories like aLIGO/Virgo, LISA, ET and others. If the energy scale of inflation is sufficiently high, futuristic GW detectors such as BBO may have a chance to detect this primordial background. However, the irreducible contribution may not be the only GW background expected from inflation. Under some circumstances, if new species or symmetries are at play during inflation, GWs with a high amplitude and a significant deviation from scale-invariance, can also be produced (see e.g. section 6 in [15]). Contrary to the irreducible contribution, these backgrounds are model dependent. However, whenever produced, they are expected to have a much larger amplitude than the irreducible background, particularly at the frequencies accessible to direct detection experiments. In light of this possibility, GWs from inflation remain a relevant target for the upcoming ground- and space-based interferometers.

5.2 Irreducible GW background: amplification of vacuum fluctuations

The simplest inflationary models involve a single inflaton scalar field ϕ slowly rolling down its potential $V(\phi)$ during inflation, minimally coupled to gravity, and with a canonical kinetic term. We will refer to these models as canonically normalized single-field slow-roll (SFSR) scenarios. These are characterized by an action

$$S = \int d^4x \sqrt{-g} \left[\frac{m_{\rm Pl}^2}{2} R - \frac{1}{2} \partial^\mu \phi \, \partial_\mu \phi - V(\phi) \right] , \tag{5.1}$$

sources of B-modes such as primordial magnetic fields or topological defects, do not produce a B-mode angular spectrum resembling close enough the inflationary one, unless parameters in these scenarios are highly (and unnaturally) fine-tuned [191–195]. Thus, in principle, in the event of a future detection of a primordial signal (assuming astrophysical contaminants have been properly removed), the shape of the B-mode angular power spectrum could be a good discriminant by itself, to differentiate whether a signal is due to the inflationary irreducible background of GWs, or rather due to other primordial sources.

where R is the Ricci scalar and $m_{\rm Pl} = 1/\sqrt{8\pi G}$ is the reduced Planck mass. In the slow-roll regime the kinetic energy of the scalar field is negligible compared to its potential energy, $\frac{1}{2}\dot{\phi}^2 \ll V(\phi)$. This is a requisite to inflate the universe. To sustain this regime sufficiently long, it is also necessary that the acceleration of the field is suppressed compared to the field velocity per Hubble time, i.e. $|\ddot{\phi}| \ll |\dot{\phi}|/H^{-1}$. These two conditions allow to simplify both the Friedmann equation for the homogeneous and isotropic background, and the equation of motion of the homogeneous inflaton,

$$3m_{\rm Pl}^2 H^2 = V(\phi)\,(1+\epsilon_\phi/3) \simeq V(\phi) \tag{5.2}$$

$$-V'(\phi) = 3H\dot{\phi}\,(1-\eta_\phi/3) \simeq 3H\dot{\phi} \tag{5.3}$$

where we have defined the two slow-roll parameters

$$\epsilon_\phi \equiv \frac{3}{2}\frac{\dot{\phi}^2}{V}\,, \qquad \eta_\phi \equiv -\frac{\ddot{\phi}}{H\dot{\phi}} \tag{5.4}$$

The approximations in RHS of Eqs. (5.2), (5.3) are consistent only as long as both slow-roll parameters are sufficiently small, $\epsilon_\phi \ll 1$ and $\eta_\phi \ll 1$. It is then useful also to define the potential slow-roll parameters

$$\epsilon_V \equiv \frac{m_{\rm Pl}^2}{2}\left(\frac{V'}{V}\right)^2\,, \qquad \eta_V \equiv m_{\rm Pl}^2\,\frac{V''}{V}\,, \tag{5.5}$$

related to the former parameters by $\epsilon_\phi \simeq \epsilon_V$ and $\eta_\phi \simeq \eta_V - \epsilon_V$. Demanding $\epsilon_V \ll 1$ and $\eta_V \ll 1$ represents therefore a sufficient (though not necessary) condition, for obtaining and sustaining an inflationary slow-roll regime. The ϵ slow-roll parameter controls the deviation of the equation of state from pure de Sitter, $w \equiv (\frac{1}{2}\dot{\phi}^2 + V)/(\frac{1}{2}\dot{\phi}^2 - V) \simeq -1 + \frac{2}{3}\epsilon_\phi$, hence determining as well the rate of change of the inflationary Hubble rate,

$$\epsilon_H \equiv -\frac{\dot{H}}{H^2} \equiv \frac{3}{2}(1+w) \simeq \epsilon_\phi\,. \tag{5.6}$$

Note that even though we have argued that $\epsilon_\phi \simeq \epsilon_V \simeq \epsilon_H$, this double equivalence does not necessarily hold in scenarios beyond the SFSR paradigm. Nevertheless from now on, for simplicity we will write without distinction ϵ, as we will not go beyond SFSR.

Once inflation starts (say at some value $\epsilon_V \ll 1$), if the inflaton potential is sufficiently flat (i.e. $\eta_V \ll 1$) over a wide range of scalar field values, this ensures that the universe will inflate during a sufficiently long period, so that the initial condition problems of the Hot Big Bang model are solved. In the slow-roll regime $\epsilon_V, \eta_V \ll 1$, the equation of state w is close to -1, producing a quasi-exponential expansion $a(t) \sim e^{H\,t}$, with a Hubble rate H approximately constant. In reality, according to Eq. (5.6), the Hubble rate decreases with time, but the decreasing rate is 'slow-roll suppressed' as $\Delta H/H \simeq \epsilon \Delta N$, where N is the number of e-folds $dN = d\log\, a \simeq H dt$.

Let us note that although the anisotropic stress of a scalar field $\sim \partial\delta\phi\partial\delta\phi$, can act as a source term in the equation of motion of tensor perturbations, it is intrinsically of second order in the field fluctuations. Therefore, to linear order in field fluctuations, there is typically no active source of GWs during inflationHowever, unavoidable quantum fluctuations of h_{ij} are parametrically amplified by the quasi-exponential expansion of the universe. To describe this phenomenon, we need to quantize the tensor modes of the metric, considered as perturbations over the homogeneous and isotropic inflationary background.

The first step to quantize the system is to identify the canonical degrees of freedom. This can be done by expanding the pure gravitational part of action (5.1) with the metric Eq. (2.60), at second order in h_{ij} and expressed in conformal time η [196]

$$\begin{aligned} S_g^{(2)} &= -\frac{m_{\rm Pl}^2}{8}\int d\eta\, d^3\mathbf{x}\, a^2(\eta)\, \eta^{\mu\nu}\, \partial_\mu h_{ij}\, \partial_\nu h_{ij} \\ &= \frac{m_{\rm Pl}^2}{4}\sum_{r=+,\times}\int d\eta\, \frac{d^3\mathbf{k}}{(2\pi)^3}\, a^2(\eta)\, \left[|h_r'(\mathbf{k},\eta)|^2 - k^2\,|h_r(\mathbf{k},\eta)|^2\right] \\ &= \frac{1}{2}\sum_{r=+,\times}\int d\eta\, \frac{d^3\mathbf{k}}{(2\pi)^3}\, \left[|v_r'|^2 - k^2\,|v_r|^2 + \frac{a''}{a}\,|v_r|^2\right], \end{aligned} \tag{5.7}$$

where we have used the decomposition Eq. (2.56) and the orthonormal condition (2.58) in the second equality, whereas for the third equality we have introduced the variables

$$v_r(\mathbf{k},\eta) = \frac{m_{\rm Pl}}{\sqrt{2}}\, a(\eta)\, h_r(\mathbf{k},\eta)\,. \tag{5.8}$$

The action in Eq. (5.7) is equivalent to the action of two real scalar fields $v_r(\mathbf{x},\eta)$ in Minkowski space-time, with canonically conjugate momenta $\pi_r(\mathbf{x},\eta) \equiv v_r'(\mathbf{x},\eta)$, and time-dependent frequency $\omega_k^2(\eta) = k^2 - \frac{a''}{a}$. The quantization proceeds by promoting v_r and π_r to operators

$\hat{v}_r$ and $\hat{\pi}_r$ that satisfy the standard commutation relations on hyper-surfaces of constant time η,

$$\begin{aligned}\left[\hat{v}_r(\mathbf{x},\eta)\,,\,\hat{\pi}_{r'}(\mathbf{x}',\eta)\right] &= i\,\delta_{rr'}\,\delta^{(3)}(\mathbf{x}-\mathbf{x}') \\ \left[\hat{v}_r(\mathbf{x},\eta)\,,\,\hat{v}_{r'}(\mathbf{x}',\eta)\right] &= \left[\hat{\pi}_r(\mathbf{x},\eta)\,,\,\hat{\pi}_{r'}(\mathbf{x}',\eta)\right] = 0\,. \end{aligned} \tag{5.9}$$

The fields can be decomposed on the basis of the solutions of the dynamical equations derived from action Eq. (5.7). Since the background is spatially isotropic, we can write

$$\hat{v}_r(\mathbf{x},\eta) = \int \frac{d^3\mathbf{k}}{(2\pi)^3}\,\left[v_k(\eta)\,e^{-i\mathbf{k}\mathbf{x}}\,\hat{a}_{\mathbf{k}r} + v_k^*(\eta)\,e^{+i\mathbf{k}\mathbf{x}}\,\hat{a}^+_{\mathbf{k}r}\right]\,, \tag{5.10}$$

with $\hat{a}^+_{\mathbf{k}r}$ and $\hat{a}_{\mathbf{k}r}$ creation and annihilation operators satisfying the usual commutation relations

$$\left[\hat{a}_{\mathbf{k}r}\,,\,\hat{a}^+_{\mathbf{k}'r'}\right] = (2\pi)^3\delta_{rr'}\,\delta^{(3)}(\mathbf{k}-\mathbf{k}')\,, \tag{5.11}$$

$$\left[\hat{a}_{\mathbf{k}r}\,,\,\hat{a}_{\mathbf{k}'r'}\right] = \left[\hat{a}^+_{\mathbf{k}r}\,,\,\hat{a}^+_{\mathbf{k}'r'}\right] = 0\,, \tag{5.12}$$

and the mode functions $v_k(\eta)$ satisfying the equation of motion

$$v_k'' + \omega_k^2(\eta)\,v_k = 0\,, \qquad \text{with} \quad \omega_k(\eta)^2 \equiv k^2 - \frac{a''}{a} \tag{5.13}$$

Consistency between the commutation relations Eq. (5.9) and Eq. (5.12) requires the normalization condition

$$v_k\,v_k'^* - v_k^*\,v_k' = i\,. \tag{5.14}$$

Eq. (5.13) describes an harmonic oscillator with a time-dependent frequency varying from $\omega_k^2 \simeq k^2$, when the modes are sub-Hubble $aH \ll k$, to $\omega_k^2 \simeq a''/a$, when the modes become super-Hubble $aH \gg k$. For sub-Hubble modes, Eq. (5.13) reads $v_k'' + k^2 \simeq 0$, which has two linearly independent solutions, $v_k = c_{k,+}v_k^{(+)} + c_{k,-}v_k^{(-)}$, with $v_k^{(\pm)} \equiv e^{\mp ik\eta}$, and $c_k^{(\pm)}$ constants. Defining a vacuum state $|0\rangle$ as $\hat{a}_{\mathbf{k}r}\,|0\rangle = 0$, we can associate the annihilation operators $\hat{a}_{\mathbf{k}r}$ in Eq. (5.10) to the 'positive frequency modes[3]' $v_k^{(+)}$. This standard prescription corresponds

[3]They are referred to as 'positive' because they correspond to the eigenfunctions of the energy operator $\hat{H} = i\partial_\eta$ with positive eigenvalues, $\hat{H}v_k^{(+)} = +kv_k^{(+)}$.

to the so-called Bunch-Davies vacuum. A discussion of the consequences of other vacuum prescriptions for the GW background can be found in Ref. [197]. The initial condition is then set with $c_{k,-} = 0$, so that initially $v_k(\eta) \propto v_+ \propto e^{-ik\eta}$. The value of $c_{k,+} \neq 0$ is determined by the normalization condition Eq. (5.14), so that the physical solution of Eq. (5.13) for sub-Hubble modes, finally reads

$$v_k \simeq \frac{e^{-ik\eta}}{\sqrt{2k}} \qquad \text{for} \qquad k \gg aH\,. \tag{5.15}$$

The fluctuations with deep sub-Hubble wavelengths have therefore an amplitude exactly like in flat space-time.

After a mode leaves the Hubble radius during inflation ($aH \gg k$), Eq. (5.13) reads $v_k''/v_k \simeq a''/a$, which is satisfied by $v_k \simeq C_k\, a(\eta)$ (with C_k a constant), up to a sub-leading term that becomes quickly negligible [see Eq. (2.68)]. In the slow-roll regime, we can determine the constant C_k by simply matching the super-Hubble solution with the sub-Hubble solution (5.15) at $aH = k$. This gives

$$C_k a_k = \frac{1}{\sqrt{2k}} \qquad \Rightarrow \qquad |v_k(\eta)| \simeq \frac{H_k}{\sqrt{2\,k^3}}\, a(\eta) \qquad \text{for} \qquad k \ll aH\,, \tag{5.16}$$

where a subscript $_k$ indicates, from now on, that the quantity is evaluated when the mode is crossing the Hubble radius during inflation, $a_k\, H_k = k$. As $h_k \propto v_k/a$, Eq. (5.16) indicates that the amplitude of the tensor fluctuation at super-Hubble scales is constant in time. Although Eq. (5.16) has been derived following a rather imprecise method, it provides nonetheless a very good approximation to the solution in the slow-roll regime.

We can actually do much better, as Eq. (5.13) admits analytic solutions, for constant slow-roll parameters. In particular, let us notice that if we consider $\epsilon_H \equiv -d\log H/dN$ constant, then we can write the Hubble rate during inflation as $H(N + \Delta N) \simeq H(N) e^{-\epsilon\, \Delta N}$. This implies that the conformal time is $\eta \equiv \int \frac{dN}{aH} \simeq -\frac{1}{(1-\epsilon)\mathcal{H}}$, with $\mathcal{H} \equiv aH$. Taking derivatives (with respect conformal time) at both sides of the last expression, we obtain $\mathcal{H}' \simeq (1-\epsilon)\mathcal{H}^2$. Hence, the term involving the scale factor in Eq. (5.13) is $a''/a \equiv \mathcal{H}' + \mathcal{H}^2 \simeq (2-\epsilon)\mathcal{H}^2 \simeq \frac{(2-\epsilon)}{(1-\epsilon)^2\eta^2} \simeq \frac{1}{\eta^2}(2+3\epsilon)$, so that Eq. (5.13) can be written as

$$v_k'' + \left[k^2 - \frac{1}{\eta^2}\left(\nu^2 - \frac{1}{4}\right)\right] v_k = 0\,, \qquad \nu \equiv \frac{3}{2} + \epsilon \tag{5.17}$$

A slow-roll parameter $\epsilon \neq 0$ represents, therefore, a linear deviation from the exact de Sitter value $\nu \equiv \frac{3}{2}$, corresponding to $\epsilon = 0$. The general solution to Eq. (5.17), for constant ϵ, is

$$v_k = (-\eta)^{1/2} \left[c_1(k) H_\nu^{(1)}(-k\eta) + c_2(k) H_\nu^{(2)}(-k\eta) \right] , \tag{5.18}$$

where $H_\nu^{(1)}(-k\eta)$, $H_\nu^{(2)}(-k\eta)$ are Hankel functions of the first and second kind. In the deep ultraviolet regime $(-k\eta) \to \infty$, this general solution must match the plane-wave solution Eq. (5.15). Hence, using the large argument expansion of the Hankel functions, $H_\nu^{(1)}(x \gg 1) \simeq \sqrt{\frac{2}{\pi x}} e^{i(x-\nu-\pi/4)}$, $H_\nu^{(2)}(x \gg 1) \simeq \sqrt{\frac{2}{\pi x}} e^{-i(x-\nu-\pi/4)}$, we conclude that $c_2(k) = 0$ and $c_1(k) = \frac{\sqrt{\pi}}{2} e^{\frac{i}{2}\left(\nu+\frac{1}{2}\right)}$. The exact solution then becomes

$$v_k = \frac{\sqrt{\pi}}{2} e^{\frac{i}{2}\left(\nu+\frac{1}{2}\right)} \sqrt{-\eta}\, H_\nu^{(1)}(-k\eta) , \quad \forall\, k, \eta \tag{5.19}$$

Depending on the scale, this solution reduces to

$$v_k \simeq \frac{e^{-ik\eta}}{\sqrt{2k}} , \quad \text{for } -k\eta \gg 1 \tag{5.20}$$

$$v_k \simeq e^{i\frac{\pi}{2}\left(\nu-\frac{1}{2}\right)} 2^{\left(\nu-\frac{3}{2}\right)} \frac{\Gamma(\nu)}{\Gamma(3/2)} \frac{1}{\sqrt{2k}} (-k\eta)^{\frac{1}{2}-\nu} , \quad \text{for } -k\eta \ll 1 , \tag{5.21}$$

where in the second expression we have used the small argument expansion $H_\nu^{(1)}(x \ll 1) \simeq \sqrt{\frac{2}{\pi}} e^{-i\frac{\pi}{2}} 2^{\nu-\frac{3}{2}} \frac{\Gamma(\nu)}{\Gamma(3/2)} \frac{1}{x^\nu}$. The exact solution Eq. (5.19) reduces correctly, at sub-Hubble scales, to Eq. (5.15), as it should. At super-Hubble scales and in the limit $\epsilon \to 0$, the amplitude of Eq. (5.19) reduces to $|v_k| \simeq -\frac{1}{\eta\sqrt{2k^3}}$, which thanks to $aH_k\eta = -1$, matches exactly Eq. (5.16) (which was derived for exact de Sitter). In reality, as one typically expects $\epsilon \neq 0$ (i.e. the inflationary space-time is typically quasi-de Sitter), we see from the $-k\eta \ll 1$ limit in Eq. (5.21), that $|v_k|$ has a tilt at super-Hubble scales; something we will discuss shortly.

Let us remark that Eq. (5.13) describes an harmonic oscillator with a time-dependent frequency, which varies from $\omega_k^2 \simeq k^2$ to $\omega_k^2 \simeq a''/a$ $(\simeq -2a^2H^2)$, when the initially sub-Hubble modes $aH \ll k$ eventually turn super-Hubble $aH \gg k$, due to the quasi-exponential expansion. When $\omega_k^2(\eta)$ varies only adiabatically in time, i.e. $\omega_k' \ll \omega_k^2$, as long as $\omega_k^2(\eta)$ is positive, we can associate an occupation number n_k to each mode k, so that $|\Delta\mathbf{k}|^3 n_k$ represents the number density of gravitons with momentum $[\mathbf{k}, \mathbf{k}+\Delta\mathbf{k}]$. This is given by the

energy $E_k \equiv \frac{1}{2}\left(|v_k'|^2 + \omega_k^2 |v_k|^2\right)$ per mode divided by the energy ω_k per particle,

$$E_k = \left(n_k + \frac{1}{2}\right)\omega_k \qquad \Rightarrow \qquad n_k + \frac{1}{2} \equiv \frac{1}{2\omega_k}\left(|v_k'|^2 + \omega_k^2\,|v_k|^2\right) \tag{5.22}$$

where the $\frac{1}{2}$ term corresponds to the usual quantum vacuum contribution. Inserting the solution at deep sub-Hubble scales Eq. (5.15) into Eq. (5.22), gives $n_k = 0$, as it should be for vacuum in flat space-time. The occupation number n_k is an 'adiabatic invariant' when $\omega_k^2(\eta)$ is positive and varies slowly as $|\omega_k'| \ll \omega_k^2$. However, the stretching of modes during the inflationary expansion violates both conditions, resulting in an abundant production of gravitons as the modes leave the Hubble radius, turning the initial $n_k = 0$ into $n_k \gg 1$. We can check that the solution for super-Hubble modes Eq. (5.21) [Eq. (5.16) for exact de Sitter], corresponds in fact to a very large number of gravitons. Strictly speaking, the occupation number Eq. (5.22) is not well-defined during inflation, as n_k is not adiabatically conserved during the inflationary period. Let us therefore evaluate it just after inflation, assuming an instantaneous transition into a power law expansion era $a(\eta) \propto \eta^p$ after inflation ($p \geq 1/2$), established at some time $\eta = \eta_e$. Using for simplicity the result in exact de Sitter, we can plug Eq. (5.16) into Eq. (5.22), and find that for super-Hubble modes $a_e\,H_e \gg k$, $n_k \sim (H_k/H_e)^2\,(a_e\,H_e/k)^3$ if $p \neq 1$ [$n_k \sim (H_k/H_e)^2\,(a_e\,H_e/k)^4$ for a RD background with $p = 1$]. Thus, super-Hubble modes exhibit a very large occupancy $n_k \gg 1$, as it corresponds to a large ensemble of gravitons. The originally quantum nature of the tensor perturbations (e.g. non-commutation of variables) is lost (due to the time evolution leading to squeezing), but reflected in the stochastic nature of the emerging effectively classical field distribution. The quantum-to-classical transition, which occurs basically when the modes leave the Hubble radius, is studied in detail in Ref. [176–178].

In terms of the original GW field h_{ij}, Eqs. (2.56), (5.8) and (5.10), we can write

$$\hat{h}_{ij}(\mathbf{x},\eta) = \sum_{r=+,\times} \int \frac{d^3\mathbf{k}}{(2\pi)^{3/2}} \left(h_k(\eta)\, e^{i\mathbf{k}\mathbf{x}}\, \hat{a}_{\mathbf{k}r} + h_k^*(\eta)\, e^{-i\mathbf{k}\mathbf{x}}\, \hat{a}^+_{\mathbf{k}r}\right) e^r_{ij}(\hat{\mathbf{k}})\,, \tag{5.23}$$

with the amplitude of the physical tensor modes h_k at super-Hubble scales determined by Eqs. (5.8) and Eq. (5.21), as

$$|h_k(\eta)| \simeq \frac{H}{m_{\rm Pl}\,k^{3/2}}\, f(\epsilon) \left(\frac{k}{aH}\right)^{-\epsilon}, \qquad \text{for} \qquad k \ll aH \tag{5.24}$$

with $f(\epsilon) \equiv 2^{\epsilon}(1-\epsilon)^{1+\epsilon}(\Gamma\left(\frac{3}{2}+\epsilon\right)/\Gamma\left(\frac{3}{2}\right)) \simeq 1-\left(1-\ln(2)-\psi_0\left(\frac{3}{2}\right)\right)\epsilon \simeq 1-0.27\epsilon$, $\psi_0(x)$ the Digamma function. In the limit of exact de Sitter $\epsilon \to 0$, $\dot{H} \to 0$, $f(\epsilon \to 0) \to 1$ and $(k/aH)^{-\epsilon} \to 1$. Hence the amplitude reduces to[4]

$$|h_k(\eta)| \quad \longrightarrow \quad \frac{H}{m_{\rm Pl}\, k^{3/2}}\,, \qquad \text{for} \quad \epsilon \to 0\,,\ k \ll aH\,. \tag{5.25}$$

As discussed below Eq. (2.68), $h_k(\eta)$ remains constant in time after the modes leave the Hubble radius during inflation, until they re-enter the Hubble radius during the post-inflationary evolution. Eq. (5.24) evaluated at Hubble radius crossing $k = a_k H_k$ (which is exactly equivalent to Eq. (5.25) if we approximate $f(\epsilon_k) \simeq 1$), will thus provide the initial condition for the evolution of the modes once they re-enter the Hubble radius, to be discussed in the next section.

It is convenient to define a dimensionless tensor power spectrum $\mathcal{P}_h(k)$ as

$$\langle 0|\hat{h}_{ij}(\mathbf{k},\eta)\hat{h}^{*}_{ij}(\mathbf{k}',\eta)|0\rangle = \frac{2\pi^2}{k^3}\mathcal{P}_h(k)\delta^{(3)}(\mathbf{k}-\mathbf{k}')\,, \tag{5.26}$$

so that

$$\langle 0|\hat{h}_{ij}(\mathbf{x},\eta)\hat{h}_{ij}(\mathbf{x},\eta)|0\rangle = \int \frac{\mathrm{d}k}{k}\ \mathcal{P}_h(k)\,. \tag{5.27}$$

Using Eq. (5.23) evaluated at the super-Hubble solution Eq. (5.24), the orthonormal relation (2.58) for the polarization tensor, and the commutation relations Eq. (5.12) for the creation and annihilation operators, we obtain

$$\mathcal{P}_h(k) \simeq \frac{2}{\pi^2}\,\frac{H^2}{m_{\rm Pl}^2}\,f^2(\epsilon)\left(\frac{k}{aH}\right)^{-2\epsilon}, \qquad \text{for} \qquad k \ll aH\,. \tag{5.28}$$

At horizon-crossing $k = a_k H_k$, this expression reduces simply (taking $f(\epsilon) \simeq 1$) to

$$\mathcal{P}_h(k) \simeq \ \frac{2}{\pi^2}\,\frac{H_k^2}{m_{\rm Pl}^2}\ , \qquad \text{for} \qquad k = a_k H_k\,. \tag{5.29}$$

Since we saw above that the super-Hubble modes behave as a classical random field, the vacuum expectation value in Eq. (5.26) can be interpreted as a classical ensemble average

[4] Alternatively we could have deduced Eq. (5.25) by using Eq. (5.16) valid for exact de Sitter, instead of Eq. (5.21).

over a stochastic field variable. The tensor power spectrum interpreted this way, is then related to the characteristic GW amplitude introduced in Eqs. (3.10), (3.11) by $\mathcal{P}_h(k) = 2h_c^2$.

A small difference between the result in exact de Sitter Eq. (5.29) and quasi-de Sitter Eq. (5.28), is the factor $f^2(\epsilon) \simeq 1 - 0.54\epsilon$, which simply amounts for a tiny correction in amplitude of $\sim 0.5(\epsilon/0.01)\%$. A more notable difference arises however due to the fact that the spectrum becomes slightly red-tilted in the quasi-de Sitter case, i.e. $\mathcal{P}_h(k) \propto k^{n_T}$, with $n_T < 0$ but $|n_T| \ll 1$. More precisely, the spectral tilt $n_T(k)$ can be defined as[5]

$$n_T(k) = \frac{d\log\mathcal{P}_h(k)}{d\log k}\,. \tag{5.30}$$

Applying this formula to Eq. (5.28) leads immediately to the result for canonical SFSR inflation scenarios (where ϵ is small but non-vanishing),

$$n_T \simeq -2\epsilon\,. \tag{5.31}$$

Of course we could have directly read out this tilt from Eq. (5.28) from the explicit $\mathcal{P}_h(k) \propto k^{n_T}$ behaviour.

Let us emphasize that the redness of the spectrum $n_T < 0$, is a direct consequence of the fact that the amplitude of the tensor spectrum at horizon crossing Eq. (5.29), is directly proportional to the (inflaton potential) energy density $H_k^2 \propto V_k(1 + \epsilon/3) \simeq V_k$. Because the Hubble rate decreases slowly during inflation, like $\dot{H} = -\epsilon_H H^2$ [recall Eq. (5.6)], the amplitude of the spectrum Eq. (5.29) at different moments of horizon crossing, changes accordingly to the change of H_k^2 as time goes by. Applying therefore Eq. (5.30) over the spectrum Eq. (5.29) at horizon crossing[6], gives

$$n_T(k) \simeq \frac{d\log V_k}{d\log a_k} \simeq \frac{\dot{\phi}_k}{H_k}\frac{V_k'}{V_k} \equiv -(2\epsilon_\phi)^{1/2}(2\epsilon_V)^{1/2}\,(1-\epsilon_\phi/3)^{-1/2} \simeq -2\epsilon\,. \tag{5.32}$$

As expected, this alternative computation leads consistently to the same result as in Eq. (5.31).

The primordial scalar perturbations generated from inflation can be studied in a similar

[5] With this definition we also encompass the possibility that n_T is a function of the scale k, even if this is not the case in canonical SFSR scenarios.

[6] Note that this is different from what we did previously, when we applied Eq. (5.30) to the general spectrum Eq. (5.28) at arbitrary super-Hubble scales $-k\eta \ll 1$.

way as we did for GWs. In single field inflationary models, the so-called comoving curvature perturbation $\mathcal{R}$ is conserved on super-Hubble scales [198]. In slow-roll models with a canonical kinetic term, its (dimensionless) spectrum,

$$\langle 0|\mathcal{R}(\mathbf{k},\eta)\mathcal{R}^*(\mathbf{k}',\eta)|0\rangle = \frac{2\pi^2}{k^3}\mathcal{P}_{\mathcal{R}}(k)\delta^{(3)}(\mathbf{k}-\mathbf{k}')\,, \tag{5.33}$$

takes a value at horizon crossing as

$$\mathcal{P}_{\mathcal{R}} \simeq \frac{1}{4\pi^2}\frac{H_*^4}{\dot{\phi}_*^2} \simeq \frac{H_*^2}{8\pi^2\epsilon m_{\rm Pl}^2} \qquad \text{for} \qquad k = a_k H_k\,. \tag{5.34}$$

The relative contribution of GW is often indicated by the tensor-to-scalar ratio r, defined as

$$r = \frac{\mathcal{P}_h(k)}{\mathcal{P}_{\mathcal{R}}(k)}\,. \tag{5.35}$$

Using Eqs. (5.29), (5.34) for the spectra and the slow-roll equations (5.2, 5.3), we find that, at horizon crossing $k = a_k H_k$,

$$r_k = 16\,\epsilon\,. \tag{5.36}$$

Together with Eq. (5.32), this gives the so-called consistency relation for SFSR inflationary models (at the lowest order in the slow-roll parameters),

$$n_T(k) = -\frac{r_k}{8}\,. \tag{5.37}$$

Remarkably, this relation is independent of the micro-physical details of the potential that is responsible for inflation: it only involves quantities that are in principle observable. The observational verification of this relation would provide a spectacular confirmation of the simplest models of inflation, and would constitute a definite proof for inflation. This relation can be modified in inflationary models, e.g. if several scalar fields are involved [199, 200] or if vacuum prescriptions differ from the standard Bunch-Davies vacuum [197].

5.3 Evolution of the inflationary background after inflation

5.3.1 The transfer function in a universe composed by radiation and matter

In chapter 3 we have derived the solution of the GW evolution equation at super-Hubble scales and found that its dominant part is constant in time, see Eq. (2.68). In the previous section 5.2, we have demonstrated that this behaviour is indeed confirmed for the quantum tensor fluctuations produced during inflation, after they have become super-Hubble. We have specified solution (2.68) to the case of inflation, by choosing the correct behaviour at sub-Hubble scales (Bunch-Davies vacuum): this gives Eqs. (5.20)-(5.21), and in turn solution (5.25) at super-Hubble scales and in the limit of exact de Sitter.

Eq. (5.25) provides therefore an initial condition for the evolution of the tensor modes produced during inflation. When the modes re-enter the horizon[7] during the subsequent phases of the evolution of the universe, they acquire a time dependence, in particular they start oscillating and decaying like $1/a(\eta)$ (c.f. section 2.4). The full solution for a generic power-law expansion factor is given in Eq. (2.64), for which one has to choose the right initial conditions for $k\eta \ll 1$, i.e. a constant amplitude given by Eq. (5.25). For a universe that is radiation dominated, once the mode has re-entered the horizon, one finds

$$h_r^{\rm RD}(\mathbf{k},\eta) = h^{\rm inf}(k)\, j_0(k\eta)\,, \tag{5.38}$$

where

$$h^{\rm inf}(k) = \frac{H}{m_{\rm Pl}k^{3/2}} \tag{5.39}$$

is the tensor amplitude set by inflation in the limit of exact de Sitter. Note that the same expression (5.38) is valid for both polarisations. For a matter dominated universe, on the other hand, the relevant solution is

$$h_r^{\rm MD}(\mathbf{k},\eta) = h^{\rm inf}(k)\,\frac{3\, j_1(k\eta)}{k\eta}\,. \tag{5.40}$$

To get the amplitude today of a tensor mode produced during inflation, one has to

[7] In the radiation and matter dominated phases, the horizon evolves in time like the Hubble scale, contrary to the inflationary period when it diverges, see e.g. [38].

distinguish the modes that entered the horizon during the matter dominated era and those that entered the horizon during the radiation dominated era. In the first case, the relevant solution is simply Eq. (5.40). In the second case, however, neither Eq. (5.38) nor Eq. (5.40) apply. To find the result at present time, for a mode that crossed the horizon during radiation domination, one can match solution (5.38) at the time of radiation-matter equality with the full solution valid in the matter era with free coefficients (see Eq. (2.64))

$$h_r^{\mathrm{MD,full}}(\mathbf{k},\eta) = \bar{A}(\mathbf{k})\frac{j_1(k\eta)}{k\eta} + \bar{B}(\mathbf{k})\frac{y_1(k\eta)}{k\eta}\,. \tag{5.41}$$

This procedure holds under the assumption that the radiation-matter transition is instantaneous. We therefore expect it to fail for modes which are comparable to the inverse duration of the transition [201]. A solution valid for these modes as well[8] can be obtained by integrating numerically the GW evolution equation (2.63), accounting for the fact that the background evolves smoothly from radiation to matter-domination, i.e. using the scale factor $a(\eta) = H_0^2\,\Omega_{\mathrm{mat}}\,a_0^3\,\eta^2/4 + H_0\,\sqrt{\Omega_{\mathrm{rad}}}\,a_0^2\,\eta$ instead of the single power-law behaviours considered in section 2.4. Still, we present here the matching procedure in order to provide some analytical insight into the numerical solution.

In order to proceed with the analytical approach, one must choose the time η_*, representing radiation-matter equality, at which to match the radiation solution (5.38) with the full solution (5.41). One possibility is to use (note that the numerical values below are found using the cosmological parameters of [30] and setting $a_0 = 1$)

$$\eta_{\mathrm{eq}} = \frac{2(\sqrt{2}-1)\sqrt{\Omega_{\mathrm{rad}}}}{a_0\,H_0\,\Omega_{\mathrm{mat}}} \simeq 86\,\mathrm{Mpc}\,, \tag{5.42}$$

derived by solving $a_{\mathrm{eq}} = a_0(\Omega_{\mathrm{rad}}/\Omega_{\mathrm{mat}}) = H_0^2\,\Omega_{\mathrm{mat}}\,a_0^3\,\eta_{\mathrm{eq}}^2/4 + H_0\,\sqrt{\Omega_{\mathrm{rad}}}\,a_0^2\,\eta_{\mathrm{eq}}$. The corresponding equality scale k_{eq} (the wave-number entering the horizon at η_{eq}) is

$$k_{\mathrm{eq}} = \frac{\sqrt{2}\,a_0\,H_0\,\Omega_{\mathrm{mat}}}{\sqrt{\Omega_{\mathrm{rad}}}} \simeq 1.3\cdot 10^{-2}\,\mathrm{Mpc}^{-1}\,. \tag{5.43}$$

However, from the left panel of Fig. 5.1 one can infer that a better choice for the matching time is the time at which the radiation $a_{\mathrm{rad}}(\eta) = H_0\sqrt{\Omega_{\mathrm{rad}}}\,a_0^2\,\eta$ and matter $a_{\mathrm{mat}}(\eta) =$

[8] For modes that enter the horizon after the universe starts accelerating at late-time, c.f. section 5.3.2

$H_0^2\,\Omega_{\rm mat}\,a_0^3\,\eta^2/4$ solutions cross, i.e. $\eta_* = 4\sqrt{\Omega_{\rm rad}}/(a_0 H_0 \Omega_{\rm mat}) \simeq 417$ Mpc. Matching at η_* better approximates the true background evolution, and therefore provides an analytical solution to the GW evolution equation that better reproduces the numerical one (as can be inferred from the right panel of Fig. 5.1). The corresponding scale k_* can be evaluated using the radiation solution $a_{\rm rad}(\eta)$: the wave-number entering the horizon at η_* is then $k_* = 1/\eta_*$.

The free coefficients of Eq. (5.41) are found via matching $h_r^{\rm MD,full}(\mathbf{k},\eta)$ and its derivative $\partial_\eta h_r^{\rm MD,full}(\mathbf{k},\eta)$, with $h_r^{\rm RD}(\mathbf{k},\eta)$ and $\partial_\eta h_r^{\rm RD}(\mathbf{k},\eta)$, respectively, at η_*. With $x_* = k\eta_*$, they read [202]:

$$\bar{A}(k) = h^{\rm inf}(k)\left[\frac{3}{2} - \frac{\cos(2x_*)}{2} + \frac{\sin(2x_*)}{x_*}\right], \tag{5.44}$$

$$\bar{B}(k) = h^{\rm inf}(k)\left[\frac{1}{x_*} - x_* - \frac{\sin(2x_*)}{2} - \frac{\cos(2x_*)}{x_*}\right]. \tag{5.45}$$

The full solution today can therefore be written as [202]

$$h_r(\mathbf{k},\eta_0) = h^{\rm inf}(k) T(k,\eta_0)\,, \tag{5.46}$$

where $T(k,\eta_0)$ is the *transfer function*:

$$T(k,\eta_0) = \begin{cases} \frac{3\,j_1(k\eta_0)}{k\eta_0}\,, & k < k_* \\ \frac{\bar{A}(k)}{h^{\rm inf}(k)}\frac{j_1(k\eta_0)}{k\eta_0} + \frac{\bar{B}(k)}{h^{\rm inf}(k)}\frac{y_1(k\eta_0)}{k\eta_0}\,, & k > k_* \end{cases}. \tag{5.47}$$

The GW energy density today from tensor modes produced during inflation becomes (c.f Eq. (3.13))

$$\begin{aligned}\rho_{\rm GW}(\eta_0) &= \frac{\langle h'_{ij}(\mathbf{x},\eta_0) h'_{ij}(\mathbf{x},\eta_0)\rangle}{32\pi G a_0^2} \\ &= \frac{1}{64\pi^3 G a_0^2}\int_0^\infty dk\, k^2\,[T'(k,\eta_0)]^2\,|h^{\rm inf}(k)|^2\,,\end{aligned} \tag{5.48}$$

where in the last equality we have used the decomposition in Eq. (5.23) and relations (5.12). Using the above relation and definition (5.27), the GW energy density parameter today can be written as

$$\Omega_{\rm GW}(k) = \frac{1}{12\,H_0^2\,a_0^2}\,[T'(k,\eta_0)]^2 \mathcal{P}_h(k)\,, \tag{5.49}$$

with the inflationary tensor power spectrum given by

$$\mathcal{P}_h(k) \simeq \frac{2}{\pi^2}\frac{H^2}{m_{\rm Pl}^2}\,, \tag{5.50}$$

in the limit of exact de Sitter as we have seen in the previous section. Note that in general one is interested in Eq. (5.49) at sub-horizon scales. Hence, it is customary to approximate $[T'(k,\eta_0)]^2 \simeq k^2\,T^2(k,\eta_0)$, given the oscillatory behaviour of the tensor modes inside the horizon (c.f. section 2.4).

As described in [203], the in-phase oscillation of all modes with a given wave-number k which re-enter the horizon at the same epoch, apparent in Eq. (5.47), is a physical effect due to the common origin (inflation) of the modes. This effect is captured by the oscillating transfer function. However, from the observational point of view, as these modes correspond to a stochastic background of GWs, it is appropriate to average the transfer function over several oscillations. At sub-horizon scales $k\eta_0 \gg 1$, and performing an oscillation-averaging procedure, one obtains

$$[T'(k,\eta_0)]^2 \underset{k\eta_0\gg 1}{\longrightarrow} \begin{cases} \eta_*^2/(2\eta_0^4)\,, & k > k_* \\ 9/(2\eta_0^4\,k^2)\,, & k < k_* \end{cases}\,. \tag{5.51}$$

By substituting the above equation in (5.49), it appears that the energy density spectrum today of the tensor modes generated during inflation is flat in k (assuming exact de Sitter) for modes that entered the horizon during the radiation era, and scaling as k^{-2} for modes that entered the horizon during the matter era.

The right panel of Fig. 5.1 shows the GW energy density power spectrum, calculated both by numerically integrating the GW evolution equation through the radiation-matter transition, and using the analytical transfer function (5.47). It appears that the analytical solution performs well, a part for modes around $k_{\rm eq}$, that enter the horizon during the radiation-matter transition.

The GW energy density power spectrum can be approximated as

$$\Omega_{\rm GW}(k) = \frac{3}{128}\,\Omega_{\rm rad}\,\mathcal{P}_h(k)\,\left[\frac{1}{2}\left(\frac{k_{\rm eq}}{k}\right)^2 + \frac{16}{9}\right]\,, \tag{5.52}$$

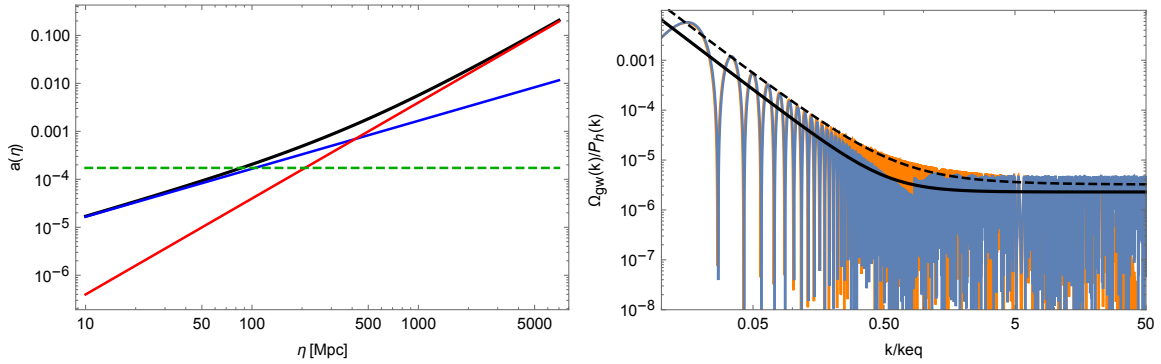

Figure 5.1: Left panel: the scale factor for a radiation-dominated universe (blue curve), a matter-dominated one (red curve), and a universe performing the transition from radiation to matter domination (black curve). The green, dashed line represents the scale factor at equality $a_{\rm eq} = a_0(\Omega_{\rm rad}/\Omega_{\rm mat})$. Right panel: the GW energy density power spectrum, normalised to the primordial inflationary spectrum $\mathcal{P}_h(k)$, as a function of normalised wave-number $k/k_{\rm eq}$. The aim is to show the effect of the transfer function when modes enter the horizon (hence the normalisation). The orange curve represents Eq. (5.48), where we have inserted the correct transfer function, found by numerically integrating the GW evolution equation through the radiation-matter transition. The blue curve is the analytical approximation, i.e. Eq. (5.48) inserting Eq. (5.47). The black curve is approximation (5.52), where we have accounted for oscillations by inserting a factor 1/2. The black, dashed curve shows the result of Ref. [204], i.e. using Eq. (5.53) for the transfer function.

where we have used $\eta_0 = 2/[a_0 H_0(\sqrt{\Omega_{\rm rad}} + \sqrt{\Omega_{\rm rad} + \Omega_{\rm mat}})]$, and we have interpolated oscillations simply by inserting a factor 1/2. The pre-factor 3/128 and the pivot wave-number $k_{\rm eq}$ have been chosen in order to recover Eq. (4) of [93]. Fig. 5.1 also shows the transfer function computed in Ref. [204], where it was derived for the first time (note that in this case oscillations have not been accounted for by introducing a factor 1/2):

$$[T'(k,\eta_0)]^2_{\rm TWL} = \left[\left(\frac{3\, j_1(k\eta_0)}{k\eta_0}\right)'\right]^2 \left(1 + 1.34\frac{k}{k_{\rm eq}} + 2.5\frac{k}{k_{\rm eq}}\right) . \tag{5.53}$$

5.3.2 Going beyond the radiation-matter universe

The above analysis is valid only under several assumptions, some of which we are going to review now in some details. Note that we concentrate only on the effects caused in the context of the standard model of particle physics and cosmology: for more exotic effects related to super-symmetry, the presence of dark fluids and dark interactions, exotic phase transitions or reheating models, see e.g. [202, 203, 205–209].

First of all, we have assumed that the transition between the radiation and the matter

era is instantaneous. Consequently, solution (5.46) is valid only for modes with wavelength much larger than the duration of this transition. For solutions without this restriction, either evaluated under the WKB approximation or fully numerical, see [201, 204].

Second, we have assumed that the universe evolves from a phase of radiation domination with $a(\eta) \propto \eta$ to a phase of matter radiation with $a(\eta) \propto \eta^2$. This is quite simplistic since the evolution of the universe can be characterised by other phases, as for example the phase of late accelerated expansion following the matter era. In order to investigate how a change in the laws of the evolution of the universe affects the above analysis and the SGWB energy density spectrum, the simplest way is to use the solution given in Ref. [203]. In this work, the behaviour of the GW amplitude at sub-horizon scale is derived by pushing the validity of the sub-horizon solution (e.g. Eq. (2.65)) up to horizon crossing, and matching it there with the constant inflationary solution. This gives

$$h_r\left(k > \frac{1}{\eta}, \eta\right) \simeq h^{\rm inf}(k) \cos[k(\eta - \eta_k) + \phi_k] \, \frac{a_k}{a(\eta)} \,, \tag{5.54}$$

where $a_k = k/H_k$ and η_k denote respectively the scale factor and the conformal time at horizon crossing, and ϕ_k is a phase that does not interest us at this point. This solution is approximate, but for $k/\mathcal{H} \gg 1$ it recovers asymptotically the behaviour of Eq. (5.46)-(5.47), as well as (5.38) and (5.40). The transfer function today becomes, using this solution, $T(k, \eta_0) \simeq \cos[k(\eta_0 - \eta_k) + \phi_k] \, (a_k/a_0)$.

Let us start with the radiation dominated era. In the above derivation (as well as in chapter 3) we have assumed that the scale factor always evolves as $a(\eta) \propto \eta \propto 1/T$. However, this neglects the fact that the particle content of the primordial thermal bath changes its nature as the temperature decreases, because particles become non-relativistic and/or get out of thermal equilibrium at different times. In the standard model this occurs for example at e^+e^- annihilation, neutrino decoupling, the QCD phase transition, the EW phase transition, etc. When a given particle species gets out of thermal equilibrium, the effective number of relativistic species contributing to the entropy, $g_S(T)$, decreases, causing the scale factor to increase faster than $1/T$ during this phase (c.f. section 3.1). Note that here we distinguish g_S, the effective number of relativistic species contributing to the entropy, from g_*, those contributing to the energy density: $g_S = g_*$ for $T > 0.1$ MeV (before neutrinos decouple),

while they differ later (c.f. section 3.1). The fast increase of $a(\eta)$ leads to an extra suppression of the tensor modes that entered the horizon before the time at which $g_S(T)$ changes. The extra suppression can be evaluated without modelling the time behaviour of the effective number of relativistic species in any detail, by using Eq. (5.54) (c.f. [202] for a more refined derivation). Let us suppose that $g_S(T)$ and $g_*(T)$ change at a time $\bar{\eta}$, going from $\bar{g}_S$, $\bar{g}_*$ to their value today g_S^0, g_*^0, and consider a mode that entered the horizon at $\eta_k < \bar{\eta}$. Using Eq. (5.54) one can compare the amplitude of the tensor mode accounting for the change in $g_S(T)$, $g_*(T)$ with the one neglecting it, i.e. assuming that g_S and g_* have always remained constant and equal to today's values, also in the past. Using $a(T) = (a_0\, T_0/T)(g_S^0/g_S(T))^{1/3}$, $\rho_{\rm rad}(T) = (\pi^2/30) g_*(T) T^4$, and identifying at horizon crossing $k = \mathcal{H}(T_k) = \sqrt{8\pi G/3}\, a_k \sqrt{\rho_{\rm rad}(T_k)}$, one obtains that the amplitude of the tensor mode with wave-number k is suppressed as

$$\frac{h_r(k,\eta_0)|_{\bar{g}}}{h_r(k,\eta_0)|_{g^0}} \simeq \frac{(a_k/a_0)|_{\bar{g}}}{(a_k/a_0)|_{g^0}} = \frac{T_k|_{g^0}}{T_k|_{\bar{g}}} \left(\frac{g_S^0}{\bar{g}_S}\right)^{1/3} = \left(\frac{g_S^0}{\bar{g}_S}\right)^{2/3} \left(\frac{\bar{g}_*}{g_*^0}\right)^{1/2} , \tag{5.55}$$

where the notation is such that $|_{\bar{g}}$ means a quantity accounting for the change in the effective number of relativistic species, while $|_{g^0}$ neglecting it. For the energy density this leads to

$$\frac{\rho_{\rm GW}(k,\eta_0)|_{\bar{g}}}{\rho_{\rm GW}(k,\eta_0)|_{g^0}} \simeq \left(\frac{g_S^0}{\bar{g}_S}\right)^{4/3} \left(\frac{\bar{g}_*}{g_*^0}\right) . \tag{5.56}$$

Here we assumed a sudden decrease of g_S and g_* at $\bar{T}$, but actually $g_S(T)$ and $g_*(T)$ decrease continuously during the radiation dominated era for $T > 0.1$ MeV. Therefore, the reduction in the tensor amplitude and energy density of a given mode k is stronger, the earlier the mode enters the horizon. As a consequence, the energy density spectrum today is no longer scale invariant for modes that entered the horizon in the radiation era, as we have found above neglecting this effect (and assuming pure de Sitter, c.f. Eq. (5.52)). If one accounts for the change in the effective number of relativistic degrees of freedom, the tensor energy spectrum today decreases with k, as shown for example in Fig. (4) of [202].

A more exotic scenario that leads in fact to an enhancement of the GW energy density, is the presence of a stiff component in the evolution of the universe, i.e. a component with equation of state parameter $w > 1/3$ [203, 205, 210–213]. If such a fluid is present in the early universe it would dominate over radiation at sufficiently early times, since the scale factor for a stiff component increases slower than radiation, $a(\eta) \propto \eta^{2/(3w+1)}$ with $2/(3w+1) < 1$

for $w > 1/3$ (and we know that at some point radiation must have dominated the universe). Clearly, a stiff component can only play a relevant role before BBN, when no constraint is present on the evolution of the universe. It can drive the expansion of the universe only for a finite amount of time, at some point between the end of inflation and the onset of BBN. During this phase, the amplitude of a GW background increases with respect to the standard radiation-dominated scenario. In fact, comparing the GW amplitudes in the two regimes as done previously, one obtains (note that $k \gg a_0 H_0$)

$$\frac{h_r^w(k,\eta_0)}{h_r^{\rm rad}(k,\eta_0)} \simeq \frac{a_k^w}{a_k^{\rm rad}} \simeq \frac{\Omega_{\rm stiff}^{\frac{1}{3w+1}}}{\sqrt{\Omega_{\rm rad}}} \left(\frac{a_0 H_0}{k}\right)^{\frac{1-3w}{3w+1}} > 1 \qquad \text{for } w > \frac{1}{3}\,, \tag{5.57}$$

where $\Omega_{\rm stiff}$ denotes the energy density parameter for the stiff fluid today, and we have used $a_k^{\rm rad} = H_0\sqrt{\Omega_{\rm rad}}\, a_0^2/k$ and

$$a_k^w = H_0^{\frac{2}{3w+1}}\, a_0^{\frac{3(1+w)}{3w+1}}\, \Omega_{\rm stiff}^{\frac{1}{3w+1}}\, k^{-\frac{2}{3w+1}}\,. \tag{5.58}$$

Note that $\eta_k = [2/(3w+1)k]^{2/(3w+1)}$. Furthermore, the GW energy density power spectrum becomes strongly blue-tilted, as opposed to the quasi-scale invariant case of the modes crossing during the radiation dominated era (c.f. Eq. (5.52)). In order to evaluate the GW energy density spectrum today for the modes that crossed the horizon during the stiff era, let us first define $k_{\rm RD} = a_{\rm RD} H_{\rm RD}$, as the comoving horizon scale at the onset of radiation-domination, when the stiff fluid just became sub-dominant. The background of GWs is enhanced for the modes $k > k_{\rm RD}$ that crossed before the end of the stiff period. Substituting $T'(k,\eta_0)^2 \simeq k^2 (a_k/a_0)^2$ derived from (5.54) in Eq. (5.49), using Eq. (5.58) in $(a_k/a_0)^2 = (k_{\rm RD}/k)^{4/(1+3w)}(a_{\rm RD}/a_0)^2$, and using $(a_{\rm RD}/a_0)^4 = \Omega_{\rm rad}(H_0/H_{\rm RD})^2$, we obtain

$$\Omega_{\rm GW}(k) = \frac{\Omega_{\rm rad}}{12}\mathcal{P}_h(k)\left(\frac{k}{k_{\rm RD}}\right)^{\frac{6w-2}{3w+1}} \qquad \text{for } k > k_{\rm RD}\,. \tag{5.59}$$

The blue-tilted scaling as $\Omega_{\rm GW} \propto (f/f_{\rm RD})^{(6w-2)(3w+1)}$ for $f > f_{\rm RD}$, represents a strong enhancement of the short-wave modes of the inflationary background, and opens up the possibility of direct detection of a SGWB of inflationary origin. The standard vacuum contribution from inflation for modes entering during the period of radiation-domination, $\Omega_{\rm GW}\big|_{\rm rad} = \frac{\Omega_{\rm rad}}{12}\mathcal{P}_h(k)$, is way below the sensitivity of present and future GW observatories

as PTA, LISA, and advanced LIGO/Virgo, c.f. Fig. 4.1 and section 4.4. The enhancement $\Omega_{\rm GW}\big|_{\rm stiff}/\Omega_{\rm GW}\big|_{\rm rad} = (f/f_{\rm RD})^{(6w-2)(3w+1)}$ is larger the bigger the frequency, and the later the phase of radiation-domination is established. If the stiff period lasts until just before BBN, say with $f_{\rm RD} \sim 10^{-10}$ Hz, the enhancement at the LISA frequencies $f_{\rm LISA} \sim 10^{-3}$ Hz, can be quite significant for a super stiff phase with $w \simeq +1$, as $\Omega_{\rm GW}\big|_{\rm stiff}/\Omega_{\rm GW}\big|_{\rm rad} = (f_{\rm LISA}/f_{\rm RD}) \sim 10^7$. For an inflationary model with energy scale saturating the upper bound determined by CMB anisotropies, $H \leq H_{\rm max} \simeq 9 \cdot 10^{13}$ GeV, $\Omega_{\rm GW}\big|_{\rm rad} = \frac{\Omega_{\rm rad}}{12}\mathcal{P}_h(k) \sim 5 \cdot 10^{-16}$, and hence $\Omega_{\rm GW}\big|_{\rm stiff}(f \simeq f_{\rm LISA}) \sim 5 \cdot 10^{-9}$, way above the sensitivity of LISA $\Omega_{\rm GW}(f \simeq f_{\rm LISA}) \gtrsim 10^{-13}$.

As mentioned above, in our previous discussions we have neglected the presence of late-time acceleration (see e.g. [204, 214]). Using solution (5.54), we can approximately quantify the difference in the GW solution today accounting (quantities denoted with superscript Λ) and not accounting (quantities denoted with superscript m) for late-time acceleration. Without accounting for late-time acceleration, the scale factor at horizon crossing is given by $a_k^m = H_0^2\,\Omega_{\rm mat}^m\,a_0^3\,(\eta_k^m)^2/4$, with $\eta_k^m = 2/k$: in this case, one must set $\Omega_{\rm mat}^m = 1$ today if one assumes spatial flatness (note that we are neglecting the residual presence of radiation in the late time universe). When accounting for late-time acceleration, the solution for the scale factor does not have an explicit analytic form; however, before the effect of the cosmological constant becomes relevant, it is well approximated by the same solution as above, accounting in this case for the fact that $h^2\Omega_{\rm mat} = 0.14$ today: $a_k^\Lambda \simeq H_0^2\,\Omega_{\rm mat}\,a_0^3\,(\eta_k^\Lambda)^2/4$ and again $\eta_k^\Lambda \simeq 2/k$. A numerical evaluation indicates that this solution is valid approximately until $\eta_\Lambda \simeq 8000$ Mpc, corresponding to $z \simeq 2.7$ and $k_\Lambda \simeq 2.5 \cdot 10^{-4}\,{\rm Mpc}^{-1}$. The ratio of the GW solution today accounting and not accounting for late-time acceleration, becomes then (using $a_k = k/H_k$, and normalising both solutions such that $a_0^\Lambda = a_0^m = 1$)

$$\begin{aligned}\frac{h_r^\Lambda(k,\eta_0)}{h_r^m(k,\eta_0)} &\simeq \frac{a_k^\Lambda}{a_k^m} = \frac{H_k^m(\eta_k^m)}{H_k^\Lambda(\eta_k^\Lambda)} = \frac{\sqrt{(1/a_k^m)^3}}{\sqrt{\Omega_{\rm mat}/(a_k^\Lambda)^3 + \Omega_\Lambda}} \\ &\simeq \begin{cases} \Omega_{\rm mat} & \text{if} \quad k > k_\Lambda \\ \frac{1}{\sqrt{\Omega_\Lambda}}\left(\frac{k}{H_0}\right)^3 > 1 & \text{if} \quad k < k_\Lambda \end{cases}\end{aligned} \tag{5.60}$$

It appears that the GW solution for the modes that enter the horizon well in the matter era, i.e. before the moment when dark energy becomes relevant, is suppressed by a factor $\Omega_{\rm mat} \simeq 0.3$, when accounting for late-time acceleration [204, 214]. This is however a calculation

artefact, since we are obliged to set $\Omega^m_{\rm mat} = 1$ if we neglect the cosmological constant but still assume spatial flatness. On the other hand, the modes that enter the horizon after the onset of the accelerated phase, have tensor amplitudes enhanced with respect to the case neglecting late-time acceleration; furthermore, the energy density power spectrum is changed to $\Omega_{\rm GW}(k) \propto k^4$ instead of the usual k^{-2} dependence given for example in Eq. (5.52). Note however that the approximation $\Omega_{\rm mat}/(a^\Lambda_k)^3 + \Omega_\Lambda \simeq \Omega_\Lambda$ is really crude: a numerical solution shows that in reality the transition occurs very gradually and it is, in fact, still taking place today. The solution given in Eq. (5.60) for $k < k_\Lambda$, as well as the claim that $\Omega_{\rm GW}(k) \propto k^4$, must be therefore considered only as indicative. Furthermore, a numerical evaluation also shows that wave-numbers around the horizon today, with $k_0 = 2.2 \cdot 10^{-4}$ Mpc, have already started exiting the horizon due to the onset of the accelerated expansion. For those, the above solution clearly does not apply[9].

Let us note that in all our derivations so far, we have neglected the presence of free-streaming neutrinos. Their contribution however must be taken into account. After they decouple, neutrinos are no longer in thermal equilibrium with the rest of the universe, and start to stream freely. Consequently, they cannot be described as a perfect fluid, and hence they develop certain out-of-equilibrium terms in their energy momentum tensor, including a tensor anisotropic stress. It is the presence of tensor perturbations in the metric that sources a tensor anisotropic stress in the neutrino fluid, analogously to what happens for an imperfect fluid with shear viscosity ν, which develops a tensor anisotropic stress as $\Pi^{\rm TT}_{ij} = -\nu \dot{h}_{ij}$. In the case of neutrinos, Ref. [216] has worked out the expression for $\Pi^{\rm TT}_{ij}$ which, once inserted into the evolution equation for tensor modes (2.51), gives an integro-differential equation for the tensor perturbation,

$$\begin{aligned} h''_{ij}(\mathbf{k},\eta) + 2\mathcal{H} h'_{ij}(\mathbf{k},\eta) \quad &+ \quad k^2 h_{ij}(\mathbf{k},\eta) = \\ &- \quad 24 \frac{\rho_\nu}{\bar{\rho}} \mathcal{H}^2 \int_{\eta_\nu}^{\eta} d\tau \left[\frac{j_2(k(\eta-\tau))}{k^2(\eta-\tau)^2} \right] h'_{ij}(\mathbf{k},\tau)\,, \end{aligned} \tag{5.61}$$

where ρ_ν and η_ν denote respectively the background neutrino energy density and the time of neutrino decoupling, and $\bar{\rho}$ is the background energy density. This equation can be solved

[9] Note that also Ref. [215] tackles the problem of the effect of the cosmological constant on the GW transfer function, but assumes an instantaneous transition between the matter dominated phase and a de Sitter expansion.

numerically, as done e.g. in [201,202,208,216], to infer the detailed effect of the free-streaming neutrinos on the tensor energy density power spectrum today: see e.g. Fig. 2 in [208]. However some features of the solution can be appreciated by directly looking at Eq. (5.61). First of all, the minus sign on the right hand side confirms that the overall effect is a damping of the amplitude of the inflationary tensor modes, and hence of the energy density power spectrum, see e.g. Fig. 2 in [208] or Fig. 4 in [202]. Secondly, free-streaming neutrinos only affect modes that are inside the horizon, as outside the horizon we expect $h'_{ij} = 0$ for the inflationary GW background. In other words, the effect from free streaming neutrinos respects, as it should, causality. On the other hand, the source term on the r.h.s. of (5.61) is proportional to $\mathcal{H}^2$, meaning that modes that are inside the horizon $k \gg \mathcal{H}$ at the onset of neutrino decoupling, are not altered by neutrino free-streaming. Furthermore, the source term is proportional to the ratio of the neutrino energy density to the one of the background universe. As long as the universe is radiation dominated this remains constant, but starts decaying after the onset of matter domination: consequently, the effect of neutrino viscosity is largely suppressed for modes that enter the horizon during the matter dominated era. To summarise, neutrino free-streaming leads to a damping in the GW energy density power spectrum of about $\sim$ 35% [202], for modes that enter the horizon between the time of neutrino decoupling and the time of matter-radiation equality, i.e. $10^{-17}\,\mathrm{Hz} \lesssim f \lesssim 10^{-11}$ Hz.

Finally, let us also notice that in our previous derivations, the period of reheating has not been modeled in any detail: the transfer function in Eq. (5.47) assumes an instantaneous transition directly from the inflationary to a radiation dominated era. However, if the scale of inflation is sufficiently low, scales entering the horizon at reheating time could fall in the sensitivity range of Earth- or Space-based detection: in this case, a more refined modeling becomes necessary. This can go from the standard accounting for inflaton oscillations around the minimum of its potential (corresponding to a matter-dominated phase if the inflaton potential is quadratic at the minimum) before the universe gets thermalised [204], to more complicated scenarios where other fields, interacting or not with the inflaton, are present, see e.g. [206–208, 217].

Chapter 6

Gravitational wave background from first order phase transitions

This chapter represents the core of the dissertation, and analyses the GW signal from first order PTs in the early universe. The first section is taken from the review [15], and summarises several aspects of the problem: the occurrence of primordial first order PTs, the shape of the generated SGWB, its main parameters, the processes sourcing it. This section is meant as a relatively concise introduction to facilitate the reading of the following ones. The section ends with two examples of SGWB spectra from first order PTs, compared with the sensitivity curve of LISA (figure 6.1). Both the spectral shape and the sensitivity curve are the most accurate, given the state of the art of the research in this topic.

The following four sections include four publications. The preamble to each section puts the article into context, summarises its main results, presents related future projects. The article in section 6.2 derives analytically the SGWB from MHD turbulence in the aftermath of a first order PT. Three articles then follow, each analysing the possibility of detection of the SGWB signal by different GW observatories: LISA in section 6.3, PTA in section 6.4, and CE in section 6.5. Depending on the frequency range in which they are operating, these detectors probe PTs occurring in different epochs of the universe's evolution. LISA can probe the electroweak symmetry breaking, and higher energies up to about 10^3 TeV. PTA can probe the QCD phase transition, occurring at an energy scale of 100 MeV. CE, on the other hand, is sensitive to hypothetical PTs at very high temperatures, from about 10^4 to 10^{10} GeV. There is no theoretical guidance on the nature of these speculative PTs: therefore,

a positive detection would be a major theoretical breakthrough.

The articles presented in sections 6.2 to 6.5 have been written at different stages of my research, the oldest being from 2009. Therefore, some aspects may vary, both amongst them and when compared to the first part of the chapter, section 6.1, because the research has progressed in the meanwhile. This concerns for example the sensitivity curves of the instruments, the role of sound waves in generating GWs, the amount of MHD turbulence developing. Some aspects are still the object of ongoing research: when this is the case, it is specified in the preamble to the section. Since the papers are self-contained, there are repetitions e.g. in the definition of the parameters and of the GW spectral shapes.

6.1 Summary

In the course of its adiabatic expansion, the universe might have undergone several phase transitions (PTs) driven by the temperature decrease. There are a variety of processes related to primordial PTs that can lead to the production of a SGWB, and often a relic SGWB is the only observable remaining after the occurrence of a PT, which can bring us relevant information on the PT nature. Topological defects for example, stable configurations of the field(s) undergoing the PT that can be left over after a spontaneous symmetry breaking, can be a powerful source of a SGWB (see e.g. section 9 of [15]). In the following, we concentrate specifically on SGWB generation by processes which are related to the occurrence of first order PTs.

First order PTs are characterised by the appearance of a barrier in the potential of the order parameter that is driving the PT, separating the false, symmetric vacuum from the true, symmetry-breaking one, which becomes more energetically favourable as the temperature decreases. In order for the field to reach the true vacuum, the potential barrier must be overtaken by quantum tunnelling or thermal fluctuations. In real space this corresponds to the nucleation of bubbles of the true vacuum in the space-filling false one. The bubbles then expand due to the pressure difference acting on their walls. As the bubbles expand, the free energy contained in the false vacuum is released. In the idealised case of a PT occurring in empty space, the released energy can only be converted into gradient energy of the bubble walls, which accelerate up to the speed of light. More realistically, since the PT is occurring in the early universe, space is filled with the primordial plasma; the greatest

part of the released energy is then converted into thermal energy, raising the temperature of the surrounding plasma. Moreover, part of the energy still goes into gradient energy of the bubble walls. However, since the field driving the transition is very likely coupled to the other fields present in the plasma, part of the released energy is also transferred to bulk motion of the surrounding fluid.

Both the field energy momentum tensor representing the gradient energy stored in the expanding bubble walls and the fluid energy momentum tensor representing the kinetic energy of the bulk plasma motions do in general have a non-zero anisotropic stress component in their space-space part Π_{ij} (c.f. Eq. (2.52)). If this latter is of the tensor type, it can act as a source of GWs (see Eq. (2.51)).

Note, however, that spherically symmetric expanding bubbles cannot produce gravitational radiation since the transverse and traceless part of the energy momentum tensor of a radial distribution of field gradients, or of velocity fields, is identically zero (c.f. e.g. Appendix A of [7]). GW production occurs since, towards the end of a first order PT, the true vacuum bubbles collide and convert the entire universe to the symmetry-broken phase. The collisions break the spherical symmetry of the bubble walls and of the bulk fluid velocity configuration surrounding them, generating a non-zero tensor anisotropic stress which actively sources GWs.

The fact that a first-order PT occurring through the nucleation of broken phase bubbles can be a source of GW, has been first pointed out in the seminal works [218, 219]. Here the GW signal was estimated using dimensional arguments and the quadrupole approximation; subsequent analyses performed numerical simulations of the collision of bubbles in vacuum, in order to give a more accurate prediction of the GW signal [220, 221], and generalized the problem also to PTs happening in a thermal environment [222].

6.1.1 Occurrence of first order phase transitions in the early universe

The nature of the primordial PTs depends on the particle theory model describing the universe at high energy. Our present knowledge of high energy physics indicates that there must have been at least two PTs in the early universe: the electroweak one and the QCD one. At temperature higher than the one probed by the Large Hadron Collider (LHC), corresponding to the electroweak symmetry breaking, there is no experimental guidance to indicate what

is the most appropriate particle theory model, and the physical picture is open to several hypothesis.

In the standard model of particle physics (SM), the electroweak phase transition (EWPT) is a cross-over, and it is not expected to lead to any appreciable cosmological signal (see e.g. [223–227]). However, deviations from the SM in the Higgs sector or the introduction of additional fields (for example because of supersymmetry) can modify the order of the EWPT with respect to the SM scenario. The discovery of the Higgs boson at the LHC confirms the paradigm of a scalar field-driven symmetry breaking in the early universe [228], and there is yet no indication of new physics near the EW energy scale. However, the order of the EWPT is not constrained by LHC data: several models leading to a first order EWPT remain viable and complying with LHC bounds. A review of these models, that can provide interesting SGWB signals in the LISA frequency band, is presented in the second part of the article constituting section 6.3. Besides a SGWB, these extensions of the standard model can provide dark matter candidates, baryogenesis, and can also alleviate the hierarchy problem (see e.g. [229–235]).

The QCDPT is also predicted to be a cross-over by lattice simulations run at zero baryon and charge chemical potentials (in the absence of lepton and baryon asymmetries) [236]. However, the lepton asymmetry is very poorly constrained in the early universe, since it could be hidden in the neutrino sector. It has been claimed that 'large' lepton asymmetry, still compatible with present constraints, might affect the dynamics of the QCDPT in a way to render it first order in the early universe [237]. A viable test of this hypothesis would be the detection of the GWs thereby emitted, as analysed in the article presented in section 6.4. Note that the energy scale of the QCDPT implies SGWB signals emitted in the PTA frequency band.

Alternatively, there are various extensions of the SM that predict strong first-order cosmological PTs not tied to the EW or QCD scales. Models solving the hierarchy problem via warped extra dimensions, as the Randall-Sundrum one, are a promising example in what concerns the production of a detectable SGWB, as demonstrated in section 6.3. There, we also discuss other scenarios, in which the dark matter is a stable bound state of a confining dark sector, often without interaction with the (beyond-)SM visible sector, except gravitationally. PTs in the dark sector can be of first order, giving rise to a SGWB just as do PTs

in scenarios interacting and/or extending the SM [238].

In general, the detection of a SWGB would provide a neat probe of the occurrence and the nature of cosmological first order PTs, bringing new information on the underlying high energy theory describing the primordial universe.

6.1.2 Relevant parameters entering the SGWB signal

The GW signal from first order PTs only depends on a few parameters that determine the evolution of the broken phase bubbles (for example their size at collision and their wall speed) and the amount of energy which is available to source the GWs, i.e. the tensor anisotropic stresses (which depend on the strength of the PT and the coupling of the field undergoing the transition with the particles in the primordial universe plasma). The values that these parameters can take depend on the characteristics and the particle nature of the PT, but the GW signal can be described in terms of them in a phenomenological, practically model-independent way. The following of this section presents, in more detail, section 1.1 of the work constituting section 6.3.

Relevant for the GW production is T_*, the temperature of the thermal bath at the time t_* when GWs are produced, i.e. towards the end of the PT when bubble collision occurs (from now on, a subscript $*$ denotes a quantity at the time of GW production). For PTs without significant supercooling and reheating, this is approximately equivalent to the nucleation temperature, $T_* \approx T_n$. The nucleation temperature is the one at which the probability of nucleating one bubble per horizon volume is of order one. This is determined by the nucleation rate (see e.g. [239])

$$\Gamma(t) = A(t)e^{-S(t)}\,, \tag{6.1}$$

where A is a pre-factor with unit of energy to the fourth power, and S is the Euclidean action of a critical bubble [240, 241]: either S_4, given by the $O(4)$-symmetric solution for vacuum transitions, or S_3/T, given by the $O(3)$-symmetric bounce solution for transitions at finite temperature. One can define an approximate inverse time duration of the PT β as the rate of variation of the bubble nucleation rate (accounting for the fact that most of the time variation of $\Gamma(t)$ is in $S(t)$)

$$\beta \equiv -\left.\frac{dS}{dt}\right|_{t_*} \simeq \left.\frac{\dot{\Gamma}}{\Gamma}\right|_{t_*}\,. \tag{6.2}$$

The ratio of the PT inverse duration β and the inverse characteristic rate of expansion of the universe at the PT time $H(T_*)$, is a fundamental parameter for the GW signal, as we will see:

$$\frac{\beta}{H_*} = T_* \left.\frac{dS}{dT}\right|_{T_*} . \tag{6.3}$$

This parameter fixes R_*, the size of the bubbles towards the end of the PT: if v_w is the bubble wall speed, in the rest frame of the fluid and far away from the bubble, one has simply $R_* \simeq v_w/\beta$.

The strength of the PT is characterised by the ratio of the vacuum energy density released in the transition to the radiation energy density in the universe at the moment of the PT (this parameter is defined in the literature also in terms of the latent heat, instead of in terms of the vacuum energy)

$$\alpha = \frac{\rho_{\rm vac}}{\rho^*_{\rm rad}} . \tag{6.4}$$

Note that, if the supercooling is large and the PT effectively occurs in vacuum, it must be characterised also by a consistent amount of reheating, in order to restore the universe in a thermal state after its completion. In this case, one expects $T_n \ll T_{\rm reh} \simeq T_*$, and the above definitions must be changed accordingly [12]:

$$\frac{\beta}{H_*} = \frac{H(T_n)}{H_*} T_n \left.\frac{dS}{dT}\right|_{T_n} , \qquad \alpha = \frac{\rho_{\rm vac}}{\rho_{\rm rad}(T_n)} . \tag{6.5}$$

In this case, the nucleation temperature can be many orders of magnitude smaller than the energy scale corresponding to the VEV at the minimum of the potential. However, the relevant temperature for the GW generation remains $T_* \simeq T_{\rm reh}$; and if the reheating process is sufficiently fast, one also has $H(T_n) \simeq H_*$.

As previously mentioned, the amplitude of the GW signal depends on the amount of energy which is available to source the GWs. The source can be in various forms, depending on the properties of the phase transition. In the most common cases, the PT occurs in a thermal environment, and the largest part of the free-energy liberated by the bubbles is converted into heat, which does not lead to any GW production. However, the PT proceeds through bubble nucleation and therefore some fraction of the free-energy also sets the bubble walls into motion. Towards the end of the phase transition, the bubbles collide and a non-

zero tensor anisotropic stress is generated, which acts as a source of GW. The anisotropic stress can be from the gradient energy of the bubble walls, or from the bulk motion that are set in the fluid by the bubbles sweeping through (provided the field performing the PT is coupled to the surrounding plasma). There are therefore two relevant parameters for the GW generation, the fraction of vacuum energy that gets converted into gradient energy of the Higgs-like field, and into bulk motion of the fluid, respectively:

$$\kappa_\phi = \frac{\rho_\phi}{\rho_{\rm vac}}\,, \qquad \kappa_v = \frac{\rho_v}{\rho_{\rm vac}}\,. \tag{6.6}$$

Note that if the PT is characterised by a large amount of supercooling, and it is therefore effectively happening in vacuum, the free-energy liberated by the bubbles is converted only into gradient energy of the bubble walls, and in this case one has simply $\kappa_\phi \simeq 1$.

6.1.3 General properties and frequency shape of the SGWB spectrum

It is easy to obtain a rough estimate of the GW amplitude, which shows how it scales with the duration and the tensor anisotropic stress of the GW source (see e.g. [7]). Let us suppose that the process leading to the tensor anisotropic stresses has a typical duration corresponding to the PT duration $1/\beta$, and that this is less than one Hubble time: $\beta/H_* > 1$. Under these hypotheses, the usual equation for GW production, Eq (2.51), provides the scaling $\beta^2 h \sim 16\pi G\,\Pi$, where h denotes the amplitude of the tensor perturbation, Π the tensor part of the energy momentum tensor of the source, and we inserted $1/\beta$ as the characteristic time on which the perturbation is evolving (we have dropped indices for simplicity). This suggests that $\dot{h} \sim 16\pi G\,\Pi/\beta$, and the GW energy density at the time of production can then be estimated as (c.f Eq. (3.13)) $\rho^*_{\rm GW} \sim \dot{h}^2/(32\pi G) \sim 8\pi G\,\Pi^2/\beta^2$. Dividing by the total energy density in the universe $\rho^*_{\rm tot} = 3H_*^2/(8\pi G)$ at the time of GW production, one has

$$\frac{\rho^*_{\rm GW}}{\rho^*_{\rm tot}} \sim \left(\frac{H_*}{\beta}\right)^2 \left(\frac{\Pi}{\rho^*_{\rm tot}}\right)^2 . \tag{6.7}$$

The above equation shows that the GW energy density scales like the square of the ratio of the GW source duration and the Hubble time, and the square of the ratio of the energy density in the source and in the universe at the source time. Using Eq. (3.30), the amplitude

of the SGWB today becomes

$$h^2\,\Omega_{\rm GW} \sim 1.6\times 10^{-5}\,\left(\frac{100}{g_*(T_p)}\right)^{1/3}\,\left(\frac{H_*}{\beta}\right)^2\left(\frac{\kappa\,\alpha}{1+\alpha}\right)^2 \tag{6.8}$$

where, to rewrite $\Pi/\rho^*_{\rm tot}$, we have used $\rho^*_{\rm tot}=\rho^*_{\rm rad}+\rho_{\rm vac}$, the definition of α given in Eq. (6.4), and we have set $\kappa\sim\Pi/\rho_{\rm vac}$, where κ can be either of the parameters defined in (6.6). As a rule of thumb, a GW signal above the sensitivity of a future interferometric detector like LISA ($h^2\Omega_{\rm GW}\gtrsim 10^{-12}$) can be generated if $(H_*/\beta)(\Pi/\rho_{\rm tot})_*\gtrsim 3\times 10^{-4}$. Therefore, detectable signals arise from very energetic processes, which involve a sizeable fraction of the total energy density in the universe, and at the same time slow processes, which minimise the value of β/H_*.

As mentioned above, the processes leading to the production of the SGWB operate towards the end of the PT, since they are related to the collision of bubbles. The characteristic wave-number k_* of the SGWB generated by these processes, i.e. the wave-number at which one expects the SGWB to peak, corresponds to the inverse typical time or length scale of the problem: in this case, either to the duration of the PT or to the bubble size, $k_*/a_*\simeq 2\pi\,\beta$ or $k_*/a_*\simeq 2\pi/R_*\simeq 2\pi\,\beta/v_w$, depending on the details of the source (note that we are equating the comoving wave.number k_* to physical quantities as β and R_*, therefore we introduce the factor a_*). If the growth of the bubble proceeds at a highly relativistic speed, the two time/length-scales are equal. Setting e.g. $k_*/a_*\simeq 2\pi\,\beta$, and using Eq. (3.31) with $x_k=2\pi\,\beta/H_*$, one obtains the following order of magnitude estimate for the characteristic frequency today:

$$f\sim 1.6\times 10^{-5}\,{\rm Hz}\,\frac{\beta}{H_*}\,\left(\frac{g_*(T_*)}{100}\right)^{\frac{1}{6}}\,\frac{T_*}{100\,{\rm GeV}}\,. \tag{6.9}$$

Since at the end of the PT one expects the entire universe to be converted to the broken phase, in general the PT must complete faster than a Hubble time, so that $\beta/H_*>1$. From Eq. (6.9) it appears that the characteristic frequency of GW emitted around the EW symmetry breaking at 100 GeV falls in the frequency range of LISA [130] for values $1\lesssim\beta/H_*\lesssim 10^5$ (c.f. section 6.3). As another example, we see from the above formula that GW production at the QCDPT at $T_*\simeq 100$ MeV can fall into the frequency range of detection with pulsar timing array, since $f\geq 10^{-8}$Hz (c.f. section 6.4). The precise value of β/H_* has to be determined in the context of a given model for the first order PT.

The slope of the GW spectrum at wave-numbers smaller than the Hubble radius at the time of production, $k < a_* H_*$, can be determined on general grounds, valid for any transient stochastic source after inflation. It is a consequence of the fact that the causal process (the PT) generating the GW signal cannot operate on time/length-scales larger than $(a_* H_*)^{-1}$. Therefore, the anisotropic stresses $\Pi_{ij}(\mathbf{k}, t)$ sourcing the metric perturbations in Eq. (2.51) are not correlated for $k < a_* H_*$, and the anisotropic stress power spectrum $\Pi(k, \eta, \zeta)$ (c.f. Eq. (3.33)) is expected to be flat in k (white noise) up to the wave-number k_*. Eq. (3.41), valid in the radiation era, then shows that the spectrum of GW energy density per logarithmic frequency interval must grow as k^3 at these large scales $k < a_* H_* \simeq 1/\eta_{\rm in}$. Thus, it is a general result, for SGWBs produced by a first order PT, that the infrared tail of the present-day GW spectrum behaves as $h^2 \Omega_{\rm GW} \propto f^3$ for scales that were super-Hubble at the time of production [8].

Note that at sub-Hubble scales $H_* < k < k_*$, the SGWB spectrum may also continue to grow as f^3 until the characteristic frequency $f_* = k_*/(2\pi)$: the inverse typical time or length scale of the problem, determining k_*, can also play the role of a maximal correlation scale, so that the anisotropic stress power spectrum remains uncorrelated, white noise, for every $k < k_*$, and the above argument applies. However, the details of the time dependence of the anisotropic stress power spectrum can also play a role in this frequency range, modifying the expected k^3 slope, while this cannot happen for super-Hubble modes. While often the case, it therefore cannot be taken for granted that $h^2 \Omega_{\rm GW} \propto f^3$ for $f < f_*$, and there are exceptions (MHD turbulence being one of these, as we will see).

For $k > k_*$, the GW power spectrum decays with a slope that depends on the details of the process sourcing the SGWB, and no general consideration is possible, a part from the fact that the total $\rho_{\rm GW}$, c.f. Eqs.(3.13) and (3.41), must be finite when integrated on the interval $0 < k < \infty$.

As mentioned earlier, the anisotropic stresses acting as a source of GW can be relative to the gradient energy of the bubble walls, or to the bulk motion in the surrounding fluid. We now proceed to describe the SGWBs due to the sources acting during a first order PT: the results of the following sections overlap with those of section 2.1 of the work constituting section 6.3, but they are presented here in more detail.

6.1.4 Contribution to the SGWB from the scalar field driving the PT: bubble wall collisions

The GW production due to the collision of the bubble walls is the easiest to model because, since the seminal paper [221], it is estimated using the 'envelope approximation'. This consists in numerically simulating the motion of the bubble walls as a propagation of spherical, infinitely thin shapes instead of using the Klein-Gordon equation to evolve the scalar field. In this approximation, the gravitational radiation is sourced only by the TT part of the energy-momentum tensor of the uncollided envelope of the spherical bubbles, ignoring the interaction region: this greatly simplifies the numerical simulation since it dispenses with the detailed dynamics of the scalar field and reduces the required computational power.

The validity of the envelope approximation has been asserted in [221, 222] for the case of strongly first order PTs happening both in vacuum and in a thermal environment, if they proceed through detonation (i.e. at supersonic speed [242]). In these cases, the energy momentum tensor representing the propagation of the bulk fluid motions sourcing the GW is effectively concentrated on a thin shell near the bubble wall. The latest numerical simulations using the envelope approximation with considerably improved numerical accuracy have been carried on in [243, 244], providing a better determination of a larger portion of the GW spectrum and consequently a more careful analysis of the high frequency behaviour with respect to previous works. The resulting SGWB spectrum is[1]

$$\begin{aligned} h^2\Omega_\phi(f) &= 1.67\times 10^{-5}\left(\frac{H_*}{\beta}\right)^2\left(\frac{\kappa_\phi\,\alpha}{1+\alpha}\right)^2\left(\frac{100}{g_*(T_*)}\right)^{\frac{1}{3}}\left(\frac{0.11\,v_w^3}{0.42+v_w^2}\right) \\ &\times \frac{3.8\,(f/f_\phi)^{2.8}}{1+2.8\,(f/f_\phi)^{3.8}} \end{aligned} \tag{6.10}$$

where the peak frequency f_ϕ corresponds roughly to the characteristic time-scale of the PT, i.e. its duration $1/\beta$ [8]. The simulations yield [243, 244]

$$\frac{f_*}{\beta} = \frac{0.62}{1.8 - 0.1 v_w + v_w^2} \tag{6.11}$$

[1] Note that, by the argument given in the previous subsection, causality should imply that at low frequency the SGWB grows as f^3. This must be the case at least for frequencies smaller than the inverse Hubble horizon at GW production; however, $f^{2.8}$ provides a better fit to the simulated result close to the peak of the spectrum [243].

which becomes, once redshifted to today

$$f_\phi = 1.65 \times 10^{-2}\,\mathrm{mHz} \left(\frac{f_*}{\beta}\right) \left(\frac{\beta}{H_*}\right) \left(\frac{T_*}{100\,\mathrm{GeV}}\right) \left(\frac{g_*(T_*)}{100}\right)^{\frac{1}{6}} \tag{6.12}$$

(c.f. Eq. (6.9)). Besides numerical simulations [243, 244], there have been also several works that have tried to model the SGWB spectrum from bubble collisions analytically, see [7, 245, 246].

6.1.5 Contribution to the SGWB from the bulk fluid motions: sound waves

The characteristics of the bulk flow depend on the strength of the coupling of the field driving the PT to the fluid particles: this coupling strongly influences the bubble evolution, as demonstrated by many analyses (see e.g. [247–252]). In general, it can be assumed that the propagation quickly reaches stability and the bubble walls expand with constant velocity v_w, which can be either subsonic (deflagration) or supersonic (detonation) (see e.g. [253] and references therein)[2]. The bubble wall speed v_w should be determined by a full analysis of the microscopic interactions, of the type of those carried out in e.g. [248, 256, 257]. However, from the point of view of GW production, the problem can be tackled by introducing a phenomenological parameter, the friction η, and by studying the bubble evolution as a function of this [253]. Both semi-analytical methods (see e.g. [258]) and numerical simulations (see e.g. [259]) show that the friction modelling the interactions influences the bubble wall velocity and the transfer of kinetic energy of the scalar field to bulk kinetic energy of the fluid [253], which are important parameters entering the GW production rate.

The most recent and detailed numerical simulations of the full system of the scalar field performing the transition and the surrounding fluid coupled to it via a friction parameter η have been performed in Refs. [260–262]. These have demonstrated that compressional modes, i.e. sound waves, are induced in the surrounding fluid by the expansion of the bubbles, due to the coupling among the scalar field and the fluid. At bubble collisions, the sound waves give rise to a non-zero tensor anisotropic stress that is a powerful source of GWs. Simulations have furthermore found that the sound waves continue to act as a source of GW well after

[2]Note that the possibility of having runaway solutions in the electroweak PT, first put forward in [254], has been excluded by a recent analysis [255].

the merging of the bubbles is completed and the scalar field has everywhere settled in the true vacuum. They remain present in the fluid until either they are damped by viscosity, or they generate shocks. The long-lasting nature of the sound waves in the primordial fluid enhances the GW signal by a factor β/H_* rendering them the most relevant contribution to the SGWB spectrum in the case of PTs which are not very strongly first order and happen in a thermal environment [260]. Note that the fact that GW sources lasting long, more than one Hubble time, are amplified by an extra β/H_* factor does not contradict the result given in Eq. (6.7), and was predicted on the basis of analytical arguments in the work presented in section 6.2, i.e. Ref. [9].

The SGWB spectrum from sound waves, fitted from the numerical results of [261], is given by

$$\begin{aligned} h^2\Omega_{\rm sw}(f) &= 2.65\times10^{-6}\left(\frac{H_*}{\beta}\right)\left(\frac{\kappa_v\,\alpha}{1+\alpha}\right)^2\left(\frac{100}{g_*(T_*)}\right)^{\frac{1}{3}} v_w \\ &\times \left(\frac{f}{f_{\rm sw}}\right)^3\left(\frac{7}{4+3\,(f/f_{\rm sw})^2}\right)^{7/2}, \end{aligned} \tag{6.13}$$

where the peak frequency is set by the characteristic size of the bubbles at the end of the transition, and it is approximatively given by $f_{\rm sw}\simeq(2/\sqrt{3})(\beta/v_w)$, which, after redshifting, becomes[3]

$$f_{\rm sw} = 1.9\times10^{-2}\,{\rm mHz}\,\frac{1}{v_w}\left(\frac{\beta}{H_*}\right)\left(\frac{T_*}{100\,{\rm GeV}}\right)\left(\frac{g_*(T_*)}{100}\right)^{\frac{1}{6}}. \tag{6.14}$$

6.1.6 Contribution to the SGWB from the bulk fluid motions: MHD turbulence

Besides sound waves, the bubble merging could also induce vortical motions in the surrounding fluid, which would constitute an independent source of GW. The primordial plasma is characterized by a very high Reynolds number (of the order of 10^{13} at 100 GeV and at the typical scale of the bubbles [9]): therefore, the energy injection caused by the collision of the bubbles is expected to lead to the formation of magneto-hydrodynamic (MHD) turbulence, which generates GW through the anisotropic stresses of the chaotic fluid motions and of the magnetic field. Note that the turbulence is expected to be accompanied by the presence of magnetic fields since the early universe plasma is fully ionised and has a very high conductiv-

[3]Note that the most recent analysis [262] finds a somewhat smaller peak frequency of the order of $f_{\rm sw}\simeq 0.3(\beta/v_w)$

ity [263,264]. Turbulence can also lead to the amplification of small magnetic fields generated by charge separation at the bubble wall (see e.g. [265]).

In the simulations of [260–262], the vortical component of the bulk fluid motions has been evaluated and was always largely sub-dominant with respect to the compressional one. However, after a characteristic time $\tau_{\rm sh} \sim (v_w/\sqrt{\kappa_v \alpha})\beta^{-1}$ (see e.g. [266]) one expects the formation of shocks, that will eventually convert the acoustic signal into a turbulent one. This happens of course only if $\tau_{\rm sh} \leq H_*^{-1}$, so if shocks can develop within one Hubble time. Up to now, the numerical simulations did not simulate strong enough PTs capable of reaching $\tau_{\rm sh}$ within the simulation time, so predictions of the GW signal from turbulence based on simulations are not available. However, analytical evaluations of the SGWB from MHD turbulence exist.

The first analyses of the GW production by turbulence had some problems that led to an overestimate of the signal [267–269] (c.f. the discussion in [11] and references therein). The most recent analytical evaluation of GW emission from MHD turbulence generated during a first-order PT and freely decaying afterwards is the one of [9]. This analytical evaluation maintains a certain level of intrinsic uncertainty, for example in that it has to rely on a theoretical turbulence model (usually, Kolmogorov turbulence is assumed) and on a model for the time decorrelation of the GW source. This uncertainty could only be addressed by numerical simulations of relativistic MHD turbulence. Furthermore, [9] neglects the possibility of helical turbulence (see e.g. [270]). Under these assumptions, the resulting contribution of MHD turbulence to the GW spectrum is [9, 11]

$$\begin{aligned} h^2\Omega_{\rm turb}(f) &= 3.35\times 10^{-4}\left(\frac{H_*}{\beta}\right)\left(\frac{\kappa_{\rm turb}\,\alpha}{1+\alpha}\right)^{\frac{3}{2}}\left(\frac{100}{g_*(T_*)}\right)^{1/3} v_w \\ &\times \frac{(f/f_{\rm turb})^3}{[1+(f/f_{\rm turb})]^{\frac{11}{3}}\,(1+8\pi f/h_*)} \end{aligned} \tag{6.15}$$

where

$$\kappa_{\rm turb} = \epsilon\,\kappa_v \tag{6.16}$$

represents the (yet unknown) fraction of bulk kinetic energy associated to the vortical motions, as opposed to the compressional modes. Similarly to the case of sound waves, there is an amplification by a factor β/H_* which is typical of sources that last longer than the

average duration $1/\beta$ of the PT. In Eq. (6.15), $h_* = 1.6 \cdot 10^{-4} (T_*/100\,\mathrm{GeV})(g_*/100)^{1/6}$ mHz is the Hubble parameter red-shifted to today: it enters also as a consequence of the fact the turbulence acts as a source of GW for several Hubble times. Similarly to the sound wave case, the peak frequency is connected to the inverse characteristic length-scale of the source, the bubble size R_* towards the end of the PT: $f_{\mathrm{turb}} \simeq (3.5/2)(\beta/v_w)$, which becomes, after red-shifting,

$$f_{\mathrm{turb}} = 2.7 \times 10^{-2}\,\mathrm{mHz}\,\frac{1}{v_w}\left(\frac{\beta}{H_*}\right)\left(\frac{T_*}{100\,\mathrm{GeV}}\right)\left(\frac{g_*(T_*)}{100}\right)^{\frac{1}{6}} . \tag{6.17}$$

6.1.7 Examples of SGWBs from a first order phase transition

In order to predict the amplitude and peak frequency of the GW signal from a specific first order PT one has to determine the value of the few parameters entering the GW spectrum, as shown in the previous subsections. These are the PT temperature T_*, the inverse duration of the PT β/H_*, the bubble wall velocity v_w, and the fraction of energy that contributes to the GW generation $(\Pi/\rho_{\mathrm{tot}})_*$. This latter becomes the factor $(\kappa\,\alpha/(1+\alpha))$ appearing in Eqs. (6.10), (6.13), (6.15), once translated into the two parameters representing the strength of the PT (α, Eq. (6.4)) and the fraction of vacuum energy that gets converted into gradient or kinetic energy (κ, Eq. (6.6)).

These parameters can only be determined within a given model of the PT, and are not all independent among each other. In the case of a thermal phase transition, one first needs to find the bounce solution of the three-dimensional Euclidean action $S_3(T)$, which quantifies the probability of thermal jumping [271]. From this, one can then calculate the fraction of space that is covered by bubbles (neglecting overlap): T_* can be defined as the temperature at which this fraction is equal to one. Moreover, knowing the action $S_3(T)$ as a function of temperature, one can calculate $\beta/H_* = T\,d(S_3/T)/dT$, which has to be evaluated towards the end of the PT to represent, as a matter of fact, the 'duration' of the PT[4].

The bubble wall velocity v_w and the fraction of energy that contributes to the GW generation $(\Pi/\rho_{\mathrm{tot}})_*$ cannot in general be evaluated solely from the action $S_3(T)$. Since these two parameters are connected to the dynamics of the bubble expansion in the primordial fluid, a knowledge of the total particle content and interactions of the theory is in principle

[4] Alternatively, it is possible to relate β to the typical bubble size at the end of the PT through v_b, $\langle R\rangle \simeq 3v_b/\beta(T)$, where $\langle R\rangle$ can be estimated from the maximum of the bubble volume distribution [271].

necessary to determine them. The bubble wall velocity v_w results from the balance among the driving force that makes the bubble expand (given by the pressure difference between the interior and the exterior of the bubble, which is connected to the latent heat) and the friction force due to the interaction of the bubble wall with the surrounding plasma, which slows down the bubble expansion. The friction can either be determined in a given particle theory model, for which all interactions are known, or it can be parametrised in terms of the independent parameter η, providing then a phenomenological description valid for several PT models [253]. Once v_w is known, it gives the boundary condition for the hydrodynamical description of the bubble growth.

The tensor anisotropic stress Π sourcing GW is in general given by the the sum of the gradient energy in the Higgs-like field driving the phase transition and of the bulk kinetic energy of the fluid set into motion by the bubble walls. This latter must be further divided into the component due to sound waves and the one due to MHD turbulence. If the PT is occurring in a thermal state and the friction is high, the bulk motion and the MHD turbulence are expected to dominate Π. The simulations of [260–262] show that the contribution from the scalar field gradient energy is largely sub-dominant. In this case, the total GW signal is given by the sum of Eqs. (6.13) and (6.15). Moreover, it is shown in Ref. [253] that the efficiency factor κ_v in Eq. (6.6), representing the fraction of vacuum energy that gets converted into bulk kinetic energy, can be related to α (Eq. (6.4)): in the limits of small and large v_w, [253] finds

$$\kappa_v \simeq \begin{cases} \alpha\,(0.73 + 0.083\sqrt{\alpha} + \alpha)^{-1} & v_w \sim 1 \\ v_w^{6/5} 6.9\,\alpha\,(1.36 - 0.037\sqrt{\alpha} + \alpha)^{-1} & v_w \lesssim 0.1\,. \end{cases} \tag{6.18}$$

If, on the contrary, the PT is very supercooled and friction is low, the role of the plasma is minor, and most of the energy remains in the form of gradient energy of the Higgs-like field. In this case, the total GW signal is given by Eq. (6.10), and furthermore, one can consistently approximate $\kappa_\phi \simeq 1$. Since the PT is very strongly first order, one has $\alpha \gg 1$, and the dependence on α of the SGWB in Eq. (6.10) effectively drops. It is also important to point out that, in general, the strength of the PT α is connected with its duration β/H_*: strong PTs last longer, leading to small β/H_*. This increases the amplitude of the GW signal, but shifts the peak frequency to low values.

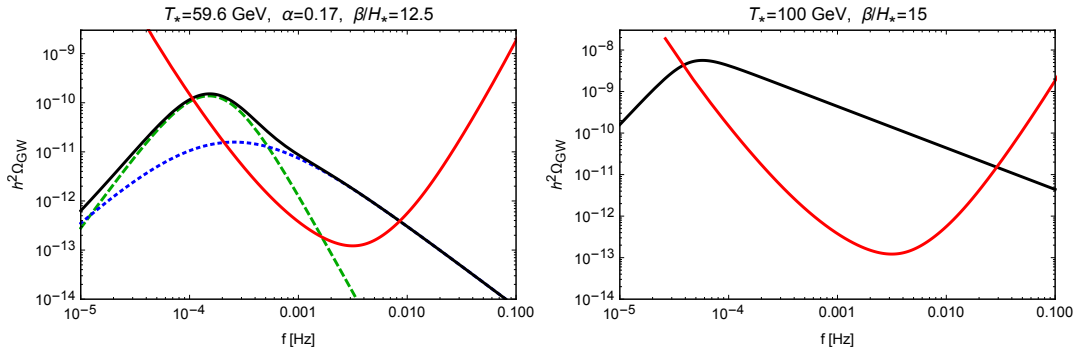

Figure 6.1: SGWB spectra in two examples of first order PT, compared with the estimated sensitivity curve of the interferometer LISA calculated from [130] (the red solid curve appearing in both pictures, c.f. section 4.4). Left plot: the Higgs portal scenario, with parameters $\alpha = 0.17$, $\beta/H_* = 12.5$ and $T_* = 59.6$ GeV, see [12]. The green, dashed curve represents the GW signal from sound waves, while the blue, dotted curve represents the GW signal from MHD turbulence, where we have taken $\epsilon = 1$ (c.f. Eq. (6.16)). Right plot: PT connected with the radion stabilization in the Randall Sundrum model, with $\beta/H_* = 15$ and $T_* = 100$ GeV, again see [12].

The article constituting section 6.3 presents a selection of PT scenarios, both related and not related to the EW symmetry breaking, that can produce SGWBs in the frequency range of the LISA interferometer. For each scenario there is a choice of benchmark values of α, β/H_* and T_* that can be realised within the model. This allows to give predictions for realistic GW signals, which can actually arise in well identified particle physics models.

We close this section with two examples of SGWB from first order PTs, taken from Ref. [12]: the Higgs portal scenario, with benchmark values $\alpha = 0.17$, $\beta/H_* = 12.5$ and $T_* = 59.6$ GeV, and the dilaton scenario, with benchmark values $\beta/H_* = 12.5$ and $T_* = 59.6$ GeV (as explained above, in this case the GW signal no longer depends on $\alpha \gg 1$). In the first case, we have set $v_w = 0.95$ as done in [12], while in the second case, since the PT is effectively happening in vacuum, we have set $v_w = 1$. The resulting GW spectra are shown in Fig. 6.1 together with the LISA sensitivity, taken from Ref. [130]. In the Higgs portal scenario the SGWB is sourced by the plasma bulk motion. We therefore plot the two contributions: the one from sound waves, Eq. (6.13), with κ_v given by the first line of Eq. (6.18); and the one from turbulence, Eq. (6.15), with $\kappa_{\rm turb} = \epsilon\,\kappa_v$. Note that we have set $\epsilon = 1$, since for the adopted benchmark point $\tau_{\rm sh} H_* \simeq 0.54$ and one therefore expects the formation of MHD turbulence. In the dilaton-like scenario, on the other hand, the PT is effectively happening in vacuum: we are therefore plotting only Eq. (6.10), with $\kappa_\phi = 1$. It appears that both scenarios can provide a SGWB detectable by LISA, which could thereby help testing the

occurrence of new physics beyond the standard model of particle physics, for models that are still viable notwithstanding LHC constraints.

6.2 Article: Gravitational waves from MHD turbulence

The article constituting the following section presents an analytical derivation of the SGWB from MHD turbulence arising after a PT. Even though the paper has been completed in 2009, the result for the shape of the SGWB is still used to date: this is the reason why I considered it worth to be included in this dissertation. The analysis improves considerably over previous ones, however, it still contains several assumptions and approximations. On the other hand, it probably represents just how far one cat get on this problem using analytical evaluations: a more realistic result for the SGWB, taking into account the detailed dynamics of the MHD turbulence, can only be obtained via numerical simulations, which are however quite difficult to perform. This is why the research on the SGWB produced by non-helical MHD turbulence did not undergo fundamental progresses after the work presented below appeared.

The main novelty of this work is that we accounted for the fact that MHD turbulence is in the free-decay regime. The source of the fluid stirring is bubble collision: a quick process, completed well within one Hubble time. We assumed that the stirring is enough to produce fully developed Kolmogorov turbulence, in one eddy turnover time. Afterwards, the turbulent motions are not sustained any longer, and decay according to the Kolmogorov time-decay laws. On the other hand, performing the analysis we have discovered that, due to the very low viscosity of the early universe fluid (which we evaluated), the free-decay is a very long process: the MHD turbulence can therefore act as a source of GWs for many Hubble times after the PT has ended. This influences the shape of the SGWB spectrum at large scales.

The turbulent velocity spectrum, and the one of the accompanying magnetic field, have been modelled in this work in a more realistic way than in previous analyses, using a smooth interpolation between large and small scales, accounting for the causality in the spatial correlation function, and keeping the source continuous in time. However, the Kraichnan-type time decorrelation, typical of turbulent fluid motions, could only be accounted for using an Ansatz for the unequal time correlator of the anisotropic stresses: this is probably the weakest assumption done in this work, which absolutely necessitates checking via numerical simulations.

In collaboration with the group of the University of Helsinki, in particular David Weir and Mark Hindmarsh, we started a project which aims at verifying and ameliorating, via numerical simulations, the SGWB obtained analytically. The initial conditions of the simulations are the end results of the previous simulations done by the same group, in which sound waves were generated. This allows to avoid simulating the initial stages of the PT, for which one has to solve both the scalar field and the fluid equations of motion. We plan to start simulating after the fluid configurations have reached terminal velocity and sound waves have developed, thereby gaining simulation time. By doing so, we do not loose any precious information, since turbulence is only expected to form in a subsequent stage, by the shocks generated at the sound wave fronts. In principle then, the new simulations should show the formation of shocks leading to turbulence. Moreover, together with Danièle Steer and a common master student, we have calculated an analytical approximation for the sound wave velocity power spectrum, tuned to the results of sound simulations. We plan to use this as well, as initial condition for the turbulent simulations: being an analytical formula, it allows to set up the initial conditions also for stronger phase transitions, for which the turbulence is expected to be more important.

Journal of Cosmology and Astroparticle Physics

The stochastic gravitational wave background from turbulence and magnetic fields generated by a first-order phase transition

Journal of Cosmology and Astroparticle Physics
An IOP and SISSA journal

The stochastic gravitational wave background from turbulence and magnetic fields generated by a first-order phase transition

Chiara Caprini,[a] **Ruth Durrer**[b] **and Géraldine Servant**[a,c]

[a]CEA, IPhT & CNRS,
URA 2306, F-91191 Gif-sur-Yvette, France
[b]Département de Physique Théorique, Université de Genève,
24 Quai E. Ansermet, CH-1211 Genève, Switzerland
[c]CERN Physics Department, Theory Division,
CH-1211 Geneva 23, Switzerland

E-mail: chiara.caprini@cea.fr, ruth.durrer@unige.ch, geraldine.servant@cern.ch

Received September 13, 2009
Revised November 11, 2009
Accepted November 11, 2009
Published December 22, 2009

Abstract. We analytically derive the spectrum of gravitational waves due to magneto-hydrodynamical turbulence generated by bubble collisions in a first-order phase transition. In contrast to previous studies, we take into account the fact that turbulence and magnetic fields act as sources of gravitational waves for many Hubble times after the phase transition is completed. This modifies the gravitational wave spectrum at large scales. We also model the initial stirring phase preceding the Kolmogorov cascade, while earlier works assume that the Kolmogorov spectrum sets in instantaneously. The continuity in time of the source is relevant for a correct determination of the peak position of the gravitational wave spectrum. We discuss how the results depend on assumptions about the unequal-time correlation of the source and motivate a realistic choice for it. Our treatment gives a similar peak frequency as previous analyses but the amplitude of the signal is reduced due to the use of a more realistic power spectrum for the magneto-hydrodynamical turbulence. For a strongly first-order electroweak phase transition, the signal is observable with the space interferometer LISA.

Keywords: gravitational waves / theory, Magnetohydrodynamics, cosmological phase transitions

ArXiv ePrint: 0909.0622

doi:10.1088/1475-7516/2009/12/024

JCAP12(2009)024

Contents

1 Introduction

Cosmological observations are often a search for 'relics' of the early universe. Relics allow us to infer the physics at a time when the Universe was much hotter and much denser than today. A famous example of this is the cosmic microwave background (CMB) [1], which literally represents a photograph of the Universe at the time when CMB photons decoupled. Another very promising relic which has not yet been observed is a gravitational wave (GW) background. Since GWs interact so little with matter and radiation, they propagate freely immediately after generation and therefore allow us a direct observation of the Universe at the time of their production. GW backgrounds have been proposed from inflation [2], from braneworlds [3], from topological defects [4], from reheating after inflation [5] and from first

JCAP12(2009)024

order phase transitions [6, 7]. In this last case, which is the topic of this paper, at least three different sources of GWs have been identified: the collisions of broken phase bubbles [8–14], fluid turbulence [15–20] and magnetic fields [21–24]. In this paper we concentrate on the latter two aspects which cannot be truly separated since the magnetic fields are processed and amplified by the turbulent fluid flow.

The GW signal from a first-order phase transition has a characteristic frequency of the order $\omega = c\,k_* a_*/a_0 = \epsilon^{-1} H_* a_*/a_0$ where $\epsilon = L_* H_*/c$ is the size of the largest bubbles in units of the horizon size at the transition, $1/H_*$. Its value depends on the particle physics model but for a strong first-order phase transition, we will set $\epsilon \sim 0.01$. Quite remarkably, for a potentially first-order electroweak (EW) phase transition at $T_* \sim 100\,\mathrm{GeV}$, this frequency is around a MilliHertz which is the frequency of best sensitivity of the planned GW satellite LISA (Laser Interferometer Space Antenna) [25], meaning that LISA is potentially a window on EW and TeV scale particle physics [26–28].

The main difference of our approach with earlier works is that we consider a long-lasting, magneto-hydrodynamic (MHD) turbulent source. The collision of bubbles of the broken phase causes an injection of energy in the primordial fluid. Since the kinetic Reynolds number of the fluid is huge, for instance $\sim 10^{13}$ at the EW epoch (c.f. section 3.5), turbulent motion sets in rapidly in the fluid. The magnetic Reynolds number being also very large, this leads to the amplification of magnetic fields generated during the phase transition [29], and MHD turbulence develops. Once the phase transition is over the source of energy injection stops. However, MHD turbulence does not cease immediately but decays like a power law. In previous studies [15–18, 20], the free decay of the turbulent velocity power spectrum has been ignored: it was assumed that turbulence was active only during the completion of the phase transition. However, since the value of the Reynolds number is very high, the dissipation is not sudden and the fluid can remain turbulent during many Hubble times.

The power law decay in time of MHD turbulence is well established theoretically [30–35], experimentally [36] and by numerical simulations [37–39]. However, there is no consensus on the actual value of the power law exponent: Kolmogorov theory predicts a faster decay than what observed in general in numerical simulations. On the other hand, both analytical analyses and numerical simulations do agree on one point: that, in the absence of helicity, the large scale part of the MHD turbulent spectrum is constant in time. Without inverse cascade the energy is dissipated on the very small scales, the correlation length grows in time, but wavenumbers much smaller than the inverse correlation length are not affected by the evolution. This is important for MHD turbulence in the early universe. The radiation dominated universe is characterised by a finite causal horizon, beyond which the turbulent motions cannot be causally connected. As previously demonstrated [17, 40], the existence of this causal horizon in a cosmological setting implies that the real-space correlation function of the stochastic velocity field has compact support. The fact that the real-space correlation function necessarily vanishes at large scales, together with the property of divergence freeness satisfied by the incompressible turbulent flow and by the magnetic field, entails the formation of a Batchelor spectrum for the turbulent velocity field and the magnetic field [17]. Namely, taking for example the velocity field, the large scale part of the spectrum grows as $P_v(k \to 0) \propto I\,k^2$, where $I \sim \langle v^2 \rangle L^5$ is the Loitsyansky's integral, $\langle v^2 \rangle$ being the typical velocity of the largest eddies and L their size (i.e. the largest scale on which turbulence develops, the correlation scale corresponding to the bubble diameter in our context). Given this form of the large scale part of the power spectrum, if it has to be constant as predicted by the theory and observed in numerical simulations, then necessarily I must be constant in time (which

JCAP12(2009)024

is also required by the Navier-Stokes equation) [41, 42].

In the following, we will assume that the kinetic energy $\langle v^2 \rangle$ and the correlation length L evolve in such a way, as to maintain the product $I \sim \langle v^2 \rangle L^5$ constant. We define the power law exponent γ such that $L \sim t^\gamma$ and $\langle v^2 \rangle \sim t^{-5\gamma}$. For generality, the exponent γ is kept unspecified in the analytical formulae, but for the numerical results we substitute the value $\gamma = -2/7$. According to Kolmogorov theory, in fact, the constancy of I together with the energy decay equation $d\langle v^2 \rangle / dt \sim -\langle v^3 \rangle / L$ lead to the Kolmogorov decay laws: the decay of the kinetic energy with time as $\langle v^2 \rangle \sim t^{-10/7}$ and the growth of the correlation scale as $L \sim t^{2/7}$ (see for example [30]). As explained in section 3.3, in the following we also assume equipartition between the turbulent and magnetic energy densities $\langle v^2 \rangle \sim \langle b^2 \rangle$: consequently, we assume the same decay law also for the magnetic field, i.e. $\langle b^2 \rangle L^5 = \text{constant}$.

The value $\gamma = 2/7$ that we use in the numerical estimates has also been derived on the basis of detailed theoretical arguments, as for example in [35]. On the other hand, as previously mentioned, numerical simulations observe a slower decay for the kinetic and magnetic energies, close to $\langle v^2 \rangle \sim \langle b^2 \rangle \propto t^{-1}$ [37–39]. However, it is not clear whether numerical simulations can efficiently model the conditions of MHD turbulence in the early universe, which is characterised by the presence of a causal horizon and develops at extremely high Reynolds number, of the order of 10^{13} (c.f. the discussion at the end of section 3.4). Therefore, in our analysis we have chosen to follow the theoretical picture of ref. [35], which in addition leads to a conservative estimate of the production of GWs: in fact, MHD turbulence which decays slower would be active as a source of GWs for a longer time.

In the following we assume this model of free decay for the turbulence, but to this 'absolute' time behaviour we also add the exponential de-correlation proposed in [43], to express the time de-correlation of the velocity field on a given scale as time goes by. We take the characteristic de-correlation frequency on a given scale to be the eddy turnover time at that scale, and assume a Gaussian functional form to express the dependence of the power spectrum on time difference.

Another new point of our analysis is that the sources of GWs, turbulent kinetic energy and magnetic field, are continuous in time. The importance of having a continuous source and its consequences on the position of the peak of the GW spectrum have been analyzed in [14] for a short lasting source: the collision of bubbles. Here, we analyze also the long lasting, MHD turbulent source. In order to do so, we need to modify the Kolmogorov decay laws, and insert an initial phase in which the proper turbulent cascade has not yet begun: during this phase, we assume that the kinetic energy starts from zero and grows linearly in time, up to when stirring is over and the free decay of turbulence starts. The linear increase has been observed in MHD simulations [44], and is also satisfied in simulations of the bubble collision source (c.f. [13, 14]). We assume that the evolution law of the stirring scale L remains equal to the Kolmogorov decay law also during the initial phase.

Contrary to previous analyses, we also model the MHD turbulence spectrum using a formula which smoothly interpolates between the large scale behavior, determined by causality, and the small scale one, given by the MHD cascade (see also [24]). This model gives a more realistic estimate of the amplitude of the MHD spectrum at the peak, which in turns determines the final amplitude of the GW spectrum. With this improved MHD spectrum, the GW peak amplitude is more than one order of magnitude smaller than previous estimates.

The paper is organized as follows. In the next section we discuss a toy model for the source to illustrate the difference between a short-lasting and a long-lasting source of GWs. In section 3 we discuss the properties of the MHD turbulence, and we determine the anisotropic

JCAP12(2009)024

stress power spectrum from this source in section 4. We then define the time after which we may neglect the GW source and determine the final GW spectrum in section 5. We discuss our results in section 6 and conclude in section 7. A discussion of the fluid viscosity and some technicalities are given in appendices for completeness.

Notation: Unless otherwise stated, we use comoving variables: t denotes conformal time, the energy injection scale L, the Kolmogoroff microscale λ (the endpoint of the Kolmogoroff spectrum), and k are respectively comoving distances and wavenumber. The index $_*$ indicates the time of the phase transition, while the index $_0$ indicates today. We normalize the scale factor $a(t_0) = 1$. $\mathcal{H}$ denotes the conformal Hubble parameter, $H_0 = h_0 100\text{km/s/Mpc}$ is the Hubble parameter today, and the critical energy density is $\rho_c = \rho_c(t_0)$. The radiation energy density parameter today is $h_0^2\Omega_{\text{rad},0} = 4.2 \times 10^{-5}$. This value includes three types of neutrinos. As we shall see, this is the relevant quantity since neutrinos (with standard masses) are still relativistic at matter-radiation equality.

2 A stochastic gravitational wave background of cosmological origin

We consider a Friedmann universe with flat spatial sections. The tensor metric perturbations are defined by

$$ds^2 = a^2(t)[-dt^2 + (\delta_{ij} + 2h_{ij})dx^i dx^j]\,. \tag{2.1}$$

In this work we want to determine the GW energy density power spectrum given by (see e.g. [21])

$$\frac{d\Omega_{\text{GW}}}{d\log k} = \frac{k^3|\dot{h}|^2}{2(2\pi)^3 G\rho_c a^2} = \frac{k^5|h'|^2}{2(2\pi)^3 G\rho_c a^2}\,, \qquad \rho_c = \rho_c(t_0)\,, \tag{2.2}$$

where $\dot{} = \frac{d}{dt}$ and $' = \frac{d}{dx}$, $x = kt$, and the GW energy power spectrum is defined as

$$\langle \dot{h}_{ij}(\mathbf{k},t)\dot{h}^*_{ij}(\mathbf{q},t)\rangle = (2\pi)^3\delta(\mathbf{k}-\mathbf{q})|\dot{h}(k,t)|^2\,. \tag{2.3}$$

Here $\langle\cdots\rangle$ is an ensemble average over the stochastic process which generates the GWs. The Dirac delta function $\delta(\mathbf{k}-\mathbf{q})$ is a consequence of statistical homogeneity.

Once the source has decayed and the wavelength under consideration is inside the horizon, the GW energy density simply scales like a^{-4}. Hence the GW energy spectrum scaled to today becomes

$$\left.\frac{d\Omega_{\text{GW}}}{d\log k}\right|_0 = \left.\frac{d\Omega_{\text{GW}}}{d\log k}\right|_t a(t)^4 = \frac{k^5 a^2}{2(2\pi)^3 G\rho_c}|h'(x)|^2\,, \qquad x \gg 1. \tag{2.4}$$

To evaluate the GWs emitted by turbulent motion in the primordial fluid and by a magnetic field we need to determine the tensor-type anisotropic stresses of these sources. They source the evolution equation for the GW perturbations,

$$\ddot{h}_{ij} + 2\mathcal{H}\dot{h}_{ij} + k^2 h_{ij} = 8\pi G a^2 T_{ij}^{(TT)}(k,t)\,. \tag{2.5}$$

In this section we consider in all generality a relativistic source, and we solve the wave equation in two cases: a long lasting source (i.e. many Hubble times), and a short lasting one (i.e. significantly less than one Hubble time). We introduce the transverse traceless tensor part of the energy momentum tensor of the source as

$$T_{ij}^{(TT)}(k,t) = (\rho+p)\tilde{\Pi}_{ij}(k,t) \qquad \text{so that} \qquad 8\pi G a^2 T_{ij}^{(TT)}(k,t) = 4\mathcal{H}^2\tilde{\Pi}_{ij}(k,t)\,, \tag{2.6}$$

JCAP12(2009)024

where we denote the dimensionless energy momentum tensor with a tilde: $\tilde{\Pi}_{ij}(\mathbf{k},t) = (P_{il}P_{jm} - 1/2P_{ij}P_{lm})\tilde{T}_{lm}(\mathbf{k},t)$. The projection tensor $P_{il}P_{jm} - 1/2P_{ij}P_{lm}$, with $P_{ij} = \delta_{ij} - \hat{k}_i\hat{k}_j$, projects onto the transverse traceless part of the stress tensor. $\tilde{\Pi}$ includes any time dependence other than the basic radiation-like evolution. We assume that the source is active only during the radiation-dominated era, where $p = \rho/3$. During adiabatic expansion $g(Ta)^3 =$ constant so that

$$\rho(t) = \frac{\rho_{\rm rad,0}}{a^4(t)}\left(\frac{g_0}{g(t)}\right)^{1/3} \quad \text{and} \quad a(t) \approx H_0\,\Omega_{\rm rad,0}^{1/2}\left(\frac{g_0}{g(t)}\right)^{1/6} t \tag{2.7}$$

where $g(t)$ is the number of relativistic degrees of freedom at time t.

2.1 Long-lasting source

Let us first concentrate on the more general case of a long lasting source. To solve eq. (2.5) we set $\mathcal{H} = 1/t$, neglecting changes in the number of effective relativistic degrees of freedom. In terms of the dimensionless variable $x = kt$ eq. (2.5) then becomes

$$h_{ij}'' + 2\frac{h_{ij}'}{x} + h_{ij} = \frac{4}{x^2}\tilde{\Pi}_{ij}\,. \tag{2.8}$$

We consider a source that is active from time $t_{\rm in}$ to time $t_{\rm fin}$, which in the long lasting case can span a period of many Hubble times. For $t > t_{\rm fin}$, we match the solution of the above equation to the homogeneous solution, $\tilde{\Pi}_{ij} = 0$. Assuming further that we are only interested in modes well inside the horizon today, $x \gg 1$, the resulting GW energy power spectrum becomes

$$\left|h'(k, x > x_{\rm fin})\right|^2 = \frac{8}{x^2}\int_{x_{\rm in}}^{x_{\rm fin}}\frac{dx_1}{x_1}\int_{x_{\rm in}}^{x_{\rm fin}}\frac{dx_2}{x_2}\cos(x_2 - x_1)\tilde{\Pi}(k, x_1, x_2) \qquad x \gg 1\,, \tag{2.9}$$

$x_1 = kt_1$, $x_2 = kt_2$, and $\tilde{\Pi}(k, x_1, x_2)$ denotes the unequal time correlator of the source,

$$\langle\tilde{\Pi}_{ij}(\mathbf{k}, t_1)\tilde{\Pi}_{ij}^*(\mathbf{q}, t_2)\rangle = (2\pi)^3\delta(\mathbf{k} - \mathbf{q})\tilde{\Pi}(k, kt_1, kt_2)\,. \tag{2.10}$$

With eq. (2.4), the power spectrum of the GW energy density parameter for a long-lasting source which is active between $t_{\rm in}$ and $t_{\rm fin}$ in the radiation era is then given by

$$\left.\frac{d\Omega_{\rm GW}}{d\log k}\right|_0 = \frac{4\,\Omega_{\rm rad,0}}{3\pi^2}\left(\frac{g_0}{g_{\rm fin}}\right)^{1/3} k^3\int_{x_{\rm in}}^{x_{\rm fin}}\frac{dx_1}{x_1}\int_{x_{\rm in}}^{x_{\rm fin}}\frac{dx_2}{x_2}\cos(x_2 - x_1)\tilde{\Pi}(k, x_1, x_2)\,. \tag{2.11}$$

This result is completely general for modes well inside the horizon today; it reduces the computation of the GW spectrum to the determination of the unequal-time correlator of the tensor-type anisotropic stress, $\tilde{\Pi}(k, x_1, x_2)$.

2.2 Short-lasting source

If the source is active for a short interval of time, essentially only during the phase transition, one can neglect the expansion of the universe during the time of action of the source, and match the solution so obtained with the one of the homogeneous equation in which expansion is taken into account. For this kind of source, we set $t_{\rm fin} = t_{\rm in} + \Delta t$, with $\Delta t/t_{\rm in} \ll 1$. Solving

JCAP12(2009)024

the wave equation (2.5) without expansion term, amounts to neglect the time-dependence of the factors $1/x_1$ and $1/x_2$ in eq. (2.9) or (2.11) during the active period, so that

$$\left|h'(k, x > x_{\rm fin})\right|^2 = \frac{8}{x_{\rm in}^2\, x^2} \int_{x_{\rm in}}^{x_{\rm fin}} dx_1 \int_{x_{\rm in}}^{x_{\rm fin}} dx_2 \cos(x_2 - x_1) \tilde{\Pi}(k, x_1, x_2)\,. \tag{2.12}$$

Also this solutions applies for modes inside the horizon today. The energy spectrum now becomes

$$\left.\frac{d\Omega_{\rm GW}}{d\log k}\right|_0 = \frac{4\ \Omega_{\rm rad,0}}{3\pi^2} \left(\frac{g_0}{g_{\rm fin}}\right)^{1/3} \mathcal{H}_{\rm in}^2\, k \int_{x_{\rm in}}^{x_{\rm fin}} dx_1 \int_{x_{\rm in}}^{x_{\rm fin}} dx_2 \cos(x_2 - x_1) \tilde{\Pi}(k, x_1, x_2)\,. \tag{2.13}$$

Obviously, the general long-lasting case reduces to this result if $(t_{\rm fin} - t_{\rm in})/t_{\rm in} \ll 1$. Summarizing:

$$\left.\frac{d\Omega_{\rm GW} h_0^2}{d\log k}\right|_0 = \mathcal{A} \begin{cases} \left(\frac{g_0}{g_{\rm fin}}\right)^{\frac{1}{3}}\ k^3 \int_{x_{\rm in}}^{x_{\rm fin}} \frac{dx_1}{x_1} \int_{x_{\rm in}}^{x_{\rm fin}} \frac{dx_2}{x_2}\ \cos(x_2 - x_1)\, \tilde{\Pi}(k, x_1, x_2) \\ \qquad\qquad\qquad\qquad \text{long-lasting source (e.g. MHD turbulence)} \\ \left(\frac{g_0}{g_*}\right)^{\frac{1}{3}} \mathcal{H}_{\rm in}^2\, k \int_{x_{\rm in}}^{x_{\rm fin}} dx_1 \int_{x_{\rm in}}^{x_{\rm fin}} dx_2\ \cos(x_2 - x_1)\, \tilde{\Pi}(k, x_1, x_2) \\ \qquad\qquad\qquad\qquad \text{short-lasting source (e.g. bubble collisions)} \end{cases} \tag{2.14}$$

with $x_1 = kt_1$, $x_2 = kt_2$, $x_{\rm in} = kt_{\rm in}$, $x_{\rm fin} = kt_{\rm fin}$ and $\mathcal{A} = \frac{4}{3\pi^2}\Omega_{\rm rad,0} h_0^2$.

2.3 Solutions for a simple source

In this section we analyze the difference between the GW spectrum generated by a short lasting and a long lasting source in a simple example which can be treated analytically. We find analytical solutions for the GW energy density spectrum (2.14). The general behaviour of the solutions in this simple case is illuminating, as it is similar to the case of the evolving source that we will treat in the rest of the paper (MHD turbulence).

We consider a tensor source $\tilde{\Pi}$ with an equal time power spectrum which depends on time solely via a function modeling the turning on and off of the source: $\tilde{\Pi}(k, t, t) \equiv \tilde{\Pi}(k) f^2(t)$. For the equal time power spectrum of the tensor source, we take a form which is motivated by turbulence and magnetic fields, see section 4:

$$\tilde{\Pi}(K, t, t) = \left(\frac{\Omega_S}{\Omega_{\rm rad}}\right)^2 L^3 \mathcal{S}(K) f^2(t)\,, \tag{2.15}$$

where Ω_S denotes the (radiation like) energy density of the source normalised to the critical energy density today (so that the ratio $\Omega_S/\Omega_{\rm rad}$ is time-independent), $K = Lk/2\pi$ is a dimensionless wavenumber, L is a characteristic scale of the problem, and $\mathcal{S}(K)$ models the scale dependence of the source. The continuous function $f(t)$ vanishes at both, $t_{\rm in}$ and $t_{\rm fin}$ and describes the switching on and off of the source. The source is active during the time interval $t_{\rm fin} - t_{\rm in}$, which can be long or short compared to the initial Hubble time, $\mathcal{H}_{\rm in}^{-1} = t_{\rm in}$.

As shown in ref. [14], the time continuity in switching the source on and off can be relevant for the GW spectrum. Inspired by results from numerical simulations of bubble nucleation during a first order phase transition [10, 13], we choose the function $f(t)$ to be

JCAP12(2009)024

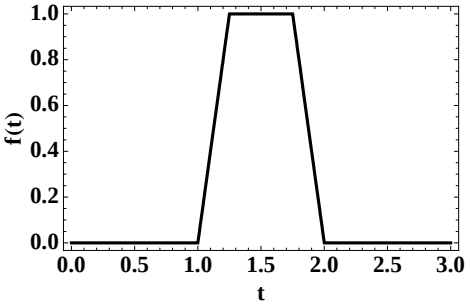

Figure 1. The function modeling the time dependence of the source used in section 2.3, eq. (2.16).

continuous but not differentiable at the initial and final times. The effect of this choice on GW spectra for short duration sources is discussed in ref. [14]. Here we shall also study its effect on sources of long duration. We set (see figure 1)

$$f(t) = \begin{cases} 0 & \text{if } t \leq t_{\rm in} \\ \frac{2(t-t_{\rm in})}{\Delta t} & \text{if } t_{\rm in} \leq t \leq t_{\rm in} + \Delta t/2 \\ 1 & \text{if } t_{\rm in} + \Delta t/2 \leq t \leq t_{\rm fin} - \Delta t/2 \\ \frac{2(t_{\rm fin}-t)}{\Delta t} & \text{if } t_{\rm fin} - \Delta t/2 \\ 0 & \text{if } t \geq t_{\rm fin}\,. \end{cases} \tag{2.16}$$

For a short lasting source, Δt is also the duration of the source (c.f. section 2.2 and ref. [12]), while a long lasting source is typically active for a much longer period of time, and Δt is the characteristic time of turning on and off. As we show below, the effect of introducing time continuity on the resulting GW spectrum is relevant only in the 'coherent' case (see figure 3). In this case, the power at small scales is less than for a discontinuous source.

To compute the solution according to eq. (2.14), we need the source power spectrum at unequal times $\tilde{\Pi}(k, t_1, t_2)$. In this section, we consider two different possibilities for the unequal time correlators, the incoherent and the totally coherent approximations, which we discussed also in the case of GWs generated by bubble collisions [12]. In section 3 we will compare these approximations with the 'top hat' ansatz [12], which turns out to be more realistic for the case of MHD turbulence.

- **Incoherent approximation**: the source is correlated only for $t_1 \simeq t_2$

$$\tilde{\Pi}(K, t_1, t_2) = \tilde{\Pi}(K, t_1, t_1)\delta(t_1 - t_2)\Delta t\, f^2(t_1)\,. \tag{2.17}$$

  Here Δt plays also the role of a very short characteristic time, over which the source remains 'coherent'. With this ansatz the time integration in (2.14) is simple, and we obtain the following result for the GW energy spectrum:

$$\left.\frac{d\Omega_{\rm GW}h_0^2}{d\log k}\right|_0 = \frac{4\Omega_{\rm rad,0}h_0^2}{3\pi^2}\left(\frac{\Omega_S}{\Omega_{\rm rad}}\right)^2 K^3\mathcal{S}(K)F(t_{\rm in}, t_{\rm fin}, \Delta t) \tag{2.18}$$

  where

$$F(t_{\rm in}, t_{\rm fin}, \Delta t) \simeq \begin{cases} \left(\frac{g_0}{g_{\rm fin}}\right)^{\frac{1}{3}} \frac{\Delta t}{t_{\rm in}} & \text{long-lasting,} \\ \left(\frac{g_0}{g_*}\right)^{\frac{1}{3}} \frac{(2\pi)^2}{3} \left(\frac{\Delta t}{t_{\rm in}}\right)^2 & \text{short-lasting.} \end{cases} \tag{2.19}$$

The result for the long-lasting case is expanded using $\Delta t \ll t_{\rm in}, t_{\rm fin}$. The full expression is given in appendix A, where we collect all analytical expressions for the convenience of the reader, see eq. (A.1).

In the incoherent approximation, the function $F(t_{\rm in}, t_{\rm fin}, \Delta t)$ resulting from the convolution of the Green function with the source, eq. (2.14), does not depend on wave-number. The GW power spectrum is therefore simply the one of the source $S(K)$, multiplied by the phase-space volume K^3, both for long lasting and for short lasting sources. The peak of the GW spectrum then coincides with the one of the source spectrum. The time integration results in the ratio between the brief coherence time Δt and the initial horizon time $t_{\rm in}$. In the long lasting case, this factor might be close to one while in the short lasting case it is always much smaller. In addition, the GW amplitude of the short lasting case is suppressed by one more factor $\Delta t/t_{\rm in}$ with respect to the long lasting one.

- **Coherent approximation**: the source is perfectly correlated at all times t_1 and t_2

$$\Pi(K, t_1, t_2) = \sqrt{\Pi(K, t_1, t_1)}\sqrt{\Pi(K, t_2, t_2)}\,. \tag{2.20}$$

In this case as well, the time integration in eq. (2.14) can be performed explicitely, and we obtain the GW energy density power spectrum (we remind that $x_{\rm in} = kt_{\rm in}$, $x_{\rm fin} = kt_{\rm fin}$, and $\Delta x = x_{\rm fin} - x_{\rm in}$)

$$\left.\frac{d\Omega_{\rm GW}h_0^2}{d\log k}\right|_0 = \frac{4\Omega_{\rm rad,0}h_0^2}{3\pi^2}\left(\frac{\Omega_S}{\Omega_{\rm rad}}\right)^2 K^3\mathcal{S}(K)F(x_{\rm in}, x_{\rm fin}, \Delta x) \tag{2.21}$$

where

$$F(x_{\rm in}, x_{\rm fin}, \Delta x) \simeq \begin{cases} \left(\frac{g_0}{g_{\rm fin}}\right)^{\frac{1}{3}}\left[\left(\mathrm{Ci}(x_{\rm fin})-\mathrm{Ci}(x_{\rm in})\right)^2+\left(\mathrm{Si}(x_{\rm fin})-\mathrm{Si}(x_{\rm in})\right)^2\right] & \text{long-lasting} \\ \left(\frac{g_0}{g_*}\right)^{\frac{1}{3}}\frac{64(2\pi)^2}{x_{\rm in}^2}\frac{\sin^4((x_{\rm fin}-x_{\rm in})/4)}{(x_{\rm fin}-x_{\rm in})^2} & \text{short-lasting.} \end{cases} \tag{2.22}$$

In the long lasting case we have again expanded to lowest order in $\Delta x/x_{\rm in}$ and $\Delta x/x_{\rm fin}$. Ci and Si denote the integral cosine and sine functions [45]. The full expression is given in appendix A.

Contrary to the incoherent case, here the function $F(x_{\rm in}, x_{\rm fin}, \Delta x)$ depends on wave-number, and the resulting GW spectrum is therefore modified with respect to the one of the source. We plot $F(x_{\rm in}, x_{\rm fin}, \Delta x)$ in figure 2. In both the long and short lasting case, $F(x_{\rm in}, x_{\rm fin}, \Delta x)$ tends to a k-independent value for wave-numbers such that $x_{\rm in} \ll 1$. The constant is $\log^2(x_{\rm fin}/x_{\rm in})$ in the long lasting case, and $\pi^2(\Delta x/x_{\rm in})^2$ in the short lasting one. In the short lasting case F remains constant up to $\Delta x \simeq 1$ where it starts oscillating and decaying like $1/(x_{\rm in}\Delta x)^2$. The long lasting case instead depends also on $x_{\rm fin}$: when $x_{\rm fin}$ becomes larger than one, the slope changes from the constant to a mild logarithmic dependence on k as $\log^2 x_{\rm in}$. Then for $x_{\rm in} \geq 1$ we have a decay like $1/x_{\rm in}^2$, up to $\Delta x \gtrsim 1$ where F also starts oscillating and decaying, with a smaller amplitude than the short lasting case, see figure 2. Hence, wavelengths which are larger than the typical switching on time are amplified by an additional factor $\min\{(\Delta x)^{-2}, (x_{\rm in}/\Delta x)^2\}$ in the long lasting case. On the other hand, wavelengths smaller than the the typical switching on time are suppressed in the long lasting case due to the presence of interferences suppressing the signal.

JCAP12(2009)024

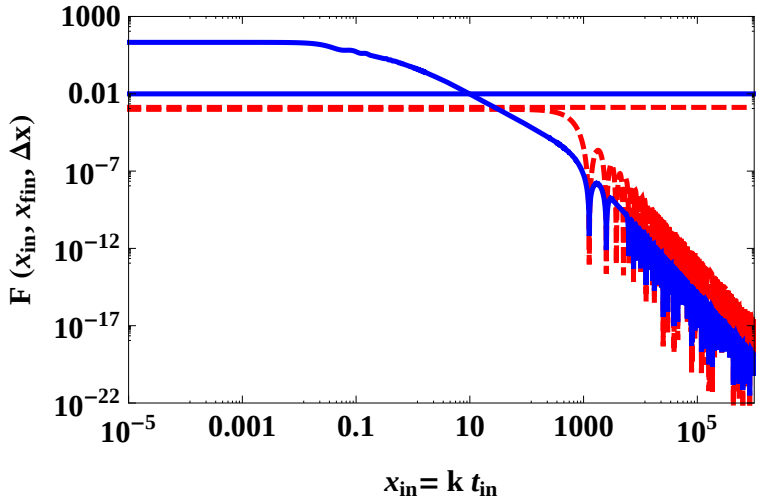

Figure 2. Comparison between a short and long-lasting source. We plot the function $F(x_{\rm in}, x_{\rm fin}, \Delta x)$ defined in eq. (2.19) (incoherent case) and eq. (2.22) (coherent case) as a function of $x_{\rm in} = kt_{\rm in}$. Blue, solid: long lasting coherent and incoherent cases with $t_{\rm fin}/t_{\rm in} = 100$ and $\Delta t = 0.01\, t_{\rm in}$. Red, dashed: short lasting coherent and incoherent cases with $t_{\rm fin}/t_{\rm in} = 1.01$, $\Delta t = 0.01\, t_{\rm in}$. The horizontal lines correspond to the incoherent case.

The functions $F(x_{\rm in}, x_{\rm fin}, \Delta x)$ for both the short and long lasting incoherent and coherent cases are shown in figure 2. The GW amplitude in the short lasting case is suppressed for low and intermediate values of k with respect to the long lasting one, both in the incoherent and in the coherent cases. However, while in the incoherent case this suppression is maintained for all k, in the coherent one interferences suppress the amplitude of the long lasting case for frequencies larger than the typical switching on frequency $\Delta x \gtrsim 1$.

Figure 3 shows the effect of introducing continuity in the process of turning on and off a long lasting source. The conclusions drawn in the analysis of ref. [14] are not modified by the long duration of the source. The incoherent spectrum is the same for a continuous and a discontinuous source, while in the coherent case there is a difference for frequencies higher than $k \gtrsim 1/\Delta t$ corresponding to the characteristic time-scale of the source. In the continuous case the slope changes, becoming steeper by a factor k^{-1} if the turning on process has a kink: $f(t)$ is continuous but not differentiable. In the discontinuous case, on the other hand, the change of slope is absent.

Summarizing, two general features can be deduced from this analysis. First, the GW energy spectrum at large scales is proportional to the phase space volume K^3 times the source power spectrum $\mathcal{S}(K)$. In the incoherent case no other wavenumber-dependence intervenes; in the coherent case, instead, the wavenumber at which this behaviour changes depends on the duration of the source, whether it is short or long lasting. Second, the GW amplitude in the short lasting case is smaller than the one in the long lasting case. In the incoherent case, this is always true; in the coherent case, this suppression can be very significant on large scales, however, it turns into an amplification for scales smaller than Δt. On super-horizon scales, the difference in the amplitude between the short lasting and long lasting sources is typically of the order of $\Delta t/t_{\rm in}$ in the incoherent case and $(\Delta t/t_{\rm in})^2$ in the coherent one.

Examples of well-motivated long-lasting sources are turbulent fluid flows initiated by

JCAP12(2009)024

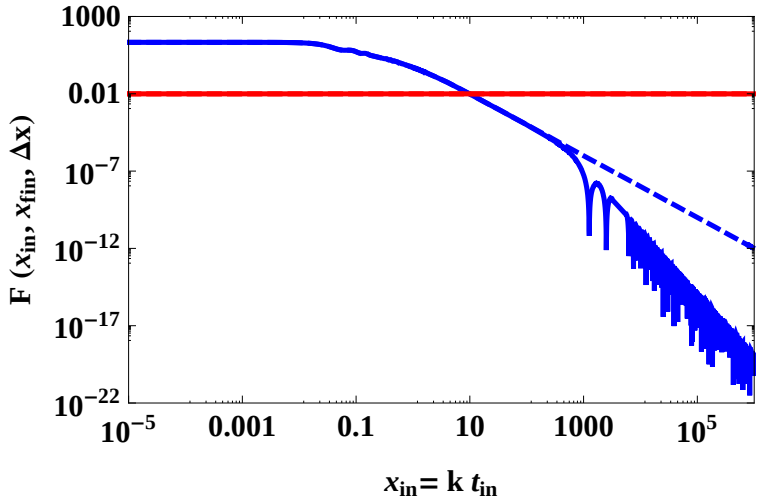

Figure 3. For a long-lasting source, comparison between the continuous (solid) and discontinuous (dashed) cases. We plot the function $F(x_{\rm in}, x_{\rm fin}, \Delta x)$ as a function of $x_{\rm in} = kt_{\rm in}$. The incoherent case is not affected by continuity as shown by the red horizontal line (the solid and dashed lines are superimposed). In the coherent case shown in blue, the slope changes in the continuous case for frequencies $k > \Delta t^{-1}$. The values of the parameters are the same as in figure 2.

instabilities generated by bubble collisions. In the following, we concentrate on this particular source. We also study the case of magnetic fields, which represent another long-lasting source of GW typically expected from first order phase transitions [29].

3 Turbulent magneto-hydrodynamics as a source of gravitational waves

3.1 General considerations

Turbulence develops if a fluid with sufficiently high Reynolds number is perturbed. If the fluid is stirred on a characteristic scale L_p (the subscript indicates that we use the physical length, not comoving length here), the Reynolds number of the flow is defined by

$$\mathrm{Re}\,(L_p) = \frac{v_L\, L_p}{\nu} \tag{3.1}$$

where v_L is the characteristic velocity on the energy injection scale L_p, and ν is the kinetic viscosity of the fluid. If $\mathrm{Re}\,(L_p) \gg 1$, the stirring develops turbulent motions. In a first order phase transition, the source of stirring is bubble collision. Therefore, the characteristic scale of the stirring is given initially by the typical bubble size towards the end of the phase transition, $L_* \sim 2v_b\beta^{-1}$ where v_b is the bubble wall velocity and β^{-1} the (comoving) duration of the phase transition (see for instance section 4 of [12] for a detailed definition). The initial energy injection scale L_* is the scale at which the largest turbulent eddies develop, and corresponds to the peak of the turbulent velocity power spectrum.

The dynamics of bubble growth at late times, towards the end of the phase transition, allows us to determine the order of magnitude of the kinetic energy involved in the turbulent flow. The bubble wall can be treated as a discontinuity, i.e. a combustion front across which energy and momentum are conserved [46]. At the front, the velocity of the fluid in the

JCAP12(2009)024

rest frame of the bubble center is given by $v_f = (v_1 - v_2)/(1 - v_1 v_2)$, where v_1 and v_2 are respectively the incoming and outgoing speed of the fluid in the rest frame of the front (see e.g. ref. [12] for more details). We assume that the typical value of the turbulent fluid velocity is given by v_f. Therefore, the kinetic energy of the turbulent flow is

$$\rho_{\rm kin} = (\rho + p)\frac{\langle v^2 \rangle}{2} \qquad \text{with} \quad \langle v^2 \rangle \sim v_f^2 \,. \tag{3.2}$$

Even though the velocities involved are large in the case of interest, we are using the formalism of non-relativistic MHD turbulence. Since the corresponding values of γ are typically of order one, we expect that the error introduced is within the uncertainty of our calculation. Furthermore, while the validity of the theory of non-relativistic turbulence may be questionable if high speeds are involved [47], it was shown in [48–50] that the Kolmogorov spectrum is recovered even in the relativistic case.[1] Still, we impose for the fluid velocity $\langle v^2 \rangle \leq c_s^2$, where $c_s = 1/\sqrt{3}$ is the sound speed in the relativistic fluid. The fluid velocity v_f is completely specified once v_b is known and the ratio $\alpha = \rho_{\rm vac}/\rho_{{\rm rad},*}$ is fixed: solving for the hydrodynamical equation allows one to relate the fluid velocity to the bubble wall velocity (see for instance [54] for more details). If the phase transition proceeds as a detonation (deflagration), then $v_1 \equiv v_b$ ($v_2 \equiv v_b$). For this paper, we choose the fluid velocity $v_f = c_s$ corresponding to $\alpha = 1/3$ and either $v_b \simeq 0.87$ (detonation) or $v_b \simeq c_s$ (deflagration) (for $\alpha > 1/3$ there is no deflagration solution). When we need to specify v_b, in the figures and the numerical values, we always consider the detonation case $v_b = 0.87$. It is straight forward to re-scale the results to lower bubble and fluid velocities.

If the fluid is stirred on the scale L_*, turbulent motions develop within a time interval of the order of the eddy turnover time τ_L. This is the characteristic time for the cascade to set in. Given the typical value of the turbulent fluid velocity v_f, the eddy turnover time on the stirring scale L_* is defined simply as $\tau_L \sim L_*/(2v_f)$. Since the fluid velocity is always smaller than the bubble wall velocity $v_f \leq v_b$, the eddy turnover time is always larger than the duration of the phase transition: $\tau_L \geq \beta^{-1}$. In the following we identify the time interval Δt given in section 2.3 as $\Delta t = \tau_L$. For short-lasting turbulence, this means that the source lasts for only one eddy turnover time. In the long-lasting case (which is the relevant one as we will see), this means that turbulence is 'turned on' in one eddy turnover time τ_L.

In the cosmological context the fluid is ionized and has not only a very high kinetic Reynolds number (which we evaluate in section 3.5) but also a very high magnetic Reynolds number $\mathrm{R_m}$, defined by (see appendix B)

$$\mathrm{R_m}(L_p) = \frac{L_p v_L}{\mu} \,, \qquad \text{where} \qquad \mu = \frac{1}{4\pi\sigma} \tag{3.3}$$

is the magnetic diffusivity and σ denotes the conductivity. High values of the magnetic Reynolds number require an MHD treatment of the cosmic plasma. Moreover, the magnetic Prandl number

$$\mathrm{P_m} \equiv \frac{\mathrm{R_m}(L)}{\mathrm{Re}\,(L)} = \frac{\nu}{\mu} \tag{3.4}$$

is much larger than unity, as we calculate in appendix B. Therefore, the characteristics of the plasma in the early universe entail the formation of MHD turbulence. The seed magnetic

[1] It is remarkable that recent simulations of quark gluon plasma instabilities in the process of thermalization in heavy ion collisions show similarities with a Kolmogorov scaling [51–53].

JCAP12(2009)024

field can be generated by several mechanisms [29], and is then amplified by the currents due to the turbulent flow of charged particles [31, 55]. The magnetic field itself is also a source of GWs. In the following we make the simplifying but reasonable assumption of equipartition: the total kinetic energy in the turbulent motion is equal to the magnetic field energy. Note however, that this assumption need not hold for each wave number k, so that we can allow for different spectra for the magnetic field energy and the turbulent kinetic energy at small scales.

In the remainder of this section we present our model for the power spectra of turbulence and magnetic fields, as well as their time evolution. We evaluate the Reynold number in the early universe and describe how it evolves with time, which will help us to determine when MHD turbulence is expected to end.

3.2 The turbulent velocity power spectrum

The power spectrum of the turbulent velocity field at equal times is of the form[2]

$$\langle v_i(\mathbf{k},t) v_j^*(\mathbf{q},t)\rangle = (2\pi)^3 \delta(\mathbf{k}-\mathbf{q})\, P_{ij}\, P_v(k,t)\,, \tag{3.5}$$

where the projector $P_{ij} = \delta_{ij} - \hat{k}_i \hat{k}_j$ comes from the fact that the turbulent velocity field $\mathbf{v}(\mathbf{x},t)$ is divergence free. An ansatz for the unequal time correlator will be given in section 3.6. In previous works, the turbulent velocity power spectrum $P_v(k,t)$ was either assumed to be given only by the inertial range $k^{-11/3}$ [15, 16, 18, 20], or naively determined by intersecting the k^2 behaviour at very small scales with the inertial range $k^{-11/3}$ behaviour [17]. Both approaches overestimate the peak amplitude of the turbulent source and thus overestimate the GW amplitude. In the present study, we use a more realistic, smooth function to describe the spectrum, proposed by Von Kármán [56] (see also page 244 of [57]). It is given by the following interpolating formula (here in terms of comoving quantities):

$$P_v(K) = \mathcal{C}_v \langle v^2\rangle\, L^3\, \frac{K^2}{(1+K^2)^{17/6}} \times \begin{cases} 1 \text{ for } 0 \le K \le \frac{L}{\lambda} \\ 0 \text{ for } K \ge \frac{L}{\lambda}\,, \end{cases} \tag{3.6}$$

where we again use the dimensionless variable

$$K = kL/2\pi \tag{3.7}$$

and λ denotes the Kolmogorov microscale, beyond which turbulent motions are absent and we set the spectrum to zero. The kinetic energy of the turbulent flow is given in eq. (3.2): using this definition, we rewrite $\langle v^2\rangle$ in terms of the ratio of the total kinetic energy to the radiation energy density,

$$\langle v^2\rangle = \frac{3}{2}\frac{\Omega_T}{\Omega_{\rm rad}}\,. \tag{3.8}$$

In our numerical estimates, we will use $\langle v^2\rangle = 1/3$, thus corresponding to $\Omega_T/\Omega_{\rm rad} = 2/9$. In equation (3.6), the constant $\mathcal{C}_v = \frac{55}{108\pi^{3/2}}\frac{\Gamma(5/6)}{\Gamma(1/3)} \approx 0.0385$ comes from the normalization of the kinetic energy spectrum, $E(k) = k^2 P_v(k)/(2\pi^2)$,

$$\frac{\rho_{\rm kin}}{\rho+p} = \frac{\langle v^2\rangle}{2} = \frac{3}{4}\frac{\Omega_T}{\Omega_{\rm rad}} = \int_0^\infty dk E(k) = \frac{1}{2\pi^2}\int_0^\infty dk\, k^2 P_v(k)\,. \tag{3.9}$$

[2] In this paper we neglect the presence of a helical component in the velocity and magnetic field power spectra (c.f. eq. (3.15)). Non-zero helicity, possibly arising from a macroscopic parity violation in the early universe, affects the decay of MHD turbulence, as demonstrated for example in [37], and the subsequent generation of GWs. For GW production by primordial helical MHD turbulence we refer to the analysis of refs. [20, 24].

JCAP12(2009)024

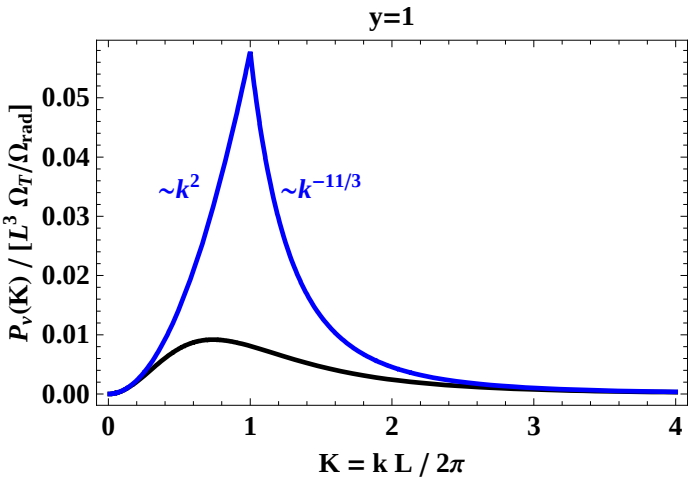

Figure 4. Comparison between the turbulent velocity power spectrum obtained by intersecting the k^2 behaviour at small scale with the inertial range $k^{-11/3}$ behaviour (blue), as done in the literature, with the Von Kármán spectrum (black).

Expression (3.6) smoothly interpolates between the large scale, K^2 behaviour, and the inertial range $K^{-11/3}$, which is reached for $K \gtrsim 3$. The peak is at $K_{\rm peak} = \sqrt{6/11} \sim 0.74$, which corresponds roughly to the energy injection scale at $K = kL/2\pi = 1$. The peak amplitude is smaller by a factor ~ 6 compared to the amplitude obtained when naively extrapolating the $k^{-11/3}$ behaviour down to the energy injection scale $K = 1$, as shown in figure 4. This is an important point when we compare the amplitude of the GW signal with previous estimates in the literature. Note that expression (3.6) is analytic for $k \to 0$, which is required for causally generated, incompressible turbulence in the cosmological context [17].

In the inertial range, the characteristic velocity on a given scale $2\pi/k$ is approximately given by [30]

$$v_k^2 \sim kE(k) \simeq 6\pi \mathcal{C}_v \frac{\Omega_T}{\Omega_{\rm rad}} K^{-2/3} \qquad \text{for } K \gtrsim 3\,. \tag{3.10}$$

Thus, the characteristic velocity on the energy injection scale, which is related to the total kinetic energy in the turbulence, is:

$$v_L^2 \simeq 6\pi \mathcal{C}_v \frac{\Omega_T}{\Omega_{\rm rad}} = 4\pi \mathcal{C}_v \langle v^2 \rangle\,. \tag{3.11}$$

3.3 The magnetic field power spectrum

The power spectrum of the MHD processed magnetic field is closely related to the one of the turbulent velocity field. Here we treat the two sources exactly on the same footing. Since the energy density of a cosmological magnetic field scales like radiation, we can use eq. (2.14) to evaluate the GW spectrum sourced by the magnetic field, provided that we define the normalized magnetic field vector

$$b_i = \sqrt{\frac{3}{16\pi\rho_{\rm rad}}} B_i\,, \tag{3.12}$$

JCAP12(2009)024

so that the transverse traceless (TT) part of the magnetic field energy momentum tensor is

$$\left[T_{ij}^{B}(\mathbf{x},t)\right]^{(TT)} = \left[\frac{B_i(\mathbf{x},t)B_j(\mathbf{x},t)}{4\pi}\right]^{(TT)} = \frac{4}{3}\rho_{\rm rad}(t)\left[b_i(\mathbf{x},t)b_j(\mathbf{x},t)\right]^{(TT)} = (\rho+p)\tilde{\Pi}_{ij}^{B}(\mathbf{x},t)\,. \tag{3.13}$$

The normalized magnetic field b_i is equivalent to the dimensionless turbulent velocity field v_i. We define a parameter analogous to eq. (3.8), given by the ratio of the magnetic field energy density to the radiation energy density

$$\langle b^2\rangle = \frac{3}{2}\frac{\Omega_B}{\Omega_{\rm rad}} = 2\frac{\rho_B}{\rho+p}\,, \qquad \text{with} \qquad \rho_B = \frac{\langle B^2\rangle}{8\pi}\,. \tag{3.14}$$

In the following we assume equipartition between the magnetic and turbulent energy densities at the time when the latent heat is released, therefore $\langle v^2\rangle \simeq \langle b^2\rangle$ (however, the scaling of the GW spectra with the source energy density is kept explicit). The slope of the high frequency tail of the magnetic power spectrum in fully developed MHD turbulence is not precisely known: it could be of the Kolmogorov type, or it could satisfy the Iroshnikov-Kraichnan [58] or Goldreich-Sridhar [59] spectral slopes. While in the presence of a strong background magnetic field, the spectrum of the field perpendicular to the background field is of the Iroshnikov-Kraichnan type according to refs. [60–62], in the isotropic case, the relevant one in cosmology, the simulations of ref. [61] indicate a Kolmogorov-type slope. However, to diversify the treatment of the magnetic source from the turbulent one, we choose to consider the Iroshnikov-Kraichnan spectrum; the GW spectrum resulting from a Kolmogorov magnetic field is not very different and it can be readily derived from the turbulent one.

The low frequency tail of the spectrum is determined by causality and by the fact that $\mathbf{B}$ is divergence free. Like for turbulence, we use the interpolating formula from ref. [56] to find the equal time magnetic power spectrum

$$\langle b_i(\mathbf{k},t)b_j^*(\mathbf{q},t)\rangle = (2\pi)^3\delta(\mathbf{k}-\mathbf{q})\,P_{ij}\,P_b(k,t)\,, \tag{3.15}$$

$$P_b(k,t) = \frac{3}{2}\,\mathcal{C}_b\,\frac{\Omega_B}{\Omega_{\rm rad}}\,L^3\,\frac{K^2}{(1+K^2)^{11/4}} \times \begin{cases} 1 \text{ for } 0 \le K \le \frac{L}{\lambda} \\ 0 \text{ for } K \ge \frac{L}{\lambda}\,. \end{cases} \tag{3.16}$$

The normalization constant $\mathcal{C}_b = \frac{7}{16\pi^{3/2}}\frac{\Gamma(3/4)}{\Gamma(1/4)} \approx 0.0265$ is calculated in the same way as in eq. (3.9). The magnetic field and the turbulent flow being generated by the same physical process, namely bubble nucleation and collision, we assume that they share the same correlation scale L and Kolmogorov microscale λ.

3.4 Freely decaying turbulence

The turbulence stirring time is given by the duration of the phase transition which is typically much shorter than one Hubble time. Calling $t_{\rm in}$ the time at which the phase transition starts, one has $\beta^{-1} \ll \mathcal{H}_{\rm in}^{-1}$. As discussed in section 3.1, the typical time interval over which turbulence is established is the eddy turnover time τ_L. Moreover, Kolmogorov turbulence can be generated only if $\tau_L \le \mathcal{H}_{\rm in}^{-1}$. This condition translates into a lower bound for the turbulent fluid velocity, in terms of the phase transition parameters:

$$v_f \gtrsim (\mathcal{H}_{\rm in}/\beta)v_b\,. \tag{3.17}$$

If $\tau_L \le \mathcal{H}_{\rm in}^{-1}$, turbulence sets in after a short interval of time $\Delta t \equiv \tau_L \le t_{\rm in}$. After the completion of the phase transition (once bubbles have percolated), the stirring is over and

JCAP12(2009)024

the turbulence enters the free decay regime, i.e. the total kinetic energy is dissipated (see for example [30]). The physical quantities appearing in the turbulent (3.6) and magnetic (3.16) spectra are comoving, but they also have an additional 'absolute' time dependence due to the evolution of the turbulent cascade and the decay of the total energy. As already mentioned in the introduction, the existence of a maximal correlation length in the universe (the horizon) and the consequent Batchelor spectrum (i.e. k^2 at large scales), imply that $(\Omega_T/\Omega_{\rm rad})L^5$ is constant in time [17, 41, 42]. According to this, we assume the following laws for the growth of the correlation scale and the decay of the kinetic energy:

$$L(t) = L_* \left(\frac{t-t_{\rm in}}{\tau_L}\right)^{\gamma}, \qquad \gamma > 0 \tag{3.18}$$

$$\frac{\Omega_T}{\Omega_{\rm rad}}(t) = \frac{\Omega_{T*}}{\Omega_{\rm rad*}} \begin{cases} \frac{t-t_{\rm in}}{\tau_L}, & t_{\rm in} \le t \le t_{\rm in}+\tau_L\,, \\ \left(\frac{\tau_L}{t-t_{\rm in}}\right)^{5\gamma}, & t \ge t_{\rm in}+\tau_L\,. \end{cases} \tag{3.19}$$

When the phase transition starts, at $t_{\rm in}$, both the correlation length and the kinetic energy vanish. This insures that the source is continuous in time. At a time $t_* = t_{\rm in} + \tau_L$, after the completion of the phase transition, turbulence is fully developed. The stirring scale is given by L_*, and $\frac{\Omega_{T*}}{\Omega_{\rm rad*}}$ is the total kinetic energy in the turbulent fluid, normalized to the radiation energy at time t_*. We assume that the energy cascade responsible for the Kolmogorov spectrum starts at this stage. At times $t \ge t_* = t_{\rm in} + \tau_L$ turbulence enters the free decay phase, and the correlation scale and the kinetic energy evolve following the condition $(\Omega_T/\Omega_{\rm rad})L^5$ =constant.

The simple linear interpolation between these two behaviors given in (3.19) has been introduced to mimic the turning on of the source in the bubble collision case, inferred from numerical simulations, see [13]. The linear increase of the magnetic energy density in MHD turbulence has also been observed in simulations [44]. After this initial phase, for Kolmogorov turbulence which we shall adopt here, the energy decay law infers the value $\gamma = 2/7$ (see e.g. [30] and the introduction). For generality, we keep γ unspecified in the analytical formulae. When numerical results are presented, we substitute the value $\gamma = 2/7$.

In order to show explicitly its time evolution, we re-express the velocity power spectrum eq. (3.6) in terms of the time-independent variable $K_* = kL_*/2\pi$. Introducing the dimensionless time variable

$$y = \frac{t-t_{\rm in}}{\tau_L}\,,$$

consequently $L(t) = L_*\, y^{\gamma}$, and using $K = K_*\, y^{\gamma}$ we obtain:

$$P_v\,(K_*, y) = \frac{3}{2}\,\mathcal{C}_v \frac{\Omega_{T*}}{\Omega_{\rm rad*}}\, L_*^3\, \frac{K_*^2}{(1+K_*^2 y^{2\gamma})^{17/6}} \times \begin{cases} y^{5\gamma+1} & \text{if } 0 \le y \le 1 \text{ and } 0 \le K_* \le \frac{L_*}{\lambda(y)} \\ 1 & \text{if } y \ge 1 \text{ and } 0 \le K_* \le \frac{L_*}{\lambda(y)} \\ 0 & \text{if } K_* \ge \frac{L_*}{\lambda(y)} \end{cases}$$

The time-dependence of $P_v(K_*, y)$ is shown in figure 5. The initial phase, $0 \le y \le 1$ is inserted so that the source of GW increases smoothly from zero. As already discussed, the continuity of the source at initial time is an important issue for the resulting GW spectrum [14]. However, since the duration of this initial phase is short, we assume that the details of the source spectrum during this phase are not relevant and we do not model them in any detail. In particular, we do not expect the inertial range $K_*^{-11/3}$ for $K_* \gtrsim 3$ to be already developed in this initial phase, because the real energy cascade has not yet started.

JCAP12(2009)024

Nevertheless, for simplicity we keep the same form of the spectrum as a function of K_* in the two phases: the turbulent free decay phase, $y \geq 1$, is actually the most relevant one for the GW generation. During this phase, the large scale part of the power spectrum $K_* \ll 1$ remains constant. We also show the characteristic velocity and the kinetic energy as functions of K_* for different times in figure 6.

In the following we assume that the turbulent magnetic field also undergoes the same time decay as the turbulent velocity field. Even though the precise decay law of the magnetic field energy density is not known in general for MHD turbulence, both analytical [32–35] and numerical [37–39] analyses seem to agree with the fact that the magnetic field power spectrum is persistent on large scales. Together with the condition that the spectrum, in a cosmological setting, should be of the Batchelor type (i.e. k^2 at large scales) due to the presence of a cosmological horizon, constancy in time at large scales entails the existence of a conserved quantity analogous to Loitsyansky's invariant: $(\Omega_B/\Omega_{\rm rad})L^5$ =constant. This gives the same decay as for the turbulent flow. Equivalent scaling laws (once generalized to the Batchelor case) are obtained from the argument of self-similarity [32, 38] and direct cascade [34, 39]. Therefore, we also assume in the magnetic case,

$$
\begin{aligned}
L(t) &= L_* y^{\gamma} \\
\frac{\Omega_B}{\Omega_{\rm rad}}(t) &= \frac{\Omega_{B*}}{\Omega_{\rm rad*}} \begin{cases} y & 0 \leq y \leq 1 \\ y^{-5\gamma} & y \geq 1 \,, \end{cases} \\
P_b\left(K_*, y\right) &= \frac{3}{2}\, \mathcal{C}_b \frac{\Omega_{B*}}{\Omega_{\rm rad*}}\, L_*^3\, \frac{K_*^2}{(1+K_*^2 y^{2\gamma})^{11/4}} \times \begin{cases} y^{5\gamma+1} & \text{if } 0 \leq y \leq 1 \text{ and } 0 \leq K_* \leq \frac{L_*}{\lambda(y)} \\ 1 & \text{if } y \geq 1 \text{ and } 0 \leq K_* \leq \frac{L_*}{\lambda(y)} \\ 0 & \text{if } K_* \geq \frac{L_*}{\lambda(y)} \,. \end{cases}
\end{aligned}
$$

Our argument for assuming this particular form of the time decay in MHD turbulence relies on approximative, analytical considerations, and given the high non-linearity of the problem it is conceivable that only numerical simulations will be able to find the correct scaling. For simplicity, and in order to be able to proceed with our analytical estimate, we are forced to make the above mentioned, rather crude assumptions for the scaling. Nonetheless, we would like to stress here once again the importance of the presence of a causal horizon, unavoidable in the cosmological setting. This prevents the formation of long range correlations at least beyond the horizon scale, a feature which certainly affects the decay law and that can not be accounted for in numerical MHD simulations which go on for times larger than the box size.

3.5 How long does turbulence last?

In this section we confirm that turbulence is generated during a phase transition, and we determine when it ends according to the free decay picture described above. For this we evaluate the Reynolds number defined in eq. (3.1) at the energy injection scale L corresponding to $K = kL/2\pi = 1$. We distinguish the physical length with a subscript $_p$

$$
L_p(T) = L(y) \frac{T_0}{T} \left(\frac{g_0}{g(T)}\right)^{1/3} \tag{3.20}
$$

from the comoving scale $L(y) = L_* y^{\gamma}$. The kinematic viscosity $\nu(T)$ is derived in appendix B:

$$
\nu(T) \approx \begin{cases} 22\ T^{-1} & T \gtrsim 100\ \text{GeV} \\ 5\ 10^8\ \text{GeV}^4\ T^{-5} & T \lesssim 100\ \text{GeV} \\ 2\ 10^9\ \text{GeV}^4\ T^{-5} & T \lesssim 100\ \text{MeV} \end{cases} \tag{3.21}
$$

JCAP12(2009)024

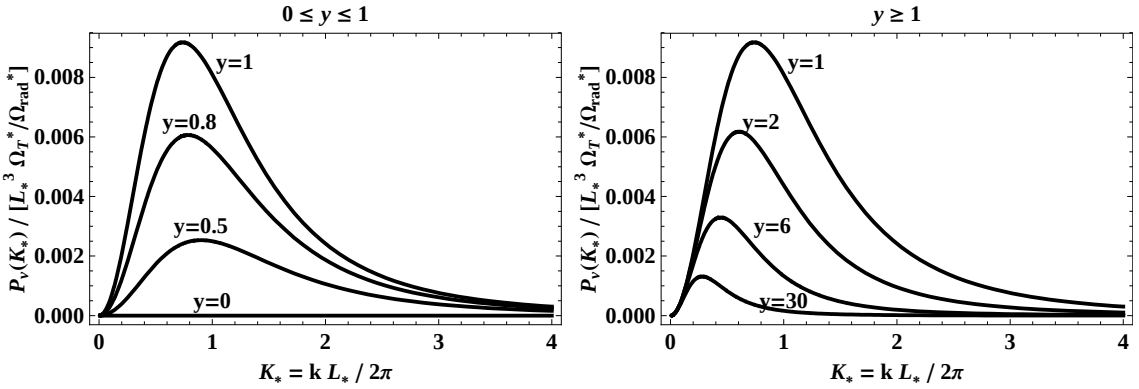

Figure 5. The normalized velocity power spectrum as a function of wavenumber K_* for different times. Left: the phase in which the turbulence is developing, $0 \leq y \leq 1$. Right: the phase of free decay, $y \geq 1$. The Kolmogorov microscale is outside the plot range (c.f. end of section 3.5).

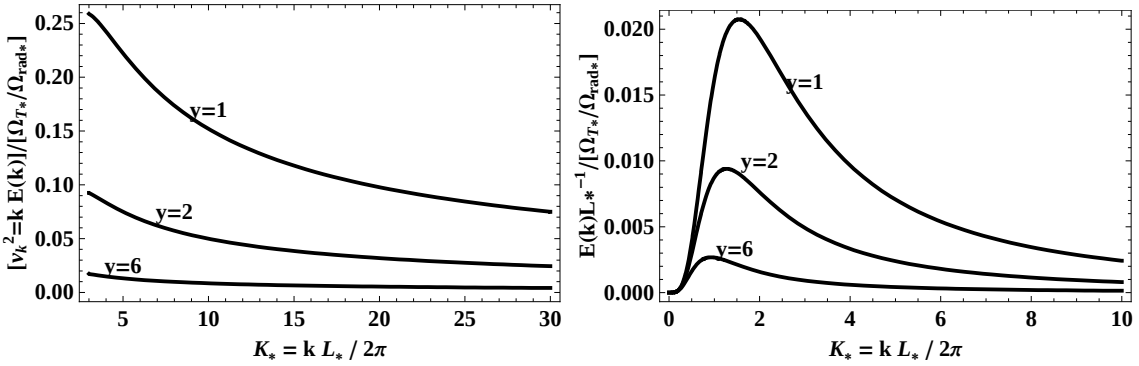

Figure 6. Left: the characteristic velocity $v_k^2 \sim kE(k) = 4\pi K_*^3 P_v(K_*)/L_*^3$ as a function of wavenumber at different times in the inertial range $K_* \gtrsim 3$ during the free decay phase, $y \geq 1$. Right: the kinetic energy $E(k)/L_* = 2K_*^2 P_v(K_*)/L_*^3$. The Kolmogorov microscale is outside the plot range.

The jumps in the viscosity introduce an uncertainty in the evaluation of the parameters, for which we can only give the correct order of magnitude.

For $v_L \equiv v_k(k = 2\pi/L)$, we use the relation (3.10). Eq. (3.10) is valid only during the cascade, the free decay phase $y \geq 1$, and in the inertial range $K \gtrsim 3$. To estimate the Reynolds number, we extrapolate it to $K = 1$, thus making a small error. However, the following estimate is valid only for times $y \geq 1$. We have

$$v_L^2(y) \sim 6\pi \mathcal{C}_v \frac{\Omega_{T*}}{\Omega_{\rm rad*}} y^{-5\gamma}\,, \quad \text{for} \quad y \geq 1\,. \tag{3.22}$$

Inserting this in (3.1) we obtain for temperatures $T \leq T_*$ corresponding to $y \geq 1$

$$\mathrm{Re}\,(L(T)) = \mathrm{Re}\,(L_*)\frac{T_*}{T}\,\frac{\nu(T_*)}{\nu(T)}\,y^{-\frac{3}{2}\gamma}\left(\frac{g_*}{g(T)}\right)^{1/3} \quad \text{with} \tag{3.23}$$

$$\mathrm{Re}\,(L_*) = \sqrt{6\pi\mathcal{C}\frac{\Omega_{T*}}{\Omega_{\rm rad*}}}\,\frac{L_*}{\nu(T_*)}\,\frac{T_0}{T_*}\left(\frac{g_0}{g_*}\right)^{1/3}. \tag{3.24}$$

JCAP12(2009)024

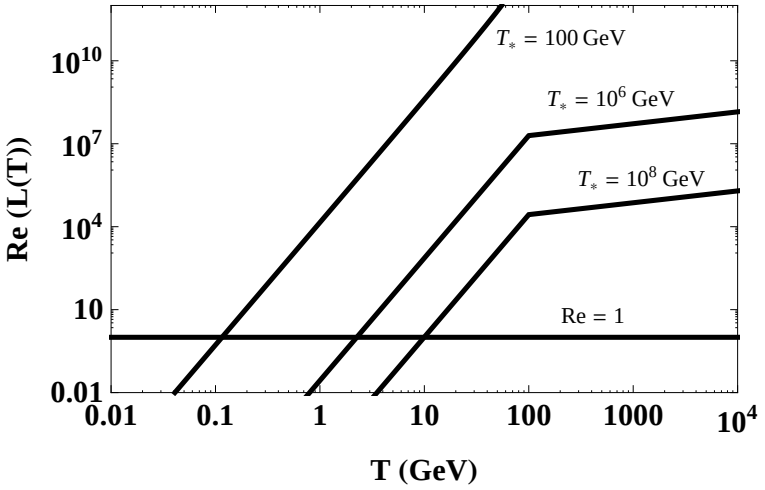

Figure 7. Evolution of the Reynolds number at the energy injection scale $L_p(T)$ as a function of temperature, assuming a phase transition with $\beta/\mathcal{H}_* = 100$, $\frac{\Omega_{T*}}{\Omega_{\rm rad*}} = 2/9$ and $\gamma = 2/7$, for three phase transition temperatures: $T_* = 100, 10^6$ and 10^8 GeV. The temperature at which the Reynolds number decays below 1 (horizontal line) represents approximatively the end of the turbulence: this typically happens at temperatures $\sim 100\,$MeV, 2 GeV and 8 GeV respectively.

$\mathrm{Re}\,(L(T))$ is plotted for different values of T_* in figure 7. If we consider the EW phase transition, for which $T_* \sim 100$ GeV, and we fix $\beta/\mathcal{H}_* = 100$, $\Omega_{T*}/\Omega_{\rm rad*} = 2/9$ corresponding to $v_f = c_s$, $v_b = 0.87$ corresponding to detonations (see section 3.1), and $\gamma = 2/7$, we find the value

$$\mathrm{Re}\,(L(T_* = 100\ \mathrm{GeV})) \sim 10^{13}\,. \tag{3.25}$$

This confirms that turbulence develops once the primordial fluid is stirred on the scale $L_* = 2v_b/\beta$. In appendix B we also derive

$$\mathrm{P_m} = \frac{\nu}{\mu} \simeq 10^{12} \left(\frac{\mathrm{GeV}}{T}\right)^4\,, \qquad 1\ \mathrm{MeV} < T < 100\ \mathrm{GeV}\,, \tag{3.26}$$

so that

$$\mathrm{R_m}(L(T)) = \mathrm{Re}\,(L(T))\mathrm{P_m}(T) \simeq 10^{12}\,\mathrm{Re}\,(L(T)) \left(\frac{\mathrm{GeV}}{T}\right)^4\,, \tag{3.27}$$

$$\mathrm{R_m}(L(T_* = 100\ \mathrm{GeV})) \sim 10^{17}\,. \tag{3.28}$$

We now want to determine the wavelength up to which the cascade is present, and the time up to which MHD turbulence persists. The turbulent cascade stops when viscosity becomes important, and this happens at scales smaller than the Kolmogorov microscale λ, defined by

$$\mathrm{Re}\,(\lambda) = \frac{v_\lambda\,\lambda_p}{\nu} \equiv 1 \qquad \text{hence} \qquad \frac{L}{\lambda} = \frac{v_\lambda}{v_L}\,\mathrm{Re}\,(L) = \mathrm{Re}\,(L)^{3/4}\,, \tag{3.29}$$

JCAP12(2009)024

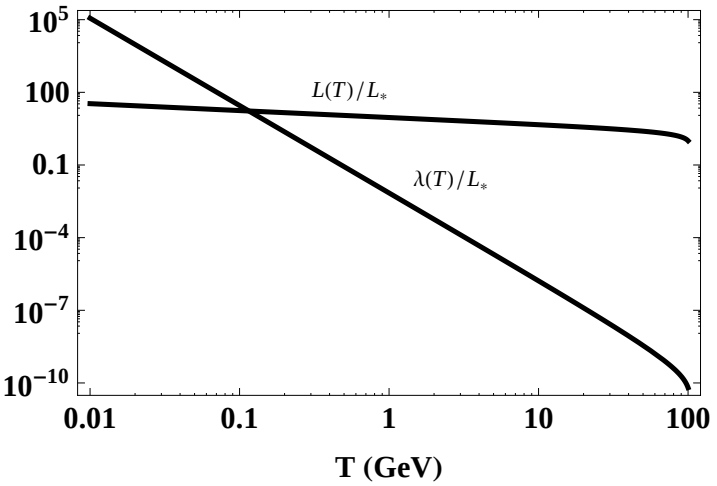

Figure 8. Evolution of the stirring scale $L(T)$ and the Kolmogorov microscale $\lambda(T) = L(T)/[\mathrm{Re}\,(L(T))]^{3/4}$ with temperature, for $T_* = 100\,\mathrm{GeV}$, $\beta/\mathcal{H}_* = 100$, $\frac{\Omega_{T*}}{\Omega_{\mathrm{rad}*}} = 2/9$ and $\gamma = 2/7$.

where for the last equality we use (3.10). Therefore, the Kolmogorov microscale also grows during free decay, according to:

$$\lambda(T) = \lambda_* \left(\frac{T}{T_*} \frac{\nu(T)}{\nu(T_*)} \left(\frac{g(T)}{g_*} \right)^{1/3} \right)^{3/4} y^{\frac{17}{8}\gamma} . \tag{3.30}$$

The temperature dependence of $\lambda(T)$ and $L(T)$ is illustrated in figure 8. The ratio of the initial scales determining the extension of the turbulent inertial range is $L_*/\lambda_* = \mathcal{O}(10^{10})$, for $T_* = 100$ GeV, $\beta/\mathcal{H}_* = 100$, $\Omega_{T*}/\Omega_{\mathrm{rad}*} = 2/9$, $v_b = 0.87$ and $\gamma = 2/7$.

Since $\lambda(T)$ grows faster than $L(T)$, there always exists a temperature at which the two scale cross, as shown in figure 8. We define the end of turbulence when the entire inertial range ($K \gtrsim 3$) is dissipated, namely when the dissipation scale has grown to reach

$$\frac{L(T_{\mathrm{fin}})}{\lambda(T_{\mathrm{fin}})} = 3 \quad \Rightarrow \quad \mathrm{Re}\,(L(T_{\mathrm{fin}})) = 3^{4/3} . \tag{3.31}$$

If turbulence starts at $T_* = 100$ GeV, using again the values $\beta/\mathcal{H}_* = 100$, $\Omega_{T*}/\Omega_{\mathrm{rad}*} = 2/9$ and $\gamma = 2/7$, we find $T_{\mathrm{fin}} \simeq 120$ MeV. Therefore, turbulence acts as source of GWs for many Hubble times.

Once turbulent motions are dissipated, the magnetic field fluctuations at scales larger than the dissipation scale remain frozen in the primordial plasma. Hence, in principle, the magnetic field continues acting as a source of GW also after the end of turbulence. However, we neglect this extra contribution to the GW spectra since it will not affect the spectrum at the interesting scales, around the peak, where the signal may be visible. These scales in fact have entered the horizon well before the end of turbulence and further GW production is strongly suppressed at later times.

JCAP12(2009)024

3.6 Time de-correlation of the spectrum of magneto-hydrodynamical turbulence

In order to evaluate the GW power spectrum generated from MHD turbulence, the equal time velocity and magnetic field power spectra given in eqs. (3.5), (3.6) and eqs. (3.15), (3.16) are not enough. We need to know the unequal time velocity power spectrum,

$$\langle v_i(\mathbf{k}, t_1) v_j^*(\mathbf{q}, t_2)\rangle = (2\pi)^3 \delta(\mathbf{k}-\mathbf{q})\, P_{ij}\, P_v(k, t_1, t_2)\,, \tag{3.32}$$

and equivalently for the magnetic field. To model the unequal time velocity power spectrum, we multiply the equal time one (3.6) with the exponential time de-correlation proposed by Kraichnan in [43] and also used in [18]. The temporal de-correlation of the velocity field described in [43] operates only in the inertial range and during the cascade, which in our case means $K \gtrsim 3$ and $t \geq t_*$. The characteristic de-correlation time scale is given by the eddy turnover time: $\tau_\ell = \ell/(2v_\ell)$, for a characteristic eddy of size $\ell = 2\pi/k$ well in the inertial range. To model the de-correlation Kraichnan proposes a Gaussian functional form,

$$g(t_1, t_2) = \exp(-\pi (t_1 - t_2)^2/(4\tau_\ell^2))\,. \tag{3.33}$$

In our approach, the magnetic field undergoes the same de-correlation as the turbulent field.

In the case of freely decaying MHD turbulence under consideration here, the eddy turnover time τ_ℓ is itself time-dependent, through the characteristic velocity on the same scale, v_ℓ. Using the formula of the characteristic velocity in the inertial range (3.10), and the evolution equations for the kinetic energy and the correlation scale (3.19) and (3.18) we obtain

$$\tau_\ell(y) = \frac{\ell}{2v_\ell} = \tau_\ell^*\; y^{\frac{17}{6}\gamma} \qquad \text{where} \qquad \tau_\ell^* = \frac{L_*^{\frac{1}{3}}\; \ell^{\frac{2}{3}}}{2\sqrt{6\pi \mathcal{C}_v \frac{\Omega_{T*}}{\Omega_{\mathrm{rad}*}}}}\,, \tag{3.34}$$

and the above equation is valid only during the cascade $y \geq 1$ and $K \gtrsim 3$. Setting $y = (t_1 - t_{\mathrm{in}})/\tau_L$, and $z = (t_2 - t_{\mathrm{in}})/\tau_L$, we arrive at the following expression for the velocity unequal time power spectrum (the magnetic field spectrum is readily derived from the expression below, substituting $\mathcal{C}_v$ by $\mathcal{C}_b$, Ω_T by Ω_B and 17/6 by 11/4):

$$\begin{aligned} P_v(K, y, z) = {} & \frac{3}{2}\mathcal{C}_v \frac{\Omega_T}{\Omega_{\mathrm{rad}}}(y, z)\, L^3(y, z)\, \frac{K^2(y, z)}{[1 + K^2(y, z)]^{17/6}} \\ & \times \begin{cases} 1 & \text{for } K(y,z) < 3 \\ \exp\left(-\frac{\pi}{4}(y-z)^2 \left(\frac{\tau_L}{\tau_\ell(y,z)}\right)^2\right) & \text{for } 3 < K(y,z) < \frac{L}{\lambda} \text{ and } y, z \geq 1 \\ 0 & \text{for } K(y,z) > \frac{L}{\lambda} \end{cases} \end{aligned} \tag{3.35}$$

Here the notation $\frac{\Omega_T}{\Omega_{\mathrm{rad}}}(y, z)$ (and so on) is to remind that the variables K, L, $\Omega_T/\Omega_{\mathrm{rad}}$ and τ_ℓ depend on time. In principle, we need to specify at which time these variables have to be evaluated. This choice must satisfy the constraint that the unequal time power spectrum (3.32) is symmetric under the exchange of t_1 and t_2. As explained in the next section, we avoid the problem by modeling de-correlation of the Kraichnan type directly in the anisotropic stresses of the source.

JCAP12(2009)024

4 The anisotropic stress power spectrum

In order to determine the GW energy density power spectrum generated by the MHD turbulent source, we need to calculate the anisotropic stress power spectrum (2.10) at different times, substitute it into eq. (2.14), and evaluate the time integral.

The tensor anisotropic stress is the transverse traceless part of the energy momentum tensor $\tilde{\Pi}_{ij}(\mathbf{k},t) = (P_{il}P_{jm} - 1/2P_{ij}P_{lm})\tilde{T}_{lm}(\mathbf{k},t)$, where we denote the dimensionless energy momentum tensor with a tilde, see eq. (2.6). The part of the energy momentum tensor of our sources which contributes to the anisotropic stress is given by $\tilde{T}^{(T)}_{lm}(\mathbf{x},t) = v_l(\mathbf{x},t)v_m(\mathbf{x},t)$ and $\tilde{T}^{(B)}_{lm}(\mathbf{x},t) = b_l(\mathbf{x},t)b_m(\mathbf{x},t)$. The anisotropic stress power spectrum is then

$$\langle \Pi_{ij}(\mathbf{k},t_1)\Pi^*_{ij}(\mathbf{q},t_2)\rangle = (2\pi)^3\delta(\mathbf{k}-\mathbf{q})\Pi(k,t_1,t_2) = \mathcal{P}_{abcd}\langle T_{ab}(\mathbf{k},t_1)T^*_{cd}(\mathbf{q},t_2)\rangle\,, \tag{4.1}$$

where we omit the tildes for simplicity and

$$\mathcal{P}_{abcd} = \left(P_{ia}P_{jb} - \frac{1}{2}P_{ij}P_{ab}\right)(\mathbf{k})\left(P_{ic}P_{jd} - \frac{1}{2}P_{ij}P_{cd}\right)(\mathbf{q})\,. \tag{4.2}$$

For the turbulent source, one has

$$\begin{aligned}\langle \Pi_{ij}(\mathbf{k}_1,t_1)\Pi^*_{ij}(\mathbf{k}_2,t_2)\rangle &= \\ &= \mathcal{P}_{abcd}\int\frac{d^3p}{(2\pi)^3}\int\frac{d^3q}{(2\pi)^3}\langle v_a(\mathbf{k}_1-\mathbf{p},t_1)v_b(\mathbf{p},t_1)v^*_c(\mathbf{k}_2-\mathbf{q},t_2)v^*_d(\mathbf{q},t_2)\rangle\,.\end{aligned} \tag{4.3}$$

In order to proceed analytically, we assume that we can decompose the four point correlation function into products of the power spectra, using Wick's theorem like for a Gaussian random field. Since turbulence is not truly Gaussian, this is of course not strictly correct but it is usually adopted as a reasonable approximation to close the hierarchy (i.e. to avoid using equations involving higher order correlators). We refer to [21] and appendix C for details of the determination of $\Pi(k,t_1,t_2)$. The bottom line is that the anisotropic stress power spectrum is given by the convolution of the unequal time velocity power spectrum, c.f. eq. (C.3). This quantity is in principle determined once we know how the source behaves in time. In our case it is given by the Kraichnan de-correlation model, once we have chosen an appropriate way of symmetrizing in time, see eq. (3.35).

On the other hand, the anisotropic stress power spectrum should, by definition, be a positive kernel, i.e. such that

$$\int dt_1\int dt_2\,\Pi(k,t_1,t_2)f(t_1)f^*(t_2) \geq 0 \qquad \forall\ f(t)\,. \tag{4.4}$$

This follows simply from the definition of the velocity power spectrum, eq. (4.1), making use of the inequality

$$\langle\left|\int dt_1\,\Pi_{ij}(\mathbf{k},t_1)f(t_1)\right|^2\rangle \geq 0\,. \tag{4.5}$$

Comparing eq. (4.4) with the definition of the GW spectrum eq. (2.14), we see that in the GW case the function $f(t)$ is replaced by the Green function of the GW wave equation, $f(t_1) = \cos(kt_1)/t_1$ or $\sin(kt_1)/t_1$ (the factor $1/t_1$ is absent for the short lasting case). Since the trigonometric functions are a complete basis, the property (4.4) is automatically satisfied, if it holds for the Green function with arbitrary values of k. Therefore, inserting the unequal time source power spectrum eq. (3.35), which accounts for Kraichnan de-correlation, in the

JCAP12(2009)024

convolution given by eqs. (4.3) and (C.3), and performing the integration over the momenta, should give back an anisotropic stress power spectrum which is a positive kernel. However, we have tried different ways of symmetrizing eq. (3.35) without succeeding in obtaining a positive kernel. This may be related to the inaccuracy of our analytical estimates, to our choice of symmetrization, or it could be an indication that either Wick's theorem or free decay together with Kraichnan de-correlation, although reasonable assumptions for the evolution of MHD turbulence, are not entirely appropriate for the source we are considering. Only a full numerical simulation of the turbulent and magnetic fields could help to understand the shortcomings of our approach.

The same problem can arise when trying to obtain the source power spectrum by Fourier transforming the space correlation function, but this is circumvented since the source is modeled directly in Fourier space (the power spectrum is well known in the MHD turbulent case). However, in order to calculate the GW spectrum one has to evaluate also the time Fourier transform: this is not a common procedure and no general solution is given in the literature. The problem is worsened by the fact that we want to account for the free decay of turbulence. If the only time dependence of the turbulent power spectrum was the Kraichnan de-correlation, which is Gaussian in the time difference, the spectrum resulting after time Fourier transforming would be positive. However, the free decay introduces an additional absolute time dependence which is more difficult to handle. Moreover, having to evaluate the anisotropic stress power spectrum further increases the difficulty of finding the correct time behaviour that would provide a positive kernel. Note that the same problem arose in the analytical evaluation of the GW signal coming from bubble collisions [12].

In order to proceed, we model the source in such a way, that $\Pi(k, t_1, t_2)$ is a positive kernel by construction. This is most easily done directly for the anisotropic stress power spectrum. In previous analyses [12] we have already tackled this problem and proposed three forms for the unequal time anisotropic stress power spectrum which are positive kernels. In section 2.3 we presented the incoherent (2.17) and coherent (2.20) cases, for which the source is never correlated, respectively always correlated in time. We apply them in the following to the MHD turbulent source. We believe, however, that the top hat correlation introduced in ref. [12] is the relevant one for MHD turbulence, since it best mimics the Kraichnan de-correlation. In the top hat model one assumes that $\Pi(k, t_1, t_2)$ is correlated if $|t_1 - t_2| < x_c/k$ and uncorrelated otherwise. Here x_c is a parameter of order unity. We shall choose $x_c = 1$ for our numerical results. Since $\Pi(k, t_1, t_2)$ has to be symmetric in t_1 and t_2 we set

$$\begin{aligned}\Pi(k, t_1, t_2) = \frac{1}{2}\Big[&\Pi(k, t_1, t_1)\,\Theta(t_2 - t_1)\,\Theta\left(\frac{x_c}{k} - (t_2 - t_1)\right) \\ &+ \Pi(k, t_2, t_2)\,\Theta(t_1 - t_2)\,\Theta\left(\frac{x_c}{k} - (t_1 - t_2)\right)\Big]\,. \end{aligned} \tag{4.6}$$

This way of correlating the source at unequal times is intermediate between the coherent and incoherent approximations; instead of being correlated at all times or only for $t_1 = t_2$, here we account for the fact that longer wavelengths de-correlate at larger time differences. While the term $\Theta(t_1 - t_2)$ is there only to make the function symmetric and does not influence the time continuity of the source, the term $\Theta(x_c/k - |t_1 - t_2|)$ should in principle be replaced by an exponential decay to keep the source continuous. We have tried this, and a part from a much slower convergence of the numerical integrals since the integrand oscillates rapidly for large values of $k|t_1 - t_2|$, we found no difference in the final result. Moreover, inserting (4.6) in the integral (2.11), we find that the GW energy power spectrum is not given by the Fourier transform of the source and continuity does not affect the final spectrum in this case (c.f. [14]).

JCAP12(2009)024

Assuming that the Kraichnan time de-correlation trivially extends from the turbulent velocity field to the anisotropic stress, it is clear that it gives a behaviour quite similar to the top hat de-correlation: according to (3.33), the source is no longer correlated for time intervals $|t_1 - t_2| \gtrsim (2/\sqrt{\pi})\tau_\ell$. Accounting for the fact that the eddy turnover time is simply the inverse of the characteristic frequency of the source $\omega_\ell = 1/\tau_\ell$, and that the GW Green function selects the diagonal of the time Fourier transform of the source, for which $|\omega| = k$, we find that the Kraichnan de-correlation gives back the same condition as the top hat de-correlation, namely correlation is lost for time differences

$$|t_1 - t_2| \gtrsim \frac{2}{\sqrt{\pi}} \frac{1}{\omega_\ell} \simeq \frac{x_c}{k} \qquad \text{with } x_c \simeq 1\,. \tag{4.7}$$

Even though the top hat case best reproduces turbulent de-correlation, in the following we evaluate the GW spectra also for the coherent and incoherent cases and compare the results. In order to proceed with the calculation, we now evaluate the equal time anisotropic stress power spectrum, see eq. (4.6).

4.1 The equal time anisotropic stress power spectrum for magneto-hydro dynamical turbulence

The equal time anisotropic stress power spectrum is given by the convolution of the equal time velocity and magnetic field power spectra multiplied by an angular dependence coming from the projector in eq. (4.3), see eq. (C.3). As already mentioned above, we refer to [21] and appendix C for a derivation. In terms of the variable $K = K_* y^\gamma$, using the velocity power spectrum given in eq. (3.20), we find

$$\Pi_v(K, y, y) = \frac{9}{2}\,\pi\,\mathcal{C}_v^2 \left(\frac{\Omega_T}{\Omega_{\rm rad}}(y)\right)^2 L^3(y)\,\mathcal{I}_v(K, y, y)\,, \tag{4.8}$$

where $y = (t_1 - t_{\rm in})/\tau_L$ and $\mathcal{I}_v$ is given by

$$\mathcal{I}_v(K, y, y) = \int_0^\infty dQ\, \frac{Q^4}{(1+Q^2)^{17/6}} \int_{-1}^1 d\chi\, (1+\chi^2) \frac{2K^2 + Q^2(1+\chi^2) - 4KQ\chi}{(1 + K^2 - 2\chi KQ + Q^2)^{17/6}}\,, \tag{4.9}$$

with $Q = Lq/2\pi$, $\chi = \hat{k}\cdot\hat{q}$. The magnetic field anisotropic stress power spectrum is equivalent to the above expressions, substituting Ω_T with Ω_B, $\mathcal{C}_v$ with $\mathcal{C}_b$ and the power law 17/6 with 11/4. The integrals cannot be performed analytically, so we solve them numerically and derive fits in terms of the variable $K = K_* y^\gamma$. Within this approach we do not account for the small scale cutoff L/λ when fitting the convolution. We explain below how this cutoff is taken into account. We find, for the turbulence and the magnetic field respectively:

$$\mathcal{I}_v(K_*, y, y) \simeq 0.098 \left[1 + \left(\frac{K_* y^\gamma}{4}\right)^{4/3} + \left(\frac{K_* y^\gamma}{3.3}\right)^{11/3}\right]^{-1} \tag{4.10}$$

$$\mathcal{I}_b(K_*, y, y) \simeq 0.12 \left[1 + \left(\frac{K_* y^\gamma}{4}\right)^{4/3} + \left(\frac{K_* y^\gamma}{3.5}\right)^{7/2}\right]^{-1} \tag{4.11}$$

The fits are shown in figure 9.

JCAP12(2009)024

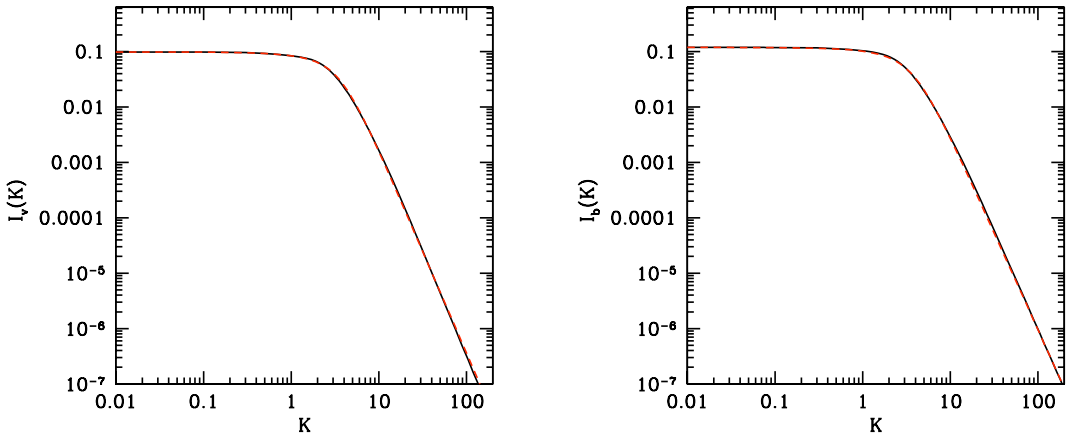

Figure 9. Black, solid lines: the integral in eq. (4.9), left: for the turbulence anisotropic stress, and right: for the magnetic field anisotropic stress, as a function of $K = K_* y^\gamma$, together with their fits given in eqs. (4.10) and (4.11) (shown as red, dashed lines).

4.2 The final time of the magneto-hydrodynamical turbulent source

As demonstrated in section 3.5, MHD turbulence can act as a source of GWs for many Hubble times, while it undergoes free decay. The source generally switches off at the end of the turbulence, when $\mathrm{Re}\,(L_p(T_{\rm fin})) = 3^{4/3}$ (see eq. (3.31)). If $T_* = 100\,\mathrm{GeV}$, we have found $T_{\rm fin} \simeq 120\,\mathrm{MeV}$. However, we have seen in section 3.5 that the Kolmogorov microscale grows in time, and for wavenumbers above this cutoff the source has decayed. This means that the final time of integration in eq. (2.11) must be defined as the minimum of $t(T_{\rm fin})$ and the time at which a given mode k is equal to the upper cutoff. For later times, that mode k is not generating GWs any longer; however, if the time at which k is equal to the upper cutoff comes after the end of the turbulence, we should take the end of the turbulence $t(T_{\rm fin})$ as the final time of action of the source on the scale k. This is the way in which we include the upper cutoff L/λ appearing in eq. (3.35) in the calculation of the GW spectrum, even though we have neglected it for simplicity in the evaluation of the anisotropic stress power spectra (4.10), (4.11).

We introduce t_k as the time at which $k = 4\pi/\lambda(t_k)$, where the extra factor of 2 comes from the fact that $\mathcal{I}_v(K_*, y, z)$, being the convolution of the velocity power spectrum (3.35) (and equivalently for the magnetic field power spectrum), it will go to zero at twice the velocity power spectrum cutoff. Using the time evolution of the dissipation scale λ, eq. (3.30), we find

$$\frac{t_k}{\tau_L} = \left[\frac{L_*}{\lambda_*}\frac{2}{K_*}\left(\frac{t_*}{\tau_L}\right)^3\right]^{\frac{1}{17\gamma/8+3}} \qquad \text{if} \quad T_* \leq 100\ \mathrm{GeV}\,, \quad T_{\rm fin} \geq 100\ \mathrm{MeV} \tag{4.12}$$

$$\frac{t_k}{\tau_L} = \left[\frac{L_*}{\lambda_*}\frac{2}{K_*}\right]^{\frac{8}{17\gamma}} \qquad \text{if} \quad T_{\rm fin} \geq 100\ \mathrm{GeV}\,, \tag{4.13}$$

where the different behaviour depending on the initial and final temperature is due to the different evolution of the viscosity, given in eq. (3.21). Finally, the time at which turbulence

at a given scale k ends is $t_{\rm fin}(k)$ given by

$$\frac{t_{\rm fin}(k)}{\tau_L} = \min\left\{\frac{t(T_{\rm fin})}{\tau_L}\,,\ \frac{t_k}{\tau_L}\right\} \tag{4.14}$$

where $t(T_{\rm fin}) \simeq T_0\,/\,(T_{\rm fin}\,H_0\sqrt{\Omega_{\rm rad}})$ and $T_{\rm fin}$ denotes the end of the MHD turbulence by the dissipation of the entire Kolmogorov range, defined in section 3.5. For the usual set of values $T_* = 100$ GeV, $\beta/\mathcal{H}_* = 100$, $\Omega_{T*}/\Omega_{\rm rad*} = 2/9$, $v_b = 0.87$ and $\gamma = 2/7$, we find

$$\frac{t_{\rm fin}(k)}{\tau_L} \simeq \begin{cases} 2\times 10^4 & \text{for } K_* \lesssim 0.07 \\ \left(\frac{2\ 10^{14}}{K_*}\right)^{\frac{28}{101}} & \text{for } K_* \gtrsim 0.07\,. \end{cases} \tag{4.15}$$

5 The gravitational wave spectrum

We are now ready to evaluate the integrals in eq. (2.11). We consider the three approximations for the unequal time correlator of the anisotropic stress tensor mentioned above, namely incoherent, coherent and top hat. All we need is the anisotropic stress power spectrum taken at equal times, which is given in eqs. (4.10) and (4.11). These are then inserted into eq. (2.11). The GW power spectra obtained in this way are always positive. The figures of the GW energy density spectra shown below are calculated for the set of parameter values given at the end of the previous section. Under the equipartition hypothesis, we fix the magnetic field energy density to the same value of the turbulent one: $\frac{\Omega_{T*}}{\Omega_{\rm rad*}} = \frac{\Omega^*_B}{\Omega^*_{\rm rad}} = \frac{2}{9}$.

Even though we have demonstrated in section 3.5 that MHD turbulence can last for many Hubble times, at the end of this section we also consider the case of GW generated by MHD turbulence confined in time to the duration of the phase transition. We find this analysis illuminating to understand our results and useful to compare with the results obtained in previous works.

From now on we use a common notation for both the GW spectra generated by turbulence and by the magnetic field, with $s = v$ or b denoting respectively the turbulence and magnetic field source.

- **Incoherent approximation**: in this case the anisotropic stress spectrum at unequal times is given by (c.f. eq. (2.17) and (4.10) resp (4.11)):

$$\Pi(K_*, y, z) = \frac{9}{2}\,\pi\,\mathcal{C}_s^2\left(\frac{\Omega_S}{\Omega_{\rm rad}}(y)\right)^2 L^3(y)\,\mathcal{I}_s(K_*, y, y)\ \delta(y-z)\,, \tag{5.1}$$

  where we have chosen τ_L as the short characteristic time over which the source remains coherent. From the anisotropic stress formula given above we find the spectrum:

$$\begin{aligned}\left.\frac{d\Omega_{\rm GW}h_0^2}{d\log k}\right|_0 &= 12(2\pi)^2\,\mathcal{C}_s^2\,\Omega_{{\rm rad},0}h_0^2\left(\frac{g_0}{g_{\rm fin}}\right)^{\frac{1}{3}}\left(\frac{\Omega_{S*}}{\Omega_{\rm rad*}}\right)^2 K_*^3 \\ &\times\left\{\int_0^1 \frac{dy\ y^{3\gamma+2}}{\left[y+\frac{t_{\rm in}}{\tau_L}\right]^2}\,\mathcal{I}_s(K_*,y,y) + \int_1^{y_{\rm fin}} \frac{dy\ y^{-7\gamma}}{\left[y+\frac{t_{\rm in}}{\tau_L}\right]^2}\,\mathcal{I}_s(K_*,y,y)\right\}\end{aligned} \tag{5.2}$$

  where $\tau_L = L_*/(2v_L)$ is the initial eddy turnover time at the scale L_* for $y = 1$, and $v_L = \sqrt{6\pi\mathcal{C}_v\frac{\Omega_{T*}}{\Omega_{\rm rad*}}}$ denotes the initial eddy turn-over speed, eq. (3.22); moreover, see section 3.4

$$\frac{t_{\rm in}}{\tau_L} = \frac{t_*}{\tau_L} - 1 \qquad \text{where} \qquad \frac{t_*}{\tau_L} = \frac{v_L}{v_b}\frac{\beta}{\mathcal{H}_*}\,, \tag{5.3}$$

JCAP12(2009)024

$y_{\rm fin}$ is given by $(t_{\rm fin}(k) - t_{\rm in})/\tau_L$ and $t_{\rm fin}(k)$ is defined in section 4.2. The spectra $\mathcal{I}_s(K_*, y, y)$ are given in eqs. (4.10) and (4.11).

We recover the same behaviour as in section 2.3. The GW power spectrum is proportional to the phase space volume K_*^3 times the source power spectrum. The slope at large scales is therefore K_*^3, the one at small scales is K_*^{3+n} where $n = -11/3$ for the turbulence and $n = -7/2$ for the magnetic field. The peak is at $K_*^{\rm peak} \simeq 5.9$ for turbulence and $K_*^{\rm peak} \simeq 7$ for the magnetic field. The results are shown in figure 11 for the usual choice of the parameter values. The incoherent approximation is the one leading to the highest peak amplitude:

$$\left.\frac{d\Omega_{\rm GW}h_0^2}{d\log k}\right|^{(\rm turb)}_{K_*^{\rm peak}} \simeq 4\times 10^{-10} \qquad K_*^{\rm peak} \simeq 5.9\,, \tag{5.4}$$

$$\left.\frac{d\Omega_{\rm GW}h_0^2}{d\log k}\right|^{(\rm mag)}_{K_*^{\rm peak}} \simeq 3\times 10^{-10} \qquad K_*^{\rm peak} \simeq 7\,. \tag{5.5}$$

- **Coherent approximation**: According to eq. (2.20), we have

$$\Pi(K_*, y, z) = \frac{9}{2}\,\pi\,\mathcal{C}_s^2\,\frac{\Omega_S}{\Omega_{\rm rad}}(y)L^{\frac{3}{2}}(y)\,\frac{\Omega_S}{\Omega_{\rm rad}}(z)L^{\frac{3}{2}}(z)\,\sqrt{\mathcal{I}_s(K_*,y,y)}\sqrt{\mathcal{I}_s(K_*,z,z)}\,. \tag{5.6}$$

The GW spectrum is positive by construction, but it is oscillatory:

$$\begin{aligned}\left.\frac{d\Omega_{\rm GW}h_0^2}{d\log k}\right|_0 &= 12(2\pi)^2\,\mathcal{C}_s^2\,\Omega_{{\rm rad},0}h_0^2\left(\frac{g_0}{g_{\rm fin}}\right)^{\frac{1}{3}}\left(\frac{\Omega_{S*}}{\Omega_{\rm rad*}}\right)^2 K_*^3 \\ &\times\left\{\left[\int_0^1 dy\,\frac{y^{3\gamma/2+1}}{y+\frac{t_{\rm in}}{\tau_L}}\,\sqrt{\mathcal{I}_s(K_*,y,y)}\cos\left(\frac{\pi K_*}{v_L}y\right)\right.\right. \\ &\left.+\int_1^{y_{\rm fin}} dy\,\frac{y^{-7\gamma/2}}{y+\frac{t_{\rm in}}{\tau_L}}\,\sqrt{\mathcal{I}_s(K_*,y,y)}\cos\left(\frac{\pi K_*}{v_L}y\right)\right]^2 \\ &+\left[\int_0^1 dy\,\frac{y^{3\gamma/2+1}}{y+\frac{t_{\rm in}}{\tau_L}}\,\sqrt{\mathcal{I}_s(K_*,y,y)}\sin\left(\frac{\pi K_*}{v_L}y\right)\right. \\ &\left.\left.+\int_1^{y_{\rm fin}} dy\,\frac{y^{-7\gamma/2}}{y+\frac{t_{\rm in}}{\tau_L}}\,\sqrt{\mathcal{I}_s(K_*,y,y)}\sin\left(\frac{\pi K_*}{v_L}y\right)\right]^2\right\}.\end{aligned} \tag{5.7}$$

As discussed in ref. [14] and in section 2.3, the calculation in the coherent case is more involved than the incoherent one, since the GW power spectrum is not simply proportional to the source power spectrum, but it is given by the square of its time Fourier transform. The source is characterized by the space correlation scale L_* and the time correlation scale τ_L, related by $L_* = 2v_L\tau_L$. Since $v_L \lesssim 0.4$ (the upper bound is given by eq. (3.11) with $\langle v^2\rangle = 1/3$), we have $L_* < \tau_L$. On scales larger than both the characteristic spatial correlation scale L_* and time correlation scale τ_L, the Fourier transform of the source is constant because the source is not correlated (white noise). Therefore, for wave-numbers $k \lesssim 2\pi/\tau_L < 2\pi/L_*$, corresponding to $K_* \lesssim L_*/\tau_L$, we recover the K_*^3 behaviour like in the incoherent case. However, for $k \gtrsim 2\pi/\tau_L$ the time Fourier transform is no longer constant and starts to decay as a power law, the

JCAP12(2009)024

exponent depending on the time differentiability properties of the source [14]. Since we have chosen a source which is continuous but not differentiable at initial time $t_{\rm in}$ (see the time evolution laws of the energy and the correlation scales given in eqs. (3.18), (3.19)), this implies a decay like k^{-2} for the time Fourier transform of the source. Therefore, the GW power spectrum (5.7) (the square of the Fourier transform, multiplied by K_*^3) decays like K_*^{-1} at intermediate scales $L_*/\tau_L \lesssim K_* \lesssim 1$. This behaviour is satisfied up to the wave-number corresponding to the spatial correlation scale: $k \simeq 2\pi/L_*$. Afterwards, the spectrum decays with a power law given by the time Fourier transform multiplied by the power law decay of the source. In the case of turbulence, for $K_* \gtrsim 1$ one has therefore the power law decay $K_*^{-14/3} = K_*^3 \times (K_*^{-2})^2 \times (K_*^{-11/6})^2$; while in the magnetic field case this becomes $K_*^{-9/2} = K_*^3 \times (K_*^{-2})^2 \times (K_*^{-7/4})^2$.

The form of the power spectrum, in particular the wave-number at which the spectrum peaks is determined by the ratio $\frac{L_*}{\tau_L} = 2\sqrt{6\pi \mathcal{C}_v \frac{\Omega_{T*}}{\Omega_{\rm rad*}}}$. In figure 10, we show the GW spectrum from turbulence for the coherent case for two values of this ratio: the case when the kinetic energy density in the turbulence in maximal $\langle v^2 \rangle = 1/3$, corresponding to $\frac{\Omega_{T*}}{\Omega_{\rm rad*}} = 2/9$, and another one in which the kinetic energy involved is much smaller, $\langle v^2 \rangle = 10^{-3}$, corresponding to $\frac{\Omega_{T*}}{\Omega_{\rm rad*}} = 2/3 \times 10^{-3}$. Notice that not only the amplitude but also the peak position differs, and that the power law behaviour derived above is recovered. The form of the GW spectrum in the coherent case is also shown in figure 11 for the usual choice of the parameters. The coherent approximation leads to the smallest peak amplitude:

$$\left.\frac{d\Omega_{\rm GW} h_0^2}{d\log k}\right|^{\rm (turb)}_{K_*^{\rm peak}} \simeq 10^{-13} \qquad K_*^{\rm peak} \simeq 0.4\,, \tag{5.8}$$

$$\left.\frac{d\Omega_{\rm GW} h_0^2}{d\log k}\right|^{\rm (mag)}_{K_*^{\rm peak}} \simeq 8 \times 10^{-14} \qquad K_*^{\rm peak} \simeq 0.4\,. \tag{5.9}$$

- **Top hat approximation**: this is the most realistic case for the MHD turbulent source, since it mimics a de-correlation in time of the Kraichnan type as discussed in section 4:

$$\Pi(K_*, y, z) = \frac{9}{4}\,\pi\,\mathcal{C}_s^2 \left[\left(\frac{\Omega_S}{\Omega_{\rm rad}}(y)\right)^2 L^3(y)\,\mathcal{I}_s(K_*, y, y)\,\Theta(z-y)\,\Theta\left(\frac{v_L x_c}{\pi K_*} - (z-y)\right) + \left(\frac{\Omega_S}{\Omega_{\rm rad}}(z)\right)^2 L^3(z)\,\mathcal{I}_s(K_*, z, z)\,\Theta(y-z)\,\Theta\left(\frac{v_L x_c}{\pi K_*} - (y-z)\right)\right]. \tag{5.10}$$

We choose the value $x_c = 1$, as in the Kraichnan model, so that the integral determining the GW spectrum is positive. It is given by:

$$\left.\frac{d\Omega_{\rm GW} h_0^2}{d\log k}\right|_0 = 12(2\pi)^2\,\mathcal{C}_s^2\,\Omega_{{\rm rad},0} h_0^2 \left(\frac{g_0}{g_{\rm fin}}\right)^{\frac{1}{3}} \left(\frac{\Omega_{S*}}{\Omega_{\rm rad*}}\right)^2 K_*^3 \times \left[\int_0^1 dy\,\frac{y^{3\gamma+2}}{y + \frac{t_{\rm in}}{\tau_L}}\,\mathcal{I}_s(K_*, y, y) \int_y^{y_{\rm top}} \frac{dz}{z + \frac{t_{\rm in}}{\tau_L}} \cos\left(\frac{\pi K_*}{v_L}(z-y)\right) + \int_1^{y_{\rm fin}} dy\,\frac{y^{-7\gamma}}{y + \frac{t_{\rm in}}{\tau_L}}\,\mathcal{I}_s(K_*, y, y) \int_y^{y_{\rm top}} \frac{dz}{z + \frac{t_{\rm in}}{\tau_L}} \cos\left(\frac{\pi K_*}{v_L}(z-y)\right)\right] \tag{5.11}$$

JCAP12(2009)024

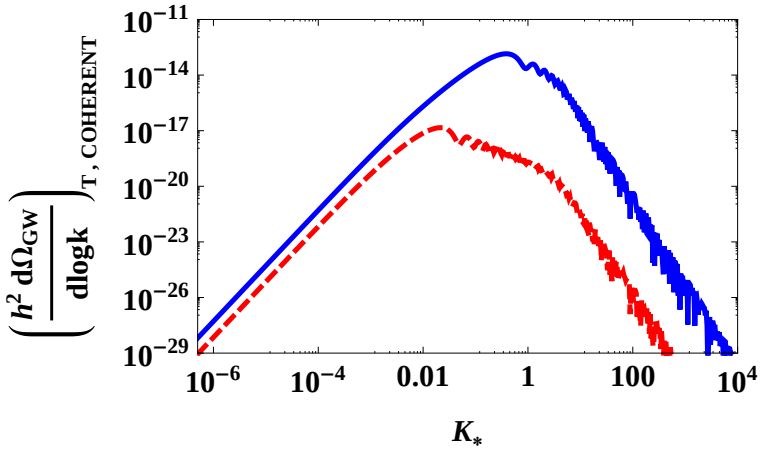

Figure 10. The GW energy density power spectrum from turbulence in the coherent case for $T_* = 100\,\mathrm{GeV}$, $\beta/\mathcal{H}_* = 100$, $v_b = 0.87$, $\gamma = 2/7$, and $g_{\rm fin} = 47.75$. Blue, solid: $\Omega_{T*}/\Omega_{\rm rad*} = 2/9$. The peak is at about $K_*^{\rm peak} \simeq 0.4$, not far from the value $L_*/\tau_L = 2(6\pi\mathcal{C}_v\Omega_{T*}/\Omega_{\rm rad*})^{1/2} \simeq 0.8$. The small scale behaviour for $K_* > K_*^{\rm peak}$ is $K_*^{-14/3}$. Red, dashed: $\Omega_{T*}/\Omega_{\rm rad*} = 2/3 \times 10^{-3}$. The peak position is at $K_* \simeq 0.02$, again not far from the value $L_*/\tau_L = 2(6\pi\mathcal{C}_v\Omega_{T*}/\Omega_{\rm rad*})^{1/2} \simeq 0.04$. In this case the slope K_*^{-1} for intermediate wave-numbers is well visible.

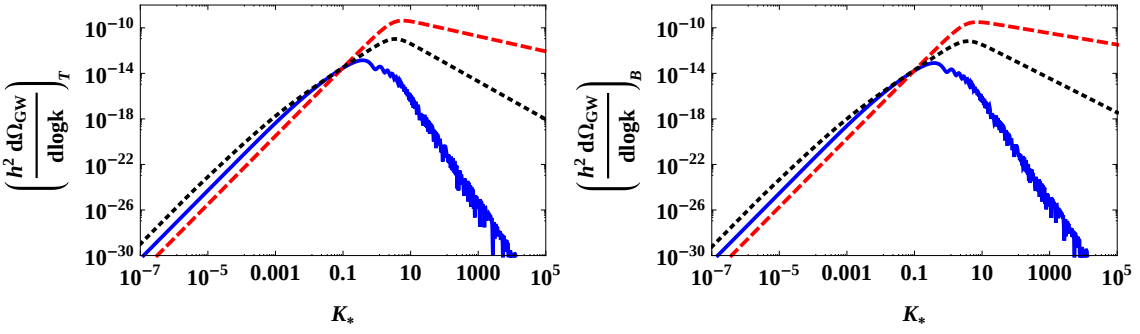

Figure 11. The GW energy density spectrum in the incoherent (red, long-dashed), top hat (black, short-dashed) and coherent (blue solid) cases. Left from turbulence, right from magnetic field, for $T_* = 100\,\mathrm{GeV}$, $\beta/\mathcal{H}_* = 100$, $\frac{\Omega_{S*}}{\Omega_{\rm rad*}} = 2/9$, $v_b = 0.87$, $\gamma = 2/7$, $g_{\rm fin} = 47.75$ (and $x_c = 1$ for the tophat case).

where

$$y_{\rm top} = \min\left[y_{\rm fin}\,,\ y + \frac{v_L\,x_c}{\pi\,K_*}\right]\,. \tag{5.12}$$

As in the incoherent case, the spectrum bears no relation with the time Fourier transform of the source (c.f. [14]). The integral in z can be estimated simply as the integrand evaluated at the lower bound, multiplied by one oscillation period: therefore, at high wave-numbers we expect the slope $K_*^{-5/3}$ for the turbulent case, and $K_*^{-3/2}$ for the magnetic field case. Moreover, the peak position corresponds to the spatial correlation scale of the source: $K_* \simeq 3.5$ for the turbulence and $K_* \simeq 3.7$ for the magnetic field.

JCAP12(2009)024

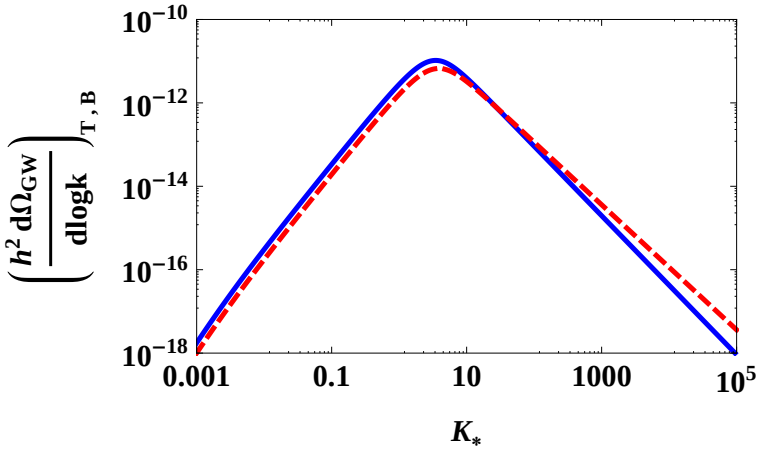

Figure 12. The GW energy density spectrum in the top hat case. Blue, solid from turbulence and red, dashed from the magnetic field for $T_* = 100\,\mathrm{GeV}$, $\beta/\mathcal{H}_* = 100$, $\frac{\Omega_{S*}}{\Omega_{\mathrm{rad}*}} = 2/9$, $v_b = 0.87$, $\gamma = 2/7$, $g_{\mathrm{fin}} = 47.75$, $x_c = 1$.

The result is shown in figure 11 and 12, for $x_c = 1$; the dependence on the value of $0 < x_c < \pi$ is weak. In this case the amplitude at the peak takes an intermediate value between the incoherent and coherent cases:

$$\left.\frac{d\Omega_{\mathrm{GW}}h_0^2}{d\log k}\right|^{(\mathrm{turb})}_{K_*^{\mathrm{peak}}} \simeq 10^{-11} \qquad K_*^{\mathrm{peak}} \simeq 3.5\,, \tag{5.13}$$

$$\left.\frac{d\Omega_{\mathrm{GW}}h_0^2}{d\log k}\right|^{(\mathrm{mag})}_{K_*^{\mathrm{peak}}} \simeq 7\times 10^{-12} \qquad K_*^{\mathrm{peak}} \simeq 3.7\,. \tag{5.14}$$

6 Discussion

6.1 Comparison with the gravitational wave spectrum from bubble collisions

In the case of bubble collisions [12], we have also studied the different assumptions for the unequal time power spectrum of the source: coherent, incoherent and top-hat. Numerical simulations of bubble collisions [13] indicate that the coherent case is the relevant one for bubbles. This can be understood by the following argument: we consider a bubble collision event starting at time t_n with tensor anisotropic stress given by $f_n(\mathbf{k}, t - t_n)$. Summing over all the collision events of the phase transition we obtain for the total anisotropic stress of bubble collisions (c.f. [14])

$$\langle \Pi(\mathbf{k},t)\Pi^*(\mathbf{k}',t')\rangle = \sum_{n=1}^{N}\sum_{m=1}^{N}\langle e^{i(\mathbf{k}\cdot\mathbf{x}_n - \mathbf{k}'\cdot\mathbf{x}_m)}\hat{f}_n(\mathbf{k}, t-t_n)\hat{f}_m^*(\mathbf{k}', t'-t_m)\rangle\,, \tag{6.1}$$

where $\mathbf{x}_n$ is the center of the n-th collision event. To recover the simulation result, we now have to make two fundamental assumptions. First we assume that different collision events are not correlated,

$$\langle e^{i(\mathbf{k}\cdot\mathbf{x}_n - \mathbf{k}'\cdot\mathbf{x}_m)}\rangle = V^{-1}\delta_{nm}\delta(\mathbf{k}-\mathbf{k}')\,, \tag{6.2}$$

JCAP12(2009)024

here the volume V restores the dimensions. This leads to

$$\Pi(k,t,t') = \frac{1}{(2\pi)^3 V}\sum_{n=1}^{N}\langle f_n(\mathbf{k},t-t_n)f_n^*(\mathbf{k},t'-t_n)\rangle\,. \tag{6.3}$$

Second, we assume that one typical collision event is totally coherent, so that $\langle f_n(\mathbf{k},\Delta t)f_n^*(\mathbf{k},\Delta t')\rangle = f(\mathbf{k},\Delta t)f^*(\mathbf{k},\Delta t')$ where $f(\mathbf{k},\Delta t) \equiv \sqrt{\langle|f_n(\mathbf{k},\Delta t)|^2\rangle}$ is the square root of the power spectrum of a typical collision event, and $\Delta t = t - t_n$. Furthermore, since bubbles only exist during the phase transition the duration of which is much shorter than one Hubble time, the expansion of the universe can be neglected and the anisotropic stress spectrum is a function of the time difference $t - t' = \Delta t - \Delta t'$ only. Equation (6.3) becomes

$$\Pi(k,t,t') = \frac{2N}{(2\pi)^3 V} f(\mathbf{k},\Delta t)f(\mathbf{k},\Delta t') = \sqrt{\Pi(k,t,t)\Pi(k,t',t')}\,, \tag{6.4}$$

which is the form of the coherent approximation. Therefore, assuming that one collision event is totally coherent in time and that different collisions are uncorrelated implies that bubble collisions represent a totally coherent source of GWs.

However, for turbulence, we do not expect this to hold. There are no well isolated uncorrelated events which can be treated independently. Besides, one expects correlations to decay in time over a timescale which is related to the spatial extension of the source. This has motivated the Kraichnan de-correlation ansatz given in [43] and eq. (3.33), which we have simplified to the the top hat de-correlation in section 4 in order to obtain a positive kernel, see eq. (4.6) and the discussion following it. To summarize, we can conclude that bubble collisions are well represented by the coherent case, while MHD turbulence is well represented by the top-hat case.

6.2 Comparison with short-lasting turbulence

Once MHD turbulence is generated, it decays following the 'absolute' time dependence described in section 3.2, which applies to freely decaying, non-helical turbulence. In this section we compare our results with the ones from MHD turbulence that lasts for less than one Hubble time and where the time-dependent decay is neglected. This was always assumed in previous analyses. This allows us to verify the general statements of section 2.3 in a more realistic case. Note however that, with respect to previous analyses which assumed either a discontinuous [17] or a stationary [15, 18, 20] source, here we consider a source with a finite time duration, but continuous in time. The importance of having a continuous source has been discussed in [14].

The aim of this section is simply to test the results of section 2.3 in a realistic case. We therefore concentrate only on the source from the turbulent velocity field, and we do not discuss the magnetic field for which the results are similar. We set the duration of the source to one eddy turnover time τ_L: $t_{\rm fin} = t_{\rm in} + \tau_L$ [15]. We model the switching on and off of the source with the same function as in bubble collisions [14]:

$$f(y) = 4y(1-y) \tag{6.5}$$

with $y = (t - t_{\rm in})/\tau_L$. Since L and $\Omega_T/\Omega_{\rm rad}$ do not evolve in time, the turbulent spectrum becomes

$$P_v(K_*) = \frac{3}{2}\mathcal{C}_v\,\frac{\Omega_{T*}}{\Omega_{\rm rad*}}\,L_*^3\,\frac{K_*^2}{[1+K_*^2]^{17/6}}f(y)\,, \tag{6.6}$$

JCAP12(2009)024

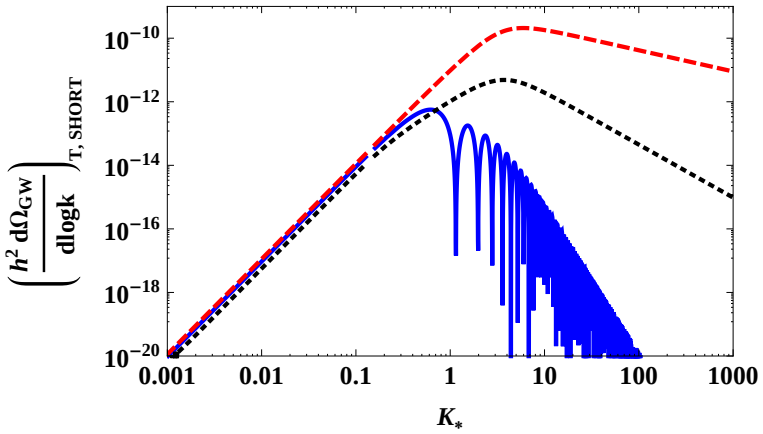

Figure 13. The GW energy density spectrum for short lasting turbulence. Blue, solid: coherent; black, short-dashed: top hat; red, long-dashed: incoherent.

and the anisotropic stress power spectrum is

$$\Pi(K_*, y, y) = \frac{9}{2}\,\pi\,\mathcal{C}_v^2 \left(\frac{\Omega_{T*}}{\Omega_{\rm rad*}}\right)^2 L_*^3\, \mathcal{I}_v(K_*)\, f^2(y)\,, \tag{6.7}$$

where $\mathcal{I}_v(K_*)$ is given by eq. (4.10) with $y = 1$. Inserting this in eq. (2.13) one finds after some manipulations

$$\left.\frac{d\Omega_{\rm GW}h_0^2}{d\log k}\right|_0 = 12(2\pi)^2\,\mathcal{C}_v^2\Omega_{{\rm rad},0}h_0^2 \left(\frac{g_0}{g_*}\right)^{\frac{1}{3}} \left(\frac{\Omega_{T*}}{\Omega_{\rm rad*}}\right)^2 (\mathcal{H}_*\tau_L)^2 K_*^3\, \mathcal{I}(K_*) \times \\ \times \int_0^1 dy \int_0^1 dz \cos\left(\frac{\pi\, K_*}{v_L}(y-z)\right) F(y,z) \tag{6.8}$$

with

$$F(y,z) = \begin{cases} f^2(y)\,\delta(y-z) & \text{incoherent} \\ f(y)\,f(z) & \text{coherent} \\ \frac{1}{2}\left[f^2(y)\Theta(z-y)\,\Theta\left(\frac{v_L\,x_c}{\pi\,K_*} - (z-y)\right) + y \leftrightarrow z\right] & \text{top hat.} \end{cases} \tag{6.9}$$

Figure 13 shows the GW energy density spectra from short lasting turbulence in the incoherent, coherent and top hat cases. The relative amplitudes between the different approximations is similar to the long lasting case and the peak positions are also not very different. In figure 14 we compare the long-lasting and the short-lasting cases.

One first notices that the change in amplitude of the GW spectrum is generically much less than expected from our general arguments in section 2.3. This is because our realistic source, unlike the one considered in section 2.3, is decaying with the decay time τ_L, which here corresponds to the duration of the short lasting source. Therefore, the fact that the source is long lasting does not amplify the signal as expected, because its characteristic decay time is the same as the duration of the short lasting source. In the incoherent approximation, the overall amplification of the long lasting source is about a factor two, instead of the factor $(\tau_L\mathcal{H}_*)^{-1}$ which we found for the toy model. The long lasting coherent approximation, on the other hand, is amplified at large scales by about a factor of $(\tau_L\mathcal{H}_*)^{-1} \simeq 80$ compared to

JCAP12(2009)024

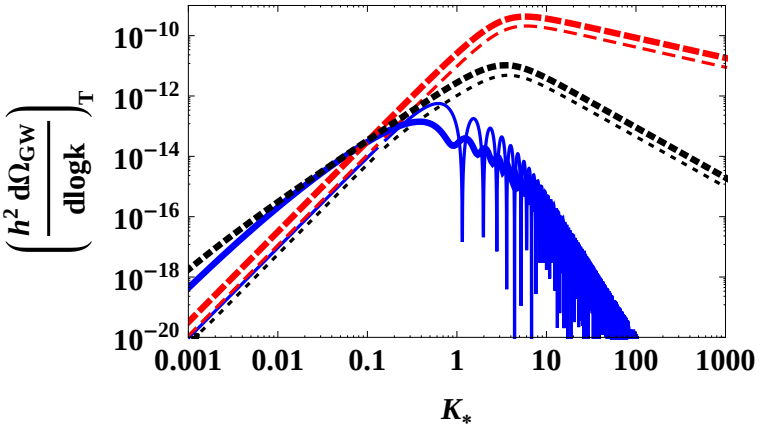

Figure 14. Comparison between the long-lasting case, represented by thick lines and the short-lasting one, represented by thin lines (incoherent: red, long-dashed; coherent: blue, solid; top hat: black, short-dashed).

the short lasting one, instead of the expected $(\tau_L \mathcal{H}_*)^{-2}$. As already seen in section 2.3, in the coherent case the signal at the peak from short-lasting turbulence is higher than the long-lasting result: this comes from the fact that in the long-lasting case interference can reduce the final amplitude if the source is present and coherent over several oscillation periods.

The top-hat case, which we did not analyze in section 2.3, shows an intermediate behavior between the incoherent and coherent ones: at long wavelengths, $K_* \ll K_*^{\rm peak}$, the long lasting signal is enhanced by about two orders of magnitude, i.e. the same amplification as for the coherent case, $(\tau_L \mathcal{H}_*)^{-1}$; around the peak, the long and short lasting top hat cases differ by about a factor two, equivalent to the incoherent case.

To summarize, due to the fact that the long lasting source decays with a characteristic time τ_L corresponding to the duration of the short lasting source, the amplification factor $(\tau_L \mathcal{H}_*)^{-2}$, expected at large scales, is reduced to $(\tau_L \mathcal{H}_*)^{-1}$ for the coherent and top-hat approximations, and the amplification is virtually absent in the incoherent approximation. In all cases it is a factor $(\tau_L \mathcal{H}_*)$ less than expected due to the rapid decay of the source.

7 Conclusion

In this work, we have calculated the GW emission from MHD turbulence generated during a first order phase transition and freely decaying afterwards. This is the first paper which takes into account the free decay of turbulence, and models the source in a continuous fashion.

For the source power spectrum we use a new ansatz that interpolates analytically between the large scale and small scale behaviors, determined respectively by causality and by the Kolmogorov (or Iroshnikov-Kraichnan) theory. Previous analyses had either considered only the Kolmogorov range, ignoring the large scale part of the spectrum and continuing the Kolmogorov slope up to the peak [15, 16, 18, 20], or joined the two behaviors at the peak [17]. This caused an overestimation of the source spectrum amplitude at the peak of about a factor six, leading to an overestimation of nearly two orders of magnitude for the GW spectrum (c.f. for example eq. (56) of [17]). The interpolating formula which we adopt here models the spectrum of MHD turbulence in a more realistic way.

JCAP12(2009)024

We also take into account the time de-correlation of MHD turbulence following the model proposed by Kraichnan in [43]. However, in order to recover a positive result for the GW energy density spectrum, we cannot directly apply the Kraichnan de-correlation in the velocity and magnetic field power spectra, but we have to model it in Fourier space as a de-correlation of the anisotropic stress power spectrum. We claim that in the case of MHD turbulence, neither the coherent [17] nor the stationary [15, 18, 20] approximations previously used in the literature are the correct ones, but the anisotropic stresses at different times have to be modeled in a way similar to our top hat ansatz.

Moreover, previous analyses have considered either a MHD source which is discontinuous in time (i.e. instantaneous turning on of the Kolmogorov spectrum) [17] or a source which is stationary (i.e. neglecting the fact that the source is actually turned on and off) [15, 18, 20]. Here instead the source is continuous in time, starting with zero energy and building up the Kolmogorov spectrum after one eddy turnover time. It then starts free decay, since the stirring due to the phase transition lasts only for about one eddy turnover time. Due to the free decay, the source is absent on scales smaller than the time dependent Kolmogorov microscale, and is completely dissipated once the Kolmogorov microscale has reached the energy injection scale and the entire Kolmogorov range has decayed. We have evaluated the temperature of the universe, $T_{\rm fin}$, at which this happens, as a function of the temperature at which MHD turbulence is generated, T_*, and we have found that the process of dissipation lasts for many Hubble times. For instance, for the EW phase transition, $T_* \sim 100\,\mathrm{GeV}$ and $T_{\rm fin} \sim 120\,\mathrm{MeV}$. Therefore, MHD turbulence has to be modeled as a long lasting GW source. Nevertheless, since the characteristic decay time of the source is still given by the eddy turnover time which is much smaller than the expansion time of the Universe, the amplification due to the long duration is less significant than what is expected from a source which is not decaying in time. Especially the peak amplitude is enhanced only by about a factor of two due to the long duration of the source. On the other hand, the long duration of the source becomes important on very large scales: here the GW spectrum from the long lasting source is amplified with respect to the short lasting case by about two orders of magnitude.

The top hat ansatz together with the time continuity of the source have some interesting consequences on the peak position and amplitude of the GW spectrum. In ref. [14] it has been shown that, in the coherent case, time continuity affects the slope of the spectrum at small scales and also moves the peak of the GW spectrum from the characteristic length scale of the source (here L_*) to its characteristic time scale (here τ_L). If the two scales are well separated (for instance if the fluid velocity is significantly smaller than the speed of light), this causes a reduction of the amplitude at the peak. The fact that for MHD turbulence the top hat ansatz is the relevant one, fixes the peak position of the GW spectrum at the characteristic length scale of the turbulent source.

To summarize, our final result for the GW spectrum from MHD turbulence for the most realistic case, the top-hat de-correlation, has the following main features:

- The peak frequency is given by $K_* \simeq 3.5$ for the turbulence and $K_* \simeq 3.7$ for the magnetic field. Given the degree of precision of our analytical estimate, we can neglect

JCAP12(2009)024

this small difference. The peak frequency from MHD turbulence thus corresponds to

$$
\begin{aligned}
f_{\rm peak}^{\rm MHD} &= \frac{k_{\rm peak}}{2\pi} \simeq \frac{3.5}{L_*} = 3.5\,\frac{\beta}{2v_b} \\
&\simeq 3\times 10^{-2}\,{\rm mHz}\,\left(\frac{g_*}{100}\right)^{1/6}\,\frac{T_*}{100\,{\rm GeV}}\,\frac{\beta}{\mathcal{H}_*}\,\frac{1}{v_b} \\
&\simeq 3.4\ {\rm mHz}\,,
\end{aligned}
\tag{7.1}
$$

where we have used $\mathcal{H}_* = (g_0/g_*)^{1/6}\,(T_*/T_0)\,H_0\sqrt{\Omega_{\rm rad}}$, and the last line gives the value for the EW phase transition with $\beta/\mathcal{H}_* = 100$, $T_* = 100\,{\rm GeV}$, $v_f = 1/\sqrt{3}$ and $v_b \simeq 0.87$.

- The peak amplitude for the above values of the parameters is $h_0^2\Omega_{\rm GW}(K_*^{\rm peak}) \simeq 10^{-11}$. Using that $h(f) = 1.26\times 10^{-15}\sqrt{h_0^2\Omega_{\rm GW}(f)}({\rm mHz}/f)$ (see [63]), we obtain the maximal GW amplitude $h(f_{\rm peak}) \simeq 2\times 10^{-21}$ which is detectable with LISA (see figure 15). The suppression of the peak amplitude by more than one order of magnitude compared e.g. to ref. [18], is mainly due to the fact that we use the more realistic interpolating spectrum for the MHD turbulent source (see figure 4).

- The slope of $d\Omega_{\rm GW}/d\log(k)$ is the usual k^3 on large scales $k < k_{\rm peak}$, but on small scales, $k > k_{\rm peak}$, it decays only like $k^{-5/3}$ and $k^{-3/2}$ for turbulence and magnetic field respectively, see figure 12.

In figures 15 and 16 we compare the GW spectrum from MHD turbulence with the experimental sensitivities of LISA [25], AGIS [64], LIGO [65] and the Big Bang Observer (BBO) [66]. Note that the sensitivity curve of LISA plotted in the figures represents only the noise of the instrument, and the data analysis can actually improve the detection down to a level of $h_0^2\Omega_{\rm GW} \sim 5\times 10^{-13}$ [67].

With respect to the GW signal from bubble collisions analyzed in ref. [12], the peak frequency of the GW spectrum from MHD turbulence is larger by about a factor two. Note however that, as already pointed out in [14], the work of ref. [12] has to be corrected in two aspects: first, the source analyzed there was not continuous, and secondly, the relevant approximation for the anisotropic stresses generated by bubble collisions is the coherent and not the top hat one. These modifications are work in progress and may well lead to some correction in the results of [12]. The peak amplitude of the GW signal from MHD turbulence is somewhat higher than the signal from bubble collisions, but it decays faster than the k^{-1} decay which has been seen in the latest simulations of bubble collisions [13].

Nevertheless, there is still considerable uncertainty in our analytical modeling which probably can only be addressed by numerical simulations of relativistic MHD turbulence of the kind developed after a first order phase transition. For example, in this work we have added the results from the turbulent velocity field and the magnetic field incoherently. One could argue, however, that these fields are correlated and have both a Kolmogorov spectrum in the inertial range. One could then use $s_i = b_i + v_i \simeq 2v_i$ as transverse vector-field with $\Pi_{ij}(\mathbf{s}) \simeq 4\Pi_{ij}(\mathbf{v})$. Instead of the results presented here we would then obtain 16 times the GW energy density spectrum from turbulence, which would enhance the total result for $\Omega_{\rm GW}$ by about a factor of 8 and the one for $h(f)$ by $\sqrt{8}$. Therefore, our results are probably to be taken within about a factor of a few for the GW amplitude $h(f)$ and within an order of magnitude for the energy density $d\Omega_{\rm GW}/d\log(k)$.

JCAP12(2009)024

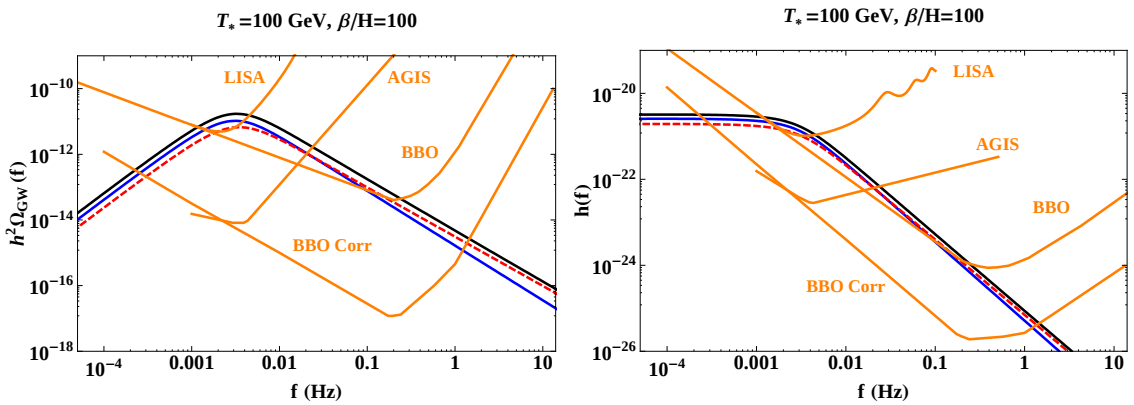

Figure 15. The GW energy density (left) and the GW characteristic amplitude (right) from turbulence only (blue, solid), magnetic field only (red, dashed) and the total MHD turbulence (black, solid) generated at the EW phase transition with $T_* = 100\,\mathrm{GeV}$, $\beta/\mathcal{H}_* = 100$, $\Omega_{S*}/\Omega_{\mathrm{rad}*} = 2/9$, $v_b = 0.87$, $\gamma = 2/7$, $x_c = 1$ and $g_{\mathrm{fin}} = 47.75$, together with the sensitivities of LISA [25], BBO [66], AGIS [64] and 'BBO Corr' (improved from BBO with data analysis) taken from [68].

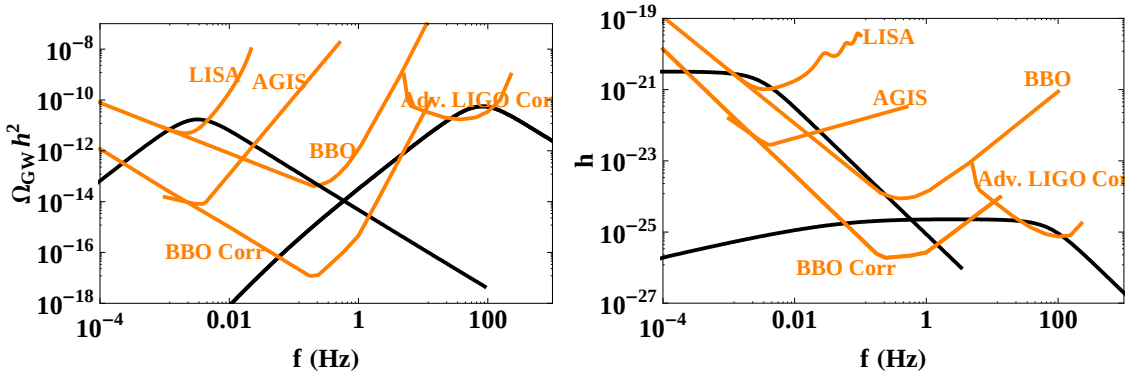

Figure 16. Sensitivities of LISA, AGIS, BBO and Advanced LIGO (orange) compared with two GW spectra (black) generated by MHD turbulence from a phase transition at respectively $T_* = 100\,\mathrm{GeV}$ with $\beta/\mathcal{H}_* = 100$, and $T_* = 5.10^6\,\mathrm{GeV}$ with $\beta/\mathcal{H}_* = 50$; $\Omega_{S*}/\Omega_{\mathrm{rad}*} = 2/9$, $v_b = 0.87$, $\gamma = 2/7$, and $x_c = 1$. The Advanced LIGO sensitivity is optimized by making use of correlations between two ground-based detectors [69].

Acknowledgments

We thank Kandu Subramanian for useful suggestions, and we acknowledge discussions with Axel Brandenburg, Karsten Jedamzik and Tina Kahniashvili. We are grateful for the hospitality of Nordita where this work was completed. RD acknowledges support from the Swiss National Science Foundation. The work of GS is supported by the European Research Council. CC thanks the University of Geneva and CERN for hospitality.

JCAP12(2009)024

A Analytical expressions for section 2.3

Here we give the full expression for eqs. (2.19) and (2.22).

- **Incoherent constant source**

$$F(t_{\rm in},t_{\rm fin},\Delta t)=\begin{cases}\left(\frac{g_0}{g_{\rm fin}}\right)^{\frac{1}{3}}8\Big[1-\frac{t_{\rm fin}}{\Delta t}\log\left(\frac{t_{\rm fin}}{t_{\rm fin}-\Delta t/2}\right)-\frac{t_{\rm in}}{\Delta t}\log\left(\frac{t_{\rm in}+\Delta t/2}{t_{\rm in}}\right)\Big]\\ \simeq\left(\frac{g_0}{g_{\rm fin}}\right)^{\frac{1}{3}}\frac{\Delta t}{t_{\rm in}} \qquad \text{long-lasting,}\\ \left(\frac{g_0}{g_*}\right)^{\frac{1}{3}}\frac{(2\pi)^2}{3}\left(\frac{\Delta t}{t_{\rm in}}\right)^2 \qquad \text{short-lasting.}\end{cases} \tag{A.1}$$

- **Coherent constant source**

$$F(x_{\rm in},x_{\rm fin},\Delta x)=\begin{cases}\left(\frac{g_0}{g_{\rm fin}}\right)^{\frac{1}{3}}\frac{4}{\Delta x^2}\Big\{\Big[x_{\rm fin}{\rm Ci}(x_{\rm fin})+x_{\rm in}{\rm Ci}(x_{\rm in})\\ \quad-(x_{\rm fin}-\Delta x/2){\rm Ci}(x_{\rm fin}-\Delta x/2)-(x_{\rm in}+\Delta x/2){\rm Ci}(x_{\rm in}+\Delta x/2)\\ \quad-\sin(x_{\rm fin})-\sin(x_{\rm in})+\sin(x_{\rm fin}-\Delta x/2)+\sin(x_{\rm in}+\Delta x/2)\Big]^2\\ \quad+\Big[x_{\rm fin}{\rm Si}(x_{\rm fin})+x_{\rm in}{\rm Si}(x_{\rm in})\\ \quad-(x_{\rm fin}-\Delta x/2){\rm Si}(x_{\rm fin}-\Delta x/2)-(x_{\rm in}+\Delta x/2){\rm Si}(x_{\rm in}+\Delta x/2)\\ \quad+\cos(x_{\rm fin})+\cos(x_{\rm in})-\cos(x_{\rm fin}-\Delta x/2)-\cos(x_{\rm in}+\Delta x/2)\Big]^2\Big\}\\ \quad\simeq\left(\frac{g_0}{g_{\rm fin}}\right)^{\frac{1}{3}}\Big[({\rm Ci}(x_{\rm fin})-{\rm Ci}(x_{\rm in}))^2+({\rm Si}(x_{\rm fin})-{\rm Si}(x_{\rm in}))^2\Big]+\mathcal{O}(\Delta x)\\ \quad\text{long-lasting}\,,\\ \left(\frac{g_0}{g_*}\right)^{\frac{1}{3}}\frac{64(2\pi)^2}{x_{\rm in}^2}\frac{\sin^4((x_{\rm fin}-x_{\rm in})/4)}{(x_{\rm fin}-x_{\rm in})^2} \qquad \text{short-lasting.}\end{cases}$$

B Viscosity and magnetic diffusivity

The Reynolds number defined in eq. (3.1) is inversely proportional to the kinematic viscosity ν given by

$$\nu=\frac{\bar\eta}{\rho+p}, \tag{B.1}$$

where $\bar\eta$ is the shear viscosity. The kinematic viscosity is the transport coefficient that characterizes the diffusion of transverse momentum due to collisions in a medium, and is roughly the mean free path $\ell_{\rm mfp}$ of excitations. In fact one has [70]

$$\bar\eta=\frac{4}{15}\frac{\pi^2}{30}g_*T^4\,\ell_{\rm mfp} \qquad \text{so that} \qquad \nu=\frac{\ell_{\rm mfp}}{5}\,. \tag{B.2}$$

The largest viscosity comes from the weakest interactions, since it is inversely proportional to the scattering cross section of the processes responsible for transport. Simple parametric

JCAP12(2009)024

estimates using kinetic theory show that the shear viscosity at high temperature (where T is much larger than the mass of the diffusing particle) behaves as (to leading-log accuracy):

$$\bar{\eta} = C \frac{T^3}{g^4 \log g^{-1}} \tag{B.3}$$

where g is the appropriate coupling constant (depending on the temperature and the length scale at which one wants to compute the Reynolds number) and C is a numerical coefficient that can only be obtained from a detailed analysis.

After EW symmetry breaking, neutrino interactions are suppressed by a factor $(T/M_W)^4$. In this regime, neutrinos have the longest mean free path and dominate the viscosity. We use [71]

$$\ell_{\rm mfp} \approx (3 G_F^2 T^5)^{-1} \,, \tag{B.4}$$

leading to

$$\nu(T \lesssim 100 \text{ GeV}) \approx 4.9 \times 10^8 \, \frac{\text{GeV}^4}{T^5} \,. \tag{B.5}$$

At temperatures smaller than 100 MeV, after the QCD phase transition, the particle content changes and consequently the neutrino mean free path increases to

$$\ell_{\rm mfp} \approx \frac{10}{9} (G_F^2 T^5)^{-1} \tag{B.6}$$

leading to

$$\nu(T \lesssim 100 \text{ MeV}) \approx 1.6 \times 10^9 \, \frac{\text{GeV}^4}{T^5} \,. \tag{B.7}$$

At temperatures above the EW phase transition, neutrino interactions are no longer suppressed. The shear viscosity is dominated by right handed lepton transport and given by [72]

$$\bar{\eta} \approx \left(\frac{5}{2}\right)^3 \zeta(5)^2 \left(\frac{12}{\pi}\right)^5 \frac{3/2}{9\pi^2 + 224(5+1/2)} \frac{T^3}{g'^4 \log g'^{-1}} \tag{B.8}$$

where g' is the hypercharge coupling. This leads to

$$\nu(T \gtrsim 100 \text{ GeV}) \approx \frac{21.6}{T} \,. \tag{B.9}$$

The evolution of ν with temperature is plotted in figure 17. The neutrinos remain the relevant particles controlling the viscosity until they decouple at $T \sim 1.4\,\text{MeV}$, after which photons take over. Even if there was some source of turbulence after the EW phase transition, turbulence is expected to terminate anyway around 1 MeV. Indeed, e^+e^- annihilation reduces the plasma electron population and increases the photon diffusion length hence also the kinematic viscosity, leading to a decrease of the Reynolds number below one.

Since we have only found non-relativistic derivations in the literature [31, 55, 73], let us estimate here in some detail the magnetic diffusivity and the magnetic Prandl number for relativistic electrons in the cosmic plasma with temperatures $1\,\text{MeV} < T < 100\,\text{GeV}$,

$$\text{P}_{\rm m}(T) \equiv \frac{\text{R}_{\rm m}(L,T)}{\text{Re}\,(L,T)} = \frac{\nu(T)}{\mu(T)} \,. \tag{B.10}$$

We want to determine $\text{P}_{\rm m}(T)$ when the electrons are relativistic and their dominant interactions are electromagnetic.

JCAP12(2009)024

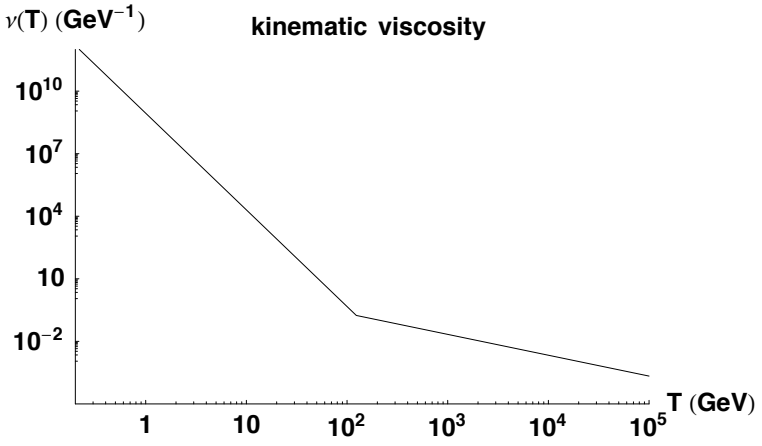

Figure 17. Evolution with temperature of the kinematic viscosity $\nu(T)$.

To determine the magnetic diffusivity $\mu(T)$ we derive an expression for the conductivity $\sigma(T)$. The Lorentz force acting on an electron is

$$m_e \frac{du^\mu}{d\tau} = eF^{\mu\nu}u_\nu \,.$$

If we average this equation over a fluid element containing many electrons, the magnetic field term is sub-dominant. Even though the electrons are highly relativistic, the average fluid velocity is small. Furthermore $\gamma = 1/\sqrt{1-v_e^2} \simeq T/m_e$ is nearly constant and we may neglect the contribution $d\gamma/d\tau$ from $du^i/d\tau = d(\gamma v^i)/d\tau$ above. With $d\tau = \gamma^{-1}dt = (m_e/T)dt$, this yields the following equation for the mean velocity of the electron fluid:

$$\frac{d\mathbf{v}}{dt} = \frac{e}{T}\,\mathbf{E}\,.$$

If we denote the collision time for the electrons by t_c, they can acquire velocities of the order $\mathbf{v} \simeq \frac{e}{T}\,\mathbf{E}\,t_c$ between successive collisions. Hence the current is

$$\mathbf{J} \simeq en_e\mathbf{v} \simeq t_c\frac{e^2 n_e}{T}\mathbf{E} \equiv \sigma\mathbf{E}$$

so that the conductivity becomes

$$\sigma = t_c\frac{e^2 n_e}{T}\,.$$

We now derive an estimate for t_c from Coulomb interactions. For a strong collision between the electron and another charged particle we need an impact parameter b such that $e^2/b > E_e \simeq T$. Hence the cross section becomes $\sigma_t \sim \pi b^2 \simeq \pi e^4/T^2$ (this simple argumentation neglects the Coulomb logarithms which enhance the cross section by $\ln(1/\alpha_{\rm min})$ where $\alpha_{\rm min}$ is the minimal deflection angle [73]). With $v_e = 1$ the time between collisions is therefore $t_c = 1/(\sigma_t n_e) \simeq T^2/(\pi e^4 n_e)$ and

$$\sigma \simeq \frac{T}{\pi e^2}\,. \tag{B.11}$$

JCAP12(2009)024

Note that this result is independent of the electron density. This is physically sensible as n_e enhances the current on the one hand but it reduces in the same way the collision time.

With (B.11) we obtain for the magnetic diffusivity

$$\mu(T) \equiv \frac{1}{4\pi\sigma} \simeq \frac{e^2}{4T} \simeq \frac{10^{-3}}{T}\,. \tag{B.12}$$

Inserting the kinematic viscosity from eqs. (B.5) or (B.7) we obtain for the Prandl number

$$\mathrm{P_m} = \frac{\nu}{\mu} \simeq 10^{12} \left(\frac{\mathrm{GeV}}{T}\right)^4\,. \tag{B.13}$$

This number is larger than 1 for all temperatures $1\,\mathrm{MeV} < T < 100\,\mathrm{GeV}$ where the derivation applies. Hence currents and magnetic fields can develop and we are in the regime where MHD turbulence applies.

C The unequal time anisotropic stress power spectrum

As mentioned in the main text, the unequal time anisotropic stress power spectrum $\Pi(k, t_1, t_2)$ is given by the convolution of the unequal time source power spectrum. The details of the derivation (for the formally identical case of a magnetic field) can be found in ref. [21]; here we just give its main steps. One starts with eq. (4.3). Wick's theorem gives

$$\begin{aligned}\langle v^i(\mathbf{k}) v^{*j}(\mathbf{q}) v^n(\mathbf{s}) v^{*m}(\mathbf{p})\rangle = \\ = \langle v^i(\mathbf{k}) v^{*j}(\mathbf{q})\rangle \langle v^n(\mathbf{s}) v^{*m}(\mathbf{p})\rangle + \\ \langle v^i(\mathbf{k}) v^n(\mathbf{s})\rangle \langle v^{*j}(\mathbf{q}) v^{*m}(\mathbf{p})\rangle + \\ \langle v^i(\mathbf{k}) v^{*m}(\mathbf{p})\rangle \langle v^n(\mathbf{s}) v^{*j}(\mathbf{q})\rangle\,.\end{aligned} \tag{C.1}$$

This has to be inserted in eq. (4.3) together with the definition of the velocity power spectrum (3.32). Applying the projection operator gives the angular dependence,

$$\begin{aligned}\mathcal{P}^{abcd}(\hat{\mathbf{k}})[(\delta^{ac} - \hat{q}^a\hat{q}^c)(\delta^{bd} - (\widehat{\mathbf{k}-\mathbf{q}})^b(\widehat{\mathbf{k}-\mathbf{q}})^d) \\ + (\delta^{ad} - \hat{q}^a\hat{q}^d)(\delta^{bc} - (\widehat{\mathbf{k}-\mathbf{q}})^b(\widehat{\mathbf{k}-\mathbf{q}})^c)] = \\ = 1 + (\hat{\mathbf{k}}\cdot(\widehat{\mathbf{k}-\mathbf{q}}))^2 + (\hat{\mathbf{k}}\cdot\hat{\mathbf{q}})^2 + (\hat{\mathbf{k}}\cdot\hat{\mathbf{q}})^2(\hat{\mathbf{k}}\cdot(\widehat{\mathbf{k}-\mathbf{q}}))^2\,.\end{aligned} \tag{C.2}$$

Comparing then with eq. (4.1), one arrives at the result:

$$\Pi_v(k, t_1, t_2) = \int d^3p P_v(p, t_1, t_2) P_v(|\mathbf{k}-\mathbf{p}|, t_1, t_2)(1+\gamma^2)(1+\beta^2)\,, \tag{C.3}$$

with $\gamma = \hat{\mathbf{k}}\cdot\hat{\mathbf{p}}$, $\beta = \hat{\mathbf{k}}\cdot\widehat{\mathbf{k}-\mathbf{p}}$.

References

[1] R. Durrer, *The cosmic microwave background*, Cambridge University Press, Cambridge U.K. (2008).

[2] See for example A. Starobinsky, *Relict gravitation radiation spectrum and initial state of the universe* (in Russian), *Pisma Zh. Eksp. Teor. Fiz.* **30** (1979) 719 [*JETP Lett.* **30** (1979) 682] [SPIRES];
V. Mukhanov, *Physical foundations of cosmology*, Cambridge University Press, Cambridge U.K. (2005).

JCAP12(2009)024

[3] See for example L. Randall and G. Servant, *Gravitational waves from warped spacetime*, *JHEP* **05** (2007) 054 [hep-ph/0607158] [SPIRES];
R. Durrer and M. Ruser, *The dynamical Casimir effect in braneworlds*, *Phys. Rev. Lett.* **99** (2007) 071601 [arXiv:0704.0756] [SPIRES].

[4] See for example R. Durrer, M. Kunz and A. Melchiorri, *Cosmic Microwave Background anisotropies from scaling seeds: global defect models*, *Phys. Rev.* **D 59** (1999) 123005 [astro-ph/9811174] [SPIRES];
N. Bevis, M. Hindmarsh, M. Kunz and J. Urrestilla, *CMB power spectrum contribution from cosmic strings using field-evolution simulations of the Abelian Higgs model*, *Phys. Rev.* **D 75** (2007) 065015 [astro-ph/0605018] [SPIRES];
L. Leblond, B. Shlaer and X. Siemens, *Gravitational waves from broken cosmic strings: the bursts and the beads*, *Phys. Rev.* **D 79** (2009) 123519 [arXiv:0903.4686] [SPIRES].

[5] R. Easther, J.T. Giblin Jr. and E.A. Lim, *Gravitational wave production at the end of inflation*, *Phys. Rev. Lett.* **99** (2007) 221301 [astro-ph/0612294] [SPIRES];
J. Garcia-Bellido and D.G. Figueroa, *A stochastic background of gravitational waves from hybrid preheating*, *Phys. Rev. Lett.* **98** (2007) 061302 [astro-ph/0701014] [SPIRES];
J. Garcia-Bellido, D.G. Figueroa and A. Sastre, *A gravitational wave background from reheating after hybrid inflation*, *Phys. Rev.* **D 77** (2008) 043517 [arXiv:0707.0839] [SPIRES];
J.F. Dufaux, A. Bergman, G.N. Felder, L. Kofman and J.-P. Uzan, *Theory and numerics of gravitational waves from preheating after inflation*, *Phys. Rev.* **D 76** (2007) 123517 [arXiv:0707.0875] [SPIRES].

[6] E. Witten, *Cosmic separation of phases*, *Phys. Rev.* **D 30** (1984) 272 [SPIRES].

[7] C. Hogan, *Gravitational radiation from cosmological phase transitions*, *Mon. Not. Roy. Astron. Soc.* **218** (1986) 629.

[8] A. Kosowsky, M.S. Turner and R. Watkins, *Gravitational radiation from colliding vacuum bubbles*, *Phys. Rev.* **D 45** (1992) 4514 [SPIRES].

[9] A. Kosowsky, M.S. Turner and R. Watkins, *Gravitational waves from first order cosmological phase transitions*, *Phys. Rev. Lett.* **69** (1992) 2026 [SPIRES].

[10] A. Kosowsky and M.S. Turner, *Gravitational radiation from colliding vacuum bubbles: envelope approximation to many bubble collisions*, *Phys. Rev.* **D 47** (1993) 4372 [astro-ph/9211004] [SPIRES].

[11] M. Kamionkowski, A. Kosowsky and M.S. Turner, *Gravitational radiation from first order phase transitions*, *Phys. Rev.* **D 49** (1994) 2837 [astro-ph/9310044] [SPIRES].

[12] C. Caprini, R. Durrer and G. Servant, *Gravitational wave generation from bubble collisions in first-order phase transitions: an analytic approach*, *Phys. Rev.* **D 77** (2008) 124015 [arXiv:0711.2593] [SPIRES].

[13] S.J. Huber and T. Konstandin, *Gravitational wave production by collisions: more bubbles*, *JCAP* **09** (2008) 022 [arXiv:0806.1828] [SPIRES].

[14] C. Caprini et al., *General properties of the gravitational wave spectrum from phase transitions*, *Phys. Rev.* **D 79** (2009) 083519 [arXiv:0901.1661] [SPIRES].

[15] A. Kosowsky, A. Mack and T. Kahniashvili, *Gravitational radiation from cosmological turbulence*, *Phys. Rev.* **D 66** (2002) 024030 [astro-ph/0111483] [SPIRES].

[16] A.D. Dolgov, D. Grasso and A. Nicolis, *Relic backgrounds of gravitational waves from cosmic turbulence*, *Phys. Rev.* **D 66** (2002) 103505 [astro-ph/0206461] [SPIRES].

[17] C. Caprini and R. Durrer, *Gravitational waves from stochastic relativistic sources: primordial turbulence and magnetic fields*, *Phys. Rev.* **D 74** (2006) 063521 [astro-ph/0603476] [SPIRES].

[18] G. Gogoberidze, T. Kahniashvili and A. Kosowsky, *The spectrum of gravitational radiation from primordial turbulence*, *Phys. Rev.* **D 76** (2007) 083002 [arXiv:0705.1733] [SPIRES].

JCAP12(2009)024

[19] A. Megevand, *Gravitational waves from deflagration bubbles in first-order phase transitions*, *Phys. Rev.* **D 78** (2008) 084003 [arXiv:0804.0391] [SPIRES].

[20] T. Kahniashvili, L. Campanelli, G. Gogoberidze, Y. Maravin and B. Ratra, *Gravitational radiation from primordial helical inverse cascade MHD turbulence*, *Phys. Rev.* **D 78** (2008) 123006 [*Erratum ibid.* **D 79** (2009) 109901] [arXiv:0809.1899] [SPIRES].

[21] C. Caprini and R. Durrer, *Gravitational wave production: a strong constraint on primordial magnetic fields*, *Phys. Rev.* **D 65** (2001) 023517 [astro-ph/0106244] [SPIRES].

[22] C. Caprini and R. Durrer, *Limits on stochastic magnetic fields: a defense of our paper*, *Phys. Rev.* **D 72** (2005) 088301 [astro-ph/0504553] [SPIRES].

[23] T. Kahniashvili, L. Kisslinger and T. Stevens, *Gravitational radiation generated by magnetic fields in cosmological phase transitions*, arXiv:0905.0643 [SPIRES].

[24] C. Caprini, R. Durrer and E. Fenu, *Can the observed large scale magnetic fields be seeded by helical primordial fields?*, *JCAP* **11** (2009) 001 [arXiv:0906.4976] [SPIRES].

[25] *LISA, the Laser Interferometer Space Antenna homepage*, http://lisa.jpl.nasa.gov/.

[26] R. Apreda, M. Maggiore, A. Nicolis and A. Riotto, *Gravitational waves from electroweak phase transitions*, *Nucl. Phys.* **B 631** (2002) 342 [gr-qc/0107033] [SPIRES].

[27] A. Nicolis, *Relic gravitational waves from colliding bubbles and cosmic turbulence*, *Class. Quant. Grav.* **21** (2004) L27 [gr-qc/0303084] [SPIRES].

[28] C. Grojean and G. Servant, *Gravitational waves from phase transitions at the electroweak scale and beyond*, *Phys. Rev.* **D 75** (2007) 043507 [hep-ph/0607107] [SPIRES].

[29] C.J. Hogan, *Magnetohydrodynamic effects of a first-order cosmological phase transition*, *Phys. Rev. Lett.* **51** (1983) 1488 [SPIRES];
J.M. Quashnock et al., *Magnetic field generation during the cosmological QCD phase transition*, *Astrophys. J.* **344** (1989) L49;
T. Vachaspati, *Magnetic fields from cosmological phase transitions*, *Phys. Lett.* **B 265** (1991) 258 [SPIRES];
B. Cheng and A.V. Olinto, *Primordial magnetic fields generated in the quark-hadron transition*, *Phys. Rev.* **D 50** (1994) 2412 [SPIRES];
T.W.B. Kibble and A. Vilenkin, *Phase equilibration in bubble collisions*, *Phys. Rev.* **D 52** (1995) 679 [hep-ph/9501266] [SPIRES];
G. Baym, D. Bödeker and L.D. McLerran, *Magnetic fields produced by phase transition bubbles in the electroweak phase transition*, *Phys. Rev.* **D 53** (1996) 662 [hep-ph/9507429] [SPIRES];
G. Sigl, A.V. Olinto and K. Jedamzik, *Primordial magnetic fields from cosmological first order phase transitions*, *Phys. Rev.* **D 55** (1997) 4582 [astro-ph/9610201] [SPIRES];
M. Joyce and M.E. Shaposhnikov, *Primordial magnetic fields, right electrons and the Abelian anomaly*, *Phys. Rev. Lett.* **79** (1997) 1193 [astro-ph/9703005] [SPIRES];
J. Ahonen and K. Enqvist, *Magnetic field generation in first order phase transition bubble collisions*, *Phys. Rev.* **D 57** (1998) 664 [hep-ph/9704334] [SPIRES];
D. Boyanovsky and H.J. de Vega, *Primordial magnetic fields from out of equilibrium cosmological phase transitions*, *AIP Conf. Proc.* **784** (2005) 434 [astro-ph/0502212] [SPIRES];
A. Diaz-Gil, J. Garcia-Bellido, M. Garcia Perez and A. Gonzalez-Arroyo, *Magnetic field production during preheating at the electroweak scale*, *Phys. Rev. Lett.* **100** (2008) 241301 [arXiv:0712.4263] [SPIRES];
T. Stevens and M.B. Johnson, *Magnetic seed field generation from electroweak bubble collisions, with bubble walls of finite thickness*, *Phys. Rev.* **D 80** (2009) 083011 [arXiv:0903.2227] [SPIRES].

[30] P.A. Davidson, *Turbulence*, Oxford University Press, Oxford U.K. (2004).

[31] D. Biskamp, *Magnetohydrodynamical turbulence*, Cambridge University Press, Cambridge U.K. (2003).

JCAP12(2009)024

[32] P. Olesen, *On inverse cascades in astrophysics*, *Phys. Lett.* **B 398** (1997) 321 [astro-ph/9610154] [SPIRES].

[33] T. Shiromizu, *Inverse cascade of primordial magnetic field in MHD turbulence*, *Phys. Lett.* **B 443** (1998) 127 [astro-ph/9810339] [SPIRES].

[34] D.T. Son, *Magnetohydrodynamics of the early universe and the evolution of primordial magnetic fields*, *Phys. Rev.* **D 59** (1999) 63008.

[35] L. Campanelli, *Scaling laws in MHD turbulence*, *Phys. Rev.* **D 70** (2004) 083009 [astro-ph/0407056] [SPIRES]; *Evolution of magnetic fields in freely decaying magnetohydrodynamic turbulence*, *Phys. Rev. Lett.* **98** (2007) 251302 [arXiv:0705.2308] [SPIRES].

[36] See for example M.R. Smith et al., *Decay of vorticity in homogeneous turbulence*, *Phys. Rev. Lett.* **71** (1993) 2583.

[37] D. Biskamp and W.C. Muller, *Decay laws for three-dimensional magnetohydrodynamic turbulence*, *Phys. Rev. Lett.* **83** (1999) 2195.

[38] M. Christensson, M. Hindmarsh and A. Brandenburg, *Inverse cascade in decaying* 3*D magnetohydrodynamic turbulence*, astro-ph/0011321 [SPIRES].

[39] R. Banerjee and K. Jedamzik, *The evolution of cosmic magnetic fields: from the very early universe, to recombination, to the present*, *Phys. Rev.* **D 70** (2004) 123003 [astro-ph/0410032] [SPIRES].

[40] R. Durrer and C. Caprini, *Primordial magnetic fields and causality*, *JCAP* **11** (2003) 010 [astro-ph/0305059] [SPIRES].

[41] L.G. Loitsyansky, *Some basic laws of isotropic turbulent flow*, report no. 440, Central Aero-Hydrodynamical Institute, Moscow Russia (1939) translated as *N.A.N.A. Technical Memorandum* 1079.

[42] L.D. Landau and E.M. Lifshitz, *Fluid mechanics*, volume 6 of the *Course of theoretical physics*, Pergamon Press, New York U.S.A. (1989).

[43] R.H. Kraichnan, *Approximations for steady-state isotropic turbulence*, *Phys. Fluids* **7** (1964) 1163.

[44] J. Cho, E. Vishniac, A. Beresnyak, A. Lazarian and D. Ryu, *Growth of magnetic fields induced by turbulent motions*, *Astrophys. J.* **693** (2009) 1449 [arXiv:0812.0817] [SPIRES].

[45] M. Abramowitz and I. Stegun, *Handbook of mathematical functions*, IX Printing, Dover Publications, New York U.S.A. (1970).

[46] P.J. Steinhardt, *Relativistic detonation waves and bubble growth in false vacuum decay*, *Phys. Rev.* **D 25** (1982) 2074 [SPIRES].

[47] C.P. Dettmann and N.E. Frankel, *Stochastic dynamics of relativistic turbulence*, *Phys. Rev.* **E 53** (1996) 5502.

[48] J. Cho, *Simulation of relativistic force-free magnetohydrodynamic turbulence*, *Astrophys. J.* **621** (2005) 324 [astro-ph/0408318] [SPIRES].

[49] R. Micha and I.I. Tkachev, *Relativistic turbulence: a long way from preheating to equilibrium*, *Phys. Rev. Lett.* **90** (2003) 121301 [hep-ph/0210202] [SPIRES].

[50] R. Micha and I.I. Tkachev, *Turbulent thermalization*, *Phys. Rev.* **D 70** (2004) 043538 [hep-ph/0403101] [SPIRES].

[51] P. Arnold and G.D. Moore, *The turbulent spectrum created by non-Abelian plasma instabilities*, *Phys. Rev.* **D 73** (2006) 025013 [hep-ph/0509226] [SPIRES].

[52] A.H. Mueller, A.I. Shoshi and S.M.H. Wong, *On Kolmogorov wave turbulence in QCD*, *Nucl. Phys.* **B 760** (2007) 145 [hep-ph/0607136] [SPIRES].

JCAP12(2009)024

[53] J. Berges, S. Scheffler and D. Sexty, *Turbulence in nonabelian gauge theory*, *Phys. Lett.* **B 681** (2009) 362 [arXiv:0811.4293] [SPIRES].

[54] J.R. Espinosa, J.M. No, T. Konstandin and G. Servant, in preparation.

[55] A. Brandenburg and K. Subramanian, *Astrophysical magnetic fields and nonlinear dynamo theory*, *Phys. Rept.* **417** (2005) 1 [astro-ph/0405052] [SPIRES].

[56] T. von Kármán, *Progress in the statistical theory of turbulence*, *Proc. Nat. Acad. Sci.* **34** (1948) 530.

[57] J.O. Hinze, *Turbulence*, McGraw-Hill series in mechanical engineering, Mcgraw-Hill, New York U.S.A. (1975).

[58] P. Iroshnikov, *Turbulence of a conducting fluid in a strong magnetic field*, *Astron. Zh.* **40** (1963) 742;
R.H. Kraichnan, *Inertial-range spectrum of hydromagnetic turbulence*, *Phys. Fluids* **8** (1965) 1385.

[59] P. Goldreich and S. Sridhar, *Toward a theory of interstellar turbulence. 2. Strong Alfvenic turbulence*, *Astrophys. J.* **438** (1995) 763 [SPIRES].

[60] J. Maron and P. Goldreich, *Simulations of incompressible magnetohydrodynamic turbulence*, *Astrophys. J.* **554** (2001) 1175.

[61] W.-C. Muller and R. Grappin, *Spectral energy dynamics in magnetohydrodynamic turbulence*, *Phys. Rev. Lett.* **95** (2005) 114502 [SPIRES].

[62] G. Gogoberidze, *On the nature of incompressible magnetohydrodynamic turbulence*, *Phys. Plasmas* **14** (2007) 022304.

[63] M. Maggiore, *Gravitational waves vol. 1: theory and experiments*, Oxford University Press, Oxford U.K. (2007) [ISBN:978-0-19-857074-5] [SPIRES].

[64] S. Dimopoulos, P.W. Graham, J.M. Hogan, M.A. Kasevich and S. Rajendran, *An Atomic Gravitational wave Interferometric Sensor (AGIS)*, *Phys. Rev.* **D 78** (2008) 122002 [arXiv:0806.2125] [SPIRES].

[65] *LIGO: Livingston Laser Interferometer Gravitational-wave Observatory homepage*, http://www.ligo.caltech.edu.

[66] G.M. Harry, P. Fritschel, D.A. Shaddock, W. Folkner and E.S. Phinney, *Laser interferometry for the big bang observer*, *Class. Quant. Grav.* **23** (2006) 4887 [*Erratum ibid.* **23** (2006) 7361] [SPIRES].

[67] N. Cornish, private communication.

[68] A. Buonanno, G. Sigl, G.G. Raffelt, H.-T. Janka and E. Muller, *Stochastic gravitational wave background from cosmological supernovae*, *Phys. Rev.* **D 72** (2005) 084001 [astro-ph/0412277] [SPIRES].

[69] A. Buonanno, *TASI lectures on gravitational waves*, gr-qc/0303085 [SPIRES].

[70] S. Weinberg, *Entropy generation and the survival of protogalaxies in an expanding universe*, *Astrophys. J.* **168** (1971) 175 [SPIRES].

[71] A. Heckler and C.J. Hogan, *Neutrino heat conduction and inhomogeneities in the early universe*, *Phys. Rev.* **D 47** (1993) 4256 [SPIRES].

[72] P. Arnold, G.D. Moore and L.G. Yaffe, *Transport coefficients in high temperature gauge theories: (I) leading-log results*, *JHEP* **11** (2000) 001 [hep-ph/0010177] [SPIRES].

[73] L.D. Landau and E.M. Lifschitz, *Lehrbuch der theoretischen Physik Band X: Physikalische Kinetik* (in German), Akademie Verlag, Berlin Germany (1983).

JCAP12(2009)024

6.3 Article: Gravitational wave signal from first order phase transitions at LISA

The article presented in the following section has been conceived and completed in the context of the LISA Cosmology Working Group, that I am coordinating together with Germano Nardini and, since 2018, Robert Caldwell. The project of a space-based GW interferometer, called eLISA at that time, was under study by ESA: in particular, they constituted a committee (the GOAT committee) with the duty of advising ESA about the best design for the interferometer, balancing cost and scientific reach. The committee asked the community of the eLISA Consortium to help in assessing the scientific potential of the several eLISA configurations under examination. The Cosmology Working Group organised a kick-off meeting in CERN in 2015, where the community was reassembled, and it was decided to perform a common effort to work out the sensitivity of four of the proposed eLISA configurations to SGWBs generated by first order PTs. A sub-group of the Working Group members worked together on this topic and produced the paper presented below. My contribution has been mainly the prediction of the GW signals and the analysis of the eLISA sensitivity: in particular, sections 1 to 3 and Figs. 1 to 7 of the following paper. Note that, for MHD turbulence, this work adopts the SGWB spectral shape derived in the previous section 6.2.

The paper has been useful for the community. One reason is that it summarises the most relevant PT models (both of the EWPT and others) that can provide interesting signals for eLISA, remaining unconstrained by particle physics experiments, in particular the LHC. However, the main reason is that, for the first time, it puts together all the contributions to the GW signal (bubble wall collision, sound waves, MHD turbulence), providing concise and easy-to-use formulas for the SGWB spectra. Moreover, it presents the sensitivity reach of four eLISA configurations in a subset of the PT parameter space constituted by (α, β/H_*, T_*). Therefore, PT model builders have been using this paper both to predict the SGWB from their model, and to quickly assess whether it was detectable at eLISA.

The result of the analysis is, that configurations of the interferometer with three arms have the best potential to probe the PT parameter space (also, but not only, because they allow for a much better characterisation of the noise - c.f section 4.4 of chapter 4). The paper, together with their companions assessing eLISA scientific potential concerning massive black

hole binaries [272] and standard sirens [1], was relevant for the choice made by ESA of maintaining a three-arm design for eLISA. An interferometer with three arms of 2.5 million km arm-length and 4 years of nominal time duration was finally approved by ESA in 2017 under the name of LISA, and is scheduled to launch in 2034 (c.f. chapter 4.4 and [130]). The approval was triggered in particular by the great success of the LISA Pathfinder mission [151].

The Cosmology Working Group is currently preparing a follow-up of the article presented below. It will contain updated results concerning the PT models, it will use the new LISA sensitivity curve to assess the parameter space tested by the interferometer, and it will include updated shapes for the GW spectra, when available. Together with the article, a web-tool will be provided to be used by the community to test whether the SGWB signal from a given PT model can be detected by LISA. There is an ongoing debate within the Working Group, whether to make this paper a living review: that would allow to keep it up to date as new results appear, on the interferometer data analysis and/or on the SGWB spectra and sources.

For example, another activity of the Cosmology Working Group consists in developing new data analysis techniques to evaluate the detectability of a SGWB. It is clear that verifying that the SGWB overcomes the Power Law-Integrated Curve (c.f. section 4.4.1) is only the first step: one should also establish the accuracy with which the parameters of the SGWB can be measured. Furthermore, it is essential to ascertain whether the spectral shape of the SGWB can be determined, as this is the only possibility we have to potentially distinguish among different SGWB sources from the early universe. Last but not least, techniques for removing the astrophysical foregrounds must be worked out, if we want to access SGWB of primordial origin with smaller amplitude than the foregrounds. All these issues are currently under study within the LISA Consortium Working Groups, and important results are to be expected in the next few years.

Science with the space-based interferometer eLISA. II: gravitational waves from cosmological phase transitions

Journal of Cosmology and Astroparticle Physics
An IOP and SISSA journal

Science with the space-based interferometer eLISA. II: gravitational waves from cosmological phase transitions

Chiara Caprini,[a] **Mark Hindmarsh,**[b,c] **Stephan Huber,**[b] **Thomas Konstandin,**[d] **Jonathan Kozaczuk,**[e] **Germano Nardini,**[f] **Jose Miguel No,**[b] **Antoine Petiteau,**[g] **Pedro Schwaller,**[d] **Géraldine Servant**[d,h] **and David J. Weir**[i]

[a]IPhT, CEA Saclay and CNRS UMR3681,
91191 Gif-sur-Yvette, France
[b]Department of Physics and Astronomy, University of Sussex,
BN1 9QH, Brighton, U.K.
[c]Department of Physics and Helsinki Institute of Physics, University of Helsinki,
PL 64, FI-00014 Helsinki, Finland
[d]DESY,
Notkestrasse 85, D-22607 Hamburg, Germany
[e]TRIUMF,
4004 Wesbrook Mall, Vancouver, BC V6T 2A3, Canada
[f]ITP, AEC, University of Bern,
Sidlerstrasse 5, CH-3012, Bern, Switzerland
[g]APC, Université Paris Diderot, Observatoire de Paris, Sorbonne Paris Cité,
10 rue Alice Domon et Léonie Duquet, 75205 Paris Cedex 13, France
[h]Institute of Theoretical Physics, Univ. Hamburg,
D-22761 Hamburg, Germany
[i]Institute of Mathematics and Natural Sciences, University of Stavanger,
4036 Stavanger, Norway

E-mail: chiara.caprini@cea.fr, m.b.hindmarsh@sussex.ac.uk, S.Huber@sussex.ac.uk, thomas.konstandin@desy.de, jkozaczuk@triumf.ca, nardini@itp.bern.ch, J.M.No@sussex.ac.uk, petiteau@apc.univ-paris7.fr, pedro.schwaller@desy.de, geraldine.servant@desy.de, david.weir@uis.no

Received January 23, 2016
Accepted March 19, 2016
Published April 1, 2016

doi:10.1088/1475-7516/2016/04/001

JCAP04(2016)001

Abstract. We investigate the potential for the eLISA space-based interferometer to detect the stochastic gravitational wave background produced by strong first-order cosmological phase transitions. We discuss the resulting contributions from bubble collisions, magnetohydrodynamic turbulence, and sound waves to the stochastic background, and estimate the total corresponding signal predicted in gravitational waves. The projected sensitivity of eLISA to cosmological phase transitions is computed in a model-independent way for various detector designs and configurations. By applying these results to several specific models, we demonstrate that eLISA is able to probe many well-motivated scenarios beyond the Standard Model of particle physics predicting strong first-order cosmological phase transitions in the early Universe.

Keywords: cosmological phase transitions, cosmology of theories beyond the SM, gravitational wave detectors, primordial gravitational waves (theory)

ArXiv ePrint: 1512.06239

JCAP04(2016)001

Contents

1 Introduction

Phase transitions (PTs) are ubiquitous in nature. Boiling liquid into gas, the emergence of superconductivity, superfluidity, and permanent magnetization in ferromagnetic materials are some well-known examples of this phenomenon. Intriguingly, PTs can also be *cosmological*: regions of the universe can abruptly transition from one ground state to another. In the language of quantum field theory, this typically corresponds to the appearance or change of a scalar field operator's vacuum expectation value (VEV).

A *first-order* cosmological PT can occur when two local minima of the free energy co-exist for some range of temperatures. If this is the case, the relevant scalar field can quantum mechanically 'tunnel' or thermally fluctuate into the new phase. These quantum

JCAP04(2016)001

or thermal processes proceed via the nucleation of bubbles in a sea of metastable phase. The bubbles will then expand and eventually collide with each other. This sequence of events can give rise to a significant stochastic background of gravitational waves (GWs), as we describe below, and provides an attractive target for the next space-based GW observer, the eLISA interferometer [1].

First-order cosmological PTs are predicted in many scenarios beyond the Standard Model of particle physics. They can be tied to the production of the observed baryon asymmetry, to the nature of dark matter, or simply be a byproduct of an extended scalar sector. Consequently, eLISA can be a vital tool in exploring possibilities for new physics, complementing existing observational efforts at colliders, precision and cosmic frontier experiments.

The purpose of this paper is to quantitatively assess the extent to which eLISA can test realistic scenarios predicting strong first-order PTs in the early Universe. Currently, a design study is in progress within the European Space Agency to define the most scientifically promising configuration of eLISA. The characteristics of the configuration that remain open or undetermined are the low-frequency noise level, soon to be tested by the LISA Pathfinder [2], the number of laser links (four or six, corresponding to two or three interferometer arms), the length of the interferometer arms (1, 2, or 5 million km), and the duration of the mission (2 or 5 years).

As part of the design study, the scientific potential of each possible eLISA configuration is currently being analyzed and scrutinized. This paper is the second in a series that evaluates the impact of the aforementioned four key design specifications on the scientific performance of eLISA. The first considered the primary scientific target of eLISA: the GW signal from massive black hole binaries [3]. In this paper, we specifically address eLISA's potential to detect a stochastic GW background arising from a first-order PT. As we will see, our conclusions in this regard depend quite sensitively on the experimental configuration. For a more detailed discussion on the status of the eLISA mission and its possible designs, we refer the reader to the first paper of this series [3].

The remainder of this study is structured as follows. We provide an overview of GW generation at a first-order cosmological PT in section 2. Model-independent projections of the eLISA sensitivity to such signals are presented in section 3. We then discuss several specific examples of models predicting strong GW signatures through a first-order PT in section 4, either associated with electroweak symmetry breaking (section 4.2) or otherwise (section 4.3). Section 5 comprises a summary and our conclusions. Some additional details of our analysis are provided in appendix A.

1.1 Definitions and notation

Before proceeding, we comment briefly on our notation, which generally coincides with that found in e.g. ref. [4], and identify the quantities important for computing the GW signal from cosmological PTs.

In what follows, T_* denotes the temperature of the thermal bath at the time t_* when GWs are produced. For typical transitions without significant reheating, this is approximately equivalent to the nucleation temperature, $T_* \approx T_n$. For the remainder of this section we assume that this is the case, deferring the treatment of scenarios with large reheating effects to section 2.2.3. The bubble nucleation rate is [5]

$$\Gamma(t) = A(t)e^{-S(t)}\,, \tag{1.1}$$

JCAP04(2016)001

where S is the Euclidean action of a critical bubble.[1] T_n is then defined as the temperature at which Γ becomes large enough to nucleate a bubble per horizon volume with probability of order 1.

In terms of $\Gamma(t)$, the (approximate) inverse time duration of the PT is defined as

$$\beta \equiv -\left.\frac{dS}{dt}\right|_{t=t_*} \simeq \frac{\dot{\Gamma}}{\Gamma}\,. \tag{1.2}$$

A key parameter controlling the GW signal is the fraction β/H_*, where H_* is the Hubble parameter at T_*. The smaller β/H_* is, the stronger the phase transition and consequently the GW signal. Provided $T_* \approx T_n$, this ratio can be expressed as

$$\frac{\beta}{H_*} = T_* \left.\frac{dS}{dT}\right|_{T_*}\,. \tag{1.3}$$

A second key parameter, α, is the ratio of the vacuum energy density released in the transition to that of the radiation bath.[2] For transitions without significant reheating,

$$\alpha = \frac{\rho_{\rm vac}}{\rho^*_{\rm rad}}\,, \tag{1.4}$$

where $\rho^*_{\rm rad} = g_*\pi^2 T_*^4/30$, and g_* is the number of relativistic degrees of freedom in the plasma at T_*.

The characteristic frequency of the signal at the time of emission is set roughly by H_* (see section 2.1). For PTs taking place at the electroweak epoch, the observed frequency today, which is redshifted by a factor of (T_0/T_*), is typically in the milliHertz range. eLISA, which is sensitive to frequencies in this range, may therefore provide a window to electroweak scale physics.

Other important parameters are [6]

$$\kappa_v = \frac{\rho_v}{\rho_{\rm vac}}\,, \qquad \kappa_\phi = \frac{\rho_\phi}{\rho_{\rm vac}}\,, \tag{1.5}$$

the fraction of vacuum energy that gets converted into bulk motion of the fluid and into gradient energy of the Higgs-like field, respectively. Finally, v_w denotes the bubble wall velocity in the rest frame of the fluid far away from the bubble.

2 Prediction of the gravitational wave signal

As mentioned above, a first-order PT proceeds by the nucleation and expansion of bubbles of a new phase. Isolated spherical bubbles do not source GWs. It is therefore processes arising during the collision of bubbles that are relevant for GW physics (we ignore possible instabilities [7, 8]).

Depending on the details of the model, the bubble walls can move with velocities up to the speed of light. If the dynamics of the PT involve only a single field with no relevant

[1] In principle, there are many solutions to the Euclidean equations of motion that can contribute to the action. In practice, only the solution with the lowest action is relevant. For vacuum transitions, this is the $O(4)$-symmetric solution with Euclidean action S_4, while at finite temperature the $O(3)$-symmetric bounce is the relevant solution, with Euclidean action S_3/T. Then, at a given time, $S(t) \approx \min\{S_4, S_3/T\}$.

[2] Notice that in parts of the literature, α is defined in terms of the latent heat of the PT and not in terms of the vacuum energy. In the limit of strong PTs and large supercooling these two definitions coincide.

JCAP04(2016)001

couplings to the thermal bath, then the bubble walls move relativistically in what is known as a vacuum transition.

Thermal PTs, in which the scalar field is coupled to a plasma of light fields, typically involve slower wall velocities due to the effective friction term coupling the field to the plasma [9]. It is, however, still possible to get luminal wall velocities [10]. For thermal PTs, if velocities are subsonic $v_w < 1/\sqrt{3}$, a shock forms in the plasma in front of the bubble wall; if velocities are supersonic $v_w > 1/\sqrt{3}$, a rarefaction wave forms behind the bubble wall.

The spectrum of the stochastic GW background arising from cosmological PTs depends on various sources. These are outlined in section 2.1. Which sources are most relevant in a given PT scenario depends sensitively on the dynamics of bubble expansion. We discuss the various possibilities in section 2.2.

2.1 Contributions to the gravitational wave spectrum

To varying degrees, three processes are involved in the production of GWs at a first-order PT:

- Collisions of bubble walls and (where relevant) shocks in the plasma. These can be treated by a technique now generally referred to as the 'envelope approximation' [11–16]. As described below, this approximation can be used to compute the contribution to the GW spectrum from the scalar field, ϕ, itself.
- Sound waves in the plasma after the bubbles have collided but before expansion has dissipated the kinetic energy in the plasma [17–20].
- Magnetohydrodynamic (MHD) turbulence in the plasma forming after the bubbles have collided [21–26].

These three processes generically coexist, and the corresponding contributions to the stochastic GW background should linearly combine, at least approximately, so that

$$h^2\Omega_{\rm GW} \simeq h^2\Omega_\phi + h^2\Omega_{\rm sw} + h^2\Omega_{\rm turb}\,. \tag{2.1}$$

Let us briefly review each contribution in more detail.

2.1.1 Scalar field contribution

The GW contribution from the scalar field involved in the PT can be treated using the envelope approximation [11–14]. In this approximation, a fraction κ of the latent heat of the PT is deposited in a thin shell close to the PT front. The energy in each shell is then assumed to quickly disperse after colliding with another shell such that the energy is primarily stored in the envelope of uncollided shells.[3] Numerical simulations utilizing the envelope approximation suggest that the GW contribution to the spectrum is given by [16]

$$h^2\Omega_{\rm env}(f) = 1.67\times10^{-5}\left(\frac{H_*}{\beta}\right)^2\left(\frac{\kappa\alpha}{1+\alpha}\right)^2\left(\frac{100}{g_*}\right)^{\frac{1}{3}}\left(\frac{0.11\,v_w^3}{0.42+v_w^2}\right)S_{\rm env}(f)\,, \tag{2.2}$$

where $S_{\rm env}(f)$ parametrises the spectral shape of the GW radiation. A fit to simulation data [16] yields

$$S_{\rm env}(f) = \frac{3.8\,(f/f_{\rm env})^{2.8}}{1+2.8\,(f/f_{\rm env})^{3.8}}\,, \tag{2.3}$$

[3] The envelope approximation we adopt here neglects the fact that the scalar field can perform oscillations as it settles into the true vacuum after wall collisions, as demonstrated e.g. in [27].

JCAP04(2016)001

with the slopes of the spectrum in the limit of small and large frequencies given respectively by $S_{\rm env} \propto f^q$ with $q = 2.8$ and $S_{\rm env} \propto f^{-p}$ with $p = 1$. Causality implies that at low frequency the spectral index is $q = 3$ [28]. This has to be the case at least for frequencies smaller than the inverse Hubble horizon at GW production, eq. (2.6). However, $q = 2.8$ provides a better fit to the simulated result close to the peak of the spectrum and we adopt this spectral index in the following.

The peak frequency of the contribution to the spectrum from bubble collisions, $f_{\rm env}$, is determined by the characteristic time-scale of the PT, i.e. its duration $1/\beta$ [25, 28]. From simulations, the peak frequency (at t_*) is approximately given by [16]

$$\frac{f_*}{\beta} = \left(\frac{0.62}{1.8 - 0.1 v_w + v_w^2} \right) . \tag{2.4}$$

This value is then red-shifted to yield the peak frequency today [14],

$$f_{\rm env} = 16.5 \times 10^{-3}\,{\rm mHz} \left(\frac{f_*}{\beta} \right) \left(\frac{\beta}{H_*} \right) \left(\frac{T_*}{100\,{\rm GeV}} \right) \left(\frac{g_*}{100} \right)^{\frac{1}{6}} . \tag{2.5}$$

In going from eq. (2.4) to eq. (2.5) we use the value of the inverse Hubble time at GW production, redshifted to today,

$$h_* = 16.5 \times 10^{-3}\,{\rm mHz} \left(\frac{T_*}{100\,{\rm GeV}} \right) \left(\frac{g_*}{100} \right)^{\frac{1}{6}} \tag{2.6}$$

along with the assumption that the Universe transitioned directly to a radiation-dominated phase after the PT and has expanded adiabatically ever since.

The envelope approximation can be readily applied to the GW contribution arising from the scalar field itself,

$$h^2 \Omega_\phi(f) = h^2 \Omega_{\rm env}(f) \big|_{\kappa = \kappa_\phi} , \tag{2.7}$$

where κ_ϕ denotes the fraction of latent heat transformed into the kinetic energy of the scalar field. Its size depends on the details of the bubble expansion, as we discuss in section 2.2.

2.1.2 Sound waves

Percolation produces bulk motion in the fluid in the form of sound waves. Acoustic production of GWs is an area of active research, and a definitive model covering all relevant v_w and α is not yet available [17, 20]. For generic values of v_w (meaning values more than about 10% away from the sound speed or the speed of light), the numerical results of [20] are fitted reasonably by

$$h^2 \Omega_{\rm sw}(f) = 2.65 \times 10^{-6} \left(\frac{H_*}{\beta} \right) \left(\frac{\kappa_v \alpha}{1+\alpha} \right)^2 \left(\frac{100}{g_*} \right)^{\frac{1}{3}} v_w \, S_{\rm sw}(f) , \tag{2.8}$$

where the efficiency κ_v denotes the fraction of latent heat that is transformed into bulk motion of the fluid, and depends on the expansion mode of the bubble (see section 2.2).

The numerical simulations performed in ref. [20] indicate that the contribution from acoustic production can be modelled by a broken power law, with the causal slope $q = 3$ for values of the frequency below the peak frequency, and a power law $-p$ above the peak, with $p \gtrsim 3$. It can be shown that the signal-to-noise ratios for GW detection are rather insensitive

JCAP04(2016)001

to the precise value of p if it is greater than 3. For the purposes of this analysis we take $p = 4$. We adopt the following spectral shape $S_{\rm sw}(f)$ in eq. (2.8):

$$S_{\rm sw}(f) = (f/f_{\rm sw})^3 \left(\frac{7}{4 + 3\,(f/f_{\rm sw})^2}\right)^{7/2} . \tag{2.9}$$

The peak frequency $f_{\rm sw}$ is not yet well understood. The overall scale is set by the average bubble separation $R_* = (8\pi)^{\frac{1}{3}} v_w/\beta$, but the peak position is found numerically to be less than R_*. A conservative estimate that complies with the above spectral shape is $f_{\rm sw} = (2/\sqrt{3})(\beta/v_w)$, which, after redshifting, becomes

$$f_{\rm sw} = 1.9 \times 10^{-2}\,{\rm mHz}\,\frac{1}{v_w}\left(\frac{\beta}{H_*}\right)\left(\frac{T_*}{100\,{\rm GeV}}\right)\left(\frac{g_*}{100}\right)^{\frac{1}{6}} . \tag{2.10}$$

The parametric dependence of the GW spectrum in eq. (2.8) differs by a factor β/H_* with respect to the envelope result in eq. (2.2). The enhancement of the spectral amplitude by a factor β/H_* for long-lasting sources w.r.t. to short lasting ones has been predicted on the basis of analytical arguments in ref. [25]. Simulations show that the sound waves typically remain active as a source of GW much longer than the collisions of the bubble walls [20]. We therefore believe that the β/H_* factor is tied to the duration of the source, and is robust. The same amplification is observed in the case of MHD turbulence which is also a long-lasting source (it takes several Hubble times to dissipate [25]).

We emphasize that the simulations used to arrive at eqs. (2.8)–(2.10) were restricted to values of $\alpha \lesssim 0.1$ and the maximum root mean square fluid velocity $\sqrt{\kappa\alpha_v}$ was about 0.05. The extent to which the results of these simulations can be extrapolated to larger α remains to be investigated. In particular, we expect that the development of weak shocks at $t_{\rm sh} \sim (v_w/\sqrt{\kappa\alpha_v})\beta^{-1}$ (see e.g. [29]) will eventually convert the acoustic signal to a turbulent one, described in the next section. We urge the reader to keep this in mind when interpreting our results below.

2.1.3 MHD turbulence

Percolation can also induce turbulence in the plasma, and in particular MHD turbulence since the plasma is fully ionized. Considering Kolmogorov-type turbulence as proposed in ref. [30], its contribution to the GW spectrum in eq. (2.1) can be modelled as[4] [6, 25]

$$h^2\Omega_{\rm turb}(f) = 3.35 \times 10^{-4}\left(\frac{H_*}{\beta}\right)\left(\frac{\kappa_{\rm turb}\,\alpha}{1+\alpha}\right)^{\frac{3}{2}}\left(\frac{100}{g_*}\right)^{1/3} v_w\, S_{\rm turb}(f)\,, \tag{2.11}$$

where $\kappa_{\rm turb}$ denotes the fraction of latent heat that is transformed into MHD turbulence (note the different dependence on this parameter w.r.t. to the sound wave and scalar field cases). Similarly to the case of sound waves, one recognizes the amplification by a factor β/H_* which is typical of sources that last longer than the average duration $1/\beta$ of the PT. The spectral shape has been found analytically and is given by [6, 25]

$$S_{\rm turb}(f) = \frac{(f/f_{\rm turb})^3}{[1 + (f/f_{\rm turb})]^{\frac{11}{3}}\,(1 + 8\pi f/h_*)} . \tag{2.12}$$

[4]Note that MHD turbulence after a primordial PT can also be helical, as pointed out e.g. in ref. [23]. Here we neglect the GW signal from a possible helical component, which in the context of eLISA will be the subject of a subsequent study.

JCAP04(2016)001

The explicit dependence on the Hubble rate h_* (cf. eq. (2.6)) is also a consequence of the fact the turbulence acts as a source of GW for several Hubble times. The causal slope $q = 3$ is recovered for frequencies smaller than h_*, but it changes to $q = 2$ for intermediate (sub-Hubble) values of the frequency $h_* < f < f_{\rm turb}$, again due to the long duration of the GW source [25]. At large frequency $f \gg f_{\rm turb}$ the slope is determined by the Kolmogorov turbulence model, $p = 5/3$.

Similarly to the sound wave case, the peak frequency is connected to the inverse characteristic length-scale of the source, the bubble size R_* towards the end of the PT. Analytic arguments show that this is due to the particular time de-correlation properties of the turbulent source [25]. One has $f_{\rm turb} \simeq (3.5/2)(\beta/v_w)$, which becomes, after redshifting,

$$f_{\rm turb} = 2.7 \times 10^{-2}\,{\rm mHz}\,\frac{1}{v_w}\left(\frac{\beta}{H_*}\right)\left(\frac{T_*}{100\,{\rm GeV}}\right)\left(\frac{g_*}{100}\right)^{\frac{1}{6}}\,. \tag{2.13}$$

Note that, contrary to the envelope and sound wave cases, the spectral shape of the GW spectrum in eq. (2.12) has not been tuned such that $f_{\rm turb}$ exactly corresponds to the maximum of $S_{\rm turb}(f)$. Here $f_{\rm turb}$ is inherited from the physical arguments underlying the analytical evaluation carried out in ref. [25].

2.2 Dynamics of the phase transition: three cases

The relative importance of each contribution discussed above w.r.t. GW generation depends strongly on the features of the PT and its dynamics. The bubble wall velocity plays a key role in this respect. If the wall velocity is small, the thermal bath can efficiently absorb the energy available in the PT, and the GW spectrum is thus suppressed. If the wall velocity is instead relativistic, a large portion of the energy budget can go into bulk motion or even in the kinetic energy of the wall itself. Moreover, in the case of relativistic bubble wall velocities, qualitatively different scenarios can arise, depending on whether the bubble wall reaches a terminal velocity or not. In the latter ('runaway') case, a further important distinction is whether or not plasma effects play an important role in bubble expansion. Below, we consider these different scenarios in turn.[5] We stress that, when analyzing the GW spectrum predicted in a particular particle physics model, it is important to understand which of the following scenarios apply.

2.2.1 Case 1: non-runaway bubbles

Bubbles expanding in a plasma can reach a relativistic terminal velocity. In this case, the energy in the scalar field is negligible (it only scales with the surface of the bubble and not with the volume) and the most relevant contributions to the signal are expected to arise from the bulk motion of the fluid. This can be in the form of sound waves and/or MHD turbulence. Combining these contributions, we approximate the total spectrum as

$$h^2\Omega_{\rm GW} \simeq h^2\Omega_{\rm sw} + h^2\Omega_{\rm turb}\,. \tag{2.14}$$

As shown in the previous sections, these expressions involve κ_v, the efficiency factor for conversion of the latent heat into bulk motion [9, 14]. In the limits of small and large v_w, it is approximately given by

$$\kappa_v \simeq \begin{cases} \alpha\,(0.73 + 0.083\sqrt{\alpha} + \alpha)^{-1} & v_w \sim 1 \\ v_w^{6/5} 6.9\,\alpha\,(1.36 - 0.037\sqrt{\alpha} + \alpha)^{-1}\,, & v_w \lesssim 0.1 \end{cases} \tag{2.15}$$

[5] We do not analyze the case of non-relativistic wall velocity since it tends to yield GW spectra that are not detectable in the forthcoming future.

JCAP04(2016)001

Full expressions for κ_v are given in ref. [9], which we utilize below (note that κ_v is called κ in ref. [9]).

The GW spectra also depend on v_w, which is model-dependent. We choose $v_w = 0.95$ for concreteness, since scenarios with nearly luminal wall velocities are more promising from the standpoint of observable gravitational radiation.

In the GW contribution from MHD turbulence, eq. (2.11), we take

$$\kappa_{\rm turb} = \epsilon\, \kappa_v \,, \tag{2.16}$$

with ϵ representing the fraction of bulk motion which is turbulent. Recent simulations suggest that only at most $5 - 10\%$ of the bulk motion from the bubble walls is converted into vorticity (cf. e.g. table II in [20]). However, these simulations lasted for less than one eddy turn-over time so one would not expect significant turbulence to have developed. The onset of turbulence is expected after shocks develop at $t_{\rm sh} \sim (v_w/\sqrt{\kappa\alpha_v})\beta^{-1}$, which is less than a Hubble time for stronger transitions. More work is needed to understand how turbulence develops from the acoustic waves, and to allow for the uncertainty in what follows we conservatively set $\epsilon = 0.05$. This strongly suppresses the role of turbulence as far as the detection of GW from the PT is concerned, thereby underestimating the signal in the case that weak shocks develop within one Hubble time. As we will see, turbulence can only slightly improve the signal-to-noise ratio in extreme cases for which the PT is very slow, i.e. $\beta \simeq H_*$. A more accurate balance between acoustic and turbulent gravitational wave production remains to be investigated, as does the possible contribution from the magnetic field.

2.2.2 Case 2: runaway bubbles in a plasma

If a model predicts a first-order PT already at the mean-field level, it is possible for the bubble wall to accelerate without bound and hence run away [10], with $v_w \to c$. Although the existence of a runaway configuration does not guarantee that it will be realized [31, 32], it is generally difficult to prevent strong transitions from reaching the runaway regime, if it exists.

Bubbles can run away even if expanding in a thermal plasma. In this case, the energy density stored in the Higgs-like field profile cannot be neglected, since it is known to dominate as $\alpha \to \infty$ (Case 3 below). The total contribution to the GW signal can be approximated in this case by

$$h^2\Omega_{\rm GW} \simeq h^2\Omega_\phi + h^2\Omega_{\rm sw} + h^2\Omega_{\rm turb} \,, \tag{2.17}$$

where we have reintroduced Ω_ϕ, the part sourced by gradients in the scalar field. This contribution is well-modeled by the envelope approximation (see section 2.1.1).

The following picture emerges in this case [9]. As α is increased, the wall velocity quickly becomes relativistic. We denote by α_∞ the minimum value of α such that bubbles run away (i.e. no longer reach a terminal velocity in the plasma frame). For $\alpha > \alpha_\infty$, the fraction of the total phase transition energy budget deposited into the fluid saturates. Beyond this value, the fluid profile no longer changes with increasing α and the surplus energy goes into accelerating the bubble wall. This surplus energy is parameterized by the fraction

$$\kappa_\phi \equiv \frac{\alpha - \alpha_\infty}{\alpha} \geq 0 \,. \tag{2.18}$$

JCAP04(2016)001

Only the fraction α_∞/α of the total energy budget is then transformed into bulk motion and thermal energy according to eq. (2.15):

$$\begin{aligned} \kappa_v &\equiv \frac{\alpha_\infty}{\alpha}\kappa_\infty\,, \\ \kappa_{\rm therm} &\equiv (1-\kappa_\infty)\,\frac{\alpha_\infty}{\alpha}\,, \\ \kappa_\infty &\equiv \frac{\alpha_\infty}{0.73+0.083\sqrt{\alpha_\infty}+\alpha_\infty}\,. \end{aligned} \tag{2.19}$$

The parameter α_∞ is model-dependent. Denoting the tunneling field[6] as ϕ with corresponding vacuum expectation value ϕ_* inside the bubble immediately after tunneling, one can express α_∞ as [9]

$$\alpha_\infty \simeq \frac{30}{24\pi^2}\frac{\sum_a c_a \Delta m_a^2(\phi_*)}{g_* T_*^2}\,, \tag{2.20}$$

for the typical case with $T_* \approx T_n$. In the above expression, the sum runs over all particles a that are light in the initial phase and heavy in the final phase, $\Delta m_a^2(\phi_*)$ is the difference of their (field-dependent) squared masses in the two phases, g_* again corresponds to the effective number of relativistic degrees of freedom in the initial phase, and c_a is equal to N_a for bosons and $\frac{1}{2}N_a$ for fermions, with N_a the number of the degrees of freedom for the species a. For electroweak PTs in models with Standard Model-like particle content ($g_* = 106.75$, $a \in \{W^\pm, Z, t\}$ and $N_W = 6$, $N_Z = 3$, $N_t = 12$),[7] this parameter is approximately given by[8]

$$\alpha_\infty \simeq 4.9\times 10^{-3}\left(\frac{\phi_*}{T_*}\right)^2\,. \tag{2.21}$$

Since most scenarios beyond the Standard Model do not feature new relativistic degrees of freedom or new particles with couplings to the Higgs comparable to those of the $\mathrm{SU}(2)_L$ gauge bosons or top quark, eq. (2.21) is typically a reliable estimate for electroweak PTs, although one should verify this explicitly with the exact expressions found in ref. [9].

By definition, reasonably strong first-order PTs in a radiation-dominated epoch feature $\phi_*/T_* \gtrsim 1$. On the other hand, heuristically, models with $\phi_*/T_* \gtrsim 10$ are more likely to fall into the large-α case (described in the next section) for which α_∞ becomes irrelevant. We therefore expect $\alpha_\infty \sim 0.005$–0.5 for scenarios belonging to Case 2.

2.2.3 Case 3: runaway bubbles in vacuum

Finally, some models predict PTs that occur in a vacuum-dominated epoch. This situation arises in models with a significant amount of supercooling. In this case, plasma effects are negligible, and the bubble wall will accelerate indefinitely, with v_w quickly approaching the speed of light, as in Case 2 above.

The temperature T_* in this situation is given approximately by the reheat temperature after percolation, $T_* \approx T_{\rm reh}$. So far, in most of our expressions we have assumed $T_* \approx T_n \approx T_{\rm reh}$, as is appropriate for transitions in a radiation-dominated epoch and without significant reheating. However, in the vacuum case, one instead generally expects $T_n \ll T_{\rm reh} \approx T_*$, since

[6] Here, ϕ should be thought of as a vector in field space for scenarios in which more than one field changes its VEV during the transition.

[7] The Higgs and Goldstone contributions are typically numerically negligible.

[8] Note that the expression above differs from that in ref. [9]; we believe this discrepancy is due to an algebraic error in the latter.

JCAP04(2016)001

Name	C1	C2	C3	C4
Full name	N2A5M5L6	N2A1M5L6	N2A2M5L4	N1A1M2L4
# links	6	6	4	4
Arm length [km]	5M	1M	2M	1M
Duration [years]	5	5	5	2
Noise level	N2	N2	N2	N1

Table 1. Properties of the representative eLISA configurations chosen for this study. The corresponding sensitivity curves are shown in figure 1. More details on these configurations and their sensitivity curves can be found in ref. [3] and ref. [33] respectively.

$T_{\rm reh}$ is governed by the vacuum energy released during the transition. The definitions of α and β/H_* should be adjusted accordingly. In particular, for vacuum transitions, Equations (1.3) and (1.4) should be replaced by

$$\frac{\beta}{H_*} = \frac{H(T_n)}{H_*} T_n \left.\frac{dS}{dT}\right|_{T_n}, \qquad \alpha = \frac{\rho_{\rm vac}}{\rho_{\rm rad}(T_n)}. \tag{2.22}$$

Notice that for fast reheating one obtains $H(T_n) \simeq H_*$ even though $T_n \ll T_*$. This is because energy conservation ensures that the vacuum energy that dominates $H(T_n)$ is transformed without loss into the radiation energy that dominates H_*.

As $T_n \to 0$, $\alpha \to \infty$ and the α dependence drops out of the predicted GW signal in this scenario (cf. eq. (2.2)). Also, in this limit, only the Higgs field contribution is significant, from which it follows that

$$h^2\Omega_{\rm GW} \simeq h^2\Omega_\phi\,, \tag{2.23}$$

where $h^2\Omega_\phi$ is given in eq. (2.7), and eq. (2.2) with $\kappa_\phi = 1$, $v_w = 1$. There is no significant plasma contribution in this case, by definition. Note that, if the reheating of the Standard Model sector is slow, there will be a period of matter domination immediately following the transition, which would change the redshift, and hence eq. (2.5). We will not consider this particular case further.

3 eLISA sensitivity

3.1 Detection threshold

In this analysis we consider four representative configurations for eLISA, which we name C1-C4 and which are listed in table 1. The corresponding eLISA sensitivity curves can be found in ref. [3] for the target GW source, massive black hole binaries. On the other hand, here we are interested in a stochastic background of GWs, which is statistically homogeneous and isotopic. The purpose of this section is to briefly explain how one can obtain sensitivity curves which correctly represent the prospects for detecting a stochastic GW background with eLISA for a given configuration (more details will be presented in an upcoming study [33]).

For the C1-C4 configurations, the resulting eLISA sensitivity to a stochastic GW background is shown in figure 1. The most promising clearly appears to be C1, which corresponds to the old LISA configuration: it has 6 links, 5 million km arm length, a duration of 5 years and noise level corresponding to that expected to be found by the LISA Pathfinder (labeled as N2 and henceforth called "LISA Pathfinder expected"). The least sensitive is C4, with 4

JCAP04(2016)001

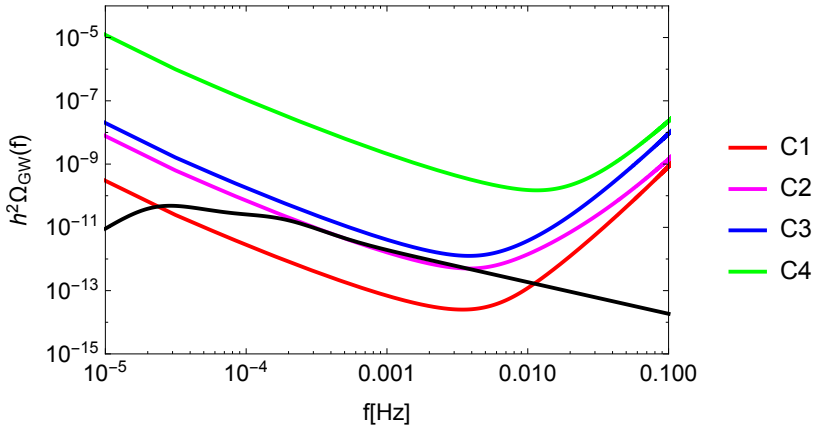

Figure 1. Sensitivity curves of the C1-C4 configurations given in table 1 compared with a typical GW signal. We have chosen the signal predicted in the Higgs portal scenario described in section 4.2.2, with benchmark values $T_* = 59.6$, $\alpha = 0.17$, $\beta/H_* = 12.54$, $\phi_*/T_* = 4.07$ (see table 3).

links, 1 million km arm length, a duration of 2 years and noise level corresponding to 10 times larger than expected (N1, also dubbed "LISA Pathfinder required"). For the intermediate configurations, we have fixed the duration to five years and the noise level to LISA Pathfinder expected, since these two characteristics are likely achievable. An open question, which we would like to answer with this analysis, is whether it is more efficient to add a pair of laser links or to increase the arm length for the purpose of probing the occurrence of first-order PTs in the early Universe. *The outcome, as we will see, is that adding a pair of laser links leads to a larger gain in sensitivity than increasing the arm length from 1 to 2 million km.*

To assess the detectability of the GW signal, we consider the signal-to-noise ratio [34],

$$\mathrm{SNR} = \sqrt{\mathcal{T} \int_{f_{\min}}^{f_{\max}} df \left[\frac{h^2\Omega_{\mathrm{GW}}(f)}{h^2\Omega_{\mathrm{Sens}}(f)} \right]^2}, \tag{3.1}$$

where $h^2\Omega_{\mathrm{Sens}}(f)$ denotes the sensitivity of a given eLISA configuration and $\mathcal{T}$ is the duration of the mission in years [33]. Whenever SNR is larger than a threshold $\mathrm{SNR}_{\mathrm{thr}}$, the signal $h^2\Omega_{\mathrm{GW}}(f)$ can be detected. Quantifying $\mathrm{SNR}_{\mathrm{thr}}$ is not an easy task. We briefly describe how this can be done here, referring the interested reader to ref. [33] for more details.

Applying a Bayesian method, refs. [35, 36] found that the old LISA configuration over one year can detect a white-noise stochastic background at the level of $h^2\Omega_{\mathrm{GW}}^{\mathrm{L6}} = 1 \times 10^{-13}$. This sensitivity can be achieved by exploiting the fact that, with three interferometer arms (i.e. three pairs of laser links), it is possible to form two (virtually) noise-independent detectors, in which the noise is uncorrelated whereas the GW signal is correlated. This technique is safe and robust, although it remains to be tested with realistic noise levels. On the other hand, this technique cannot be applied to the two-arm configurations, and the level of detectable GW background is degraded. With the same Bayesian method, and assuming good prior knowledge of the noise, ref. [36] finds that with a four-link but otherwise LISA-like configuration over one year one can detect a white-noise stochastic background at the level of $h^2\Omega_{\mathrm{GW}}^{\mathrm{L4}} = 3.5 \times 10^{-13}$.

These levels of sensitivity $h^2\Omega_{\mathrm{GW}}^{\mathrm{L6,L4}}$ do account for the presence of the confusion noise from galactic binaries: refs. [35, 36] show that this latter can be estimated, and therefore

JCAP04(2016)001

extracted, together with the cosmological signal using the Bayesian method. This is why we do not include it in the sensitivity curves of the C1-C4 configurations shown in figure 1.

For the present detection analysis, we use the above results and convert them into corresponding values of $\mathrm{SNR}_{\mathrm{thr}}$. We compare the $h^2\Omega_{\mathrm{GW}}^{\mathrm{L6}}$ and $h^2\Omega_{\mathrm{GW}}^{\mathrm{L4}}$ detection levels with the power law sensitivity curve for each six-link (respectively, four-link) configuration. The power law sensitivity curve is a concept developed in [34] with the aim of accounting for the improvement in the usual sensitivity curves of a GW detector that comes from the broadband nature of a stochastic signal. The curve is given by the envelope of power laws $\Omega_\beta(f/f_{\mathrm{ref}})^\beta$ that can be detected with $\mathrm{SNR}=1$, varying β. For each eLISA configuration, we compute the power law sensitivity curve, and the SNR corresponding to the detection levels $h^2\Omega_{\mathrm{GW}}^{\mathrm{L6}}$ and $h^2\Omega_{\mathrm{GW}}^{\mathrm{L4}}$. To be conservative, for the four-link configurations we increase the detectability level to $h^2\Omega_{\mathrm{GW}}^{\mathrm{L4}}=10^{-12}$. This yields $\mathrm{SNR}=10$ for all six-link configurations and $\mathrm{SNR}=50$ for all four-link configurations. We then interpret these values as $\mathrm{SNR}_{\mathrm{thr}}$. In other words, we classify a given GW background $h^2\Omega_{\mathrm{GW}}(f)$ as detectable by a six-link configuration (four-link) if, once inserted into eq. (3.1), it returns $\mathrm{SNR}>10$ ($\mathrm{SNR}>50$) [33]. Since we choose $\mathrm{SNR}_{\mathrm{thr}}$ based on [35, 36], the confusion noise from galactic binaries is accounted for in our analysis.

3.2 Examples of gravitational wave spectra

We have seen in section 2.1 that the GW spectrum from a first-order PT is in general given by the sum of three contributions: that of the scalar field gradients, sound waves and MHD turbulence. The relative importance of each contribution depends on the details of the PT dynamics, as discussed in section 2.2. Here we provide some examples of spectra to show the interplay among the aforementioned contributions. This helps to clarify the model-independent sensitivity contours derived in the next section.

In figure 2 we show examples of GW spectra that can arise if the PT proceeds through non-runaway bubbles (Case 1 above), for fixed T_*, α and v_w, and varying β/H_*. The total spectrum is given in eq. (2.14) by the sum of the signal generated by sound waves and by MHD turbulence. Since we set $\epsilon=0.05$ the signal from sound waves is dominant (cf. eq. (2.16)). Turbulence can play a role at high frequencies, because the signal from sound waves decays faster (i.e. with $p=4$ as opposed to $p=5/3$, cf. eqs. (2.9) and (2.12)) and the peak positions are not that different (cf. eqs. (2.10) and (2.13)). Increasing β/H_* at fixed T_* and v_w causes the peak position to shift towards larger frequencies, and the overall amplitude to decrease. Correspondingly, the contribution from turbulence becomes less and less important because of the suppression due to the factor $8\pi f/h_*$ in eq. (2.12).

If the PT proceeds through runaway bubbles in a plasma (Case 2 above), the gradients of the scalar field also act as a source of GW together with sound waves and MHD turbulence. The corresponding examples of GW spectra are shown in figure 3, for fixed T_*, α, v_w and α_∞, and varying β/H_*. Note that fixing α_∞ sets the relative amplitude of the scalar field-related and the fluid-related contributions. For small β/H_* the contribution from the scalar field can dominate the GW spectrum, since the β/H_* enhancement of the amplitude that operates for long-lasting sources is less relevant (cf. eqs. (2.8) and (2.2)). As β/H_* increases, the sound wave contribution gains importance (provided that α_∞ is large enough). At sufficiently high frequencies however the scalar field contribution always dominates because of its shallow decay: $p=1$ as opposed to $p=4$ and $p=5/3$, see eqs. (2.3), (2.9) and (2.12).

It is apparent that the total GW spectrum arising from a first-order PT depends on the interplay among the contributions of the different sources, which in turn are determined by the specific dynamics of the PT. On the one hand this is encouraging, since it opens up the pos-

JCAP04(2016)001

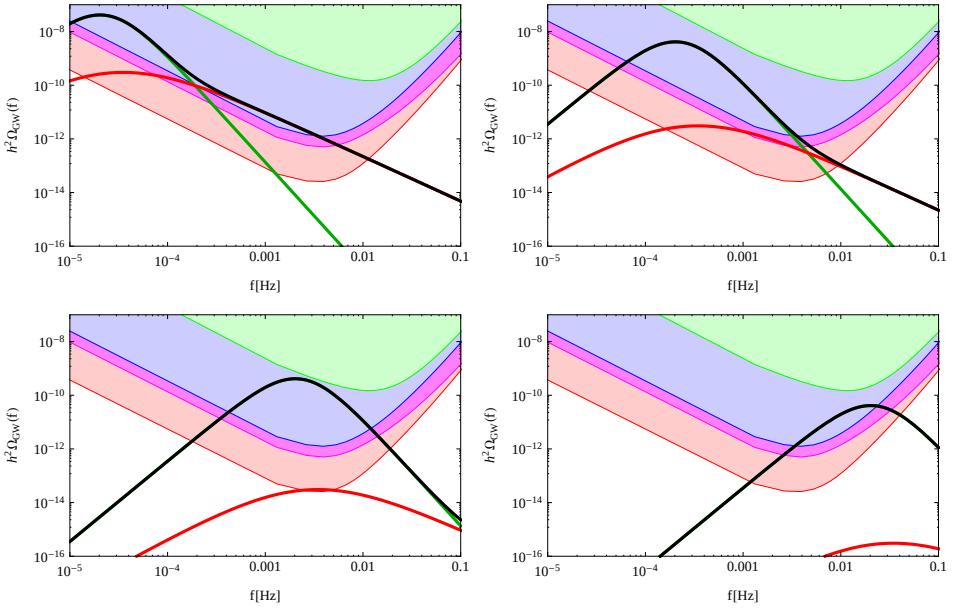

Figure 2. Example of GW spectra in Case 1, for fixed $T_* = 100\,\mathrm{GeV}$, $\alpha = 0.5$, $v_w = 0.95$, and varying β/H_*: from left to right, $\beta/H_* = 1$ and $\beta/H_* = 10$ (top), $\beta/H_* = 100$ and $\beta/H_* = 1000$ (bottom). The black line denotes the total GW spectrum, the green line the contribution from sound waves, the red line the contribution from MHD turbulence. The shaded areas represent the regions detectable by the C1 (red), C2 (magenta), C3 (blue) and C4 (green) configurations.

sibility of investigating the dynamics of the PT. On the other hand, this is probably feasible only in the most optimistic PT scenarios and for the best eLISA configurations. Note that the highest GW signals are expected for runaway bubbles in vacuum (Case 3 above) for which the GW spectrum has the simplest shape, being determined only by the scalar field contribution.

3.3 Sensitivity to a first-order phase transition

With the eLISA sensitivity to a stochastic GW background determined, we would like to assess eLISA's ability to detect GWs from primordial first-order PTs in a way that is as model-independent as possible. We have shown in the previous section that the predictions of the GW spectra differ in the three cases described in sections 2.2.1–2.2.3: we must therefore consider them separately. The most straightforward is Case 3, runaway bubbles in vacuum, since the GW spectrum depends only on the parameters β/H_* and T_*. If plasma effects are important, the GW signal depends in addition on α, v_w and ϵ, and moreover on α_∞ for the case of runaway bubble walls at finite α.

Once a model predicting a strong first-order PT is chosen, these parameters are fixed. However, even without choosing a model, general considerations prevent these quantities from varying completely independently. For example, α, β/H_* and T_* are related: as α increases, β/H_* and T_* typically decrease. This behaviour is due to the shape of the Euclidean action of the tunneling solution, $S(T)$, as a function of temperature [38]; therefore, we can expect it to hold quite generally, and to occur in many different models predicting a strong first-order PT. However, the relationship between α, β/H_* and T_* cannot be specified analytically or numerically in more precise terms without knowing $S(T)$ in detail i.e. without restricting oneself to a given model. Therefore, it is not possible to perform a model-independent analysis

JCAP04(2016)001

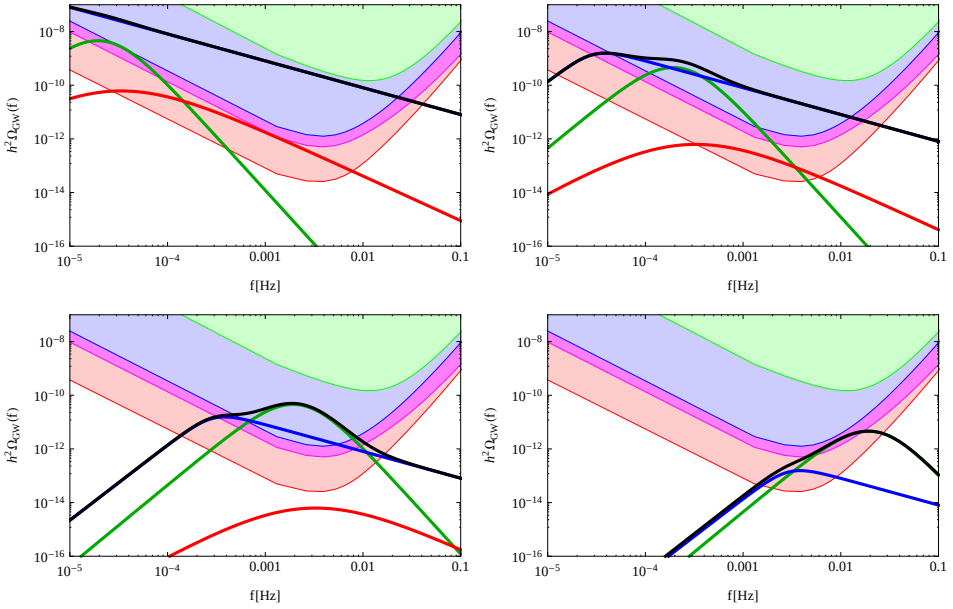

Figure 3. Example of GW spectra in Case 2, for fixed $T_* = 100\,\text{GeV}$, $\alpha = 1$, $v_w = 1$, $\alpha_\infty = 0.3$, and varying β/H_*: from left to right, $\beta/H_* = 1$ and $\beta/H_* = 10$ (top), $\beta/H_* = 100$ and $\beta/H_* = 1000$ (bottom). The black line denotes the total GW spectrum, the blue line the contribution from the scalar field, the green line the contribution from sound waves, the red line the contribution from MHD turbulence. The shaded areas represent the regions detectable by the C1 (red), C2 (magenta), C3 (blue) and C4 (green) configurations.

that realistically accounts for the relation among α, β/H_* and T_*. As a consequence, in the following we have chosen to let them vary freely,[9] and in figures 4, 5 we present contour plots in the plane $(\alpha\,,\ \beta/H_*)$ for different values of T_* and representative choices of v_w, ϵ and α_∞. In figure 6 the sensitivity is instead shown in the $(T_*\,,\ \beta/H_*)$ plane. It is important to keep in mind that not all the points of the detection regions shown in figures 4–6 can be realized within a realistic model. See [6] for a very similar analysis in the 2012 eLISA configuration (also called NGO at the time).

Figure 4 shows the regions in $(\alpha\,,\ \beta/H_*)$ which are accessible by the four eLISA configurations described in section 3.1 for several values of T_* in the case of non-runaway bubble walls (taking $v_w = 0.95$). We have set $\epsilon = 0.05$. In all figures, the regions detectable by eLISA for each eLISA configuration are shaded. As anticipated, *the two six-link configurations provide the best reach.*

The behaviour of the curves in figure 4 can be understood as follows. Larger values of α and lower values of β/H_* are easier for eLISA to detect because the amplitude of the GW spectrum increases with α and decreases with β/H_*. At fixed T_* and small β/H_* only the high frequency tail of the spectrum can enter the sensitivity curve: as α increases, this happens at correspondingly smaller values of β/H_*. On the other hand, as β/H_* increases for a fixed value of α, the signal peak enters the detectable region, and finally exits it again for very high β/H_*. The contours flatten out at high α, as the α-dependence drops out from the GW spectrum amplitude for $\alpha \gg 1$. Increasing the temperature causes smaller α-values

[9] A preliminary analysis of this type was carried out in [4] under the simplifying but arbitrary assumption of a Jouguet detonation, which allows to express the bubble wall velocity as a function of α.

JCAP04(2016)001

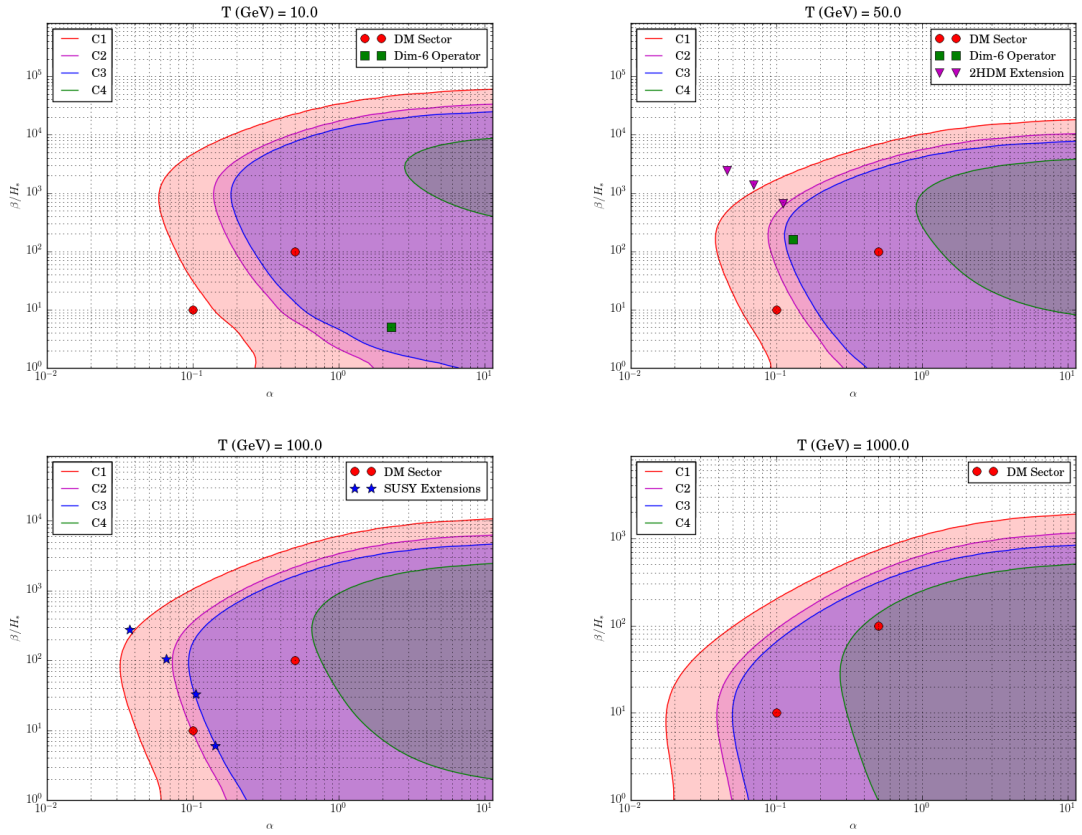

Figure 4. Projected eLISA sensitivity to Case 1: non-runaway relativistic bubble walls. Results are displayed for four values of T_* (indicated) and the four eLISA configurations described in table 1. The detectable region is shaded. Also shown are benchmarks from various specific models, discussed in section 4. All other parameters are as described in the text. Note that the values of T_* chosen correspond only approximately to the precise values for the benchmark points. The GW signal is given primarily by the contribution of sound waves (turbulence is negligible for the chosen value of ϵ).

to enter the detection region, because the peak frequency of the spectrum is shifted towards higher frequencies where the eLISA sensitivity is better. However, detection requires β/H_* to be small enough: as we have seen, increasing β/H_* at fixed T_* causes the peak frequency to shift beyond the frequency window detectable by eLISA.

In figure 4 we also show the benchmarks from various specific models, discussed in section 4. The values of T_* in each panel are chosen so as to approximately match the PT temperatures of the benchmarks.

Figure 5 applies to runaway bubbles (i.e. $v_w = 1$) at finite α. Again we take $\epsilon = 0.05$ and show several values of T_* tuned to match the benchmarks of the models presented in section 4. For concreteness, we have to fix the value of α_∞ in each panel: it is apparent that the contours of the detectable regions depends strongly on α_∞. In appendix A we provide extra figures showing the variation of the contours with α_∞. Each benchmark point of figure 5 represents a model with a given value of α_∞ according to eq. (2.21) (cf. the tables in section 4). Consequently, for each panel we have chosen a value of α_∞ which is representative of all benchmarks, following the criterion that the position of the benchmark

JCAP04(2016)001

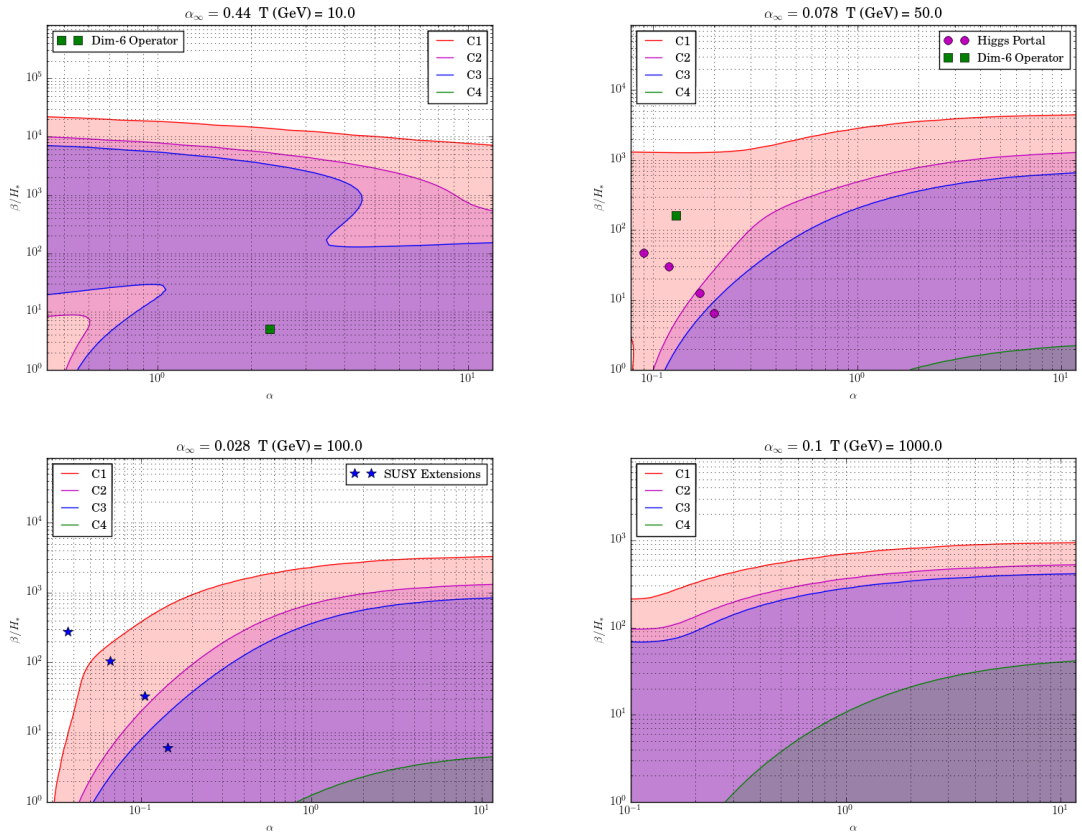

Figure 5. Projected eLISA sensitivity to Case 2: runaway bubble walls with finite α. Results are displayed for four values of T_* and α_∞ (indicated) and the four eLISA configurations described in table 1. The detectable region is shaded. Also shown are benchmarks from various specific models, discussed in section 4. All other parameters are as described in the text. Note that the values of T_* and α_∞ chosen correspond only approximately to the precise values for the benchmark points (as described in the text). The GW signal is given primarily by the contribution of the scalar field and of the sound waves.

points with respect to the contours remains as unaltered as possible. For $T_* = 1\,\text{TeV}$ there are no benchmarks: we have fixed $\alpha_\infty = 0.1$. Note that in the four panels we only plot the region $\alpha \geq \alpha_\infty$, for which the scalar field plays a role. For an explanation of the behaviour of the curves in figure 5 we refer the reader to appendix A.

We reiterate that the sound wave contributions in figures 2–5 rely on extrapolating the results found by simulations for $\alpha \lesssim 0.1$ and small fluid velocities to stronger transitions. The validity of this extrapolation remains to be determined. The reader should bear this in mind when interpreting our results, especially in cases where the sound wave contribution dominates for $\alpha \gtrsim 0.1$ (e.g. Case 1).

Finally, the projected eLISA sensitivity for Case 3 (runaway bubbles in vacuum) is shown in figure 6. This case is parametrically simpler than the other two. The GW signal, due entirely to the scalar field contribution, only depends on T_* and β/H_*. eLISA's sensitivity to the stochastic background peaks for frequencies around $1 - 10$ mHz. Therefore, as the temperature increases, the GW peak frequency f_{env} approaches this region from below, and higher and higher values of β/H_* are detectable. However at some point the predicted peak

JCAP04(2016)001

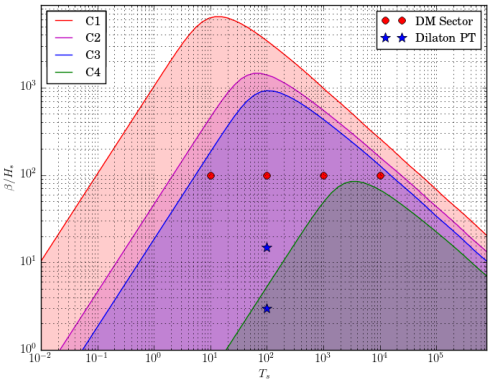

Figure 6. Projected eLISA sensitivity to Case 3: runaway bubble walls in vacuum. The region detectable by each configuration (cf. table 1) is shaded. Also pictured are the predictions corresponding to the benchmark points discussed in section 4 that fall under Case 3.

frequency increases above the optimal eLISA value, and larger amplitudes are necessary for detection; the detectable values of β/H_* start to decrease accordingly.

3.4 Summary of model-independent projections

The model-independent analysis of this section shows that *the six-link configurations provide the most coverage to first-order cosmological phase transitions. The configuration with four links and 2 million km arm length is, however, not much worse than that with six links and 1 million km arm length.* Note that much better knowledge of the instrumental noise and astrophysical backgrounds would be needed to use the four-link configurations, since one cannot cross-correlate the signal of the two effective, coincident detectors that the six-link configurations provide. This is accounted for in the above analysis through the technique explained in section 3.1, and in particular through the increase of $\mathrm{SNR}_{\mathrm{thr}}$. We stress that *our comparison between the four- and six-link configurations would change substantially if the analysis of ref. [36] were found to be unfeasible in practice, and/or the assumed prior knowledge of the noise were unachievable.*

We now move on to consider how specific models map on to the model-independent parameter space we have been discussing so far.

4 Testing specific models with strong phase transitions

Many scenarios beyond the Standard Model of particle physics predict first-order cosmological PTs.

Such a transition could have occurred during electroweak symmetry breaking. Provided the Universe reached sufficiently high temperatures after inflation, electroweak gauge symmetry was likely unbroken after reheating. As the Universe cooled, the symmetry would then have been spontaneously broken when a Higgs field, charged under $\mathrm{SU}(2)_L \times \mathrm{U}(1)_Y$, acquired a VEV. In the Standard Model of particle physics, and for the observed value of the Higgs mass, no transition occurs; electroweak symmetry is instead broken at a cross-

JCAP04(2016)001

over [39, 40].[10] However, many well-motivated extensions of the Standard Model predict a strong first-order electroweak PT instead of a cross-over. Such a transition could have played a role in generating the observed baryon asymmetry through the mechanism of electroweak baryogenesis [42] and produced a spectrum of gravitational radiation observable by eLISA, through the mechanisms described above in section 2.[11]

Alternatively, there are various extensions of the SM that predict strong first-order cosmological PTs not tied to the electroweak scale (or baryogenesis). Models solving the hierarchy problem via warped extra dimensions and dark matter sectors with non-trivial gauge structure are two such scenarios.

In the remainder of this section, we discuss several specific examples of models that predict strong first-order cosmological PTs, at the electroweak scale (section 4.2) or beyond (section 4.3), with GW signals detectable by eLISA. Before proceeding, however, we briefly outline different mechanisms for generating strong PTs in the early Universe.

4.1 Mechanisms for generating a strong first-order phase transition

There are a variety of well-studied mechanisms for generating a strongly first-order PT in scenarios beyond the Standard Model. Thermal loops of new bosonic modes can contribute a large cubic term to the finite temperature effective potential. This occurs for example in the minimal supersymmetric extension of the Standard Model (MSSM) with a light scalar top quark (stop). Even if the new degrees of freedom do not contribute substantially to the finite-temperature cubic term, it is also possible to rely primarily on the SM gauge boson contributions for the barrier, provided the free-energy difference between vacua at zero temperature is small enough (this in turn depends on the interplay of various terms in the potential), as may occur in extended Higgs sectors. Alternatively, new tree-level terms in the scalar potential can directly source a barrier (which can persist to zero temperature). This can occur either through new renormalizable or non-renormalizable operators. In the former case, even if no cubic terms are present in the potential, a tree-level barrier can arise at finite temperature if one of the scalar fields obtains a non-vanishing VEV in an earlier (not necessarily first-order) PT.

The aforementioned mechanisms typically rely on polynomial potentials, in which case the critical temperature, the nucleation temperature, the VEV of the scalar field at the minimum of the potential and the position of the barrier in field space all typically share a common scale. An alternative and intriguing possibility arises in models with a dilaton-like potential that is nearly conformal. The potential can be described by a scale invariant function modulated by a slow evolution across scales, similar to the Coleman-Weinberg mechanism in which a slow Renormalisation Group evolution of the potential parameters can generate widely separated scales for the various aforementioned quantities. The potential in this case is very shallow, and the position of the barrier and the minimum of the potential can be very far apart. As a result, a significant amount of supercooling and therefore a strong first-order PT can be obtained without a substantial tuning of parameters.

In the remainder of this section, we review some well-motivated scenarios for physics beyond the Standard Model that can feature strong first-order PTs via (combinations of) the

[10] A GW spectrum is nonetheless generated by equilibrium phenomena in the electroweak plasma, such as scatterings between thermal constituents and collective phenomena. The resulting spectrum [41] is however tens of orders of magnitude below eLISA sensitivity.

[11] Typically, transport-driven electroweak baryogenesis requires sub-sonic bubble wall velocities, corresponding to small GW signals. There are exceptions however; see e.g. ref. [43, 44].

JCAP04(2016)001

mechanisms mentioned above. Our aim is to determine reasonable values of α, β/H_* and T_* that can actually arise in realistic particle physics models. For each model, we provide some benchmark points (shown in figures 4–6) and compute the parameters relevant for predicting the spectrum of gravitational radiation. We also comment on the detectability by eLISA in each case.

4.2 Strong phase transitions at the electroweak scale

4.2.1 Supersymmetric extensions of the standard model

Supersymmetric theories with low-energy soft-breaking terms are theoretically well-motivated models featuring new scalar fields that can naturally lead to strong electroweak PTs and, in turn, to sizeable GW signals.

The most well-studied supersymmetric extension of the SM is the MSSM. This theory can give rise to a reasonably strong electroweak PT, provided the lightest scalar top quark has a mass below that of the top quark [45, 46]. This rough upper bound decreases substantially when the Higgs boson mass is fixed at around 125 GeV [47, 48], pushing the model into severe tension with LHC stop searches and Higgs rate measurements [49–52]. At the same time, independent of the PT, the MSSM is losing its original appeal due to the large amount of fine-tuning required to obtain a Higgs mass of 125 GeV. Both tensions can be alleviated in non-minimal supersymmetric models.

In singlet extensions of the MSSM, new F-term contributions can increase the tree-level Higgs mass and, consequently, reduce the fine tuning of the electroweak sector (compared to to the MSSM). Moreover, the presence of the scalar singlet enriches the Higgs sector and has important consequences for the electroweak PT. Even after imposing discrete symmetries on the field interactions, the (reduced) parameter space still allows for strong PTs [53–55] while complying with all Run-I LHC bounds [56–58]. In particular, in the regime where the electroweak PT occurs in two steps (i.e. with the singlet acquiring a VEV first, and electroweak symmetry breaking occurring at a subsequent transition), very strong electroweak PTs seem likely [59].

For instance, in the four benchmark points of the singlet extension of the MSSM studied in ref. [59], the tree-level barrier between the minima along the singlet and the SM-like Higgs directions of the potential efficiently strengthens the electroweak PT. The properties of the PTs corresponding to these four points were obtained and studied in ref. [59]; the results are quoted in table 2. Notably, all points fulfill the runaway requirement. Relativistic wall velocities are thus expected, although obstructions could prevent the bubble from actually reaching the runaway regime. Since the existence of these obstructions remains to be studied in this model, we consider the GW signal in both the runaway and the non-runaway scenarios (Case 1 and Case 2, in the language of section 2.2). The prospects for detecting the GW background from these benchmark points at eLISA are shown in figures 4 and 5 (bottom left panels) where the values of α and β/H_* of table 2 are displayed (the approximation $T_* \simeq 100\,\text{GeV}$ has been used). We find that (cf. figure 4) *only the most sensitive eLISA configuration can probe the electroweak PT of the majority of the considered benchmark points. For the relativistic non-runaway scenario, the C2 (six-link) configuration can probe two benchmark points, while if the runaway scenario is realized* (cf. figure 5) *it can only probe one of them.*

Other extensions of the MSSM beyond that considered in ref. [59] are possible. However, such models seem unlikely to predict much stronger signals than those considered here, at least for electroweak (i.e. $\mathrm{SU}(2)_L \times \mathrm{U}(1)_Y$-breaking) transitions and without significantly departing from minimality. The predictions could differ substantially when considering PTs occurring before the electroweak transition. Further study is required to clarify this possibility.

JCAP04(2016)001

	A	B	C	D
T_* [GeV]	112.3	94.7	82.5	76.4
α	0.037	0.066	0.105	0.143
β/H_*	277	105.9	33.2	6.0
ϕ_*/T_*	1.89	2.40	2.83	3.12

Table 2. Characteristics of the electroweak PT predicted for the benchmark points of the singlet extension of the MSSM analyzed in ref. [59] (see section 4.2.1).

4.2.2 The standard model with additional scalars

Another simple class of scenarios that can give rise to observable GWs are (non-supersymmetric) extensions of the Standard Model scalar sector. The new scalar(s) can either be singlets or charged under the Standard Model gauge groups.

New SM gauge singlet scalar fields can couple directly to the Higgs field via renormalizable operators. Such models are attractive from the standpoint of dark matter [60], baryogenesis [61], and solutions to the hierarchy problem without colored top partners [62]. New terms in the tree-level potential can allow for strong electroweak PTs and an observable level of gravitational radiation.

To see what this entails, let us consider the Higgs portal scenario with a real gauge singlet scalar field, which is the simplest case and illustrates some key features of this scenario. We will restrict ourselves to the case where the new gauge singlet scalar, S, is charged under a discrete $\mathbb{Z}_2$ symmetry and has no VEV at zero temperature [63]. All other Standard Model particles are assumed to transform trivially under the new $\mathbb{Z}_2$ symmetry. The most general renormalizable scalar potential in this case can be written as

$$V(H,S) = -\mu^2(H^\dagger H) + \lambda(H^\dagger H)^2 + \frac{1}{2}a_2(H^\dagger H)S^2 + \frac{1}{2}b_2S^2 + \frac{1}{4}b_4S^4\,. \tag{4.1}$$

Here, the CP-even neutral component of H is identified with the 125 GeV Standard Model-like Higgs. The discrete symmetry ensures that S is stable. The singlet can thus contribute to the observed dark matter relic abundance. Note that S can also be a component of a scalar charged under other symmetries (e.g. a hidden sector gauge group). One should also bear in mind that this model resides in a subspace of a larger model parameter space without the $\mathbb{Z}_2$ symmetry. Going beyond the $\mathbb{Z}_2$ limit opens up additional parameter space for a strong first-order PT.

This "Higgs portal" model can give rise to a strong electroweak PT in primarily two ways. If the parameter $b_2 < 0$, the singlet can be destabilized from the origin at finite temperature (along the S direction in field space). The $H^\dagger H S^2$ term then provides a cubic term to the effective potential, and hence can contribute to a barrier along the direction connecting the $\langle S\rangle \neq 0$ and electroweak vacua (in which $\langle S\rangle = 0$). This is another example of a two-step transition. Alternatively, if $b_2 > 0$, the singlet will be stabilized at the origin at all temperatures. Nevertheless, large zero-temperature loop effects can lower the SM-like Higgs quartic coupling to increase the value of $\phi(T_n)$ inside the bubble. Finite-temperature loop effects can also play a role (alongside the SM gauge, Higgs, and Goldstone bosons) in contributing to a barrier between the origin and the electroweak vacuum in this case.

To illustrate the characteristics of the electroweak PT in this scenario, we consider four benchmark points. These points, labeled A–D, are chosen such that $m_S = 250\,\text{GeV}$,

JCAP04(2016)001

	A	B	C	D
T_* [GeV]	70.6	65.2	59.6	56.4
α	0.09	0.12	0.17	0.20
β/H_*	47.35	29.96	12.54	6.42
ϕ_*/T_*	3.39	3.70	4.07	4.32

Table 3. Characteristics of the electroweak PT predicted for the Higgs portal benchmark points discussed in section 4.2.2.

and correspond to $(a_2, b_4) = (2.8, 2.1)$, $(2.9, 2.6)$, $(3.0, 3.3)$, and $(3.1, 4.0)$, respectively; they satisfy all current phenomenological constraints and are particularly difficult to test at colliders [65]. The corresponding PT parameters are displayed in table 3; they are obtained by using the full 1-loop finite-temperature effective potential and including the resummation of daisy diagrams. For such strong transitions, the bubble wall is expected to run away without obstruction [32], corresponding to Case 2 of section 2.2. The sensitivity of eLISA to these points is shown in figure 5, top-right panel. We find that *the most sensitive eLISA configuration can probe all four benchmark points, while C2 (six-links) and C3 (four-links) can probe benchmark point D, with point C residing at the edge of the region detectable by C2)*. The observational situation is therefore similar to the one discussed in section 4.2.1.

While the benchmarks shown above feature thermal transitions (i.e. the $O(3)$-symmetric bounce minimizes the four-dimensional Euclidean action at T_n), it should be noted that this model can allow for a metastable electroweak-symmetric phase to persist to zero temperature. This suggests that very strongly supercooled transitions occurring in vacuum (Case 3) may be possible. The resulting GW signals in this case have not been previously analyzed, but would be worthwhile to consider in future work.

New scalars charged under the SM gauge group are also phenomenologically and theoretically well-motivated. When transforming nontrivially under the electroweak gauge group, such scalars can participate in electroweak symmetry breaking, with a potentially significant impact on the electroweak PT. The simplest realization of this scenario is that of a two-Higgs-doublet-model (2HDM), in which the SM Higgs sector is enlarged by a second scalar doublet. These scenarios can accommodate electroweak baryogenesis [66] and can result in the generation of GWs at the electroweak PT (with preliminary studies having been carried out in [67]). The scalar potential is[12]

$$V(H_1, H_2) = \mu_1^2 |H_1|^2 + \mu_2^2 |H_2|^2 - \mu^2 \left[H_1^\dagger H_2 + \text{h.c.}\right] + \frac{\lambda_1}{2} |H_1|^4 + \frac{\lambda_2}{2} |H_2|^4 + \lambda_3 |H_1|^2 |H_2|^2 + \lambda_4 \left|H_1^\dagger H_2\right|^2 + \frac{\lambda_5}{2} \left[\left(H_1^\dagger H_2\right)^2 + \text{h.c.}\right] . \tag{4.2}$$

After electroweak symmetry breaking, the presence of the two doublets H_1, H_2 yields three new physical states in addition to the 125 GeV Higgs h: a charged scalar $H^\pm$ and two neutral states H_0, A_0.

In this class of scenarios, a strong electroweak PT is driven by a decrease in the free-energy difference between the electroweak-symmetric local maximum and electroweak-broken phase at $T = 0$, w.r.t. the SM prediction. The effect of this decrease on the strength of PT

[12] We assume for simplicity CP conservation, as well as a $\mathbb{Z}_2$ symmetry (softly broken by μ^2 in eq. (4.2)) for phenomenological reasons, namely the absence of flavour-changing neutral currents in the Higgs sector.

JCAP04(2016)001

	A	B	C
T_* [GeV]	68.71	61.25	51.64
α	0.046	0.070	0.111
β/H_*	2446	1383	663
ϕ_*/T_*	3.15	3.69	4.53

Table 4. Characteristics of the electroweak PT predicted for the benchmark points considered for the 2HDM in section 4.2.2.

is in fact similar to the reduction of the SM-like Higgs quartic coupling occurring for singlet "Higgs-portal" scenarios with $b_2 > 0$, as described above. Moreover, such a decrease in the free energy difference between the origin (in field space) and the vacuum with broken electroweak symmetry is highly correlated with a large mass splitting between the new states A_0, H_0 [68, 69], which provides an appealing connection to LHC signatures.

For 2HDM scenarios, it is always true that $\alpha < \alpha_\infty$, and so these models belong to Case 1 of section 2.2. We present here three benchmark points studied in [70] with increasing strength of the electroweak PT, labelled A–C in table 4. The eLISA sensitivity to these benchmarks is shown in figure 4, top-right panel. We find that *only one benchmark point lies in the region detectable by C1. This point may also be marginally detectable by C2. Four-link configurations provide no access to this model.*

Finally, let us also point out that new scalar fields can also be charged under the SM color group, $SU(3)_c$. Such a scalar could trigger a strong first-order color-breaking transition in the early universe [71]. The broken gauge symmetry can be restored by a subsequent transition to the standard electroweak vacuum. As argued in ref. [71], color-breaking transitions in this two-step setup typically occur at temperatures close to the TeV scale. This may provide another interesting target for the eLISA experiment. We leave a study of the GW signatures of this scenario to future work.

4.2.3 The standard model with higher-dimensional operators

We have seen that tree level modifications of the Higgs potential can easily make the electroweak PT strongly first-order. The models of the previous sections considered cases in which new terms in the potential involving new (relatively light) scalar fields significantly strengthen the electroweak PT. Alternatively, the effects of *heavy* new physics on the PT can be studied and illustrated in a model-independent manner using an effective field theory approach, for instance by adding dimension-6 operators in the Higgs potential allowing for a negative quartic coupling [37, 72]:

$$V(\phi) = \mu^2|\phi|^2 - \lambda|\phi|^4 + \frac{|\phi|^6}{\Lambda^2} \ . \tag{4.3}$$

This model illustrates the typical correlations expected between small values of β/H_* and large α mentioned earlier. Contours of α and β/H_* were computed in the (m_h, Λ)-plane for the complete one-loop finite temperature effective potential associated with eq. (4.3) in ref. [37]. The region corresponding to a sizable GW signal from the electroweak PT is confined to values of Λ below 1 TeV. The tension between such a low cutoff and the LHC bounds remains to be investigated. Nevertheless, focusing on the GW signal, we consider two benchmark points where Λ is around 600 GeV [38], both in the relativistic, non-runaway

JCAP04(2016)001

	A	B
T_* [GeV]	63	26
α	0.13	2.3
β/H_*	160	5
ϕ_*/T_*	4	9.5

Table 5. Characteristics of the electroweak PT in the SM plus a dimension-6 effective operator for two benchmark points taken from ref. [38]: $\Lambda \sim 600\,\text{GeV}$ (A) and $\Lambda \sim 576\,\text{GeV}$ (B), see section 4.2.3.

case and in the runaway with finite α case (the predicted wall velocity remains to be studied in such non-renormalizable models, although runaways seem likely, given the tree-level origin of the barrier between vacua). The resulting features of the electroweak PT are quoted in table 5. We find that *for most benchmark points the GW signal can be detected by all eLISA configurations except C4. However, only C1 can detect all benchmark points.*

4.3 Strong phase transitions beyond the electroweak scale

As we have seen, observable GWs may have been produced at the electroweak scale in various scenarios beyond the Standard Model. However, there are other scenarios for new physics that may have given rise to a strong first-order cosmological PT in the early Universe. We discuss two such examples here.

4.3.1 Dilaton-like potentials and naturally supercooled transitions

Models with a spontaneously broken (approximate) conformal symmetry feature a pseudo-Nambu-Goldstone boson associated with the broken symmetry; this field is known as the dilaton. The scalar potential $V_\sigma(\sigma)$ of the dilaton field, σ, can be parametrized by a scale invariant function modulated by weakly scale-dependent function:

$$V_\sigma(\sigma) = \sigma^4 \times P(\sigma^\epsilon) \quad \text{where} \quad |\epsilon| \ll 1 \tag{4.4}$$

A particularly interesting and well-motivated class of scenarios arises when the quadratic term for the Higgs field ϕ is controlled by the VEV of the dilaton σ:

$$V(\sigma, \phi) = V_\sigma(\sigma) + \frac{\lambda}{4}(\phi^2 - \xi\, \sigma^2)^2 \tag{4.5}$$

where ξ is a constant. In particular, this potential is precisely that of the 5D Randall-Sundrum models [75], which provide an elegant solution to the hierarchy problem of the SM.

Assuming the Higgs is localized on the IR brane at a distance $y = r$ from the UV brane (localized at $y = 0$), the 4D effective action for the Higgs is

$$\mathcal{L}_4 = e^{-2k\pi r}\eta^{\mu\nu} D_\mu \tilde{H} D_\nu \tilde{H} - e^{-4k\pi r}\lambda(|\tilde{H}|^2 - v_P^2)^2 = \eta^{\mu\nu} D_\mu H D_\nu H - \lambda\left(|H|^2 - \frac{v_P^2}{k^2}\sigma^2\right)^2 \tag{4.6}$$

where $v_P \sim \Lambda_{UV} \sim m_{Pl} \sim k$, H is the canonically normalized field $H = e^{-k\pi r}\tilde{H}$ and the radion field is

$$\sigma \equiv k e^{-k\pi r}. \tag{4.7}$$

We also define the scale

$$\Lambda_{IR} \equiv \langle \sigma \rangle \tag{4.8}$$

which is generated once the radion is stabilized and is exponentially warped down from the Planck scale due to the Anti de Sitter (AdS) geometry. We also have $\xi = v^2/\Lambda_{IR}^2$. For the 5D AdS metric, the effective 4D potential for the radion was shown to be dilaton-like (eq. (4.4)), independently of the inter-brane distance stabilization mechanism [76–78]. We therefore recover the scalar potential eq. (4.5) for the coupled radion-Higgs system. Solving the weak/Planck scale hierarchy leads to $\Lambda_{IR} \sim \mathcal{O}(\text{TeV})$.

The cosmological implications of the potential $V_\sigma(\sigma)$ in eq. (4.5) were considered in refs. [73, 74]. A very strong first-order PT typically occurs for this type of potential. In the first investigation of the associated PT, it was argued that the transition to the minimum of the radion potential could not complete [79]. This conclusion essentially followed from a thin-wall estimate of the critical bubble action and assuming that tunneling would take place directly to the minimum of the potential. The key point stressed in ref. [80] is that the PT can actually complete through tunneling to a value of the field much smaller than the value at the minimum of the potential and subsequently rolling towards the minimum. This is typical of very shallow potentials. As emphasized in ref. [74], the value of the field at tunneling, σ_r, is $\sigma_r \sim \sqrt{\sigma_+ \sigma_-}$ where σ_+ and $\sigma_- = \Lambda_{IR}$ are the positions of the maximum and minimum of the potential respectively. The nucleation temperature T_n is proportional to σ_r and given by [74, 81]

$$T_n \sim 0.1\sqrt{\sigma_+ \sigma_-} \sim 0.1\ \Lambda_{IR}\ \sqrt{\frac{\sigma_+}{\sigma_-}}\ . \tag{4.9}$$

For a standard polynomial potential, $\sigma_+ \sim \sigma_- \sim \sigma_r \sim T_n$. In contrast, for the very shallow dilaton-like potential, $\sigma_+ \ll \sigma_-$, and the nucleation temperature is parametrically much smaller than the scale associated with the minimum of the potential. We therefore naturally get a stage of supercooling before the PT completes. The hierarchy between σ_- and σ_+ can be as large as the Planck scale/weak scale hierarchy: $\sigma_-/\sigma_+ \lesssim \Lambda_{UV}/\Lambda_{IR}$. Therefore the nucleation temperature can be as low as $T_n \sim 0.1\Lambda_{IR}\sqrt{\Lambda_{IR}/\Lambda_{UV}}$ [74]. We obtain $T_n \sim 35\,\text{MeV}$ if $\Lambda_{IR} = 5\,\text{TeV}$ and $\Lambda_{UV} = M_{Pl}$, while $T_n \sim 0.1\,\text{GeV}$ if $\Lambda_{IR} = 1\,\text{TeV}$ and $\Lambda_{UV} = 10^{10}\,\text{GeV}$. Note that at scales below Λ_{QCD}, eq. (4.4) will be modified, since QCD breaks conformal invariance. While a delayed electroweak PT down to the QCD scale is in principle a general outcome in this framework (and interesting from the standpoint of e.g. cold electroweak baryogenesis with the QCD axion [82]), this modification of the scalar potential around the QCD scale, which we do not account for here, will affect the detailed predictions of this model.

We have argued that the nucleation temperature of the PT associated with a potential of the form in eq. (4.4) can be many orders of magnitude smaller than the scale given by the VEV at the minimum of the potential. In this case, plasma effects can be ignored and the GW signal comes from runaway bubbles in vacuum. As discussed in section 2.2.3, while the PT temperature T_n can in principle be much smaller than $\Lambda_{IR} \sim \mathcal{O}(\text{TeV})$, the temperature T_* in the various GW formulae will be set by the reheating temperature, $T_* \approx T_{\text{reh}}$. This temperature is typically somewhat below Λ_{IR} and the peak frequency (eq. (2.5)) can easily fall within the range that will be probed by eLISA. In particular, for a dilaton VEV at the TeV scale, as motivated by the Randall-Sundrum scenario, and more generally by composite Higgs models which have a strongly coupled sector at the TeV scale, the predicted GW signal can be detectable by eLISA [80, 81].

JCAP04(2016)001

	A	B
T_* [GeV]	100	100
β/H_*	3	15

Table 6. Characteristics of the PT predicted for the benchmark points of the dilaton-like scenario in section 4.3.1.

The prospects for detecting the gravitational wave signal predicted by such a scenario are analyzed for two benchmark points, with PT properties summarized in table 6. The two benchmark points A and B represent the parameter space region in which this model solves the hierarchy problem without introducing a significant "little hierarchy" between the EW scale and Λ_{IR}. In computing β/H_*, eq. (2.22) is used, as is appropriate for vacuum transitions, since $T_* \approx T_{\rm reh} \gg T_n$. As shown in figure 6, *the prospects for observing GWs from this model are very good. Benchmark point A can be detected by all configurations while benchmark point B can be observed by all but C4.*

Very strong first-order PTs associated with nearly conformal dynamics at the TeV scale are interesting from the point of view of the hierarchy problem, but a similar situation may arise at a different scale. In this case, the discussion of this section remains applicable as far as the strength of the GW signal is concerned, although the predicted peak frequency will be affected.

4.3.2 First-order phase transitions in a dark matter sector

Models in which dark matter (DM) is a stable bound state of a confining dark sector are well motivated. Common examples are SU(N) dark sectors with n_f light dark quarks, where the DM candidate is a dark baryon-like state [83], as well as cases with no massless quarks, in which case dark glueballs are DM candidates [84]. The DM mass is typically of the order of the confinement scale, which in turn is set by the scale of the associated symmetry breaking PT. In a large class of models the PT is first order, and therefore can give rise to a GW signal.

Viable DM models of this class have masses ranging from $\mathcal{O}(10)$ MeV up to $\mathcal{O}(100)$ TeV. The GW signal falls into the eLISA frequency range for DM masses ranging from 10 GeV to 10 TeV. In particular the high mass range is difficult to test in current collider experiments, and GWs provide a unique window to probe some aspects of these models.

The first-order nature of the PT in these models can be determined from very basic symmetry arguments [85]. For an SU(N) dark sector with $N \geq 3$ and n_f light quarks the PT is first order for $n_f = 0$ or $3 \leq n_f \lesssim 4N$. The PTs occur in the non-perturbative regime of the theories, so the details of the dynamics are currently not known. This can be improved in the future using lattice simulations.

Some models might feature a rather weak PT, which will typically make them inaccessible by eLISA. On the other hand, studies of holographic PTs [73, 74, 79–81] discussed in section 4.3.1 find cases with very strong transitions, and therefore one can hope that models close to the conformal window (i.e. with n_f close to $4N$) will also fall into this class. Thus, we expect at least a subset of the models to feature a sufficiently strong signal to be detectable by eLISA.

We consider a scenario with relativistic (non-runaway) bubbles in a plasma (Case 1), and a scenario with runaway bubble walls in vacuum (Case 3). We do not consider the possibility of runaway bubbles in a plasma (Case 2), simply because the prospects for GW detection by eLISA in this case depend sensitively on α_∞ (cf. appendix A), which is not

JCAP04(2016)001

known for these scenarios. In fact, as the present understanding of the model does not allow for proper quantitative estimates, we simply make some reasonable guesses for all of the relevant PT parameters. Specifically, in the first case we assume $T_* = 10, 50, 10^2, 10^3$ GeV. For each temperature we consider $\beta/H_* = 10$ as well as $\beta/H_* = 100$, respectively accompanied by $\alpha = 0.1$ and $\alpha = 0.5$. In the second case we assume $T_* = 10, 10^2, 10^3, 10^4$ GeV and $\beta/H_* = 100$. *We stress that these values are simply educated guesses, since our present understanding of the model does not allow for proper quantitative estimates.* We analyze the GW signal detectability for Case 1 and Case 3 in figures 4 and 6. We find that, *in Case 1, the C4 configuration can only probe one of the benchmark points, while C1 can detect all but one. C2 and C3 provide comparable sensitivity to these points. For Case 3, all but C4 can detect the benchmark points considered.*

Despite its numerous issues that require future clarification, the present model deserves some attention as it highlights a link between eLISA and DM experiments. Dark matter model building in recent years has focussed on non-minimal models with additional dynamics, and this model is a broad subclass of this category. From the point of view of theoretical particle physics there is a strong desire to find alternative ways to probe these models, since they are relatively hidden from collider and direct DM searches. In contrast, the GW signal does not depend on the interaction strength between the dark and visible sectors, and thus provides a unique way to probe these scenarios. In particular, most of the parameter space will not be excluded by other experiments within the next 20 years, and so eLISA may provide the first evidence in favor of such a dark sector. The criteria for first-order PT are simple and generic, and the models considered so far are minimal. Other classes of models in which DM is associated with a first-order PT are conceivable, and the models considered here could also be extended, for example to enhance the strength of the transition. Future work considering these possibilities is warranted.

5 Summary and conclusions

We have seen that many scenarios beyond the SM predict a GW signal from first-order phase transitions in the early Universe that can be observed by eLISA. Although ongoing efforts at the LHC will be able to test some of these scenarios, there remain many examples that cannot be probed through collider experiments on a timescale comparable to that of eLISA, if at all.

The eLISA detector has the potential to provide us with valuable information about electroweak-scale physics that cannot be obtained from high-energy colliders, for example concerning the dynamics of the electroweak phase transition and the shape of the Higgs potential, or concerning hidden sectors and dark matter at the weak scale. Violent processes in the early Universe may in fact have taken place in a sector with very feeble couplings to the SM particles; in this case the new sector might only be probed via GWs.

The eLISA interferometer is also in a good position to probe strong first-order phase transitions taking place well above the electroweak scale, in the multi-TeV regime. There are many theoretical motivations for such scenarios, for example solving the hierarchy problem or explaining the observed dark matter abundance in our Universe. In fact, we have shown that eLISA may be sensitive to cosmological phase transitions taking place at temperatures above 10 TeV, and therefore be able to probe new physics that will remain inaccessible to collider experiments for the foreseeable future.

We have demonstrated the extent to which different eLISA configurations can realistically detect the stochastic gravitational wave background arising from strong first-order cos-

JCAP04(2016)001

mological phase transitions. To do so, we considered a (model-independent) parametrization of the phase transition in terms of α, β/H_*, T_*, and α_∞. To make contact with realistic models, we analysed the predicted values for these parameters in various well-motivated scenarios.

Focusing on the eLISA designs listed in table 1, and taking into account the signal-to-noise ratio thresholds required for detection ($\mathrm{SNR}_{\mathrm{thr}} > 10$ for six links, $\mathrm{SNR}_{\mathrm{thr}} > 50$ for four links [33]), we conclude that:

- For typical electroweak phase transitions, in which all relevant dimensionful parameters are near the electroweak scale, the configuration C1 is definitively better than the others, while the configuration C4 is decisively unsatisfactory. The performances of the configurations C2 and C3 are similar, but C2 has the ability to test a larger fraction of the considered benchmark points.

- For phase transitions not strictly related to electroweak symmetry breaking, e.g. involving a dark sector or a dilaton, the predicted characteristics of the phase transitions exhibit more variation. Larger GW signals are allowed than in the electroweak case. For certain scenarios, the resulting GW spectrum can be probed by all considered eLISA designs. The C1 configuration, however, has the potential to test a much wider region of the parameter space in such models than do C2–C4.

It is worth reiterating that our results for the four-link configurations depend strongly on the assumed prior knowledge of the noise level, as well as the feasibility of the data analysis technique proposed in [36].

Finally, we emphasize that our results can be straightforwardly extended beyond the specific models considered in section 4. To do so, one should identify the main features of the bubble wall dynamics from the general considerations of section 2.2 and e.g. refs. [9, 10, 31, 32], and compute the predicted values for the parameters α, β/H_*, T_* and α_∞, as defined in sections 1.1 and 2 (in some cases only a subset of these quantities will be relevant for the predicted GW signal). The results of this procedure can then be compared directly with the appropriate eLISA sensitivity curves provided in figures 4–7. In this way, we hope this study to serve as a useful tool (and motivation) for future investigations of eLISA's potential to probe new physics scenarios predicting strong first-order phase transitions in the early Universe.

Acknowledgments

The authors would like to thank the CERN Theory Group and the University of Stavanger for hosting the Cosmology Working Group meetings. We thank Jacopo Ghiglieri and Anders Tranberg for contributing to the discussions which led to this work. GN was partly supported by the Swiss National Science Foundation (SNF) under grant 200020-155935. JK is supported by the Natural Sciences and Engineering Research Council of Canada (NSERC). TK and GN were supported by the German Science Foundation (DFG) under the Collaborative Research Center (SFB) 676 Particles, Strings and the Early Universe. MH and SH acknowledge support from the Science and Technology Facilities Council (grant number ST/J000477/1). DJW is supported by the People Programme (Marie Skłodowska-Curie actions) of the European Union Seventh Framework Programme (FP7/2007-2013) under grant agreement number PIEF-GA-2013-629425. We acknowledge PRACE for awarding us access to resource HAZEL HEN based in Germany at the High Performance Computing Center Stuttgart (HLRS). Our simulations also made use of facilities at the Finnish Centre for Scientific Computing CSC,

JCAP04(2016)001

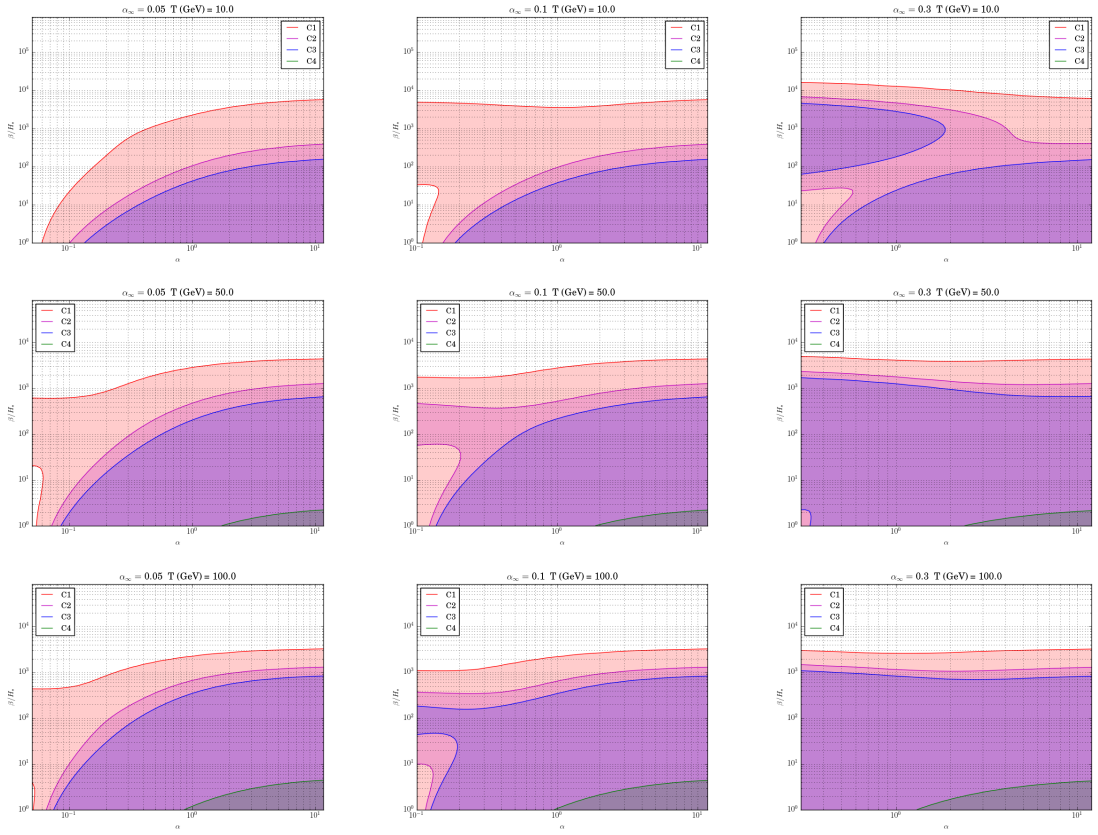

Figure 7. Detectable regions in the (α, β/H_*) plane for phase transitions with runaway bubbles at finite α (Case 2). In each row of panels we fix T_* as indicated and consider three values of α_∞, increasing from left to right.

and the COSMOS Consortium supercomputer (within the DiRAC Facility jointly funded by STFC and the Large Facilities Capital Fund of BIS). J.M.N. is supported by the People Programme (Marie curie Actions) of the European Union Seventh Framework Programme (FP7/2007-2013) under REA grant agreement PIEF-GA-2013-625809.

A Sensitivity to runaway bubbles in a plasma

If the PT proceeds as in Case 2, with runaway bubbles (i.e. $v_w = 1$) at finite α, the contours of the detectable region in the (α, β/H_*) plane depend not only on T_* and v_w, but also on α_∞. In our analysis we have consistently set v_w to values very close to one, maximizing its effect on the GW spectrum. In this appendix we aim to show how the sensitivity contours change with T_* and α_∞. We refer the reader to figure 7 where we plot the detectable regions for three values of T_* and α_∞.

From figure 7 it is apparent that the effect of increasing T_* is similar to that found by increasing α_∞. This is because, in both cases, the contribution of the sound waves to the GW spectrum gains importance. Fixing α_∞ amounts to fixing the relative contribution of the scalar field and of the sound waves, cf. eqs. (2.19). At small α_∞ and small T_* only the scalar field contribution is relevant: the typical contour-shape is that appearing in the top left panel of figure 7. For small β/H_*, only the high frequency tail $1/f$ lies within the eLISA sensitivity

JCAP04(2016)001

region. As β/H_* increases, a larger portion of the spectrum becomes observable until the peak finally exits the detectable region. Increasing β/H_* also causes the overall amplitude to diminish and therefore one needs correspondingly lager α to guarantee detectability. Starting from the situation with small α_∞ and small T_* (top left panel), one has that increasing T_* at fixed α_∞ does not change the relative contribution of the scalar field and sound waves but shifts the peak to higher frequencies. Since the peak due to the sound waves occurs at parametrically larger frequencies than that due to the scalar field (cf. eqs. (2.5) and (2.10)), this can help shift the spectrum into the detectable region, especially if β/H_* is large enough. We reiterate that the amplitude of the sound wave contribution is larger by a factor β/H_* than that of the scalar field in our treatment (cf. eqs. (2.2) and (2.8)). As a consequence, the regions at small α and large β/H_* open up with increasing T_*, in the middle left and bottom left panels of figure 7.

The same trend is observed at fixed T_* if one increases α_∞: the sound wave contribution is boosted in amplitude w.r.t. that of the scalar field and affects the detectable regions at small α and large β/H_*. Note that the amplitude of the scalar field contribution, eq. (2.2), increases with increasing α until the $\alpha-$dependence drops out at very large α and consequently the contours demarcating the detectable regions flatten at high α. On the other hand, the amplitude of the sound wave contribution at fixed α_∞ decays with growing α (cf. eqs. (2.8) and (2.19)). This behaviour is reflected in the shape of the contours in the low-α regions shown in the right panels.

References

[1] *eLISA webpage*, https://www.elisascience.org.

[2] *LISA Pathfinder webpage*, http://sci.esa.int/lisa-pathfinder/.

[3] A. Klein et al., *Science with the space-based interferometer eLISA: supermassive black hole binaries*, *Phys. Rev.* **D 93** (2016) 024003 [arXiv:1511.05581] [INSPIRE].

[4] C. Grojean and G. Servant, *Gravitational waves from phase transitions at the electroweak scale and beyond*, *Phys. Rev.* **D 75** (2007) 043507 [hep-ph/0607107] [INSPIRE].

[5] M.S. Turner, E.J. Weinberg and L.M. Widrow, *Bubble nucleation in first order inflation and other cosmological phase transitions*, *Phys. Rev.* **D 46** (1992) 2384 [INSPIRE].

[6] P. Binetruy, A. Bohe, C. Caprini and J.-F. Dufaux, *Cosmological backgrounds of gravitational waves and eLISA/NGO: phase transitions, cosmic strings and other sources*, *JCAP* **06** (2012) 027 [arXiv:1201.0983] [INSPIRE].

[7] A. Megevand and F.A. Membiela, *Stability of cosmological deflagration fronts*, *Phys. Rev.* **D 89** (2014) 103507 [arXiv:1311.2453] [INSPIRE].

[8] A. Megevand and F.A. Membiela, *Stability of cosmological detonation fronts*, *Phys. Rev.* **D 89** (2014) 103503 [arXiv:1402.5791] [INSPIRE].

[9] J.R. Espinosa, T. Konstandin, J.M. No and G. Servant, *Energy budget of cosmological first-order phase transitions*, *JCAP* **06** (2010) 028 [arXiv:1004.4187] [INSPIRE].

[10] D. Bödeker and G.D. Moore, *Can electroweak bubble walls run away?*, *JCAP* **05** (2009) 009 [arXiv:0903.4099] [INSPIRE].

[11] A. Kosowsky, M.S. Turner and R. Watkins, *Gravitational radiation from colliding vacuum bubbles*, *Phys. Rev.* **D 45** (1992) 4514 [INSPIRE].

[12] A. Kosowsky, M.S. Turner and R. Watkins, *Gravitational waves from first order cosmological phase transitions*, *Phys. Rev. Lett.* **69** (1992) 2026 [INSPIRE].

JCAP04(2016)001

[13] A. Kosowsky and M.S. Turner, *Gravitational radiation from colliding vacuum bubbles: envelope approximation to many bubble collisions*, *Phys. Rev.* **D 47** (1993) 4372 [astro-ph/9211004] [INSPIRE].

[14] M. Kamionkowski, A. Kosowsky and M.S. Turner, *Gravitational radiation from first order phase transitions*, *Phys. Rev.* **D 49** (1994) 2837 [astro-ph/9310044] [INSPIRE].

[15] C. Caprini, R. Durrer and G. Servant, *Gravitational wave generation from bubble collisions in first-order phase transitions: an analytic approach*, *Phys. Rev.* **D 77** (2008) 124015 [arXiv:0711.2593] [INSPIRE].

[16] S.J. Huber and T. Konstandin, *Gravitational wave production by collisions: more bubbles*, *JCAP* **09** (2008) 022 [arXiv:0806.1828] [INSPIRE].

[17] M. Hindmarsh, S.J. Huber, K. Rummukainen and D.J. Weir, *Gravitational waves from the sound of a first order phase transition*, *Phys. Rev. Lett.* **112** (2014) 041301 [arXiv:1304.2433] [INSPIRE].

[18] J.T. Giblin, Jr. and J.B. Mertens, *Vacuum bubbles in the presence of a relativistic fluid*, *JHEP* **12** (2013) 042 [arXiv:1310.2948] [INSPIRE].

[19] J.T. Giblin and J.B. Mertens, *Gravitional radiation from first-order phase transitions in the presence of a fluid*, *Phys. Rev.* **D 90** (2014) 023532 [arXiv:1405.4005] [INSPIRE].

[20] M. Hindmarsh, S.J. Huber, K. Rummukainen and D.J. Weir, *Numerical simulations of acoustically generated gravitational waves at a first order phase transition*, *Phys. Rev.* **D 92** (2015) 123009 [arXiv:1504.03291] [INSPIRE].

[21] C. Caprini and R. Durrer, *Gravitational waves from stochastic relativistic sources: primordial turbulence and magnetic fields*, *Phys. Rev.* **D 74** (2006) 063521 [astro-ph/0603476] [INSPIRE].

[22] T. Kahniashvili, A. Kosowsky, G. Gogoberidze and Y. Maravin, *Detectability of gravitational waves from phase transitions*, *Phys. Rev.* **D 78** (2008) 043003 [arXiv:0806.0293] [INSPIRE].

[23] T. Kahniashvili, L. Campanelli, G. Gogoberidze, Y. Maravin and B. Ratra, *Gravitational radiation from primordial helical inverse cascade MHD turbulence*, *Phys. Rev.* **D 78** (2008) 123006 [*Erratum ibid.* **D 79** (2009) 109901] [arXiv:0809.1899] [INSPIRE].

[24] T. Kahniashvili, L. Kisslinger and T. Stevens, *Gravitational radiation generated by magnetic fields in cosmological phase transitions*, *Phys. Rev.* **D 81** (2010) 023004 [arXiv:0905.0643] [INSPIRE].

[25] C. Caprini, R. Durrer and G. Servant, *The stochastic gravitational wave background from turbulence and magnetic fields generated by a first-order phase transition*, *JCAP* **12** (2009) 024 [arXiv:0909.0622] [INSPIRE].

[26] L. Kisslinger and T. Kahniashvili, *Polarized gravitational waves from cosmological phase transitions*, *Phys. Rev.* **D 92** (2015) 043006 [arXiv:1505.03680] [INSPIRE].

[27] H.L. Child and J.T. Giblin, Jr., *Gravitational radiation from first-order phase transitions*, *JCAP* **10** (2012) 001 [arXiv:1207.6408] [INSPIRE].

[28] C. Caprini, R. Durrer, T. Konstandin and G. Servant, *General properties of the gravitational wave spectrum from phase transitions*, *Phys. Rev.* **D 79** (2009) 083519 [arXiv:0901.1661] [INSPIRE].

[29] U.-L. Pen and N. Turok, *Shocks in the early universe*, arXiv:1510.02985 [INSPIRE].

[30] A. Kosowsky, A. Mack and T. Kahniashvili, *Gravitational radiation from cosmological turbulence*, *Phys. Rev.* **D 66** (2002) 024030 [astro-ph/0111483] [INSPIRE].

[31] T. Konstandin and J.M. No, *Hydrodynamic obstruction to bubble expansion*, *JCAP* **02** (2011) 008 [arXiv:1011.3735] [INSPIRE].

JCAP04(2016)001

[32] J. Kozaczuk, *Bubble expansion and the viability of singlet-driven electroweak baryogenesis*, *JHEP* **10** (2015) 135 [arXiv:1506.04741] [INSPIRE].

[33] A. Petiteau, *eLISA sensitivity curves for stochastic backgrounds*, in preparation.

[34] E. Thrane and J.D. Romano, *Sensitivity curves for searches for gravitational-wave backgrounds*, *Phys. Rev.* **D 88** (2013) 124032 [arXiv:1310.5300] [INSPIRE].

[35] M.R. Adams and N.J. Cornish, *Discriminating between a stochastic gravitational wave background and instrument noise*, *Phys. Rev.* **D 82** (2010) 022002 [arXiv:1002.1291] [INSPIRE].

[36] M.R. Adams and N.J. Cornish, *Detecting a stochastic gravitational wave background in the presence of a galactic foreground and instrument noise*, *Phys. Rev.* **D 89** (2014) 022001 [arXiv:1307.4116] [INSPIRE].

[37] C. Delaunay, C. Grojean and J.D. Wells, *Dynamics of non-renormalizable electroweak symmetry breaking*, *JHEP* **04** (2008) 029 [arXiv:0711.2511] [INSPIRE].

[38] S.J. Huber and T. Konstandin, *Production of gravitational waves in the NMSSM*, *JCAP* **05** (2008) 017 [arXiv:0709.2091] [INSPIRE].

[39] K. Kajantie, M. Laine, K. Rummukainen and M.E. Shaposhnikov, *The electroweak phase transition: a nonperturbative analysis*, *Nucl. Phys.* **B 466** (1996) 189 [hep-lat/9510020] [INSPIRE].

[40] K. Kajantie, M. Laine, K. Rummukainen and M.E. Shaposhnikov, *Is there a hot electroweak phase transition at $m_H \gtrsim m_W$?*, *Phys. Rev. Lett.* **77** (1996) 2887 [hep-ph/9605288] [INSPIRE].

[41] J. Ghiglieri and M. Laine, *Gravitational wave background from standard model physics: qualitative features*, *JCAP* **07** (2015) 022 [arXiv:1504.02569] [INSPIRE].

[42] D.E. Morrissey and M.J. Ramsey-Musolf, *Electroweak baryogenesis*, *New J. Phys.* **14** (2012) 125003 [arXiv:1206.2942] [INSPIRE].

[43] C. Caprini and J.M. No, *Supersonic electroweak baryogenesis: achieving baryogenesis for fast bubble walls*, *JCAP* **01** (2012) 031 [arXiv:1111.1726] [INSPIRE].

[44] J.M. No, *Large gravitational wave background signals in electroweak baryogenesis scenarios*, *Phys. Rev.* **D 84** (2011) 124025 [arXiv:1103.2159] [INSPIRE].

[45] M. Carena, M. Quirós and C.E.M. Wagner, *Opening the window for electroweak baryogenesis*, *Phys. Lett.* **B 380** (1996) 81 [hep-ph/9603420] [INSPIRE].

[46] D. Delepine, J.M. Gerard, R. Gonzalez Felipe and J. Weyers, *A light stop and electroweak baryogenesis*, *Phys. Lett.* **B 386** (1996) 183 [hep-ph/9604440] [INSPIRE].

[47] M. Carena, G. Nardini, M. Quirós and C.E.M. Wagner, *The baryogenesis window in the MSSM*, *Nucl. Phys.* **B 812** (2009) 243 [arXiv:0809.3760] [INSPIRE].

[48] M. Laine, G. Nardini and K. Rummukainen, *Lattice study of an electroweak phase transition at $m_h \sim 126$ GeV*, *JCAP* **01** (2013) 011 [arXiv:1211.7344] [INSPIRE].

[49] A. Menon and D.E. Morrissey, *Higgs boson signatures of MSSM electroweak baryogenesis*, *Phys. Rev.* **D 79** (2009) 115020 [arXiv:0903.3038] [INSPIRE].

[50] T. Cohen, D.E. Morrissey and A. Pierce, *Electroweak baryogenesis and Higgs signatures*, *Phys. Rev.* **D 86** (2012) 013009 [arXiv:1203.2924] [INSPIRE].

[51] D. Curtin, P. Jaiswal and P. Meade, *Excluding electroweak baryogenesis in the MSSM*, *JHEP* **08** (2012) 005 [arXiv:1203.2932] [INSPIRE].

[52] M. Carena, G. Nardini, M. Quirós and C.E.M. Wagner, *MSSM electroweak baryogenesis and LHC data*, *JHEP* **02** (2013) 001 [arXiv:1207.6330] [INSPIRE].

JCAP04(2016)001

[53] M. Pietroni, *The electroweak phase transition in a nonminimal supersymmetric model*, *Nucl. Phys.* **B 402** (1993) 27 [hep-ph/9207227] [INSPIRE].

[54] A.T. Davies, C.D. Froggatt and R.G. Moorhouse, *Electroweak baryogenesis in the next-to-minimal supersymmetric model*, *Phys. Lett.* **B 372** (1996) 88 [hep-ph/9603388] [INSPIRE].

[55] R. Apreda, M. Maggiore, A. Nicolis and A. Riotto, *Gravitational waves from electroweak phase transitions*, *Nucl. Phys.* **B 631** (2002) 342 [gr-qc/0107033] [INSPIRE].

[56] J. Kozaczuk, S. Profumo and C.L. Wainwright, *Electroweak baryogenesis and the Fermi gamma-ray line*, *Phys. Rev.* **D 87** (2013) 075011 [arXiv:1302.4781] [INSPIRE].

[57] W. Huang, Z. Kang, J. Shu, P. Wu and J.M. Yang, *New insights in the electroweak phase transition in the NMSSM*, *Phys. Rev.* **D 91** (2015) 025006 [arXiv:1405.1152] [INSPIRE].

[58] J. Kozaczuk, S. Profumo, L.S. Haskins and C.L. Wainwright, *Cosmological phase transitions and their properties in the NMSSM*, *JHEP* **01** (2015) 144 [arXiv:1407.4134] [INSPIRE].

[59] S.J. Huber, T. Konstandin, G. Nardini and I. Rues, *Detectable gravitational waves from very strong phase transitions in the general NMSSM*, *JCAP* **03** (2016) 036 [arXiv:1512.06357] [INSPIRE].

[60] N. Craig, H.K. Lou, M. McCullough and A. Thalapillil, *The Higgs portal above threshold*, *JHEP* **02** (2016) 127 [arXiv:1412.0258] [INSPIRE].

[61] S. Profumo, M.J. Ramsey-Musolf, C.L. Wainwright and P. Winslow, *Singlet-catalyzed electroweak phase transitions and precision Higgs boson studies*, *Phys. Rev.* **D 91** (2015) 035018 [arXiv:1407.5342] [INSPIRE].

[62] N. Craig, C. Englert and M. McCullough, *New probe of naturalness*, *Phys. Rev. Lett.* **111** (2013) 121803 [arXiv:1305.5251] [INSPIRE].

[63] J.R. Espinosa, T. Konstandin and F. Riva, *Strong electroweak phase transitions in the standard model with a singlet*, *Nucl. Phys.* **B 854** (2012) 592 [arXiv:1107.5441] [INSPIRE].

[64] C.-Y. Chen, S. Dawson and I.M. Lewis, *Exploring resonant di-Higgs boson production in the Higgs singlet model*, *Phys. Rev.* **D 91** (2015) 035015 [arXiv:1410.5488] [INSPIRE].

[65] D. Curtin, P. Meade and C.-T. Yu, *Testing electroweak baryogenesis with future colliders*, *JHEP* **11** (2014) 127 [arXiv:1409.0005] [INSPIRE].

[66] L. Fromme, S.J. Huber and M. Seniuch, *Baryogenesis in the two-Higgs doublet model*, *JHEP* **11** (2006) 038 [hep-ph/0605242] [INSPIRE].

[67] M. Kakizaki, S. Kanemura and T. Matsui, *Gravitational waves as a probe of extended scalar sectors with the first order electroweak phase transition*, *Phys. Rev.* **D 92** (2015) 115007 [arXiv:1509.08394] [INSPIRE].

[68] G.C. Dorsch, S.J. Huber and J.M. No, *A strong electroweak phase transition in the 2HDM after LHC8*, *JHEP* **10** (2013) 029 [arXiv:1305.6610] [INSPIRE].

[69] G.C. Dorsch, S.J. Huber, K. Mimasu and J.M. No, *Echoes of the electroweak phase transition: discovering a second higgs doublet through $A_0 \to ZH_0$*, *Phys. Rev. Lett.* **113** (2014) 211802 [arXiv:1405.5537] [INSPIRE].

[70] G.C. Dorsch, S.J. Huber, K. Mimasu and J.M. No, *Hierarchical vs degenerate 2HDM: the LHC Run 1 legacy at the onset of Run 2*, arXiv:1601.04545 [INSPIRE].

[71] H.H. Patel, M.J. Ramsey-Musolf and M.B. Wise, *Color breaking in the early universe*, *Phys. Rev.* **D 88** (2013) 015003 [arXiv:1303.1140] [INSPIRE].

[72] C. Grojean, G. Servant and J.D. Wells, *First-order electroweak phase transition in the standard model with a low cutoff*, *Phys. Rev.* **D 71** (2005) 036001 [hep-ph/0407019] [INSPIRE].

JCAP04(2016)001

[73] G. Nardini, M. Quirós and A. Wulzer, *A confining strong first-order electroweak phase transition*, *JHEP* **09** (2007) 077 [arXiv:0706.3388] [INSPIRE].

[74] T. Konstandin and G. Servant, *Cosmological consequences of nearly conformal dynamics at the TeV scale*, *JCAP* **12** (2011) 009 [arXiv:1104.4791] [INSPIRE].

[75] L. Randall and R. Sundrum, *A large mass hierarchy from a small extra dimension*, *Phys. Rev. Lett.* **83** (1999) 3370 [hep-ph/9905221] [INSPIRE].

[76] W.D. Goldberger and M.B. Wise, *Modulus stabilization with bulk fields*, *Phys. Rev. Lett.* **83** (1999) 4922 [hep-ph/9907447] [INSPIRE].

[77] R. Rattazzi and A. Zaffaroni, *Comments on the holographic picture of the Randall-Sundrum model*, *JHEP* **04** (2001) 021 [hep-th/0012248] [INSPIRE].

[78] J. Garriga and A. Pomarol, *A stable hierarchy from Casimir forces and the holographic interpretation*, *Phys. Lett.* **B 560** (2003) 91 [hep-th/0212227] [INSPIRE].

[79] P. Creminelli, A. Nicolis and R. Rattazzi, *Holography and the electroweak phase transition*, *JHEP* **03** (2002) 051 [hep-th/0107141] [INSPIRE].

[80] L. Randall and G. Servant, *Gravitational waves from warped spacetime*, *JHEP* **05** (2007) 054 [hep-ph/0607158] [INSPIRE].

[81] T. Konstandin, G. Nardini and M. Quirós, *Gravitational backreaction effects on the holographic phase transition*, *Phys. Rev.* **D 82** (2010) 083513 [arXiv:1007.1468] [INSPIRE].

[82] G. Servant, *Baryogenesis from strong CP violation and the QCD axion*, *Phys. Rev. Lett.* **113** (2014) 171803 [arXiv:1407.0030] [INSPIRE].

[83] Y. Bai and P. Schwaller, *Scale of dark QCD*, *Phys. Rev.* **D 89** (2014) 063522 [arXiv:1306.4676] [INSPIRE].

[84] K.K. Boddy, J.L. Feng, M. Kaplinghat and T.M.P. Tait, *Self-interacting dark matter from a non-Abelian hidden sector*, *Phys. Rev.* **D 89** (2014) 115017 [arXiv:1402.3629] [INSPIRE].

[85] P. Schwaller, *Gravitational waves from a dark phase transition*, *Phys. Rev. Lett.* **115** (2015) 181101 [arXiv:1504.07263] [INSPIRE].

JCAP04(2016)001

6.4 Article: Gravitational wave signal from first order phase transitions at PTA

In the article constituting the following section we analyse the SGWB that would be generated under the hypothesis of a first order primordial QCDPT. Though quite old, we include it here as it represents yet another example of the ability of GW detectors to probe different phases in the evolution of the primordial universe: a GW signal produced at the energy scale of the QCDPT falls in the frequency range of PTA observatories (c.f. section 3.3)

The main result of this analysis is that the PT must occur (unnaturally?) slowly, in order for the SGWB peak to fall in the range of frequencies probed by PTA. Furthermore, present constraints on the SGWB from PTA are at best of the order of $h^2\Omega_{gw} \sim 10^{-9}$ (c.f. section 4.3), meaning that the SGWB predicted here would only be marginally detectable today, for choices of the parameters governing the signal that are not too extreme. Note that the most probable SGWB source in the nanoHertz band are super-massive black hole binaries, but a future detection of the SGWB by PTA could also be used to constrain the parameter space of an hypothetical first order QCDPT, if the SGWB frequency shape remains undetermined, not allowing to ascertain the SGWB origin.

At the time of the analysis presented below, it was not known that sound waves were an important source of GWs in the aftermath of a first order PT; consequently, only bubble collision and MHD turbulence have been accounted for. Moreover, in the absence of theoretical guidance, we assumed equipartition between the gradient energy in the bubble walls, and the kinetic turbulent energy. Hopefully, progress will be made in the near future on this particular point, thanks to the new numerical simulations discussed in the preamble of section 6.2.

Here we apply to the QCDPT the GW production framework developed for perturbative, scalar-field driven PTs, as the results for the SGWB spectra are virtually independent on the PT nature and only rely on the formation and evolution of broken phase bubbles coupled to the surrounding plasma. An important feature of this work, is that it provides for the first time the interpolation formula for the GW spectrum from MDH turbulence derived in the paper of section 6.2. This formula has been re-used in the paper of section 6.3 and consequently in many works analysing the SGWB from primordial PTs.

PHYSICAL REVIEW D **82,** 063511 (2010)

Detection of gravitational waves from the QCD phase transition with pulsar timing arrays

Chiara Caprini,[1] Ruth Durrer,[2] and Xavier Siemens[3]

[1]*CEA, IPhT and CNRS, URA 2306, F-91191 Gif-sur-Yvette, France*
[2]*Département de Physique Théorique, Université de Genève, 24 quai Ernest Ansermet, CH-1211 Genève 4, Switzerland*
[3]*Center for Gravitation and Cosmology, Department of Physics, University of Wisconsin–Milwaukee, P.O. Box 413, Milwaukee, Wisconsin 53201, USA*

(Received 7 July 2010; published 8 September 2010)

If the cosmological QCD phase transition is strongly first order and lasts sufficiently long, it generates a background of gravitational waves which may be detected via pulsar timing experiments. We estimate the amplitude and the spectral shape of such a background and we discuss its detectability prospects.

DOI: 10.1103/PhysRevD.82.063511 PACS numbers: 98.80.−k, 25.75.Nq, 04.30.Db, 04.80.Nn

I. INTRODUCTION

Gravitational waves (GWs) are space-time fluctuations that propagate at the speed of light through empty space; they were predicted by Einstein in 1916 [1]. Because of the weakness of the gravitational interaction, GWs could provide information about astrophysics and cosmology from regions and epochs of the Universe from which electromagnetic radiation cannot propagate freely. For the same reason, however, GWs have thus far eluded direct detection, despite considerable efforts.

Advanced configurations of existing ground-based interferometers such as LIGO [2] and VIRGO [3] are expected to detect GWs in the next years. Terrestrial interferometers have the best sensitivity at a frequency $f \sim 100$ Hz, and are severely limited by seismic noise below a few Hertz. GWs with significantly lower frequency, $f \sim 10^{-9}$ Hz, are also expected to be detected by pulsar timing experiments in the next decade [4,5]. A worldwide collaboration of astronomers, the International Pulsar Timing Array (IPTA) project [4], has been formed with the goal of detecting nano-Hz GWs using millisecond pulsars. Millisecond pulsars are rapidly rotating, highly magnetized neutron stars which emit a beam of electromagnetic radiation that sweeps over the Earth once per rotation. They constitute extremely accurate clocks that could be used to detect GWs. Candidates for the generation of a GW background in the nano-Hz band are supermassive black hole binary mergers [6–11] and cosmic strings [12–16].

In this paper we study another potential candidate: the cosmological QCD phase transition, which is believed to have taken place when the Universe had a temperature of $T_* \simeq 100$ MeV. A GW background can be generated by the QCD phase transition if it is first order, and the characteristic frequency of this background falls in the frequency band of pulsar timing experiments. We show here that, if the phase transition is sufficiently strong and lasts for a sufficiently long time, the GWs produced can be observed in future pulsar timing experiments. This possibility has been discussed for the first time by Witten in Ref. [17]. Here we present accurate predictions for the spectrum of the emitted gravitational radiation as a function of the phase transition parameters like its temperature, strength, and duration.

In the context of standard cosmology and QCD, the cosmological QCD phase transition is not even second order but a crossover, and we do not expect it to generate GWs. However, if the neutrino chemical potential is sufficiently large (still well within the bounds allowed by big bang nucleosynthesis), it can become first order [18]. Furthermore, if a sterile neutrino is the dark matter, we do expect a large neutrino chemical potential [19].

Thus, pulsar timing experiments could open a new cosmological window: the detection of a stochastic background of GWs could help to determine whether the QCD phase transition is first order. The amplitude and peak frequency of the spectrum are also sensitive to the expansion rate of the Universe during this phase transition [20], which is currently unconstrained.

In the next section we provide estimates for the GW spectrum by a first order QCD phase transition. In Sec. III we compare our results with current and expected sensitivities of pulsar timing arrays. We conclude in Sec. IV. Throughout we use the metric signature $(-, +, +, +)$ and conformal time so that the Friedmann metric is given by $ds^2 = a^2(t)(-dt^2 + d\mathbf{x}^2)$. The conformal Hubble parameter is denoted by $\mathcal{H} = \dot{a}/a = Ha$. An overdot denotes the derivative with respect to conformal time t.

II. GRAVITATIONAL WAVES FROM A FIRST ORDER QCD PHASE TRANSITION

Very violent processes in the early universe can lead to the generation of GWs. One example of such violent processes are first order phase transitions [17,21–24], which can lead to GW production via the collision of bubbles of the true vacuum [25–33] and via the turbulence and magnetic fields they can induce in the cosmic plasma [34–41].

The GWs generated by a source are determined by the linearized Einstein equation for tensor perturbations in a Friedmann background [42],

$$\ddot{h}_{\pm} + 2\frac{\dot{a}}{a}\dot{h}_{\pm} + k^2 h_{\pm} = 8\pi G a^2 \rho \Pi_{\pm}. \quad (1)$$

Here ρ is the background cosmological energy density, a is the scale factor, $\Pi_{\pm}$ are the two tensor helicity modes of the (dimensionless) anisotropic stress which is the source of GWs, and $h_{\pm}$ are the helicity modes of the GW. If an anisotropic stress is generated at some time t_* in the radiation dominated era, from a source with relative energy density $\Omega_{S*} = \rho_{S*}/\rho_*$, we expect Π to be at best of the order of Ω_{S*}. The GW energy density (from two polarizations $\pm$ which contribute equally) is given by

$$\rho_{\rm GW}(t) = \frac{\langle \dot{h}_+(\mathbf{x}, t)\dot{h}_+(\mathbf{x}, t)\rangle}{8\pi G a^2(t)}. \quad (2)$$

Because of statistical homogeneity, $\rho_{\rm GW}$ is independent of the position. The GW energy spectrum per logarithmic unit of frequency $\frac{d\rho_{\rm GW}(k,t)}{d\log(k)}$ is defined by

$$\rho_{\rm GW} = \int \frac{dk}{k}\frac{d\rho_{\rm GW}(k, t)}{d\log(k)}.$$

Detailed semianalytical and numerical calculations have been performed in the past in order to calculate the GW energy spectrum from first order phase transitions [25–41]. In this paper we simply use analytic fits to the most recent results, as presented in the following.

Concerning the GW signal from bubble collisions, we use the shape of the spectrum proposed in Ref. [33], but rescale the amplitude to agree with the numerical result of Ref. [31]. As a result, the GW energy density emitted by this source is well approximated by

bubble collisions:

$$\frac{d\Omega_{\rm GW}^{(\rm B)}h^2}{d\log k} \simeq \frac{2}{3\pi^2}h^2\Omega_{r0}\left(\frac{\mathcal{H}_*}{\beta}\right)^2\Omega_{S*}^2 v^3\frac{(k/\beta)^3}{1+(k/\beta)^4}. \quad (3)$$

Here Ω_{r0} denotes the radiation energy density today, $h = H_0/(100\ \text{km/s/Mpc})$ is the present Hubble parameter in units of 100 km/s/Mpc, β^{-1} is the duration of the phase transition, v is the expansion velocity of the bubbles, and k is the comoving wave number or frequency of the GW. The GW spectrum is proportional to the relative energy density in the source Ω_{S*}^2, to the ratio between the duration of the phase transition and the Hubble time $(\mathcal{H}_*/\beta)^2$, and to the bubble velocity v^3 [31].

The QCD phase transition is expected to happen at the temperature $T_* \simeq 100$ MeV, when the kinetic and magnetic Reynolds numbers of the cosmic fluid are very large [41]. The bubbles which rapidly expand and collide are therefore expected to generate magnetohydrodynamical (MHD) turbulence in the cosmic fluid. The kinetic energy of the turbulent motions and the magnetic fields sustained by the MHD turbulence also induce GWs: Ref. [41] presents the latest semianalytical calculation of the GW spectrum from MHD turbulence. There are two important differences with respect to the GW signal from bubbles. First, turbulence lasts beyond the duration of the phase transition: this leads to an enhancement of the signal on large (superhorizon) scales [41]. Second, the time correlation properties of the anisotropic stress source are different. For bubble collisions, the source is totally coherent (see [33,41]), while for MHD turbulence the source is coherent only over about one characteristic wavelength [41]. This leads to a difference in the peak position of the GWs from the two sources: while the signal from bubble collisions peaks at $k_p \sim \beta$, the inverse duration of the phase transition, the peak of the MHD signal is related to the bubble size: the peak wavelength becomes therefore $\lambda_p \sim R_* \simeq v/\beta$. The analysis of Ref. [41] finds a peak at about $k_p \sim \pi^2\beta/v$. We can fit the GW spectrum obtained in [41] by the following formula:

MHD turbulence:

$$\frac{d\Omega_{\rm GW}^{(\rm MHD)}h^2}{d\log k} \simeq \frac{8}{\pi^6}h^2\Omega_{r0}\frac{\mathcal{H}_*}{\beta}\Omega_{S*}^{3/2}v^4 \times \frac{(k/\beta)^3}{(1+4k/\mathcal{H}_*)[1+(v/\pi^2)(k/\beta)]^{11/3}}. \quad (4)$$

For large scales, $k \ll k_p$, both spectra in Eqs. (3) and (4) increase as k^3: this behavior is simply due to causality [37,43]. Since the anisotropic stresses are generated by a causal process, their spectrum is white noise at scales larger than the typical correlation scale of the source, which corresponds to the bubble size. The white noise spectrum is inherited by the GWs: $\langle|\dot{h}|^2\rangle \propto$ const, so that the GW energy density scales simply with the phase space volume k^3. The behavior on small scales, $k \gg k_p$, depends on the source power spectrum and on the unequal time correlation properties of the source; see Ref. [44]. In particular, the result of Eq. (3) resides on the assumption that the bubbles are infinitely thin: this assumption holds if the bubbles propagate as detonations and causes the k^{-1} slope at high wave numbers [31,33]. On the other hand, the $k^{-5/3}$ decay of Eq. (4) is a consequence of the Kolmogorov-type spectrum assumed for the MHD turbulent motions at high wave numbers. In addition, the slope of the MHD signal changes at subhorizon scales, $\mathcal{H}_* < k < k_p$, from k^3 to k^2 due to the long duration of the source (cf. [41]).

From the above formulas for the GW spectra we see that the basic ingredients which determine the peak position and amplitude are simply the fractional energy density of the source Ω_{S*}, the duration of the phase transition β^{-1}, and the bubble velocity v (besides obviously the temperature at which the phase transition occurs T_*, which is parametrized by the Hubble scale $\mathcal{H}_*$). Ω_{S*} and v are related, in a way which depends on the characteristics of the phase transition: for example, its strength, the properties of the bubble expansion, the interactions of the fluid particles with the field which is undergoing the transition, and so on. In early works on GWs from bubble collisions, it

has been assumed that the bubbles expand as a Jouguet detonation, because in this case the above parameters can be calculated quite straightforwardly [27]. However, the recent analysis of [45] demonstrates that there is no particularly justified reason for this assumption, and other kinds of solutions for the bubble expansion are possible, such as deflagrations, runway solutions, and hybrids. Reference [45] presents a model-independent description of the different regimes characterizing the bubble expansion, including the effect of friction due to the interaction of the bubble wall with the fluid particles. From a given particle physics model, one can in principle evaluate the friction parameter η and the strength of the phase transition $\alpha = \rho_{\rm vac}/\rho_{\rm rad}$. Once these two quantities are known, Ref. [45] provides a way to determine the bubble wall velocity v and the fraction of vacuum energy density which goes into kinetic energy of the bubble walls, $\kappa = \rho_{\rm kin}/\rho_{\rm vac}$. In terms of the parameter κ, the fractional source energy density for bubbles becomes

$$\Omega_{S*}^{(\rm B)} = \kappa \frac{\alpha}{\alpha + 1}.$$

In the case of MHD turbulence, one further has to convert a part of the bubble wall kinetic energy to turbulence and magnetic fields. The efficiency of this conversion is not straightforward to estimate. Reference [45] provides a relation between the bubble wall velocity and the fluid velocity at the bubble wall position v_f: in the most optimistic case, one can argue that the overall kinetic energy in turbulence is simply determined by this fluid velocity. In this case one would have $\Omega_{S*}^{(\rm MHD)} \sim v_f^2/2$.

In the absence of a way to determine α and η from a given particle physics model, in the present analysis we have decided to keep the parameters completely model independent. We make the simple assumption of equipartition, namely, we assume the same energy density in colliding bubble walls and in MHD turbulence, $\Omega_{S*}^{(\rm B)} = \Omega_{S*}^{(\rm MHD)}$. This is more a reflection of our ignorance of how this energy density will be distributed than a well-justified assumption; nevertheless, it seems to be a reasonable expectation and in the absence of a model for the phase transition it is the most straightforward assumption. We also assume a strongly first order phase transition, which induces supersonic bubble velocities, $v > c_s$. We set the temperature of the QCD phase transition at $T_* = 100$ MeV. The other parameter relevant for the GW spectra is the duration of the phase transition, parametrized by β. In the electroweak case, this is usually taken to be 1%–10% of a Hubble time: $\beta = (10\text{–}100)\mathcal{H}_*$. This value is based on the estimate given in Ref. [21], which shows that β is related to the temperature of the phase transition through $\beta/\mathcal{H}_* \sim 4\ln(m_{\rm Pl}/T_*)$, for a phase transition nucleated via thermal fluctuations. In the absence of a precise model for the QCD phase transition, in this section we have decided to take $\beta = 10\mathcal{H}_*$, which is more favorable for observations with pulsar timing experiments. The analysis of [21] demonstrates that models of phase transitions with small values of $\beta/\mathcal{H}_*$ may be rather exceptional, but cannot be ruled out by general arguments. The important point is that $\beta/\mathcal{H}_*$ must be larger than unity, otherwise the phase transition is not fast with respect to the Universe expansion and our assumptions no longer hold.

In Fig. 1 we show the GW spectrum for both, bubbles and MHD turbulence for two different choices of the parameters Ω_{S*} and v. The MHD turbulence signal dominates almost in the entire frequency range. At large scales, it is slightly higher due to the long duration of the turbulent source with respect to bubble collisions [41]. As already mentioned, the long duration of the source also causes the slope of the MHD signal to change at subhorizon scales from k^3 to k^2: consequently, for $\beta > k > \mathcal{H}_*$, i.e. $0.1 < k/\beta < 1$, the bubble collision signal prevails. This is valid up to the peak of the bubble collision signal, which arises before the turbulent one: at $k/\beta \simeq 1$, corresponding to the inverse characteristic time of the source, while the turbulent spectrum peaks at $k/\beta \simeq \pi^2/v$, corresponding to the inverse characteristic scale of the source. This causes the turbulent signal to dominate at interesting frequencies, since the total spectrum continues to rise after $k/\beta \simeq 1$ (only if the energy in turbulence is about 1 order of magnitude smaller than the one in bubble collisions, the collision signal will dominate: however, this seems somewhat unnatural given the extremely high Reynolds number

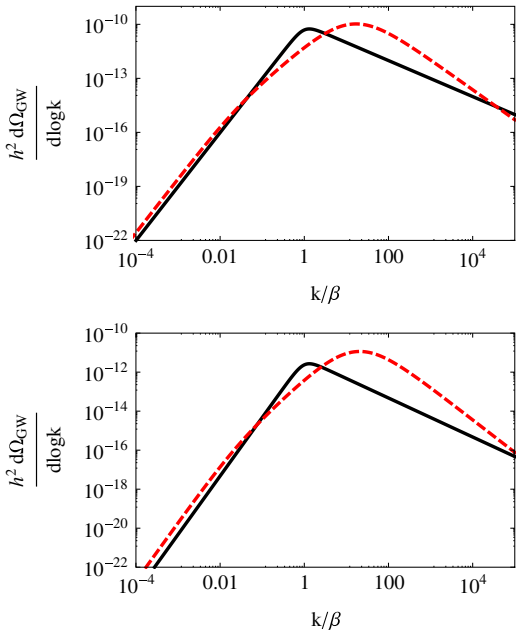

FIG. 1 (color online). The GW spectra from bubble collisions (black, solid lines) and from MHD turbulence (red, dashed lines) are shown for different values of $\Omega_{S*} = 0.1$ and $v = 0.7$ (top panel) and $\Omega_{S*} = 0.03$ and $v = 0.57 \simeq c_s$ (bottom panel). We set $\beta = 10\mathcal{H}_*$ and $T_* = 100$ MeV throughout.

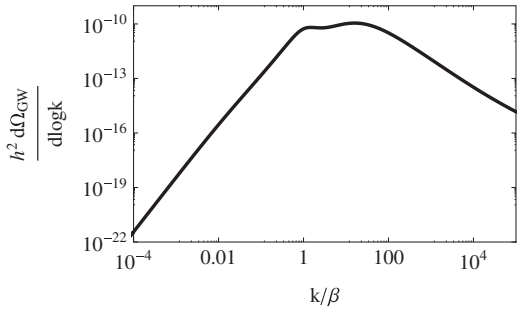

FIG. 2. The GW signal from bubble collisions and MHD turbulence for $\Omega_{S*} = 0.1$ and $\upsilon = 0.7$. We choose $\beta = 10\mathcal{H}_*$. The signal is dominated by the contribution from MHD turbulence. The bubble collision peak causes the hump on the left of the true peak of the spectrum.

of the primordial fluid, and we discard this possibility in this work).[1]

In Fig. 2 we show the total signal for the more optimistic case, $\Omega_{S*} = 0.1$ and $\upsilon = 0.7$. The peak frequency of the total GW spectrum corresponds to the MHD turbulence peak: $k/\beta \simeq \pi^2/\upsilon$, and depends on the choice $\beta = 10\mathcal{H}_*$. From $f = k/(2\pi)$ one obtains [42,44]

$$f_p \simeq 1.7 \times 10^{-9} \frac{\pi^2}{\upsilon} \frac{\beta}{\mathcal{H}_*} \left(\frac{g_*}{10}\right)^{1/6} \frac{T_*}{100\ \text{MeV}}\ \text{Hz}, \qquad (5)$$

where g_* is the number of effective relativistic degrees of freedom at the temperature T_*. With $\upsilon = 0.7$, $\beta = 10\mathcal{H}_*$, $g_* = 10$, and $T_* = 100$ MeV the peak frequency becomes $f_p \simeq 2.5 \times 10^{-7}$ Hz.

III. THE PULSAR TIMING ARRAY

Neutron stars can emit powerful beams of electromagnetic waves from their magnetic poles. As the stars rotate the beams sweep through space like the beacon of a lighthouse. If the Earth lies within the sweep of a neutron star's beams, the star is observed as a point source in space emitting short, rapid pulses of electromagnetic waves, and is referred to as a pulsar.

The electromagnetic pulses we observe arrive at a very steady rate due to the enormous moment of inertia of neutron stars. The idea to use these stable clocks to detect GWs was first put forward in the late 1970s [47–49]. Fluctuations in the time of arrival of pulses, after all known effects are subtracted, could be due to the presence of GWs. Recently pulsar timing precision has improved dramatically. Jenet and collaborators [50] have shown that the presence of nano-Hertz GWs could be detected using a pulsar timing array (PTA) consisting of 20 pulsars with timing precisions of 100 ns over a period of 5 to 10 yr (see also [4,5] for more recent PTA sensitivity estimates). Pulsar timing arrays are most sensitive in the band 10^{-9} Hz $< f < 10^{-7}$ Hz. The lower limit in frequency is given by the duration of the experiment (~ 10 yr) and the upper limit by the sampling theorem, i.e. the time between observations (~ 1 month). The spike in the sensitivity at $f = 0.3 \times 10^{-7}$ Hz seen in Fig. 3 is the frequency of the Earth's rotation around the Sun which cannot be disentangled from a GW with the same frequency.

The North American Nanohertz Observatory for Gravitational Waves (NANOGrav) [51], a collaboration of astronomers, has created a pulsar timing array—a galactic scale GW observatory using about 20 pulsars. It is a section of the IPTA, an international collaboration involving similar organizations of European and Australian astronomers. The current NANOGrav pulsar timing array sensitivity is shown in Fig. 3, together with the GW spectra we expect from the QCD phase transition as a function of frequency

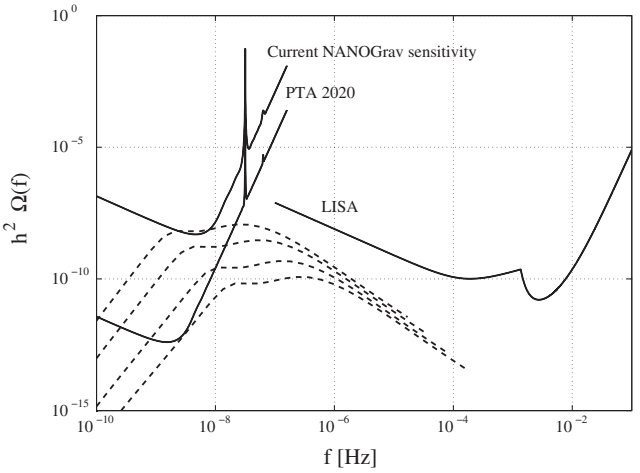

FIG. 3. Comparison of the GW spectrum $h^2\Omega(f)$ with current NANOGrav pulsar timing array sensitivity and expected sensitivity of pulsar timing experiments in 2020 [5]. We have used $h = 0.73$, $\Omega_{r0} = 8.5 \times 10^{-5}$, $\Omega_{S*} = 0.1$, and $\upsilon = 0.7$. We plot the GW spectra for the values $\mathcal{H}_*/\beta = 1$, 0.5, 0.2, and 0.1 (dashed lines from top to bottom). For $\mathcal{H}_*/\beta \sim 1$, the background of GWs can just be detected in present pulsar timing experiments, while for $0.1 \lesssim \mathcal{H}_*/\beta$ it can be detected by the planned array IPTA2020 (very high values of $\mathcal{H}_*/\beta \sim 1$ are difficult to accommodate in the case of a thermally nucleated phase transition, cf. discussion in the text). We also show the LISA sensitivity [52,53]. Unfortunately, LISA will not be able to detect a signal from a first order QCD phase transition (the electroweak phase transition is more promising in this respect [25–41,44,46]).

[1]Contrary to Ref. [46], we find that the expected peak frequency of the GW spectrum from bubble collisions is always smaller than the one from MHD turbulence, the former being related to the duration of the phase transition while the latter to the size of the bubbles. This discrepancy arises because Ref. [46] assumed that the peak frequency for the GW spectrum from MHD turbulence is related to the turbulent eddy turnover time, while in our case it is determined by the time correlation properties of the GW source, as explained in detail in Ref. [41].

$$h^2\Omega_{\rm GW}(f) = h^2\frac{d\Omega_{\rm GW}}{d\log k}, \tag{6}$$

for $\mathcal{H}_*/\beta = 1$ (top dashed line), $\mathcal{H}_*/\beta = 0.5$ (upper-middle dashed line), $\mathcal{H}_*/\beta = 0.2$ (lower-middle dashed line), and $\mathcal{H}_*/\beta = 0.1$ (bottom dashed line). We have used $h = 0.73$, $\Omega_{r0} = 8.5 \times 10^{-5}$ (which includes photons and neutrinos), $\Omega_{S*} = 0.1$ and $v = 0.7$. We have taken the frequency to be [cf. Eq. (5)]

$$f = 1.7 \times 10^{-9}\left(\frac{\beta}{\mathcal{H}_*}\right)\left(\frac{k}{\beta}\right)\ {\rm Hz}$$

i.e. chosen $T_* = 100$ MeV, $g_* = 10$, and k/β varying between 10^{-4} and 10^4 (as in Figs. 1 and 2). The signal is compared with the current sensitivity of the NANOGrav pulsar timing array, and the expected sensitivity of the IPTA pulsar timing array in 2020 [5]. For values of $0.1 \lesssim \mathcal{H}_*/\beta \lesssim 1$, the background of GWs would be detected with future pulsar timing array sensitivities. The value of $\mathcal{H}_*/\beta$ must certainly be smaller than unity for the phase transition to be fast with respect to the Hubble time and for our approximations to apply. In most cases, if the phase transition happens at a temperature much smaller than the Planck temperature, $\mathcal{H}_*/\beta$ is of the order of 0.01; however, higher values of this parameter cannot be excluded, and we adopt them here since they are more promising for detection [21].

Figure 3 also shows the sensitivity of the planned Laser Interferometer Space Antenna (LISA) [52] assuming that some of the confusion noise from white dwarf binaries can be subtracted out [53]. LISA will not be able to detect the GW signature of a first order QCD phase transition: in order to be detectable by LISA, the GW spectrum must peak at higher frequency and consequently the phase transition must occur at higher temperature. LISA can in principle detect GWs from a strongly first order EW phase transition at $T_* \simeq 100$ GeV [25–41,44,46,54].

A related quantity often used in the pulsar timing community is the (dimensionless) characteristic strain, defined by [55]

$$h_c^2(f) = \frac{3H_0^2}{2\pi^2}f^{-2}\Omega_{\rm GW}(f). \tag{7}$$

In Fig. 4 we show the same data as in Fig. 3 but in terms of the characteristic strain h_c.

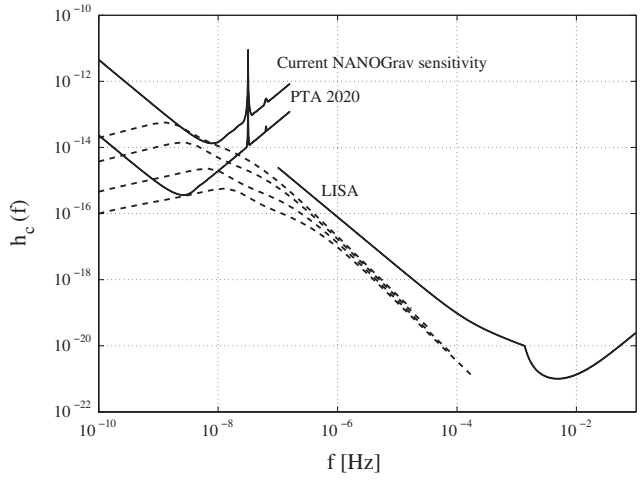

FIG. 4. Same as Fig. 3 but comparing the characteristic strain h_c as given by Eq. (7).

IV. CONCLUSION AND OUTLOOK

A stochastic background of GWs from the QCD phase transition could be detected by pulsar timing experiments if the transition is strongly first order and lasts sufficiently long with respect to the Hubble time. In standard cosmology the QCD phase transition is not even second order, but simply a crossover and in this case we do not expect it to generate GWs. However, if the neutrino chemical potential is sufficiently large [18], the QCD phase transition does become first order. The required chemical potential does not violate nucleosynthesis constraints, and if a sterile neutrino is the dark matter, we do actually expect a large neutrino chemical potential [19].

Pulsar timing experiments will reach unprecedented sensitivities in the next few years, and may open a new window on cosmology. The detection of a stochastic background with pulsar timing experiments could help to study the nature of the QCD phase transition, its duration, its strength and so on; by comparison with lattice calculations, this would allow us to determine the neutrino chemical potential and other properties of the so elusive cosmological neutrino sector. Furthermore, the amplitude and peak frequency of the spectrum are sensitive to the expansion rate of the Universe at this temperature [20], which remains unconstrained to date.

A first order QCD phase transition generating a GW background would also induce a stochastic background of magnetic fields, as studied in the past [56]. Furthermore, the GW background might have nonvanishing helicity, which would be an interesting phenomenon to investigate by itself [57].

ACKNOWLEDGMENTS

We would like to thank Paul Demorest, Andrea Lommen, Martin Luescher, Harvey Meyer, Larry Price, and Geraldine Servant for useful conversations. R. D. acknowledges support from the Swiss National Science Foundation. X. S. is supported in part by NSF Grant No. PHY-0758155 and the Research Growth Initiative at the University of Wisconsin-Milwaukee.

[1] A. Einstein, *Königlich Preussische Akademie der Wissenschaften, Sitzungsberichte* (Preussische Akademie der Wissenschaften, Berlin, 1916), pp. 688–696, reprinted in *Collected Papers of A. Einstein*, edited by A. J. Knox, J. Klein, and R. Schulmann (Princeton University Press, Princeton, NJ, 1996), Vol. 6, p. 347.

[2] A. Lazzarini and R. Weiss, LIGO Technical Report No. LIGO-E950018-02; A. Abramovici *et al.*, Science **256**, 325 (1992); http://www.ligo.caltech.edu/.

[3] F. Acernese *et al.*, Optics and Lasers in Engineering **45**, 478 (2007); http://www.virgo.infn.it/.

[4] G. Hobbs *et al.*, Classical Quantum Gravity **27**, 084013 (2010).

[5] P. Demorest, J. Lazio, and A. Lommen (NANOGrav Collaboration), arXiv:0902.2968.

[6] J. S. B. Wyithe and A. Loeb, Astrophys. J. **590**, 691 (2003).

[7] A. H. Jaffe and D. C. Backer, Astrophys. J. **583**, 616 (2003).

[8] M. Enoki, K. T. Inoue, M. Nagashima, and N. Sugiyama, Astrophys. J. **615**, 19 (2004).

[9] M. Kramer, D. C. Backer, J. M. Cordes, T. J. W. Lazio, B. W. Stappers, and S. Johnston, New Astron. Rev. **48**, 993 (2004).

[10] A. Sesana, A. Vecchio, and C. N. Colacino, Mon. Not. R. Astron. Soc. **390**, 192 (2008).

[11] A. Sesana and A. Vecchio, Phys. Rev. D **81**, 104008 (2010).

[12] T. Damour and A. Vilenkin, Phys. Rev. Lett. **85**, 3761 (2000).

[13] T. Damour and A. Vilenkin, Phys. Rev. D **64**, 064008 (2001).

[14] T. Damour and A. Vilenkin, Phys. Rev. D **71**, 063510 (2005).

[15] X. Siemens, V. Mandic, and J. Creighton, Phys. Rev. Lett. **98**, 111101 (2007).

[16] S. Olmez, V. Mandic, and X. Siemens, Phys. Rev. D **81**, 104028 (2010).

[17] E. Witten, Phys. Rev. D **30**, 272 (1984).

[18] D. Schwarz and M. Stuke, J. Cosmol. Astropart. Phys. 11 (2009) 025.

[19] A. Boyarsky, O. Ruchayskiy, and M. Shaposhnikov, Annu. Rev. Nucl. Part. Sci. **59**, 191 (2009).

[20] D. Chung and P. Zhou, Phys. Rev. D **82**, 024027 (2010).

[21] C. J. Hogan, Phys. Lett. **133B**, 172 (1983).

[22] C. J. Hogan, Mon. Not. R. Astron. Soc. **218**, 629 (1986).

[23] M. S. Turner and F. Wilczek, Phys. Rev. Lett. **65**, 3080 (1990).

[24] M. S. Turner, E. J. Weinberg, and L. M. Widrow, Phys. Rev. D **46**, 2384 (1992).

[25] A. Kosowsky, M. S. Turner, and R. Watkins, Phys. Rev. D **45**, 4514 (1992).

[26] A. Kosowsky and M. S. Turner, Phys. Rev. D **47**, 4372 (1993).

[27] M. Kamionkowski, A. Kosowski, and M. S. Turner, Phys. Rev. D **49**, 2837 (1994).

[28] R. Apreda, M. Maggiore, A. Nicolis, and A. Riotto, Classical Quantum Gravity **18**, L155 (2001).

[29] R. Apreda, M. Maggiore, A. Nicolis, and A. Riotto, Nucl. Phys. **B631**, 342 (2002).

[30] S. Huber and T. Konstandin, J. Cosmol. Astropart. Phys. 05 (2008) 017.

[31] S. Huber and T. Konstandin, J. Cosmol. Astropart. Phys. 09 (2008) 022.

[32] C. Caprini, R. Durrer, and G. Servant, Phys. Rev. D **77**, 124015 (2008).

[33] C. Caprini, R. Durrer, T. Konstandin, and G. Servant, Phys. Rev. D **79**, 083519 (2009).

[34] C. J. Hogan, Phys. Rev. Lett. **51**, 1488 (1983).

[35] A. Kosowsky, A. Mack, and T. Kahniashvili, Phys. Rev. D **66**, 024030 (2002).

[36] A. D. Dolgov, D. Grasso, and A. Nicolis, Phys. Rev. D **66**, 103505 (2002).

[37] C. Caprini and R. Durrer, Phys. Rev. D **74**, 063521 (2006).

[38] G. Gogoberizde, T. Kahniashvili, and A. Kosowsky, Phys. Rev. D **76**, 083002 (2007).

[39] T. Kahniashvili, G. Gogoberidze, and B. Ratra, Phys. Rev. Lett. **100**, 231301 (2008).

[40] T. Kahniashvili, L. Campanelli, G. Gogoberidze, Y. Maravin, and B. Ratra, Phys. Rev. D **78**, 123006 (2008).

[41] C. Caprini, R. Durrer, and G. Servant, J. Cosmol. Astropart. Phys. 12 (2009) 024.

[42] R. Durrer, *The Cosmic Microwave Background* (Cambridge University Press, Cambridge, England, 2008).

[43] R. Durrer and C. Caprini, J. Cosmol. Astropart. Phys. 11 (2003) 010.

[44] R. Durrer, J. Phys. Conf. Ser. **222**, 012021 (2010).

[45] J. R. Espinosa, T. Konstandin, J. M. No, and G. Servant, J. Cosmol. Astropart. Phys. 06 (2010) 028.

[46] A. Nicolis, Classical Quantum Gravity **21**, L27 (2004).

[47] M. V. Sazhin, Sov. Astron. **22**, 36 (1978).

[48] S. Detweiler, Astrophys. J. **234**, 1100 (1979).

[49] D. R. Lorimer and M. Kramer, *Handbook of Pulsar Astronomy* (Cambridge University Press, Cambridge, England, 2005).

[50] F. A. Jenet, G. B. Hobbs, K. J. Lee, and R. N. Manchester, Astrophys. J. **625**, L123 (2005).

[51] http://nanograv.org/.

[52] P. L. Bender, K. Danzmann, and the LISA Study Team, MPQ233 (1998) [http://lisa.gsfc.nasa.gov/Documentation/ppa2.08.pdf]; http://lisa.nasa.gov/.

[53] S. A. Hughes, Mon. Not. R. Astron. Soc. **331**, 805 (2002).

[54] A. Ashoorioon and T. Konstandin, J. High Energy Phys. 07 (2009) 086.

[55] M. Maggiore, Phys. Rep. **331**, 283 (2000).

[56] J. M. Quashnock *et al.*, Astrophys. J. **344**, L49 (1989); B. Cheng and A. V. Olinto, Phys. Rev. D **50**, 2421 (1994); G. Baym *et al.*, Phys. Rev. D **53**, 662 (1996); M. McNeil Forbes and A. R. Zhitnitsky, Phys. Rev. Lett. **85**, 5268 (2000); T. Boeckel and J. Schaffner-Bielich, Phys. Rev. Lett. **105**, 041301 (2010).

[57] C. Caprini, R. Durrer, and E. Fenu, J. Cosmol. Astropart. Phys. 11 (2009) 001.

6.5 Article: Gravitational wave signal from first order phase transitions at CE

Cosmic Explorer (CE) is a proposed third generation terrestrial interferometer, with 40 km arm length [273]. It is an American proposal, comparable to the European ET (see section 4.4), but with only two arms oriented at 90 degrees. Its sensitivity extends down to frequencies of about 10 Hz, with an improvement of almost two orders of magnitude with respect to currently operating interferometers. CE is expected to reach the same sensitivity to SGWBs of LISA, namely $\Omega_{gw} \sim 10^{-12}$, but around 50 Hz. In the article presented in this section, we have studied its ability to probe first order PTs in the early universe.

Being sensitive to a higher frequency range than both LISA and PTA, CE opens up the detection possibility to very high energy scales: as shown below, it provides access to hypothetical PTs occurring at, e.g. $T_* = 10^5$ GeV, for which LISA could only detect very low values of β/H_*, i.e. PTs lasting exceptionally long. However speculative this may be, if a PT with these characteristics would have occurred in the early universe, it would provide a coincident signal in both detectors. This is the most important result of the following article: a joint detection of the same signal by both interferometers would be a major discovery (and would allow for much better parameter estimation). Even a detection by only one interferometer, either LISA or CE, combined with a null detection in the companion, could bring relevant information on the frequency shape of the signal, which is tightly connected to the SGWB nature (for example, whether it is primordial or astrophysical, from a short source or one that extends over several Hubble times, and so on). Having a network of detectors operating simultaneously at different frequency ranges would be a very valuable asset in the future for what concerns SGWBs from the early universe, that are often characterised by wide frequency spans.

In autumn 2017, the Gravitational-Wave International Committee (GWIC, gwic.ligo.org) has established a special subcommittee with the purpose of producing a community-driven plan defining a feasible path towards a future network of third-generation GW observatories. The article presented below was completed in this context.

Multi-wavelength observations of cosmological phase transitions using LISA and Cosmic Explorer

Margot Fitz Axen[a], Sharan Banagiri[a], Andrew Matas[a], Chiara Caprini[b], Vuk Mandic[a1]

[1a] *School of Physics and Astronomy, University of Minnesota, Minneapolis, MN 55455, USA*

[b] *Laboratoire Astroparticule et Cosmologie, CNRS UMR 7164, Université Paris-Diderot, 75013 Paris, France*

We reanalyze the detection possibilities for gravitational waves arising from cosmological first order phase transitions. We discuss the stochastic gravitational wave background corresponding to the three expected scenarios of phase transition dynamics. We then perform an analysis on the detection possibilities for each case using sensitivities for the next generation ground-based detector Cosmic Explorer and the current LISA proposal, using two analysis methods. We find that having both detectors allows wide detection possibilities over much of the parameter space, including those corresponding to several early Universe models.

I. INTRODUCTION

First order cosmological phase transitions (PT) are predicted in scenarios beyond the standard model of particle physics, including in the context of the electroweak symmetry breaking (see e.g. [1–4] and citations therein). Unlike second-order phase transitions in which the transition proceeds smoothly, first order phase transitions occur by the nucleation of bubbles of the new phase, which expand and collide. Energy released in the collisions along with bulk motion of any fluid present can give rise to a significant stochastic gravitational wave background [3, 5–14]. For a review of cosmological sources of the stochastic gravitational-wave background, including PT models, see [15].

The background from the electroweak PT is a target for the Laser Interferometer Space Antenna (LISA) [2, 16]. The most sensitive frequency band for LISA is $1 - 10$ mHz, and probes the Universe when it was at temperatures of $O(1$ TeV), the expected scale of the electroweak PT [2, 16]. A previous study in [3] has developed a phenomenological parameterization for the PT background, and estimated the range of models that can be detected by LISA, assuming four different LISA design proposals available at the time.

Unfortunately the electroweak PT background is not likely to be detectable by currently operating ground-based gravitational-wave detectors such as the Advanced Laser Interferometer Gravitational-wave Observatory (LIGO) and Advanced Virgo [17–19], which operate at roughly 10-5000 Hz and probe higher temperatures than LISA [20]. However, next generation ground-based detectors such as Cosmic Explorer (CE)[21] and the Einstein Telescope [22] are expected to be roughly a factor of $10^3 - 10^4$ times more sensitive to the stochastic background, and will extend the observing band to lower frequencies $\sim$5 Hz [21, 23]. Consequently, as we show below, CE may be able to measure the tail of the EW PT, or the signal from higher temperature PTs which could have spectra peaking near the CE band, if they exist.

In this study, we quantitatively assess what can be learned about the electroweak and other kinds of PTs by analyzing data from both LISA and CE simultaneously. A detection of the PT background by both LISA and CE would be a discovery of enormous significance, by providing a measurement of the energy density spectrum in two widely separated frequency bands. Even a null result in one detector could provide additional information about the PT background that the other detector could not achieve alone.

We adopt the parameterization of PTs developed in [3], using the CE sensitivity from [21] and LISA sensitivity from the most recent 2017 LISA proposal [16]. The LISA noise estimates we use differ from those considered in [3] in characteristics such as the arm length and mission duration.

This study is organized as follows. In section 2, we discuss the projected sensitivities of Cosmic Explorer and LISA. In section 3 we provide a summary of the gravitational wave background produced by PTs. In section 4 we describe analysis methods used to determine the detectability of a gravitational wave (GW) signal. Finally, in section 5 we present the results of our analysis and discuss their implications.

II. PROJECTED SENSITIVITY OF LISA AND COSMIC EXPLORER

The 2017 LISA proposal [16] calls for a space-borne gravitational wave detector in a heliocentric orbit, lagging behind the Earth by 50-65 million km. The three LISA space-crafts will be in a triangular formation, with a separation of 2.5 million km between them. From the six interferometer links along LISA arms, three time delay interferometry (TDI) data channels (A, E, and T) will be constructed in order to perform cancellation of laser phase noise. To estimate the sensitivity of these channels, we use the acceleration and displacement noise specifications from the LISA proposal [16] and follow [24] to compute the minimum sky-averaged strain amplitude needed for a narrow-band signal at a frequency f to stand

above the noise. For a channel I [1] we equate the noise power spectral density $S_I^n(f)$ with the power induced by the gravitational wave,

$$\mathcal{H}(f)\,\mathcal{R}_I(f) = S_I^n(f). \tag{1}$$

Here $\mathcal{H}(f)$ is the power spectrum of the gravitational wave and $\mathcal{R}_I(f)$ is the sky-averaged detector response to the gravitational wave for channel I, which is related to the antenna function $F_I^A(\hat{\Omega}, f)$ for the channel as,

$$\mathcal{R}_I(f) = \sum_{A=+,\times} \int \frac{d\hat{\Omega}}{4\pi} |F_I^A(\hat{\Omega}, f)|^2. \tag{2}$$

Here $\hat{\Omega}$ depicts the solid angle. We note that the detector response captures effects due to the geometry of the detector, as well as the frequency dependence arising from the relative size of the detector in comparison with the wavelength of the gravitational wave. The strain sensitivity $h_I(f)$ is then just the square root of $\mathcal{H}(f)$,

$$h(f) = \sqrt{\frac{S_I^n(f)}{\mathcal{R}_I(f)}}. \tag{3}$$

We show the sky-averaged sensitivity curve for A and E channels (we assume $R_A = R_E$) given by Equation 3 for LISA in Figure 1. For more details about constructing LISA sensitivity curves, we refer the reader to [25].

Cosmic Explorer [21] is a proposed 40 km long detector with a similar design to that of LIGO. It will extend the frequency band of Advanced LIGO and Advanced Virgo down to around 5 Hz, with sensitivity improvements of order $10\times$ relative to that of Advanced LIGO. Sensitivity curves for CE are computed from analytical models of noise sources including quantum noise, local gravitational disturbances, and thermal noise in suspensions and mirror coatings [21]. Unlike for LISA, the CE detector response can be assumed to be independent of frequency because the wavelengths of the gravitational waves targeted by these detectors are much larger than the arm-length of the detector. Figure 1 shows the CE target sensitivity.

III. PHASE TRANSITION STOCHASTIC GRAVITATIONAL WAVE BACKGROUND

The stochastic background is characterized by its spectral energy density

$$h^2\Omega_{\rm GW}(f) = h^2 \frac{f}{\rho_c} \frac{{\rm d}\rho_{\rm GW}}{{\rm d}f}, \tag{4}$$

[1] In this paper we do not consider cross power spectra, since their sensitivities are generally much smaller than the auto-power spectra.

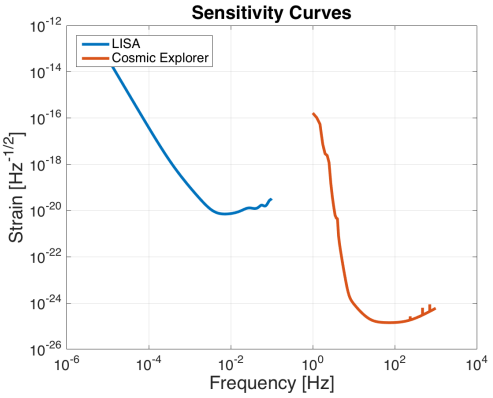

FIG. 1: This plot shows the sky averaged sensitivity curves for LISA and CE, given by Equation 1.

where $\rho_{\rm GW}$ is the energy density in gravitational waves, $\rho_c = 3H_0^2/(8\pi G)$ is the critical energy density to have a flat Universe, and the Hubble constant is $H_0 = 100h$ km/s/Mpc (we adopt the speed of light $c = 1$). The source of gravitational wave energy arising from first-order cosmological PTs is due to bubble collisions and fluid motion. In Ref. [3], three different processes are considered, whose different contributions to the total background must be calculated separately and summed. However, depending on the dynamics of the phase transition, some of these processes may provide a negligible contribution to the entire background and so can be disregarded.

The first contribution is that from the scalar field, ϕ, itself, due to the bubble wall collisions. The second contribution is from sound waves in the plasma, as the bubble wall sweeps through the surrounding fluid. The final contribution is from magneto-hydrodynamic (MHD) turbulence in the plasma. We denote these three contributions $\Omega_\phi, \Omega_{\rm SW}$, and $\Omega_{\rm turb}$, respectively. In general, the total background is [3]

$$h^2\Omega_{\rm GW}(f) = h^2\Omega_\phi(f) + h^2\Omega_{\rm SW}(f) + h^2\Omega_{\rm turb}(f). \tag{5}$$

The relative importance of these three terms depends on the dynamics of the PT.

Following [3], in this study we consider three different scenarios for the dynamics of the bubble expansion. The first scenario assumes non-runaway bubbles whose speed reaches a relativistic terminal velocity. The second scenario assumes runaway bubbles which, though expanding in the plasma, rapidly approach the speed of light. The third scenario assumes that the phase transition occurs in vacuum, consequently plasma effects are negligible and the bubbles expand at the speed of light. Note that the second scenario is excluded in the context of the electroweak symmetry breaking [26]: we therefore apply it here only for the case of speculative PTs occurring at very high temperatures, relevant for observations with the CE.

A. Main parameters describing the phase transition

We first briefly review the parameterization used throughout the rest of the study, following [3], and the relevant quantities for computing the gravitational wave background. As usual we define β as the inverse of the time duration of the phase transition. This quantity determines the size of the bubbles at the time of collision and therefore the characteristic frequency at which the GW signal peaks [2]. For a phase transition taking place at temperature T_n and ending at time t_n [2], β is given by [3]

$$\beta = \frac{\Gamma'}{\Gamma} = -\left.\frac{\mathrm{d}S}{\mathrm{d}t}\right|_{t=t_n} = T_n H(T_n)\left.\frac{\mathrm{d}S}{\mathrm{d}T}\right|_{T=T_n} \tag{6}$$

where $\Gamma(t)$ denotes the nucleation rate and S is the Euclidean action of a bubble [2]. The last expression is given by the fact that $\mathrm{d}T/\mathrm{d}t = -TH$, where H is the Hubble parameter [2].

We define $T_\star$ as the temperature of the thermal bath at the time $t_\star$ when gravitational waves are produced. A key parameter controlling the gravitational wave spectrum is $\beta/H_\star$, where $H_\star$ is the Hubble parameter at $T_\star$.

Another key parameter is α, the ratio of the latent heat released during the phase transition to that of the radiation bath. It is given by [2]

$$\alpha = \frac{\rho_{\rm vac}}{\rho_{\rm rad}(T_n)}, \tag{7}$$

where $\rho_{\rm rad}(T_n) = g_n \pi^2 T_n^4/30$ and g_n is the number of relativistic degrees of freedom in the plasma at temperature T_n [3].

B. Case 1: Non Runaway Bubbles

The first phase transition scenario considers non-runaway bubbles, which expand in the plasma and reach a terminal velocity v_w that is less than the speed of light. In this case, there are no large reheating effects and so $T_n \approx T_\star$ [3]. There are two contributions to the gravitational wave spectrum that should be considered, due to sound waves and magnetohydrodynamic turbulence in the plasma after the bubbles have collided [3]

$$h^2\Omega_{\rm GW}(f) \approx h^2\Omega_{\rm SW}(f) + h^2\Omega_{\rm turb}(f). \tag{8}$$

Gravitational waves from the scalar field play a negligible contribution in this case [9, 27, 28].

Sound waves are generated by the bubble growth, and propagate through the plasma after the transition has completed [9, 27, 28]. A model covering all relevant values of v_w and α is unavailable; however, simulations in [27, 28] give insights into the possible frequency dependence of the sound wave GW spectrum. We follow [3] which adopts the spectral shape

$$S_{\rm SW}(f) = \left(\frac{f}{f_{\rm SW}}\right)^3 \left(\frac{7}{4+3(f/f_{\rm SW})^2}\right)^{7/2}, \tag{9}$$

where the observed frequency f is related to the source frequency f_s by $f = f_s/(1+z)$. The overall scale of the sound wave peak frequency $f_{\rm SW}$ is $f_{{\rm SW},s} = 1.15\beta/v_w$, a conservative estimate that agrees with the above spectral shape [3]. The peak frequency $f_{\rm SW}$ of the observed gravitational wave spectrum is given by

$$f_{\rm SW} = \frac{f_{{\rm SW},s}}{1+z} = h_\star \left(\frac{f_{{\rm SW},s}}{\beta}\right)\left(\frac{\beta}{H_\star}\right), \tag{10}$$

where $h_\star$ is the value of the inverse Hubble time at GW production redshifted to today

$$h_\star = \frac{H_\star}{1+z} = 16.5\times 10^{-3}\mathrm{mHz}\left(\frac{T_\star}{100\ \mathrm{GeV}}\right)\left(\frac{g_\star}{100}\right)^{\frac{1}{6}}. \tag{11}$$

Finally, results from [27] are fitted reasonably by the following gravitational wave spectrum

$$h^2\Omega_{\rm SW}(f) = 2.65\times 10^{-6}\left(\frac{H_\star}{\beta}\right)\left(\frac{\kappa_\nu \alpha}{1+\alpha}\right)^2 \times \left(\frac{100}{g_\star}\right)^{\frac{1}{3}} v_w S_{\rm SW}(f), \tag{12}$$

where $\kappa_\nu = \rho_\nu/\rho_{\rm vac}$ is the fraction of vacuum energy that gets converted into bulk motion of the fluid. In the limits of large v_w, κ_ν is approximately given by [29]

$$\kappa_\nu \approx \alpha(0.73 + 0.083\sqrt{\alpha} + \alpha)^{-1} \tag{13}$$

In addition to sound waves, bubble percolation can also cause turbulence in the plasma, and in particular MHD turbulence since the plasma is ionized. For the GW signal from MHD turbulence, we adopt the spectral shape found analytically in [30] given by [3]

$$S_{\rm turb}(f) = \frac{(f/f_{\rm turb})^3}{[1+(f/f_{\rm turb})]^{11/3}(1+8\pi f/h_\star)} \tag{14}$$

Like the sound wave case, the peak frequency for the gravitational wave spectrum depends on the bubble size at the end of the transition and is given by $f_{{\rm turb},s} = 1.75\beta/v_w$ [3, 30]. Finally, the total contribution to the gravitational wave spectrum can be modelled as [30]

$$h^2\Omega_{\rm turb}(f) = 3.35\times 10^{-4}\left(\frac{H_\star}{\beta}\right)\left(\frac{\kappa_{\rm turb}\alpha}{1+\alpha}\right)^{\frac{3}{2}} \times \left(\frac{100}{g_\star}\right)^{\frac{1}{3}} v_w S_{\rm turb}(f), \tag{15}$$

where the factor $\kappa_{\rm turb} = \epsilon\kappa_\nu$ represents the fraction of the bulk motion that is turbulent.

C. Case 2: Runaway Bubbles in Plasma

The second case we consider is runaway bubbles in plasma, for which the bubble wall velocity v_w approaches the speed of light. This scenario for the bubble expansion is not realised in the context of the electroweak PT [26], but it is in principle allowed in potential phase transitions occurring at higher temperature, which must be considered in the present analysis since they are relevant for the CE, as we will see. In this case, the contribution to the spectrum from the scalar field must be added to that from sound waves and turbulence [3].

$$h^2\Omega_{\rm GW}(f) \approx h^2\Omega_\phi(f) + h^2\Omega_{\rm SW} + h^2\Omega_{\rm turb}. \tag{16}$$

Numerical simulations have been done to determine the contribution to the gravitational wave signal from the scalar field in [31], and the spectral shape of the gravitational wave spectrum is given by

$$S_\phi(f) = \frac{3.8(f/f_\phi)^{2.8}}{1+2.8(f/f_\phi)^{3.8}}. \tag{17}$$

The peak frequency from the scalar field is $f_{\phi,s} = 0.62\beta/(1.8-0.1v_w+v_w^2)$ [3, 31]. Fits to simulation data give the total contribution to the gravitational wave spectrum as [3, 31]

$$h^2\Omega_\phi(f) = 1.67\times10^{-5}\left(\frac{H_\star}{\beta}\right)^2\left(\frac{\kappa_\phi\alpha}{1+\alpha}\right)^2\left(\frac{100}{g_\star}\right)^{\frac{1}{3}} \times\left(\frac{0.11v_w^3}{0.42+v_w^2}\right)S_\phi(f), \tag{18}$$

where the parameter $\kappa_\phi = \rho_\phi/\rho_{\rm vac}$ is the fraction of vacuum energy that gets converted into energy of the scalar field. For this case, it is necessary to define a new parameter α_∞ as the minimum value of α such that bubbles run away [29]. For $\alpha > \alpha_\infty$, the contribution of the scalar field to the gravitational wave background is parametrized by [29]

$$\kappa_\phi = 1 - \frac{\alpha_\infty}{\alpha} \geq 0 \tag{19}$$

In this expression, α_∞/α is the fraction of the total energy that goes into bulk motion (κ_ν) and thermal energy ($\kappa_{\rm therm}$); the amount of this energy that goes into bulk motion is given by [29]

$$\kappa_\nu = \frac{\alpha_\infty}{\alpha}\kappa_\infty \tag{20}$$

where κ_∞ is computed similarly to Equation 13 as [29]

$$\kappa_\infty \approx \alpha_\infty(0.73+0.083\sqrt{\alpha_\infty}+\alpha_\infty)^{-1} \tag{21}$$

D. Case 3: Runaway Bubbles in Vacuum

The final case we consider is runaway bubbles in a vacuum dominated epoch, for which one only needs to consider the contribution to the spectrum from the scalar field and not from sound waves or turbulence, as those contributions are only applicable in plasma [3]

$$h^2\Omega_{\rm GW}(f) \approx h^2\Omega_\phi(f). \tag{22}$$

The spectral shape of the gravitational wave spectrum is given by Eq. 17. Furthermore, since T_n goes to 0, the parameter α approaches infinity and therefore drops out of the expression for $\Omega_{\rm GW}(f)$. In this limit, the total contribution to the gravitational wave spectrum is therefore [3, 31]

$$h^2\Omega_\phi(f) = 1.67\times10^{-5}\left(\frac{H_\star}{\beta}\right)^2\left(\frac{100}{g_\star}\right)^{\frac{1}{3}} \times\left(\frac{0.11v_w^3}{0.42+v_w^2}\right)S_\phi(f). \tag{23}$$

The computed gravitational-wave backgrounds for certain points in the parameter space of each phase transition case are shown in Figure 2, along with the sensitivity curves for LISA and Cosmic Explorer, assuming 1 year of exposure. For Cosmic Explorer, we assume two detectors are built at locations yielding the same overlap reduction function as for the two LIGO detectors. These figures provide an estimate of whether the selected models produce a spectrum that is large enough for detection in the frequency bands of LISA or Cosmic Explorer or both. In general, one expects that a spectrum rising well above a sensitivity curve should be detectable by the corresponding detector. Similarly, a spectrum well below a sensitivity curve is likely undetectable by that detector.

IV. ANALYSIS METHODS

In this section, we consider how to assess our ability to detect the gravitational wave background from first order PTs. We desire the analysis to be independent of any specific phase transition model, so relevant parameter values vary freely.

The three phase transition scenarios must be considered independently, as they have different gravitational wave spectra. For the case of runaway bubbles in vacuum (Case 3), there are only two parameters to be considered- $\beta/H_\star$ and $T_\star$. All other parameters are irrelevant at maximal bubble wall velocity and without plasma effects.

For non-runaway bubbles in plasma (Case 1), however, there are five parameters that may be varied: $\beta/H_\star$, $T_\star$, α, v_w, and ϵ. The bubble wall velocity v_w is model dependent but, as done in [3], we chose to fix this parameter to be $v_w = 0.95c$ since lower wall velocities produce less observable gravitational radiation. The fraction of bulk motion that is turbulent, represented by the parameter ϵ, is also model dependent (and not yet fully understood). We set $\epsilon = 1$, corresponding to equal amount of kinetic energy in the sound waves and turbulent fluid motions: a plausible value for the case of strong enough PTs. The

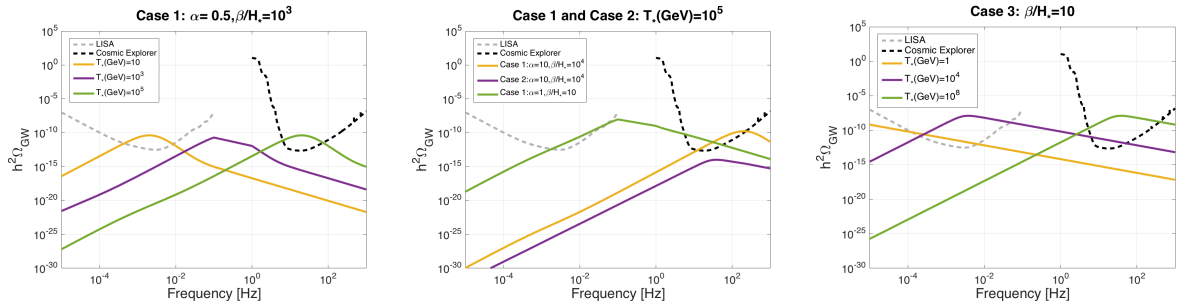

FIG. 2: These plots show the total gravitational wave spectrum for specific points in the parameter space along with time integrated sensitivity curves for LISA and Cosmic Explorer (assuming 1 year of integration time). For the first and third plots, the point in the parameter space (respectively (α, $\beta/H_\star$) and $\beta/H_\star$ alone) corresponding to the parameter values indicated in the title of each plot, is computed for three different temperatures (corresponding to the yellow, purple, and green curves). The middle plot shows indicated points of interest in the parameter space of Cases 1 and 2 at $T_\star = 100000$ GeV. These points are shown by the blue diamonds in Figures 3 and 4.

three remaining parameters, α, $\beta/H_\star$, and $T_\star$ are related but again cannot be specified without choosing a phase transition model. As done in previous analyses these are the parameters we chose to vary: specifically, we analyze the α-$\beta/H_\star$ space for several values of $T_\star$ [2, 3, 32].

For runaway bubbles in plasma (Case 2), the situation is similar. In this case, the five parameters to be considered are $\beta/H_\star$, $T_\star$, α, α_∞, and ϵ. The value of α_∞ is again model dependent. We choose to fix it to $\alpha_\infty = 0.1$, a value considered also in [3]. In addition, in the context of case 2 we fix the temperature to $T_\star = 10^5$ GeV, corresponding to an unknown PT at high temperature for which the presence of runaway bubbles in the plasma cannot be excluded. We then analyze the α-$\beta/H_\star$ space for these parameter values just as for Case 1.

We scan the two-dimensional parameter space and compute the total SGWB at 2500 points. Then at each point we use the projected sensitivities for LISA and Cosmic Explorer to evaluate whether the parameter values at the point describe a gravitational wave background that should be detectable by LISA or CE. We also determine the possibility of detection with the sensitivity of both detectors operating simultaneously.

A. Likelihood Analysis

To analyze whether a point in the parameter space was in a detectable region, we considered two analysis methods. The first is a Bayesian likelihood analysis. We first define a projected sensitivity $\Omega_{\rm Sens}$, which is related to the sky averaged sensitivity seen in Equation 3 by [24]

$$\Omega_{\rm Sens} = \frac{4\pi^2 f^3}{3H_0^2} h_I^2(f). \tag{24}$$

Inspired by similar analyses performed by LIGO [33], we then define the following likelihood function for each point in the parameter space

$$\log(L(\alpha, \beta/H_\star, T_\star)) = -\tau \sum_{f=f_{\rm min}}^{f_{\rm max}} \left[\frac{h^2\Omega_{\rm GW}(\alpha, \beta/H_\star, T_\star, f)^2}{2h^2\Omega_{\rm Sens}(f)^2} \right] \tag{25}$$

where $h^2\Omega_{\rm GW}$ is the calculated GW signal and τ is the duration of the mission, assumed to be one year for this study. The summation over frequency runs over either the LISA frequency band, CE frequency band, or frequency band of both for evaluation of the combined sensitivity of both detectors operating simultaneously.

We assume uniform priors in input parameters $\alpha, \beta/H_\star, T_\star$, implying that the Bayesian posterior distribution in these parameters is equal to the likelihood function defined above. We define a set of contours labeled by Z, for which the posterior is equal to Z. We then define the fraction of the total posterior probability contained within each contour,

$$P(Z) = \frac{\int_{L(\alpha,\beta/H_\star,T_\star)>Z} L(\alpha, \beta/H_\star, T_\star)\, d\alpha\, d(\beta/H_\star)\, dT_\star}{\int L(\alpha, \beta/H_\star, T_\star)\, d\alpha\, d(\beta/H_\star)\, dT_\star} \tag{26}$$

and identify the 95% confidence contour as the one for which $P(Z) = 0.95$.

B. SNR Analysis

In addition to the Bayesian likelihood analysis, we also considered a second method of analysis involving computing an SNR. Using the projected sensitivities of LISA and Cosmic Explorer, we consider the signal-to-noise ratio at each point of the parameter space [3]

$$\mathrm{SNR}(\alpha, \beta/H_\star, T_\star) = \sqrt{\tau \int_{f_{\rm min}}^{f_{\rm max}} df \left[\frac{h^2\Omega_{\rm GW}(\alpha, \beta/H_\star, T_\star, f)^2}{h^2\Omega_{\rm Sens}(f)^2} \right]} \tag{27}$$

If the SNR value is greater than a threshold value $\mathrm{SNR}_{\mathrm{thr}}$, then the signal at that point is detectable. Contours are made outlining all points in this detectable region.

Equations 25 and 27 are in appearance very similar. In fact, the likelihood computation is analogous to doing the SNR calculation using a value of $\mathrm{SNR}_{\mathrm{thr}} = 2$. However, due to the differences in the way contours are computed, and in particular the fact that the likelihood is defined over a uniform prior on the parameters $\{\alpha, \beta/H_\star, T_\star\}$ which are non-linearly related to $\Omega_{\mathrm{GW}}(f)$, they will produce slightly different results. In choosing a value of $\mathrm{SNR}_{\mathrm{thr}}$, we first follow [3] and consider a value of $\mathrm{SNR}_{\mathrm{thr}} = 10$, and then compute contours for $\mathrm{SNR}_{\mathrm{thr}} = 2$ for appropriate comparison to the likelihood analysis. Discrepancies between our calculations and those done in [3] for LISA are due to using a different value of ϵ along with using the most recent LISA sensitivity curves.

V. RESULTS AND DISCUSSION

Results of our analysis can be seen in Figures 3 and 4. Figure 3 shows the analysis of five temperature values for Case 1, while Figure 4 shows the analysis done for cases 2 and 3. The shaded regions correspond to the SNR analysis done for $\mathrm{SNR}_{\mathrm{thr}} = 10$. The light gray shaded regions are regions accessible to LISA, the black shaded regions are accessible to Cosmic Explorer, and the dark gray shaded regions are accessible to both operating separately. The gray dotted line shows the accessible region for both detectors operating simultaneously. The red dotted line shows the joint accessibility computed for $\mathrm{SNR}_{\mathrm{thr}} = 2$, and the solid red line denotes the joint accessibility likelihood curve.

Having both detectors operating allows wide access to many different regions of the parameter space that would be out of range of just one. For Cases 1 and 2, LISA is more sensitive to lower values of the parameter $\beta/H_\star$ while Cosmic Explorer is sensitive to higher values, allowing much of the chosen range of $\beta/H_\star$ to be accessible at higher values in the chosen range of α. Additionally, the contours for Cases 1 and 3 show that while LISA is more sensitive to the background at lower temperatures, Cosmic Explorer allows better sensitivity at higher temperatures. These results can be understood by the fact that in general, higher temperature and $\beta/H_\star$ values shift the gravitational wave spectrum to higher frequencies, being stronger in the regions accessible to next-generation terrestrial detectors rather than LISA.

Having regions of the parameter space accessible to both CE and LISA provides additional advantages in regards to constraining the spectrum. A joint detection in multiple frequency bands would be a major discovery, allowing better estimates of model parameters than would be possible with each detector separately. Similarly, a discovery by only one of the detectors would rule out corresponding areas of the parameter space.

It is evident that the method used for analysis has an impact on the computed detectable region, and therefore it is relevant to consider both. The likelihood analysis computes the greatest accessible region, while the SNR curves compute a smaller accessible region of the parameter space. However, the value of $\mathrm{SNR}_{\mathrm{thr}}$ chosen also has an impact; for $\mathrm{SNR}_{\mathrm{thr}} = 2$ the curve is closer to the likelihood curve then for $\mathrm{SNR}_{\mathrm{thr}} = 10$.

The 95% confidence likelihood curves should correspond to the analysis done for $\mathrm{SNR}_{\mathrm{thr}} = 2$, because both are calculating 2σ confidence regions. However, it is evident from the plots that the curves are not the same. For the likelihood analysis, probabilities are calculated on levels of a normalized likelihood curve and contours are made at the level Z for which 95% of the summed likelihood is above Z. These levels do not necessarily correspond to a constant SNR along the contours because the prior on these values is flat in the parameters α, $\beta/H_\star$ and $T_\star$ rather than in Ω_{GW}. For the SNR calculation, each individual point in the parameter space is considered for whether it exceeds the threshold SNR value, so it is ultimately a different calculation that yields a slightly different result. The shaded regions, corresponding to $\mathrm{SNR} = 10$, identify parts of the parameter space where a detection with strong significance could be made based on the criteria outlined in this paper. The 95% contours based on the likelihood model show where we would expect to be able to place 95% upper limits in the absence of a detection. Backgrounds in between the 95% upper limit and a strong detection would lead to a marginally detected signal; by integrating for a longer period of time, the confidence in signals would increase.

Finally, it is worth considering what these plots can tell us about detection possibilities for the gravitational wave signal from specific phase transition models. Extensions of the standard model that predict first order phase transitions at the electroweak scale are widely studied in the literature, some examples are supersymmetry (see e.g. [34]), Higgs doublet models (see e.g. [35]), and higher dimensional operators (see e.g. [31]). Other scenarios beyond the electroweak scale that predict phase transitions include an additional boson field [36, 37] or a Dark Matter scenario [38].

The work done in [3] analyzed the detectability of specific benchmark points in the parameter space illustrating models considered in other studies. We include some of these points in Figures 3 and 4 as well, shown by the colored circles in the contour plots. For Case 1, the temperature of the points is approximated to place it in a specific contour plot. As found in [3], we confirm here that many of these points are in the accessible region of LISA, which may then provide valuable insight into new physics.

In summary, we have seen how having both LISA and Cosmic Explorer together allows for wide detection possibilities for the gravitational wave background arising from phase transitions, as these detectors can probe complementary regions of the parameter space. We have used

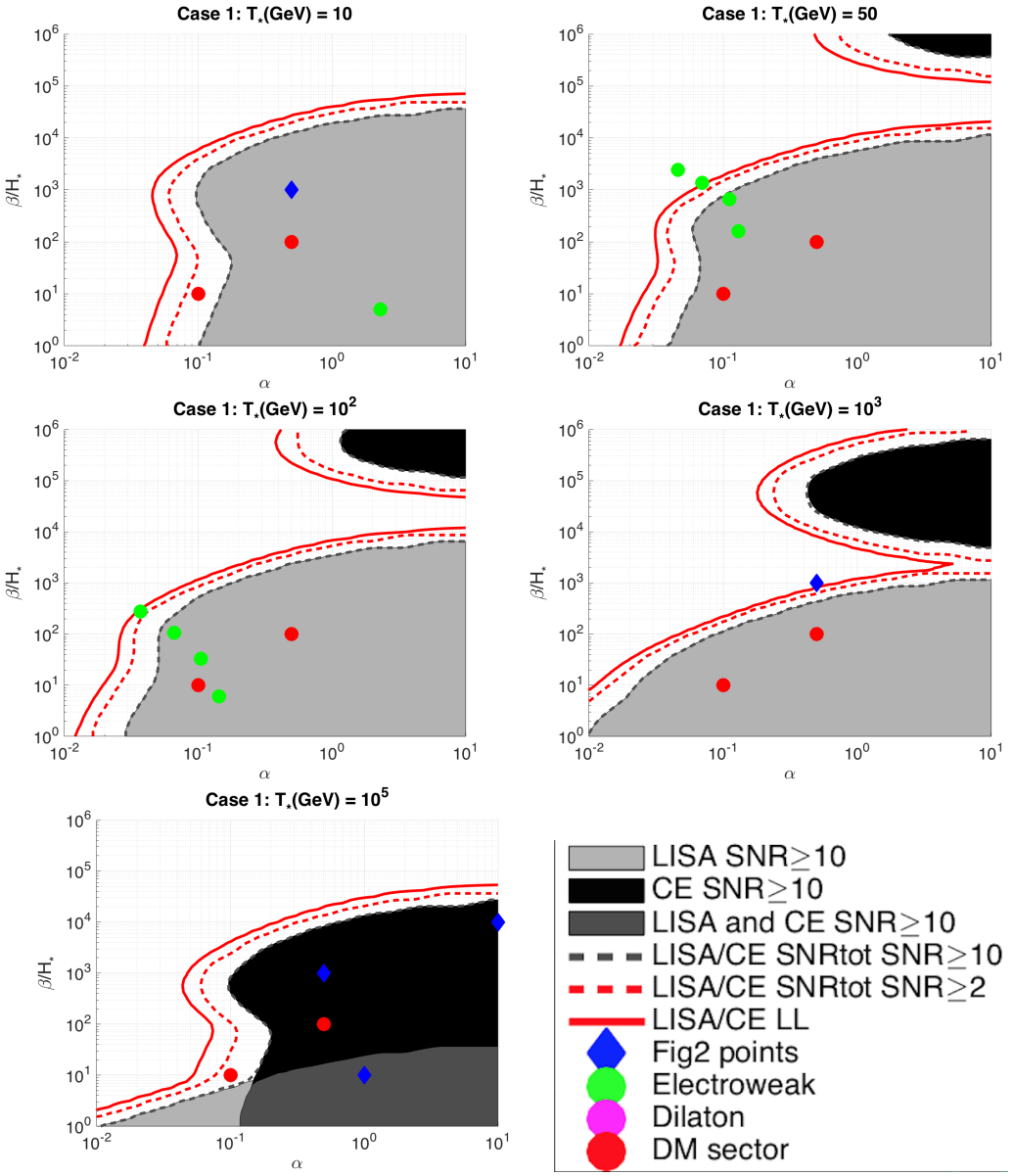

FIG. 3: Shown here are five contour plots denoting different temperatures for Case 1. Shaded regions correspond to the total parameter space accessible to LISA, CE, or both, for the SNR analysis done with $\mathrm{SNR}_{\mathrm{thr}} = 10$. The gray dotted line is the joint accessibility SNR curve for $\mathrm{SNR}_{\mathrm{thr}} = 10$. The red dotted line is the joint SNR curve for $\mathrm{SNR}_{\mathrm{thr}} = 2$. Finally, the joint likelihood analysis curve is also shown for comparison to $\mathrm{SNR}_{\mathrm{thr}} = 2$. Blue diamonds denote model choices whose spectra are shown in Figure 2. The circles show benchmark points from various PT scenarios, taken from [3].

two different analysis methods to assess the detectability and stress that neither one necessarily provides the "correct answer" but that both should be considered and compared. The regions of the parameter space accessible to LISA and Cosmic Explorer include many predicted early universe models, opening up unique possibilities to study the early universe with gravitational wave observations.

Acknowledgements: The work of MFA, AM, and VM was in part supported by the NSF grant PHY1505870.

[1] K. Kajantie, M. Laine, K. Rummukainen, and M. E. Shaposhnikov, Phys. Rev. Lett. **77**, 2887 (1996), hep-ph/9605288.

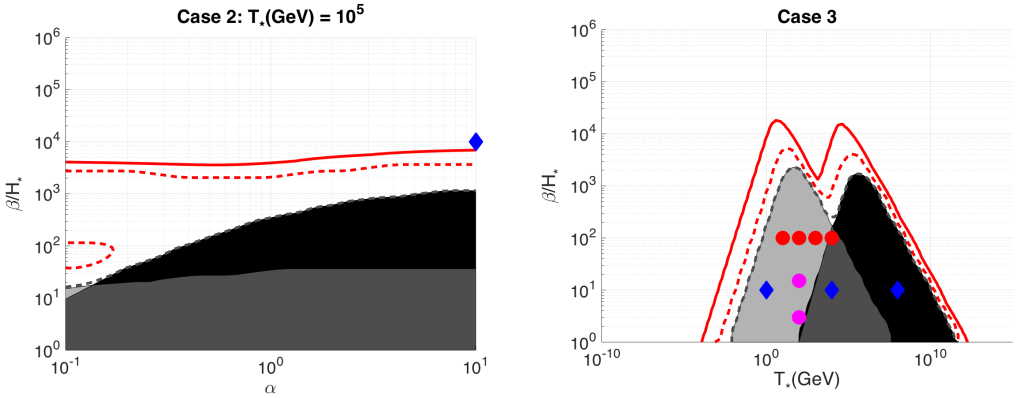

FIG. 4: Shown here are contour plots for Cases 2 and 3. Note that Case 2, in which the scalar field plays a role, is plotted only for $\alpha > \alpha_\infty$. Similar notation for the curves and shaded regions is used as in Figure 3.

[2] C. Grojean and G. Servant, Physical Review D **75**, 043507 (2007).
[3] C. Caprini et al., Journal of Cosmological and Astroparticle Physics **04**, 04001 (2016).
[4] D. J. Weir, Phil. Trans. Roy. Soc. Lond. **A376**, 20170126 (2018), arXiv:1705.01783.
[5] A. Kosowsky, M. S. Turner, and R. Watkins, Phys. Rev. D **45**, 4514 (1992).
[6] A. Kosowsky, M. S. Turner, and R. Watkins, Phys. Rev. Lett. **69**, 2026 (1992).
[7] A. Kosowsky and M. S. Turner, Phys. Rev. D **47**, 4372 (1993).
[8] M. Kamionkowski, A. Kosowsky, and M. S. Turner, Phys. Rev. D **49**, 2837 (1994).
[9] M. Hindmarsh, S. J. Huber, K. Rummukainen, and D. J. Weir, Phys. Rev. Lett. **112**, 041301 (2014).
[10] C. Caprini and R. Durrer, Phys. Rev. D **74**, 063521 (2006).
[11] C. Caprini, R. Durrer, and G. Servant, JCAP **0912**, 024 (2009).
[12] T. Kahniashvili, A. Kosowsky, G. Gogoberidze, and Y. Maravin, Phys. Rev. D **78**, 043003 (2008).
[13] T. Kahniashvili, L. Campanelli, G. Gogoberidze, Y. Maravin, and B. Ratra, Phys. Rev. D **78**, 123006 (2008).
[14] T. Kahniashvili, L. Kisslinger, and T. Stevens, Phys. Rev. D **81**, 023004 (2010).
[15] C. Caprini and D. G. Figueroa (2018), arXiv:1801.04268.
[16] *Lisa mission proposal*, Available at `https://www.elisascience.org/files/publications/LISA_L3_20170120.pdf` (2017).
[17] B. Abbott et al. (LIGO Scientific Collaboration and Virgo Collaboration), Physical Review D **91**, 022003 (2015).
[18] B. Abbott et al. (LIGO Scientific Collaboration and Virgo Collaboration), Physical Review Letters **113**, 231101 (2014).
[19] B. Abbott et al. (LIGO Scientific Collaboration and Virgo Collaboration), Classical and Quantum Gravity **32**, 074001 (2015).
[20] J. T. Giblin and E. Thrane, Phys. Rev.D **90**, 107502 (2014), arXiv: 1410.4779.
[21] B. Abbott et al. (LIGO Scientific Collaboration and Virgo Collaboration), Classical and Quantum Gravity **34**, aa51f4 (2017).
[22] *Einstein telescope design study document*, Available at `http://www.et-gw.eu/index.php/etdsdocument` (2017).
[23] B. Sathyaprakash et al., Class. Quant. Grav. **29**, 124013 (2012), [Erratum: Class. Quant. Grav.30,079501(2013)], arXiv: 1206.0331.
[24] M. R. Adams and N. J. Cornish, Physical Review D **82**, 022002 (2010).
[25] N. Cornish and T. Robson (2018), arXiv:1803.01944.
[26] D. Bodeker and G. D. Moore, JCAP **1705**, 025 (2017), arXiv:1703.08215.
[27] M. Hindmarsh, S. J. Huber, K. Rummukainen, and D. J. Weir, Phys. Rev. D **92**, 123009 (2015).
[28] M. Hindmarsh, S. J. Huber, K. Rummukainen, and D. J. Weir, Phys. Rev. D **96**, 103520 (2017).
[29] J. Espinosa, T. Konstandin, J. No, and G. Servant, Journal of Cosmology and Astroparticle Physics **06**, 028 (2010).
[30] C. Caprini, R. Durrer, and G. Servant, Journal of Cosmology and Astroparticle Physics **12**, 024 (2009).
[31] S. J. Huber and T. Konstandin, Journal of Cosmological and Astroparticle Physics **09**, 022 (2008).
[32] P. Binetruy, A. Bohe, C. Caprini, and J. F. Dufaux, JCAP **1206**, 027 (2012).
[33] V. Mandic, E. Thrane, S. Giampanis, and T. Regimbau, Phys. Rev. Lett. **109**, 171102 (2012), arXiv:1209.3847.
[34] S. J. Huber, T. Konstandin, G. Nardini, and I. Rues, Journal of Cosmology and Astroparticle Physics **2016**, 036 (2016).
[35] G. Dorsch, S. Huber, K. Mimasu, and J. No, Physical Review D **93**, 115033 (2016).
[36] L. Randall and G. Servant, JHEP **0705**, 054 (2007).
[37] T. Konstandin, G. Nardini, and M. Quiros, Phys. Rev. D **82**, 083513 (2010).
[38] P. Schwaller, Phys. Rev. Lett. **115**, 181101 (2015).

Chapter 7

Conclusion

The universe is expected to be permeated by several GW backgrounds of both astrophysical and cosmological origin. In particular, cosmological SGWBs could have been generated by a plethora of high energy phenomena possibly occurring in the primordial epochs of the universe's evolution. GWs are a very promising cosmic relic, to probe directly the currently unknown physics of the early universe, complementary to other observables such as the CMB and BBN.

In this dissertation, I concentrate mainly on one of the possible GW signals from the early universe, namely the SGWB from a first order phase transition. This has been one of the topics of my research since almost a decade, and I have tackled it both from the point of view of predicting the signal characteristics, and from the one of assessing its detectability by GW detectors. The core of the manuscript, chapter 6, starts with a section summarising the main features of the SGWB from first order PTs: sources, parameters, frequency shape. I then include four publications.

The first one, in section 6.2, has been chosen because it represents to date the most refined analytical evaluation of the SGWB from MHD turbulence in the aftermath of a first order PT. The result is still used in many articles today, but it relies on several assumptions that necessitate to be verified via numerical simulations. These are however difficult to perform. Consequently, it is only recently that we have started a project tackling numerical simulations, in collaboration with David Weir and Mark Hindmarsh.

The other three publications have been chosen because they represent neat examples of how signals from first order PTs occurring at different energy scales in the early universe, can

be probed by different GW detectors. Namely, LISA can probe energy scales around the EW symmetry breaking, PTA can probe energy scales around the QCDPT, and CE can probe much higher energy scales, around 10^6 GeV. Of these analyses, the most significant is the one presented in section 6.3. This work has been performed in the context of the LISA Cosmology Working Group, and has been relevant for the community working both on primordial GWs, and on particle physics beyond the Standard Model. In particular, model builders have used it to predict the amplitude and frequency shape of SGWBs arising in different PT models, and to assess their detectability at LISA.

The first part of the dissertation, instead, is taken from a review that I have written in collaboration with Daniel Figueroa, under invitation by the journal *Classical and Quantum Gravity*. This review describes the large majority of proposals, which have been put forward in the literature, of mechanisms, all based on theories beyond the Standard Model of particle physics, which produce GWs signals in the very early universe. These mechanisms can operate basically at any energy scale from inflation downwards, $T \lesssim 10^{16}$ GeV, until the QCD scale $T \simeq 100$ MeV. I have included in this manuscript four sections of the review. Chapters 2 to 4 present generalities on the definition of GWs, on SGWBs from the early universe, on the current SGWB observational bounds and detectors. Chapter 5 deals with the SGWB generated during slow roll inflation. Here we work out the transfer function representing the evolution of the tensor spectrum from the end of inflation until today, both numerically and via an analytical calculation. The relation between the two approaches and the regime of validity of the analytical approximation have been studied in collaboration with Pierre Auclair, the Ph.D. student I am co-supervising together with Danièle Steer.

The research I have been performing in the past years, leads me to believe that there is a real chance for a cosmological GW background to be detected in the near future. The benefits of a positive detection would be great, opening up a new observational window on the universe, but also on fundamental high-energy physics, that in all probability will never be probed at particle physics accelerators.

Curriculum Vitae

Chiara Caprini
Laboratoire Astroparticule et Cosmologie APC
CNRS, UMR 7164
10, rue Alice Domon et Léonie Duquet
75205 Paris cedex 13 (France)
Phone: +33 1 57 27 60 46
E-mail: caprini@apc.in2p3.fr
http://www.apc.univ-paris7.fr/APC_CS/fr/users/caprini

Current position:

CNRS researcher

October 2008 – August 2016, at Institut de Physique Théorique, CEA Saclay
September 2016 – now, at Laboratoire APC, Paris

Employment and education:

Institut de Physique Théorique, CEA Saclay
October 2007 – September 2008
Postdoc researcher

University of Geneva
November 2004 – September 2007
Postdoc researcher and teaching assistant

University of Oxford
October 2001 – October 2004
Ph.D. in Astrophysics
Thesis advisor: Dr. Pedro G. Ferreira
Thesis title: "The observational consequences of primordial fields"
Graduate Scholar of Oriel College (2002 – 2004)
Dan David Prize Scholar (2003)

University of Parma and University of Geneva
October 1995 – April 2001
Laurea in fisica. Final result: 110/110 *cum laude*
Thesis advisors: Prof. Ruth Durrer, Prof. Massimo Pauri
Thesis title: "Limiti sull'intensità del campo magnetico primordiale dallo spettro di onde gravitazionali indotte"

Research interests:

Cosmology and Gravitational Waves

gravitational wave background of cosmological origin; gravitational waves from compact binaries (and their propagation through the perturbed universe); primordial magnetic fields (generation and constraints); primordial phase transitions; dark energy and scalar fields in cosmology; physics of the Cosmic Microwave Background; cosmological applications of turbulence in plasmas; cosmological perturbation theory

Teaching:

- "Gravitational waves", lectures for Annual Retreat of the University of Mainz, Mainz (Germany), Sep 2017
- "Gravitational waves", lectures for the Tenth TRR33 Winter School in Cosmology, Passo del Tonale (Italy), Dec 2016
- "Gravitational waves", theoretical physics mini-course at the Centre de Physique Théorique, Université Aix-Marseille, July 2016
- "Gravitational waves", theoretical physics course of the Institut de Physique Théorique, CEA-Saclay, academic year 2015/2016
- "Gravitational waves", master level course at the University of Bielefeld (Germany), academic year 2014/2015
- "Precéptorat de mathématique I", Ecole supérieure de Physique et Chimie Industrielles (Paris), academic years 2011-2014
- "Cosmologie II", teaching assistant to Prof. Ruth Durrer, University of Geneva, academic year 2006/2007
- "Relativité Générale", teaching assistant to Prof. Ruth Durrer, University of Geneva, academic year 2005/2006
- "Méthodes Mathématiques en Physique", teaching assistant to Prof. Martin Kunz, University of Geneva, academic year 2004/2005 and 2005/2006

Professional Activities:

- **Research administration**:
  - Director of the *Groupement de Recherche Ondes Gravitationnelles* (CNRS in2p3) since 2017: organisation of the GdR activities (meetings, workshops), management of the GdR budget, financing, members, working groups, website
  - Coordinator of the Cosmology Working Group of the LISA Consortium, since 2013: management of the Working Group activities, members and documents; organisation of the Working Group workshops and teleconferences; report of the activities at LISA Consortium meetings and other conferences
  - Member of the *Groupe de Travail Physique Fondamentale* of the French Space Agency CNES, since 2017
  - Member of the LISA France Consortium, since 2008
  - Member of the *conseil scientifique* of the *Programme National* GRAM (INSU, INP, CNES), 2010-2017
  - Member of the *conseil scientifique* of the Labex P2IO, 2013-2015

- Member of the *conseil de laboratoire* of IPhT CEA-Saclay, 2010-2012

- **Student advisor**:
  - Pierre Auclair: PhD student, Programe doctoral de l'Ecole Polytechnique, Université Paris-Saclay, academic years 2018-2021
    "Cosmology with Gravitational Waves"
  - Philip Cherian: stage Master 2, Ecole Normale Supérieure (Paris), academic year 2016/2017
    "Gravitational waves from first order phase transitions"
  - Maria Chiara Guzzetti: five months visit in the context of her PhD in the University of Padova, academic year 2016/2017
    "Inflationary magnetogenesis with added helicity: constraints from non-gaussianities"
  - Patric Hoelscher: two months visit in the context of his PhD in the University of Bielefeld, academic year 2015/2016
    "Astrophysical gravitational waves in conformal gravity"
  - Paul Caucal: stage Master 2, Ecole Normale Supérieure (Paris), academic year 2015/2016
    "The stochastic gravitational wave background from sound waves generated by a first-order phase transition"
  - Emmanuel Frion: stage Master 2, Observatoire de Paris, academic year 2014/2015
    "Champs magnétiques primordiaux générés pendant l'inflation: contraintes par les non-gaussianités dans le Fond Diffus Cosmologique"
  - Renaud Boussarie: stage Master 1, Ecole Polytechnique (Palaiseau), academic year 2011/2012
    "Génération d'un champ magnétique hélicoïdal pendant l'inflation, effets sur les perturbations de la métrique"
  - Simon Bonnefoy: stage Master 2 *Cosmos, Champs et Particules*, Université Montpellier II, academic year 2010/2011
    "Fond stochastique d'ondes gravitationnelles générées par collisions de bulles lors d'une transition de phase de premier ordre"

- **Conference and seminar organisation**:
  - "LISA Cosmology Working Group Workshop", regular meetings: CERN (April 2015), University of Stavanger (September 2015), DESY Hamburg (October 2016), MITP Mainz (October 2017), University of Helsinki (June 2018), Universidad Autonónoma de Madrid (January 2019)
  - "Journées LISA France", APC (Paris), October 2017
  - "School on Gravitational Waves for Cosmology and Astrophysics", Benasque (Spain), May 2017
  - "PONT d'Avignon – Progress on Old and New Themes in cosmology", Avignon (April 2011, April 2014, April 2017)
  - "Journées Scientifiques de l'Action Spécifique GRAM", APC (Paris), June 2016
  - SOC or parallel session convener: 28th Texas Symposium on relativistic astrophysics (Geneva, December 2015), TeV Particle Astrophysics (CERN, September 2016), XI LISA Symposium (Zurich, September 2016), XII LISA Symposium (Chicago, July 2018)
  - Journal Club on Gravitational Waves, regular meeting, IAP and APC (Paris) 2016-2017

- 17th Itzykson Meeting "Heart of Darkness: Dark Energy and Modified Gravity", IPhT (CEA Saclay), June 2012
- Organiser of the Particle Physics and Cosmology seminar in IPhT (CEA Saclay), 2009-2012

- **Outreach**:
  - "Ondes gravitationnelles", seminar for high-school students, Lycée de La Plaine de Neauphle, Trappes en Yvelines (France), 2016; Lycée Albert Schweitzer, Le Raincy (France), 2017
  - "Gravitation, Virgo et trous noirs", Bar de Sciences, Paris 2017
  - "Le onde gravitazionali", seminar, Seconda festa dell'astronomia, Verona 2017; Associazione Culturale Wunderkammer, Verona 2016
  - "Cosmology and gravitational waves", seminar for high-school professors, APC Paris 2016
  - "eLISA et la détection d'ondes gravitationnelles", seminar, Festival Pint of Science, Paris 2016
  - "Les ondes gravitationnelles et l'univers primordial", Conférénce Cyclope du CEA-Saclay, 2016
  - "Gravitational waves", seminar for the non-scientific staff, IPhT CEA-Saclay, 2016
  - Conference "9th Swiss biennial on science, technics and aesthetics", participation, Luzern, Switzerland 2012
  - "L'espace et le temps en cosmologie", popular article, Scintillations N. 79, June 2009 (Journal de l'IRFU)
- **Training**:
  - CNRS training course: "Agir pour l'égalité professionnelle dans la recherche, programme SPRINGBOARD", 2015
- **Member of PhD and recruitment committees**:
  - PhD committee of Lionel Martellini, Université Côte d'Azur (Nice), academic year 2016/2017
  - *Rapporteur* for the PhD of Mauro Pieroni, APC (Paris), academic year 2015/2016
  - *Concours de maître de conférence à l'université Aix-Marseille*, academic year 2014/2015
  - PhD committee of Marc Volhanten, University of Geneva, academic year 2011/2012
  - PhD committee of Elisa Fenu, University of Geneva, academic year 2010/2011
- **Journal Referee**:
  - Since 2004, referee for Physical Review D, Physical Review Letters, JCAP, MNRAS, Physics Letters B, GRG, IJMP
  - Member of the "Nature reader advisory panel" in the year 2010/2011

List of publications:

48. L. Barack et al., "Black holes, gravitational waves and fundamental physics: a roadmap" [arXiv:1806.05195 [gr-qc]].

47. M. Fitz Axen, S. Banagiri, A. Matas, C. Caprini, V. Mandic, "Multi-wavelength observations of cosmological phase transitions using LISA and Cosmic Explorer", [arXiv:1806.02500 [astro-ph.IM]].

46. C. Caprini, P. Hölscher and D.J. Schwarz, "Astrophysical Gravitational Waves in Conformal Gravity", [arXiv:1804.01876 [gr-qc]].

45. C. Caprini and D. G. Figueroa, "Cosmological Backgrounds of Gravitational Waves", Class. Quant. Grav. **35** (2018) no.16, 163001 [arXiv:1801.04268 [astro-ph.CO]].

44. C. Caprini, M. C. Guzzetti and L. Sorbo, "Inflationary magnetogenesis with added helicity: constraints from non-gaussianities", Class. Quant. Grav. **35** (2018) no.12, 124003 [arXiv:1707.09750 [astro-ph.CO]].

43. K. Inayoshi, N. Tamanini, C. Caprini and Z. Haiman, "Probing stellar binary black hole formation in galactic nuclei via the imprint of their center of mass acceleration on their gravitational wave signal", Phys. Rev. D **96**, (2017) 063014 [arXiv:1702.06529 [astro-ph.HE]].

42. K. Danzmann *et al*, "LISA – Laser Interferometer Space Antenna", proposal in response to the ESA call for L3 mission concepts, `https://www.elisascience.org/files/publications/LISA_L3_20170120.pdf`

41. N. Bartolo *et al*, "Science with the space-based interferometer LISA. IV: Probing inflation with gravitational waves", JCAP **1612** (2016) no.12, 026 [arXiv:1610.06481 [astro-ph.CO]].

40. C. Bonvin, C. Caprini, R. Sturani and N. Tamanini, "The effect of matter structure on the gravitational waveform", Phys. Rev. D **95**, (2017) 044029 [arXiv:1609.08093 [astro-ph.CO]].

39. C. Caprini and N. Tamanini, "Constraining early and interacting dark energy with gravitational wave standard sirens: the potential of the eLISA mission", JCAP **1610** (2016) no.10, 006 [arXiv:1607.08755 [astro-ph.CO]].

38. N. Tamanini, C. Caprini, E. Barausse, A. Sesana, A. Klein and A. Petiteau, "Science with the space-based interferometer eLISA. III: Probing the expansion of the Universe using gravitational wave standard sirens", JCAP **1604** (2016) no.04, 002 [arXiv:1601.07112 [astro-ph.CO]].

37. C. Caprini *et al.*, "Science with the space-based interferometer eLISA. II: Gravitational waves from cosmological phase transitions", JCAP **1604** (2016) no.04, 001 [arXiv:1512.06239 [astro-ph.CO]].

36. C. Caprini and S. Gabici, "Gamma-ray observations of blazars and the intergalactic magnetic field spectrum", Phys. Rev. D **91** (2015) no.12, 123514 [arXiv:1504.00383 [astro-ph.CO]].

35. C. Caprini, "Stochastic background of gravitational waves from cosmological sources", J. Phys. Conf. Ser. **610** (2015) no.1, 012004, [arXiv:1501.01174 [gr-qc]] (proceedings of the X LISA Symposium)

34. C. Caprini and L. Sorbo, "Adding helicity to inflationary magnetogenesis", JCAP **1410** (2014) no.10, 056 [arXiv:1407.2809 [astro-ph.CO]].

33. C. Caprini, "Gravitational waves from first order phase transitions," PoS EPS **-HEP2013** (2013) 477.

32. C. Bonvin, C. Caprini and R. Durrer, "Magnetic fields from inflation: The CMB temperature anisotropies", Phys. Rev. D **88** (2013) 083515 [arXiv:1308.3348 [astro-ph.CO]].

31. The eLISA Consortium, "The Gravitational Universe", submitted to the European Space Agency on May 24th, 2013 for the L2/L3 selection of ESA's Cosmic Vision program [arXiv:1305.5720 [astro-ph.CO]].

30. C. Caprini, "Magnetic fields from inflation: the transition to the radiation era," proceedings of the conference "Moriond cosmology session 2012".

29. P. Amaro-Seoane, S. Aoudia, S. Babak, P. Binetruy, E. Berti, A. Bohe, C. Caprini and M. Colpi *et al.*, "Low-frequency gravitational-wave science with eLISA/NGO," proceedings of the 9th Amaldi Conference on Gravitational Waves, Class. Quant. Grav. **29** (2012) 124016 [arXiv:1202.0839 [gr-qc]].

28. P. Amaro-Seoane, S. Aoudia, S. Babak, P. Binetruy, E. Berti, A. Bohe, C. Caprini and M. Colpi *et al.*, "eLISA/NGO: Astrophysics and cosmology in the gravitational-wave millihertz regime," GW Notes **6**, 2013 [arXiv:1201.3621 [astro-ph.CO]].

27. P. Binetruy, A. Bohe, C. Caprini and J. -F. Dufaux, "Cosmological Backgrounds of Gravitational Waves and eLISA/NGO: Phase Transitions, Cosmic Strings and Other Sources," JCAP **1206** (2012) 027 [arXiv:1201.0983 [gr-qc]].

26. C. Bonvin, C. Caprini and R. Durrer, "Magnetic fields from inflation: the transition to the radiation era," Phys. Rev. D **86** (2012) 023519 [arXiv:1112.3901 [astro-ph.CO]].

25. C. Caprini and J. M. No, "Supersonic Electroweak Baryogenesis: Achieving Baryogenesis for Fast Bubble Walls," JCAP **1201** (2012) 031 [arXiv:1111.1726 [hep-ph]].

24. C. Caprini, "Limits for primordial magnetic fields," proceedings of the conference 'Texas Symposium 2010', PoS TEXAS **2010** (2010) 222 [arXiv:1103.4060 [astro-ph.CO]].

23. C. Caprini, R. Durrer and X. Siemens, "Detection of gravitational waves from the QCD phase transition with pulsar timing arrays," Phys. Rev. D **82** (2010) 063511 [arXiv:1007.1218 [astro-ph.CO]].

22. C. Caprini, "Gravitational waves from cosmological phase transitions," proceedings of the conference 'Moriond cosmology session 2010' [arXiv:1005.5291 [astro-ph.CO]].

21. C. Bonvin and C. Caprini, "CMB temperature anisotropy at large scales induced by a causal primordial magnetic field," JCAP **1005** (2010) 022 [arXiv:1004.1405 [astro-ph.CO]].

20. C. Caprini, R. Durrer and G. Servant, "The stochastic gravitational wave background from turbulence and magnetic fields generated by a first-order phase transition," JCAP **0912** (2009) 024 [arXiv:0909.0622 [astro-ph.CO]].

19. C. Caprini, R. Durrer and E. Fenu, "Can the observed large scale magnetic fields be seeded by helical primordial fields?," JCAP **0911** (2009) 001 [arXiv:0906.4976 [astro-ph.CO]].

18. C. Caprini, F. Finelli, D. Paoletti and A. Riotto, "The cosmic microwave background temperature bispectrum from scalar perturbations induced by primordial magnetic fields," JCAP **0906** (2009) 021 [arXiv:0903.1420 [astro-ph.CO]].

17. C. Caprini, R. Durrer, T. Konstandin and G. Servant, "General Properties of the Gravitational Wave Spectrum from Phase Transitions," Phys. Rev. D **79** (2009) 083519 [arXiv:0901.1661 [astro-ph]].

16. E. Babichev, P. Brax, C. Caprini, J. Martin and D. A. Steer, "Dirac Born Infeld (DBI) Cosmic Strings," JHEP **0903** (2009) 091 [arXiv:0809.2013 [hep-th]].

15. M. Douspis, P. G. Castro, C. Caprini and N. Aghanim, "Optimising large galaxy surveys for ISW detection," Astron. Astrophys. **485** (2008) 395 [arXiv:0802.0983 [astro-ph]].

14. L. Hollenstein, C. Caprini, R. Crittenden and R. Maartens, "Challenges for creating magnetic fields by cosmic defects," Phys. Rev. D **77** (2008) 063517 [arXiv:0712.1667 [astro-ph]].

13. C. Caprini, R. Durrer and G. Servant, "Gravitational wave generation from bubble collisions in first-order phase transitions: An analytic approach," Phys. Rev. D **77** (2008) 124015 [arXiv:0711.2593 [astro-ph]].

12. C. Bonvin, C. Caprini and R. Durrer, "Superluminal motion and closed signal curves," arXiv:0706.1538 [astro-ph].

11. C. Caprini, R. Durrer and R. Sturani, "On the frequency of gravitational waves," Phys. Rev. D **74** (2006) 127501 [astro-ph/0607651].

10. C. Bonvin, C. Caprini and R. Durrer, "A no-go theorem for k-essence dark energy," Phys. Rev. Lett. **97** (2006) 081303 [astro-ph/0606584].

9. C. Caprini and R. Durrer, "Gravitational waves from stochastic relativistic sources: Primordial turbulence and magnetic fields," Phys. Rev. D **74** (2006) 063521 [astro-ph/0603476].

8. C. Caprini, "Primordial magnetic fields and gravitational waves,' proceedings of the conference 'The origin and evolution of cosmic magnetism,' A. N. **327**, (2006) 5-6, 422

7. C. Caprini, " Effects of tensor perturbations induced by a primordial magnetic field,' proceedings of the conference 'Nonlinear Cosmology', ICTP Trieste. To appear in Int. J. Mod. Phys. **D** (2006)

6. C. Caprini and R. Durrer, "Limits on stochastic magnetic fields: A Defense of our paper," Phys. Rev. D **72** (2005) 088301 [astro-ph/0504553].

5. C. Caprini and P. G. Ferreira, "Constraints on the electrical charge asymmetry of the universe," JCAP **0502** (2005) 006 [hep-ph/0310066].

4. C. Caprini, R. Durrer and T. Kahniashvili, "The Cosmic microwave background and helical magnetic fields: The Tensor mode," Phys. Rev. D **69** (2004) 063006 [astro-ph/0304556].

3. R. Durrer and C. Caprini, "Primordial magnetic fields and causality," JCAP **0311** (2003) 010 [astro-ph/0305059].

2. C. Caprini, S. H. Hansen and M. Kunz, "Observational constraint on the fourth derivative of the inflaton potential," Mon. Not. Roy. Astron. Soc. **339** (2003) 212 [hep-ph/0210095].

1. C. Caprini and R. Durrer, "Gravitational wave production: A Strong constraint on primordial magnetic fields," Phys. Rev. D **65** (2001) 023517 [astro-ph/0106244].

Seminars:

- *GW sources and Cosmology*
  - 29th Texas Symposium on Relativistic Astrophysics, CTICC Cape Town, South Africa 2017
- *Primordial magnetic fields*
  - CTA day, Paris Observatory, 2017
- *Cosmology with the Gravitational Wave interferometer LISA*
  - Conference COSMO17, Paris 2017
  - DESY Theory meeting, DESY Hamburg, Germany 2017
- *Testing cosmology with gravitational waves at LISA*
  - CERN TH-Institute "Probing the dark sector and general relativity at all scales", 2017
- *LISA Science Performance*
  - CEA Saclay, France 2017
- *Probing the expansion of the universe using GW standard sirens at LISA*
  - Colloque national "Dark Energy", LAL Orsay 2017
  - TeVPA, CERN 2016
- *Cosmology with gravitational wave detection*
  - SAP (CEA Saclay), France 2017
  - University of Geneva, Switzerland 2017
  - LTP Orsay, France 2017
  - University of Amsterdam, Netherlands 2017
  - Max Planck Institute for Gravitational Physics, Potsdam, Germany 2015
  - CERN, Switzerland 2015
  - University of Portsmouth, UK 2015
  - OCA Nice, France 2015
  - University of Sussex, UK 2015
  - University of Cardiff, UK 2015
  - University of Helsinki, Finland 2015
  - University of Oslo, Norway 2015
  - University of Bielefeld, Germany 2014
  - St Cugat Forum on Astrophysics, Barcelona 2014
  - X LISA Symposium, University of Florida Gainesville 2014
  - Cajagwr seminars, Caltech, Pasadena 2014
- *The effect of matter perturbations on the chirp signal*
  - Gravitational-wave astronomy meeting in Paris, IAP 2016
- *Smoking guns of phase transitions and primordial magnetic fields*
  - Les Houches school "Cosmology after Planck: what is next?", France 2016
- *Gravitational waves: discovery and future*
  - GGI workshop "Theoretical Cosmology in the Era of Large Surveys", Florence 2016
  - IPhT Séminaire Général, CEA-Saclay 2016
- *Cosmology with gravitational waves*
  - University of Heidelberg, Germany 2016
  - CTP Université Aix-Marseille, France 2016
  - Conference "Hot topics in Modern Cosmology", Cargèse, France 2016
  - YITP Kyoto, Japan 2016
  - APC Journal Club, Paris 2016
- *Gamma-ray observations of blazars and the intergalactic magnetic field spectrum*
  - Workshop "Origin, evolution and signatures of cosmological magnetic fields", NORDITA Stockholm 2015

- *Theoretical aspects of GW stochastic backgrounds*
  - Virgo TEONGRAV meeting, Pisa 2015
- *Gravitational waves from the early universe*
  - Fourth Dutch Gravitational Wave Meeting, Leiden 2015
- *Magnetic fields from inflation*
  - GReCO seminar series, IAP Paris 2014
  - Frontiers of Fundamental Physics, Marseille 2014
- *Theory beyond the BICEP2 measurement*
  Journal Club of the François Arago Centre, Paris 2014
- *Gravitational waves from first order phase transitions*
  - 6th Iberian Gravitational-Wave Meeting, Madrid 2016
  - Workshop "Particlegenesis", KITP Santa Barbara 2014
  - EPS meeting, Stockholm 2013
  - IFAE, Universitat Autònoma de Barcelona, Spain 2012
  - Université Libre de Bruxelles, Belgium 2012
  - DAMPT General relativity seminar, Cambridge 2012
  - University of Utrecht, Netherlands 2012
  - Max Planck Institute for gravitational physics, Hannover 2011
  - University of California Santa Cruz 2010
  - University of Wisconsin, Milwaukee 2010
  - Workshop 'Gravitational Waves 2010', University of Minnesota 2010
  - Cajagwr seminars, Caltech, Pasadena 2010
- *Stochastic backgrounds of gravitational waves of cosmological origin*
  - Workshop 'Stochastic backgrounds of gravitational waves', Nice, France 2013
  - NGO science day, IAP Paris 2012
- *Primordial magnetic fields: initial conditions and CMB anisotropy at large scales*
  - Department of Astrophysics, University of Oxford, 2012
  - SISSA particle physics seminar, Trieste 2012
- *Magnetic fields from inflation: the transition to the radiation era*
  - 'Cosmo coffee' meeting, CERN 2012
  - Conference 'Moriond Cosmology', La Thuile, Italy 2012
- *Gravitational waves*
  - Workshop 'Electroweak baryogenesis in the era of the LHC', Weizmann Institute Israel 2011
- *Cosmological models of seed fields*
  - Workshop 'Theory and observations of extragalactic magnetic fields', APC Paris 2010
- *Limits for primordial magnetic fields*
  - Texas Symposium 2010, Heidelberg
- *Cosmological gravitational wave backgrounds*
  - Université Catholique de Louvain 2010
  - University College London 2010
  - GPhys workshop, IAP Paris 2010
- *Gravitational waves from cosmological sources*
  - Journées LISA France, ONERA France 2010
- *CMB anisotropy at large scales induced by a causal primordial magnetic field*
  - IAP, Paris 2010
  - LPT, Orsay 2010

- *Primordial magnetic fields and gravitational waves*
  - Conference 'Cosmological Magnetic Fields', Ascona, Switzerland 2009
- *Cosmological magnetic fields*
  - Jet propulsion Laboratory, Pasadena 2010
  - SPP Journal Club, CEA Saclay 2009
  - IPN-X seminar series, Orsay 2009
  - LPNHE Jussieu, Paris 2009
  - IPhT, CEA Saclay 2008
- *Magnetic fields in the universe*
  - LAL Workshop, Orsay 2011
  - Conference 'PONT', Avignon, France 2008
- *Gravitational waves from phase transitions*
  - Conference 'Moriond Cosmology', La Thuile, Italy 2010
  - Conference 'COSMO09', CERN 2009
  - Workshop 'The electroweak phase transition', Nordita, Stockholm 2009
  - APC, Paris 2008
  - Perimeter Institute, Waterloo, Canada 2008
  - Institut d'Astrophysique de Paris, Paris 2008
  - Journées LISA France, APC, Paris 2008
  - Institut de Physique Théorique, CEA Saclay 2008
  - Instituto Superior Técnico, Universidade Técnica de Lisboa, Portugal 2007
  - Istituto di Astrofisica Spaziale e Fisica Cosmica, INAF Bologna, Italy 2007
  - Theoretisch-Physikalisches Institut, University of Jena, Germany 2007
  - ICTP Trieste, Italy 2007
  - Conference: 'Cosmology: Facts and Fictions' Sils Maria, Switzerland 2007
  - Laboratoire de Physique Théorique d'Orsay, France 2007
  - U.K. Cosmology Meeting, King's College London, UK 2006
- *No-go theorem for k-essence dark energy*
  - 'Cosmo Coffee' meeting, CERN, 2006
  - GGI workshop 'Astroparticle and Cosmology', Florence, Italy 2006
- *Gravitational waves from stochastic relativistic sources: primordial turbulence and magnetic fields*
  - Laboratoire d'Annecy-Le-Vieux de Physique Théorique, France 2006
  - Conference '10^{eme} Journée des Lacs Alpins de Cosmologie', CERN, 2006
  - Conference 'Cosmology: Facts and Fictions', Sils Maria, 2006
- *Primordial magnetic fields and gravitational waves*
  - Institut d'Astrophysique Spatiale, Paris France 2006
- *Primordial magnetic fields*
  - 'Cosmo Coffee' meeting, CERN, 2005
- *Magnetic field perturbations*
  - Conference 'Cosmology: Facts and Fictions', Sils Maria, 2005
- *Constraints on the electrical charge asymmetry of the universe*
  - Institute of Cosmology and Gravitation, University of Portsmouth, UK 2004
  - Conference 'Cosmology: Facts and Fictions', Sils Maria, 2004
- *Magnetic fields in the early universe*
  - Department of Astrophysics, University of Oxford, UK 2004
- *Primordial magnetic fields and charge asymmetry in the universe*
  - Department of Astronomy, University of Sussex, UK 2003
  - Department of Theoretical Physics, Imperial College London, UK 2003
  - Department of Astronomy, Università di Padova, Italy 2003

- *The cosmic microwave background and helical magnetic fields: the tensor mode*
  - Conference 'Cosmology: Facts and Fictions', Sils Maria, 2003
  - Oxford-Princeton meeting, University of Oxford, 2004
  - Conference 'Nonlinear Cosmology', ICTP Trieste, 2005
- *Observational constraint on the fourth derivative of the inflaton potential*
  - Department of Theoretical Physics, University of Geneva, Switzerland 2002
- *Consequences of causality on the spectrum of a primordial magnetic field*
  - Conference '5^{eme} Journée des Lacs Alpins de Cosmologie', Laboratoire d'Annecy-Le-Vieux de Physique Théorique, 2002
- *Gravitational wave production: a strong constraint on primordial magnetic fields*
  - U.K. Cosmology Meeting, University of Sussex, 2001
  - Institute of Cosmology and Gravitation, University of Portsmouth, 2002

Selection of conferences:

- *XII LISA Symposium*, Chicago 2018 [SOC]
- *DESY Theory meeting*, DESY Hamburg, Germany 2017 [invited talk]
- *COSMO17*, Paris, France 2017 [invited talk]
- *PONT, Progress on Old and New Themes in cosmology*, Avignon, France 2011, 2014, 2017 [organisation]
- *XI LISA Symposium*, Zurich 2016 [session convener]
- *TeVPA*, CERN 2016 [talk and session convener]
- *Gravitational-wave astronomy meeting in Paris*, IAP Paris 2016 [talk]
- *Hot topics in Modern Cosmology, SW10*, Cargèse, France 2016 [invited talk]
- *Cosmology after Planck: what is next?*, Les Houches school, France 2016 [invited lecture]
- *Theoretical Cosmology in the Era of Large Surveys*, GGI Florence, 2016 [invited talk]
- *eLISA Cosmology Working Group Workshop*, CERN 2015, University of Stavanger 2015, DESY Hamburg 2016 [organisation]
- *Origin, evolution and signatures of cosmological magnetic fields*, NORDITA Stockholm, 2015 [talk]
- *28th Texas Symposium on relativistic astrophysics*, Geneva, 2015 [session convener]
- *Frontiers of Fundamental Physics*, Marseille, 2014 [talk]
- *Workshop "Particlegenesis"*, KITP Santa Barbara, 2014 [invited talk]
- *X LISA Symposium*, University of Florida Gainesville, 2014 [invited talk]
- *St Cugat Forum on Astrophysics*, St Cugat (Barcelona), 2014 [invited talk]
- *European Physical Society meeting*, Stockholm, 2013 [invited talk]
- *Stochastic backgrounds of gravitational waves*, Workshop in Nice, France, 2013 [invited talk]
- *17th Itzykson Meeting*, IPhT CEA Saclay, 2012-2014 [organisation]
- *Rencontres de Moriond - Cosmology Session*, La Thuile, Italy 2012 [talk]

- *Electroweak baryogenesis in the era of the LHC*, workshop at the Weizmann Institute, Israel 2011 [invited talk]
- *Theory and observations of extragalactic magnetic fields*, workshop, APC Paris 2010 [invited talk]
- *Texas Symposium 2010* Heidelberg (Germany) 2010 [invited talk]
- *Gravitational Waves 2010*, workshop at the University of Minnesota 2010 [invited talk]
- *Rencontres de Moriond - Cosmology Session*, La Thuile, Italy 2010 [talk]
- *COSMO09*, CERN 2009 [talk]
- *The electroweak phase transition*, workshop at Nordita, Stockholm 2009 [invited talk]
- *Cosmological Magnetic Fields*, Ascona Switzerland 2009 [invited talk]
- *Gravitational Wave Astronomy*, Aspen, USA 2008 [talk]
- *PONT, Progress on Old and New Themes in cosmology*, Avignon, France 2008 [invited talk]
- *Cosmology: Facts and Fictions*, Sils Maria, Switzerland, yearly since 2003 to 2007 [invited talk]
- *Astroparticle and Cosmology*, Galileo Galilei Institute, Florence, 2006 [talk]
- *Nonlinear cosmology: turbulence and fields*, ICTP Trieste, 2005 [invited talk]

Bibliography

[1] N. Tamanini *et al.*, JCAP **1604**, 002 (2016), [1601.07112], 10.1088/1475-7516/2016/04/002.

[2] C. Caprini and N. Tamanini, JCAP **1610**, 006 (2016), [1607.08755], 10.1088/1475-7516/2016/10/006.

[3] C. Bonvin, C. Caprini, R. Sturani and N. Tamanini, Phys. Rev. **D95**, 044029 (2017), [1609.08093], 10.1103/PhysRevD.95.044029.

[4] K. Inayoshi, N. Tamanini, C. Caprini and Z. Haiman, Phys. Rev. **D96**, 063014 (2017), [1702.06529], 10.1103/PhysRevD.96.063014.

[5] C. Caprini, P. Hölscher and D. J. Schwarz, Phys. Rev. **D98**, 084002 (2018), [1804.01876], 10.1103/PhysRevD.98.084002.

[6] C. Caprini and R. Durrer, Phys. Rev. **D74**, 063521 (2006), [astro-ph/0603476], 10.1103/PhysRevD.74.063521.

[7] C. Caprini, R. Durrer and G. Servant, Phys. Rev. **D77**, 124015 (2008), [0711.2593], 10.1103/PhysRevD.77.124015.

[8] C. Caprini, R. Durrer, T. Konstandin and G. Servant, Phys. Rev. **D79**, 083519 (2009), [0901.1661], 10.1103/PhysRevD.79.083519.

[9] C. Caprini, R. Durrer and G. Servant, JCAP **0912**, 024 (2009), [0909.0622], 10.1088/1475-7516/2009/12/024.

[10] C. Caprini, R. Durrer and X. Siemens, Phys. Rev. **D82**, 063511 (2010), [1007.1218], 10.1103/PhysRevD.82.063511.

[11] P. Binetruy, A. Bohe, C. Caprini and J.-F. Dufaux, JCAP **1206**, 027 (2012), [1201.0983], 10.1088/1475-7516/2012/06/027.

[12] C. Caprini *et al.*, JCAP **1604**, 001 (2016), [1512.06239], 10.1088/1475-7516/2016/04/001.

[13] N. Bartolo *et al.*, JCAP **1612**, 026 (2016), [1610.06481], 10.1088/1475-7516/2016/12/026.

[14] M. F. Axen, S. Banagiri, A. Matas, C. Caprini and V. Mandic, 1806.02500.

[15] C. Caprini and D. G. Figueroa, Class. Quant. Grav. **35**, 163001 (2018), [1801.04268], 10.1088/1361-6382/aac608.

[16] Virgo, LIGO Scientific, B. P. Abbott *et al.*, Phys. Rev. Lett. **116**, 061102 (2016), [1602.03837], 10.1103/PhysRevLett.116.061102.

[17] Virgo, LIGO Scientific, B. P. Abbott *et al.*, Phys. Rev. Lett. **116**, 241103 (2016), [1606.04855], 10.1103/PhysRevLett.116.241103.

[18] VIRGO, LIGO Scientific, B. P. Abbott *et al.*, Phys. Rev. Lett. **118**, 221101 (2017), [1706.01812], 10.1103/PhysRevLett.118.221101.

[19] Virgo, LIGO Scientific, B. P. Abbott *et al.*, Astrophys. J. **851**, L35 (2017), [1711.05578], 10.3847/2041-8213/aa9f0c.

[20] Virgo, LIGO Scientific, B. P. Abbott *et al.*, Phys. Rev. Lett. **119**, 141101 (2017), [1709.09660], 10.1103/PhysRevLett.119.141101.

[21] Virgo, LIGO Scientific, B. Abbott *et al.*, Phys. Rev. Lett. **119**, 161101 (2017), [1710.05832], 10.1103/PhysRevLett.119.161101.

[22] GROND, SALT Group, OzGrav, DFN, INTEGRAL, Virgo, Insight-Hxmt, MAXI Team, Fermi-LAT, J-GEM, RATIR, IceCube, CAASTRO, LWA, ePESSTO, GRAWITA, RIMAS, SKA South Africa/MeerKAT, H.E.S.S., 1M2H Team, IKI-GW Follow-up, Fermi GBM, Pi of Sky, DWF (Deeper Wider Faster Program), Dark Energy Survey, MASTER, AstroSat Cadmium Zinc Telluride Imager Team, Swift, Pierre

Auger, ASKAP, VINROUGE, JAGWAR, Chandra Team at McGill University, TTU-NRAO, GROWTH, AGILE Team, MWA, ATCA, AST3, TOROS, Pan-STARRS, NuSTAR, ATLAS Telescopes, BOOTES, CaltechNRAO, LIGO Scientific, High Time Resolution Universe Survey, Nordic Optical Telescope, Las Cumbres Observatory Group, TZAC Consortium, LOFAR, IPN, DLT40, Texas Tech University, HAWC, ANTARES, KU, Dark Energy Camera GW-EM, CALET, Euro VLBI Team, ALMA, B. P. Abbott *et al.*, Astrophys. J. **848**, L12 (2017), [1710.05833], 10.3847/2041-8213/aa91c9.

[23] P. Creminelli and F. Vernizzi, Phys. Rev. Lett. **119**, 251302 (2017), [1710.05877], 10.1103/PhysRevLett.119.251302.

[24] J. M. Ezquiaga and M. Zumalacárregui, Phys. Rev. Lett. **119**, 251304 (2017), [1710.05901], 10.1103/PhysRevLett.119.251304.

[25] T. Baker *et al.*, Phys. Rev. Lett. **119**, 251301 (2017), [1710.06394], 10.1103/PhysRevLett.119.251301.

[26] J. Sakstein and B. Jain, Phys. Rev. Lett. **119**, 251303 (2017), [1710.05893], 10.1103/PhysRevLett.119.251303.

[27] L. Lombriser and A. Taylor, JCAP **1603**, 031 (2016), [1509.08458], 10.1088/1475-7516/2016/03/031.

[28] L. Lombriser and N. A. Lima, Phys. Lett. **B765**, 382 (2017), [1602.07670], 10.1016/j.physletb.2016.12.048.

[29] LIGO Scientific, VINROUGE, Las Cumbres Observatory, DES, DLT40, Virgo, 1M2H, Dark Energy Camera GW-E, MASTER, B. P. Abbott *et al.*, Nature **551**, 85 (2017), [1710.05835], 10.1038/nature24471.

[30] Planck, P. A. R. Ade *et al.*, Astron. Astrophys. **594**, A13 (2016), [1502.01589], 10.1051/0004-6361/201525830.

[31] A. G. Riess *et al.*, Astrophys. J. **826**, 56 (2016), [1604.01424], 10.3847/0004-637X/826/1/56.

[32] M. Maggiore, Phys. Rept. **331**, 283 (2000), [gr-qc/9909001], 10.1016/S0370-1573(99)00102-7.

[33] M. Maggiore, *Gravitational Waves. Vol. 1: Theory and Experiments* (Oxford University Press, 2007).

[34] E. E. Flanagan and S. A. Hughes, New J. Phys. **7**, 204 (2005), [gr-qc/0501041], 10.1088/1367-2630/7/1/204.

[35] S. M. Carroll, *Spacetime and geometry: An introduction to general relativity* (, 2004).

[36] J. M. Bardeen, Phys. Rev. **D22**, 1882 (1980), 10.1103/PhysRevD.22.1882.

[37] J. Stewart, *Advanced General Relativity* (Cambridge University Press, Cambridge, 1993).

[38] R. Durrer, *The Cosmic Microwave Background* (Cambridge University Press, Cambridge, 2008).

[39] C. W. Misner, K. S. Thorne and J. A. Wheeler, *Gravitation* (W. H. Freeman, San Francisco, 1973).

[40] D. R. Brill and J. B. Hartle, Phys. Rev. **135**, B271 (1964), 10.1103/PhysRev.135.B271.

[41] R. A. Isaacson, Phys. Rev. **166**, 1263 (1967), 10.1103/PhysRev.166.1263.

[42] R. A. Isaacson, Phys. Rev. **166**, 1272 (1968), 10.1103/PhysRev.166.1272.

[43] M. J. Pfenning and E. Poisson, Phys. Rev. **D65**, 084001 (2002), [gr-qc/0012057], 10.1103/PhysRevD.65.084001.

[44] E. Barausse and L. Lehner, Phys. Rev. **D88**, 024029 (2013), [1306.5564], 10.1103/PhysRevD.88.024029.

[45] Planck, P. A. R. Ade *et al.*, Astron. Astrophys. **571**, A26 (2014), [1303.5086], 10.1051/0004-6361/201321546.

[46] H. Kodama and M. Sasaki, Prog. Theor. Phys. Suppl. **78**, 1 (1984), 10.1143/PTPS.78.1.

[47] S. Weinberg, *Cosmology* (Oxford University Press, Oxford, 2008).

[48] E. W. Kolb and M. S. Turner, Front. Phys. **69**, 1 (1990).

[49] Particle Data Group, C. Patrignani *et al.*, Chin. Phys. **C40**, 100001 (2016), 10.1088/1674-1137/40/10/100001.

[50] Planck, P. A. R. Ade *et al.*, Astron. Astrophys. **571**, A16 (2014), [1303.5076], 10.1051/0004-6361/201321591.

[51] B. Allen, The Stochastic gravity wave background: Sources and detection, in *Relativistic gravitation and gravitational radiation. Proceedings, School of Physics, Les Houches, France, September 26-October 6, 1995*, pp. 373–417, 1996, [gr-qc/9604033].

[52] J. Lesgourgues, Inflationary cosmology, in *Lecture notes of a course presented in the framework of the 3eme cycle de physique de Suisse romande, EPFL (Lausanne)*, 2006.

[53] L. Senatore, Lectures on Inflation, in *Proceedings, Theoretical Advanced Study Institute in Elementary Particle Physics: New Frontiers in Fields and Strings (TASI 2015): Boulder, CO, USA, June 1-26, 2015*, pp. 447–543, 2017, [1609.00716].

[54] D. S. Gorbunov and V. A. Rubakov, *Introduction to the Theory of the Early Universe, Volume 2* (World Scientific, 2011).

[55] W. Hu and M. J. White, Phys. Rev. **D56**, 596 (1997), [astro-ph/9702170], 10.1103/PhysRevD.56.596.

[56] C. Caprini, R. Durrer and T. Kahniashvili, Phys. Rev. **D69**, 063006 (2004), [astro-ph/0304556], 10.1103/PhysRevD.69.063006.

[57] J. M. Maldacena, JHEP **05**, 013 (2003), [astro-ph/0210603], 10.1088/1126-6708/2003/05/013.

[58] N. Bartolo, S. Matarrese, M. Peloso and A. Ricciardone, Phys. Rev. **D87**, 023504 (2013), [1210.3257], 10.1103/PhysRevD.87.023504.

[59] N. Bartolo, S. Matarrese, M. Peloso and M. Shiraishi, JCAP **1501**, 027 (2015), [1411.2521], 10.1088/1475-7516/2015/01/027.

[60] A. Naruko, E. Komatsu and M. Yamaguchi, JCAP **1504**, 045 (2015), [1411.5489], 10.1088/1475-7516/2015/04/045.

[61] J. L. Cook and L. Sorbo, JCAP **1311**, 047 (2013), [1307.7077], 10.1088/1475-7516/2013/11/047.

[62] L. Sorbo, JCAP **1106**, 003 (2011), [1101.1525], 10.1088/1475-7516/2011/06/003.

[63] M. M. Anber and L. Sorbo, Phys. Rev. **D85**, 123537 (2012), [1203.5849], 10.1103/PhysRevD.85.123537.

[64] J. D. Romano and N. J. Cornish, Living Rev. Rel. **20**, 2 (2017), [1608.06889], 10.1007/s41114-017-0004-1.

[65] G. Mangano *et al.*, Nucl. Phys. **B729**, 221 (2005), [hep-ph/0506164], 10.1016/j.nuclphysb.2005.09.041.

[66] F. Iocco, G. Mangano, G. Miele, O. Pisanti and P. D. Serpico, Phys. Rept. **472**, 1 (2009), [0809.0631], 10.1016/j.physrep.2009.02.002.

[67] LUNA, M. Anders *et al.*, Phys. Rev. Lett. **113**, 042501 (2014), 10.1103/PhysRevLett.113.042501.

[68] R. H. Cyburt, B. D. Fields and K. A. Olive, JCAP **0811**, 012 (2008), [0808.2818], 10.1088/1475-7516/2008/11/012.

[69] R. H. Cyburt, B. D. Fields, K. A. Olive and E. Skillman, Astropart. Phys. **23**, 313 (2005), [astro-ph/0408033], 10.1016/j.astropartphys.2005.01.005.

[70] G. Rossi, C. Yèche, N. Palanque-Delabrouille and J. Lesgourgues, Phys. Rev. **D92**, 063505 (2015), [1412.6763], 10.1103/PhysRevD.92.063505.

[71] I. Sendra and T. L. Smith, Phys. Rev. **D85**, 123002 (2012), [1203.4232], 10.1103/PhysRevD.85.123002.

[72] T. L. Smith, E. Pierpaoli and M. Kamionkowski, Phys. Rev. Lett. **97**, 021301 (2006), [astro-ph/0603144], 10.1103/PhysRevLett.97.021301.

[73] L. Bethke, D. G. Figueroa and A. Rajantie, Phys. Rev. Lett. **111**, 011301 (2013), [1304.2657], 10.1103/PhysRevLett.111.011301.

[74] L. Bethke, D. G. Figueroa and A. Rajantie, JCAP **1406**, 047 (2014), [1309.1148], 10.1088/1475-7516/2014/06/047.

[75] L. Pagano, L. Salvati and A. Melchiorri, Phys. Lett. **B760**, 823 (2016), [1508.02393], 10.1016/j.physletb.2016.07.078.

[76] R. K. Sachs and A. M. Wolfe, Astrophys. J. **147**, 73 (1967), 10.1007/s10714-007-0448-9.

[77] A. A. Starobinsky, Sov. Astron. Lett. **11**, 133 (1985).

[78] A. Kosowsky, Annals Phys. **246**, 49 (1996), [astro-ph/9501045], 10.1006/aphy.1996.0020.

[79] J. R. Bond and G. Efstathiou, Astrophys. J. **285**, L45 (1984), 10.1086/184362.

[80] J. R. Bond and G. Efstathiou, Mon. Not. Roy. Astron. Soc. **226**, 655 (1987).

[81] BICEP2, P. A. R. Ade *et al.*, Phys. Rev. Lett. **112**, 241101 (2014), [1403.3985], 10.1103/PhysRevLett.112.241101.

[82] BICEP2, Planck, P. A. R. Ade *et al.*, Phys. Rev. Lett. **114**, 101301 (2015), [1502.00612], 10.1103/PhysRevLett.114.101301.

[83] I. S. Gradshteyn and I. M. Ryzhik, *Table of Integrals, Series and Products* (Academic Press, 2014).

[84] P. Peter and J.-P. Uzan, *Primordial Cosmology* (Oxford University Press, Oxford, 2009).

[85] E. L. Wright *et al.*, Astrophys. J. **396**, L13 (1992), 10.1086/186506.

[86] B. Allen and S. Koranda, Phys. Rev. **D50**, 3713 (1994), [astro-ph/9404068], 10.1103/PhysRevD.50.3713.

[87] COBE, G. F. Smoot *et al.*, Astrophys. J. **396**, L1 (1992), 10.1086/186504.

[88] L. M. Krauss and M. J. White, Phys. Rev. Lett. **69**, 869 (1992), [hep-ph/9205212], 10.1103/PhysRevLett.69.869.

[89] S. Koranda and B. Allen, Phys. Rev. **D52**, 1902 (1995), [astro-ph/9410049], 10.1103/PhysRevD.52.1902.

[90] BICEP2, Keck Array, P. A. R. Ade *et al.*, Phys. Rev. Lett. **116**, 031302 (2016), [1510.09217], 10.1103/PhysRevLett.116.031302.

[91] G. Cabass *et al.*, Phys. Rev. **D93**, 063508 (2016), [1511.05146], 10.1103/PhysRevD.93.063508.

[92] COrE, F. R. Bouchet *et al.*, 1102.2181.

[93] P. D. Lasky *et al.*, Phys. Rev. **X6**, 011035 (2016), [1511.05994], 10.1103/PhysRevX.6.011035.

[94] P. D. Meerburg, R. Hložek, B. Hadzhiyska and J. Meyers, Phys. Rev. **D91**, 103505 (2015), [1502.00302], 10.1103/PhysRevD.91.103505.

[95] A. Ota, T. Takahashi, H. Tashiro and M. Yamaguchi, JCAP **1410**, 029 (2014), [1406.0451], 10.1088/1475-7516/2014/10/029.

[96] J. Chluba, L. Dai, D. Grin, M. Amin and M. Kamionkowski, Mon. Not. Roy. Astron. Soc. **446**, 2871 (2015), [1407.3653], 10.1093/mnras/stu2277.

[97] J. Chluba and R. A. Sunyaev, Mon. Not. Roy. Astron. Soc. **419**, 1294 (2012), [1109.6552], 10.1111/j.1365-2966.2011.19786.x.

[98] J. Chluba, Science with CMB spectral distortions, in *Proceedings, 49th Rencontres de Moriond on Cosmology: La Thuile, Italy, March 15-22, 2014*, pp. 327–334, 2014, [1405.6938].

[99] A. Wolszczan and D. A. Frail, Nature **355**, 145 (1992), 10.1038/355145a0.

[100] R. A. Hulse and J. H. Taylor, Astrophys. J. **195**, L51 (1975), 10.1086/181708.

[101] J. H. Taylor and J. M. Weisberg, Astrophys. J. **345**, 434 (1989), 10.1086/167917.

[102] D. R. Lorimer, Living Rev. Rel. **11**, 8 (2008), [0811.0762], 10.12942/lrr-2008-8.

[103] V. M. Kaspi, J. H. Taylor and M. F. Ryba, Astrophys. J. **428**, 713 (1994), 10.1086/174280.

[104] M. V. Sazhin, Vestn. Mosk. Univ. Fiz. Astron. **18**, 82 (1977).

[105] S. L. Detweiler, Astrophys. J. **234**, 1100 (1979), 10.1086/157593.

[106] R. w. Romani and J. h. Taylor, Astrophys. J. **265**, L35 (1983), 10.1086/183953.

[107] R. w. Hellings and G. s. Downs, Astrophys. J. **265**, L39 (1983), 10.1086/183954.

[108] B. Bertotti and B. J. Carr, Astrophys. J. **236**, 1000 (1980), 10.1086/157826.

[109] D. R. Stinebring, M. F. Ryba, J. H. Taylor and R. W. Romani, Phys. Rev. Lett. **65**, 285 (1990), 10.1103/PhysRevLett.65.285.

[110] S. E. Thorsett and R. J. Dewey, Phys. Rev. **D53**, 3468 (1996), 10.1103/PhysRevD.53.3468.

[111] A. N. Lommen, New limits on gravitational radiation using pulsars, in *Neutron stars, pulsars and supernova remnants. Proceedings, 270th WE-Heraeus Seminar, Bad Honnef, Germany, January 21-25, 2002*, pp. 114–125, 2002, [astro-ph/0208572].

[112] M. P. McHugh, G. Zalamansky, F. Vernotte and E. Lantz, Phys. Rev. **D54**, 5993 (1996), 10.1103/PhysRevD.54.5993.

[113] F. A. Jenet *et al.*, Astrophys. J. **653**, 1571 (2006), [astro-ph/0609013], 10.1086/508702.

[114] R. N. Manchester *et al.*, Publ. Astron. Soc. Austral. **30**, 17 (2013), [1210.6130], 10.1017/pasa.2012.017.

[115] R. D. Ferdman *et al.*, Class. Quant. Grav. **27**, 084014 (2010), [1003.3405], 10.1088/0264-9381/27/8/084014.

[116] F. Jenet *et al.*, 0909.1058.

[117] G. Hobbs *et al.*, Class. Quant. Grav. **27**, 084013 (2010), [0911.5206], 10.1088/0264-9381/27/8/084013.

[118] R. N. Manchester, Class. Quant. Grav. **30**, 224010 (2013), [1309.7392], 10.1088/0264-9381/30/22/224010.

[119] P. B. Demorest *et al.*, Astrophys. J. **762**, 94 (2013), [1201.6641], 10.1088/0004-637X/762/2/94.

[120] L. Lentati *et al.*, Mon. Not. Roy. Astron. Soc. **453**, 2576 (2015), [1504.03692], 10.1093/mnras/stv1538.

[121] J. P. W. Verbiest *et al.*, Mon. Not. Roy. Astron. Soc. **458**, 1267 (2016), [1602.03640], 10.1093/mnras/stw347.

[122] C. J. Moore, R. H. Cole and C. P. L. Berry, Class. Quant. Grav. **32**, 015014 (2015), [1408.0740], 10.1088/0264-9381/32/1/015014.

[123] A. H. Jaffe and D. C. Backer, Astrophys. J. **583**, 616 (2003), [astro-ph/0210148], 10.1086/345443.

[124] J. S. B. Wyithe and A. Loeb, Astrophys. J. **590**, 691 (2003), [astro-ph/0211556], 10.1086/375187.

[125] M. Enoki, K. T. Inoue, M. Nagashima and N. Sugiyama, Astrophys. J. **615**, 19 (2004), [astro-ph/0404389], 10.1086/424475.

[126] A. Sesana, A. Vecchio and C. N. Colacino, Mon. Not. Roy. Astron. Soc. **390**, 192 (2008), [0804.4476], 10.1111/j.1365-2966.2008.13682.x.

[127] A. Sesana, Mon. Not. Roy. Astron. Soc. **433**, 1 (2013), [1211.5375], 10.1093/mnrasl/slt034.

[128] K. Riles, Prog. Part. Nucl. Phys. **68**, 1 (2013), [1209.0667], 10.1016/j.ppnp.2012.08.001.

[129] B. F. Schutz, Class. Quant. Grav. **28**, 125023 (2011), [1102.5421], 10.1088/0264-9381/28/12/125023.

[130] H. Audley *et al.*, 1702.00786.

[131] C. J. Hogan and P. L. Bender, Phys. Rev. **D64**, 062002 (2001), [astro-ph/0104266], 10.1103/PhysRevD.64.062002.

[132] M. Tinto, J. W. Armstrong and F. B. Estabrook, Phys. Rev. **D63**, 021101 (2001), 10.1103/PhysRevD.63.021101.

[133] Mock LISA Data Challenge Task Force, S. Babak *et al.*, Class. Quant. Grav. **27**, 084009 (2010), [0912.0548], 10.1088/0264-9381/27/8/084009.

[134] E. Thrane and J. D. Romano, Phys. Rev. **D88**, 124032 (2013), [1310.5300], 10.1103/PhysRevD.88.124032.

[135] Virgo, LIGO Scientific, B. P. Abbott *et al.*, Phys. Rev. Lett. **116**, 131102 (2016), [1602.03847], 10.1103/PhysRevLett.116.131102.

[136] http://www.geo600.org.

[137] http://tamago.mtk.nao.ac.jp.

[138] LIGO Scientific, G. M. Harry, Class. Quant. Grav. **27**, 084006 (2010), 10.1088/0264-9381/27/8/084006.

[139] Virgo, F. Acernese, J. Phys. Conf. Ser. **610**, 012014 (2015), 10.1088/1742-6596/610/1/012014.

[140] https://www.advancedligo.mit.edu.

[141] https://wwwcascina.virgo.infn.it/advirgo/.

[142] Virgo, LIGO Scientific, B. P. Abbott *et al.*, Phys. Rev. Lett. **118**, 121101 (2017), [1612.02029], 10.1103/PhysRevLett.118.121101, 10.1103/PhysRevLett.119.029901.

[143] http://gwcenter.icrr.u-tokyo.ac.jp/en/.

[144] http://www.gw-indigo.org/tiki-index.php.

[145] B. Sathyaprakash *et al.*, Class. Quant. Grav. **29**, 124013 (2012), [1206.0331], 10.1088/0264-9381/29/12/124013, 10.1088/0264-9381/30/7/079501.

[146] B. Sathyaprakash *et al.*, Scientific Potential of Einstein Telescope, in *Proceedings, 46th Rencontres de Moriond on Gravitational Waves and Experimental Gravity: La Thuile, Italy, March 20-27, 2011*, pp. 127–136, 2011, [1108.1423].

[147] A. Freise *et al.*, Class. Quant. Grav. **26**, 085012 (2009), [0804.1036], 10.1088/0264-9381/26/8/085012.

[148] S. Hild, S. Chelkowski and A. Freise, 0810.0604.

[149] S. Hild *et al.*, Class. Quant. Grav. **27**, 015003 (2010), [0906.2655], 10.1088/0264-9381/27/1/015003.

[150] S. Hild *et al.*, Class. Quant. Grav. **28**, 094013 (2011), [1012.0908], 10.1088/0264-9381/28/9/094013.

[151] M. Armano *et al.*, Phys. Rev. Lett. **116**, 231101 (2016), 10.1103/PhysRevLett.116.231101.

[152] F. B. Estabrook, M. Tinto and J. W. Armstrong, Phys. Rev. **D62**, 042002 (2000), 10.1103/PhysRevD.62.042002.

[153] N. Seto, S. Kawamura and T. Nakamura, Phys. Rev. Lett. **87**, 221103 (2001), [astro-ph/0108011], 10.1103/PhysRevLett.87.221103.

[154] S. Kawamura *et al.*, Class. Quant. Grav. **23**, S125 (2006), 10.1088/0264-9381/23/8/S17.

[155] J. Crowder and N. J. Cornish, Phys. Rev. **D72**, 083005 (2005), [gr-qc/0506015], 10.1103/PhysRevD.72.083005.

[156] G. M. Harry, P. Fritschel, D. A. Shaddock, W. Folkner and E. S. Phinney, Class. Quant. Grav. **23**, 4887 (2006), 10.1088/0264-9381/23/24/C01, 10.1088/0264-9381/23/15/008.

[157] C. Cutler and J. Harms, Phys. Rev. **D73**, 042001 (2006), [gr-qc/0511092], 10.1103/PhysRevD.73.042001.

[158] C. Cutler and D. E. Holz, Phys. Rev. **D80**, 104009 (2009), [0906.3752], 10.1103/PhysRevD.80.104009.

[159] H. Kudoh, A. Taruya, T. Hiramatsu and Y. Himemoto, Phys. Rev. **D73**, 064006 (2006), [gr-qc/0511145], 10.1103/PhysRevD.73.064006.

[160] K. Yagi, Int. J. Mod. Phys. **D22**, 1341013 (2013), [1302.2388], 10.1142/S0218271813410137.

[161] S. Dimopoulos, P. W. Graham, J. M. Hogan, M. A. Kasevich and S. Rajendran, Phys. Rev. **D78**, 122002 (2008), [0806.2125], 10.1103/PhysRevD.78.122002.

[162] J. M. Hogan *et al.*, Gen. Rel. Grav. **43**, 1953 (2011), [1009.2702], 10.1007/s10714-011-1182-x.

[163] M. Hohensee *et al.*, Gen. Rel. Grav. **43**, 1905 (2011), [1001.4821], 10.1007/s10714-010-1118-x.

[164] A. H. Guth, Phys. Rev. **D23**, 347 (1981), 10.1103/PhysRevD.23.347.

[165] A. D. Linde, Phys. Lett. **108B**, 389 (1982), 10.1016/0370-2693(82)91219-9.

[166] A. Albrecht and P. J. Steinhardt, Phys. Rev. Lett. **48**, 1220 (1982), 10.1103/PhysRevLett.48.1220.

[167] R. Brout, F. Englert and E. Gunzig, Annals Phys. **115**, 78 (1978), 10.1016/0003-4916(78)90176-8.

[168] A. A. Starobinsky, Phys. Lett. **91B**, 99 (1980), 10.1016/0370-2693(80)90670-X.

[169] D. Kazanas, Astrophys. J. **241**, L59 (1980), 10.1086/183361.

[170] K. Sato, Mon. Not. Roy. Astron. Soc. **195**, 467 (1981).

[171] V. F. Mukhanov and G. V. Chibisov, JETP Lett. **33**, 532 (1981).

[172] A. H. Guth and S. Y. Pi, Phys. Rev. Lett. **49**, 1110 (1982), 10.1103/PhysRevLett.49.1110.

[173] A. A. Starobinsky, Phys. Lett. **117B**, 175 (1982), 10.1016/0370-2693(82)90541-X.

[174] S. W. Hawking, Phys. Lett. **115B**, 295 (1982), 10.1016/0370-2693(82)90373-2.

[175] J. M. Bardeen, P. J. Steinhardt and M. S. Turner, Phys. Rev. **D28**, 679 (1983), 10.1103/PhysRevD.28.679.

[176] D. Polarski and A. A. Starobinsky, Class. Quant. Grav. **13**, 377 (1996), [gr-qc/9504030], 10.1088/0264-9381/13/3/006.

[177] C. Kiefer, D. Polarski and A. A. Starobinsky, Int. J. Mod. Phys. **D7**, 455 (1998), [gr-qc/9802003], 10.1142/S0218271898000292.

[178] C. Kiefer, J. Lesgourgues, D. Polarski and A. A. Starobinsky, Class. Quant. Grav. **15**, L67 (1998), [gr-qc/9806066], 10.1088/0264-9381/15/10/002.

[179] L. P. Grishchuk, Sov. Phys. JETP **40**, 409 (1975).

[180] A. A. Starobinsky, JETP Lett. **30**, 682 (1979).

[181] V. A. Rubakov, M. V. Sazhin and A. V. Veryaskin, Phys. Lett. **115B**, 189 (1982), 10.1016/0370-2693(82)90641-4.

[182] R. Fabbri and M. d. Pollock, Phys. Lett. **125B**, 445 (1983), 10.1016/0370-2693(83)91322-9.

[183] M. Kamionkowski, A. Kosowsky and A. Stebbins, Phys. Rev. Lett. **78**, 2058 (1997), [astro-ph/9609132], 10.1103/PhysRevLett.78.2058.

[184] U. Seljak and M. Zaldarriaga, Phys. Rev. Lett. **78**, 2054 (1997), [astro-ph/9609169], 10.1103/PhysRevLett.78.2054.

[185] M. Zaldarriaga and U. Seljak, Phys. Rev. **D55**, 1830 (1997), [astro-ph/9609170], 10.1103/PhysRevD.55.1830.

[186] M. Kamionkowski, A. Kosowsky and A. Stebbins, Phys. Rev. **D55**, 7368 (1997), [astro-ph/9611125], 10.1103/PhysRevD.55.7368.

[187] R. Flauger, J. C. Hill and D. N. Spergel, JCAP **1408**, 039 (2014), [1405.7351], 10.1088/1475-7516/2014/08/039.

[188] M. J. Mortonson and U. Seljak, JCAP **1410**, 035 (2014), [1405.5857], 10.1088/1475-7516/2014/10/035.

[189] Planck, R. Adam *et al.*, Astron. Astrophys. **586**, A133 (2016), [1409.5738], 10.1051/0004-6361/201425034.

[190] Planck, P. A. R. Ade *et al.*, Astron. Astrophys. **594**, A20 (2016), [1502.02114], 10.1051/0004-6361/201525898.

[191] C. Bonvin, R. Durrer and R. Maartens, Phys. Rev. Lett. **112**, 191303 (2014), [1403.6768], 10.1103/PhysRevLett.112.191303.

[192] J. Lizarraga *et al.*, Phys. Rev. Lett. **112**, 171301 (2014), [1403.4924], 10.1103/PhysRevLett.112.171301.

[193] A. Moss and L. Pogosian, Phys. Rev. Lett. **112**, 171302 (2014), [1403.6105], 10.1103/PhysRevLett.112.171302.

[194] R. Durrer, D. G. Figueroa and M. Kunz, JCAP **1408**, 029 (2014), [1404.3855], 10.1088/1475-7516/2014/08/029.

[195] J. Lizarraga *et al.*, Phys. Rev. **D90**, 103504 (2014), [1408.4126], 10.1103/PhysRevD.90.103504.

[196] V. F. Mukhanov, H. A. Feldman and R. H. Brandenberger, Phys. Rept. **215**, 203 (1992), 10.1016/0370-1573(92)90044-Z.

[197] L. Hui and W. H. Kinney, Phys. Rev. **D65**, 103507 (2002), [astro-ph/0109107], 10.1103/PhysRevD.65.103507.

[198] A. R. Liddle and D. H. Lyth, *Cosmological inflation and large scale structure* (, 2000).

[199] D. Polarski and A. A. Starobinsky, Phys. Lett. **B356**, 196 (1995), [astro-ph/9505125], 10.1016/0370-2693(95)00842-9.

[200] J. Garcia-Bellido and D. Wands, Phys. Rev. **D53**, 5437 (1996), [astro-ph/9511029], 10.1103/PhysRevD.53.5437.

[201] J. R. Pritchard and M. Kamionkowski, Annals Phys. **318**, 2 (2005), [astro-ph/0412581], 10.1016/j.aop.2005.03.005.

[202] Y. Watanabe and E. Komatsu, Phys. Rev. **D73**, 123515 (2006), [astro-ph/0604176], 10.1103/PhysRevD.73.123515.

[203] L. A. Boyle and P. J. Steinhardt, Phys. Rev. **D77**, 063504 (2008), [astro-ph/0512014], 10.1103/PhysRevD.77.063504.

[204] M. S. Turner, M. J. White and J. E. Lidsey, Phys. Rev. **D48**, 4613 (1993), [astro-ph/9306029], 10.1103/PhysRevD.48.4613.

[205] X.-J. Liu, W. Zhao, Y. Zhang and Z.-H. Zhu, Phys. Rev. **D93**, 024031 (2016), [1509.03524], 10.1103/PhysRevD.93.024031.

[206] N. Seto and J. Yokoyama, J. Phys. Soc. Jap. **72**, 3082 (2003), [gr-qc/0305096], 10.1143/JPSJ.72.3082.

[207] K. Nakayama, S. Saito, Y. Suwa and J. Yokoyama, JCAP **0806**, 020 (2008), [0804.1827], 10.1088/1475-7516/2008/06/020.

[208] S. Kuroyanagi, T. Chiba and N. Sugiyama, Phys. Rev. **D79**, 103501 (2009), [0804.3249], 10.1103/PhysRevD.79.103501.

[209] S. Ghosh, R. Khatri and T. S. Roy, 1711.09929.

[210] M. Giovannini, Phys. Rev. **D60**, 123511 (1999), [astro-ph/9903004], 10.1103/PhysRevD.60.123511.

[211] M. Giovannini, Phys. Rev. **D58**, 083504 (1998), [hep-ph/9806329], 10.1103/PhysRevD.58.083504.

[212] L. A. Boyle and A. Buonanno, Phys. Rev. **D78**, 043531 (2008), [0708.2279], 10.1103/PhysRevD.78.043531.

[213] D. G. Figueroa and C. T. Byrnes, Phys. Lett. **B767**, 272 (2017), [1604.03905], 10.1016/j.physletb.2017.01.059.

[214] S. Kuroyanagi, C. Gordon, J. Silk and N. Sugiyama, Phys. Rev. **D81**, 083524 (2010), [0912.3683], 10.1103/PhysRevD.82.069901, 10.1103/PhysRevD.81.083524.

[215] Y. Zhang, Y. Yuan, W. Zhao and Y.-T. Chen, Class. Quant. Grav. **22**, 1383 (2005), [astro-ph/0501329], 10.1088/0264-9381/22/7/011.

[216] S. Weinberg, Phys. Rev. **D69**, 023503 (2004), [astro-ph/0306304], 10.1103/PhysRevD.69.023503.

[217] S. Kuroyanagi, T. Takahashi and S. Yokoyama, JCAP **1502**, 003 (2015), [1407.4785], 10.1088/1475-7516/2015/02/003.

[218] E. Witten, Phys. Rev. **D30**, 272 (1984), 10.1103/PhysRevD.30.272.

[219] C. J. Hogan, Mon. Not. Roy. Astron. Soc. **218**, 629 (1986).

[220] A. Kosowsky, M. S. Turner and R. Watkins, Phys. Rev. **D45**, 4514 (1992), 10.1103/PhysRevD.45.4514.

[221] A. Kosowsky and M. S. Turner, Phys. Rev. **D47**, 4372 (1993), [astro-ph/9211004], 10.1103/PhysRevD.47.4372.

[222] M. Kamionkowski, A. Kosowsky and M. S. Turner, Phys. Rev. **D49**, 2837 (1994), [astro-ph/9310044], 10.1103/PhysRevD.49.2837.

[223] M. Gurtler, E.-M. Ilgenfritz and A. Schiller, Phys. Rev. **D56**, 3888 (1997), [hep-lat/9704013], 10.1103/PhysRevD.56.3888.

[224] Y. Aoki, Phys. Rev. **D56**, 3860 (1997), [hep-lat/9612023], 10.1103/PhysRevD.56.3860.

[225] K. Kajantie, M. Laine, K. Rummukainen and M. E. Shaposhnikov, Nucl. Phys. **B466**, 189 (1996), [hep-lat/9510020], 10.1016/0550-3213(96)00052-1.

[226] K. Kajantie, M. Laine, K. Rummukainen and M. E. Shaposhnikov, Phys. Rev. Lett. **77**, 2887 (1996), [hep-ph/9605288], 10.1103/PhysRevLett.77.2887.

[227] M. Laine and K. Rummukainen, Nucl. Phys. Proc. Suppl. **73**, 180 (1999), [hep-lat/9809045], 10.1016/S0920-5632(99)85017-8.

[228] ATLAS, G. Aad *et al.*, Phys. Lett. **B716**, 1 (2012), [1207.7214], 10.1016/j.physletb.2012.08.020.

[229] M. Fairbairn and R. Hogan, JHEP **09**, 022 (2013), [1305.3452], 10.1007/JHEP09(2013)022.

[230] G. C. Dorsch, S. J. Huber and J. M. No, JHEP **10**, 029 (2013), [1305.6610], 10.1007/JHEP10(2013)029.

[231] W. Huang, J. Shu and Y. Zhang, JHEP **03**, 164 (2013), [1210.0906], 10.1007/JHEP03(2013)164.

[232] M. Laine, G. Nardini and K. Rummukainen, JCAP **1301**, 011 (2013), [1211.7344], 10.1088/1475-7516/2013/01/011.

[233] S. S. AbdusSalam and T. A. Chowdhury, JCAP **1405**, 026 (2014), [1310.8152], 10.1088/1475-7516/2014/05/026.

[234] H. Davoudiasl, I. Lewis and E. Ponton, Phys. Rev. **D87**, 093001 (2013), [1211.3449], 10.1103/PhysRevD.87.093001.

[235] H. H. Patel and M. J. Ramsey-Musolf, Phys. Rev. **D88**, 035013 (2013), [1212.5652], 10.1103/PhysRevD.88.035013.

[236] Y. Aoki, G. Endrodi, Z. Fodor, S. D. Katz and K. K. Szabo, Nature **443**, 675 (2006), [hep-lat/0611014], 10.1038/nature05120.

[237] D. J. Schwarz and M. Stuke, JCAP **0911**, 025 (2009), [0906.3434], 10.1088/1475-7516/2009/11/025, 10.1088/1475-7516/2010/10/E01.

[238] P. Schwaller, Phys. Rev. Lett. **115**, 181101 (2015), [1504.07263], 10.1103/PhysRevLett.115.181101.

[239] C. Grojean and G. Servant, Phys. Rev. **D75**, 043507 (2007), [hep-ph/0607107], 10.1103/PhysRevD.75.043507.

[240] M. Quiros, Finite temperature field theory and phase transitions, in *Proceedings, Summer School in High-energy physics and cosmology: Trieste, Italy, June 29-July 17, 1998*, pp. 187–259, 1999, [hep-ph/9901312].

[241] M. Laine and A. Vuorinen, Lect. Notes Phys. **925**, pp.1 (2016), [1701.01554], 10.1007/978-3-319-31933-9.

[242] P. J. Steinhardt, Phys. Rev. **D25**, 2074 (1982), 10.1103/PhysRevD.25.2074.

[243] S. J. Huber and T. Konstandin, JCAP **0809**, 022 (2008), [0806.1828], 10.1088/1475-7516/2008/09/022.

[244] D. J. Weir, Phys. Rev. **D93**, 124037 (2016), [1604.08429], 10.1103/PhysRevD.93.124037.

[245] R. Jinno and M. Takimoto, Phys. Rev. **D95**, 024009 (2017), [1605.01403], 10.1103/PhysRevD.95.024009.

[246] R. Jinno and M. Takimoto, 1707.03111.

[247] J. Ignatius, K. Kajantie, H. Kurki-Suonio and M. Laine, Phys. Rev. **D49**, 3854 (1994), [astro-ph/9309059], 10.1103/PhysRevD.49.3854.

[248] G. D. Moore and T. Prokopec, Phys. Rev. Lett. **75**, 777 (1995), [hep-ph/9503296], 10.1103/PhysRevLett.75.777.

[249] A. Megevand and A. D. Sanchez, Nucl. Phys. **B820**, 47 (2009), [0904.1753], 10.1016/j.nuclphysb.2009.05.007.

[250] T. Konstandin and J. M. No, JCAP **1102**, 008 (2011), [1011.3735], 10.1088/1475-7516/2011/02/008.

[251] A. Megevand and A. D. Sanchez, Nucl. Phys. **B865**, 217 (2012), [1206.2339], 10.1016/j.nuclphysb.2012.08.001.

[252] A. Megevand and F. A. Membiela, Phys. Rev. **D89**, 103507 (2014), [1311.2453], 10.1103/PhysRevD.89.103507.

[253] J. R. Espinosa, T. Konstandin, J. M. No and G. Servant, JCAP **1006**, 028 (2010), [1004.4187], 10.1088/1475-7516/2010/06/028.

[254] D. Bodeker and G. D. Moore, JCAP **0905**, 009 (2009), [0903.4099], 10.1088/1475-7516/2009/05/009.

[255] D. Bodeker and G. D. Moore, JCAP **1705**, 025 (2017), [1703.08215], 10.1088/1475-7516/2017/05/025.

[256] G. D. Moore and T. Prokopec, Phys. Rev. **D52**, 7182 (1995), [hep-ph/9506475], 10.1103/PhysRevD.52.7182.

[257] J. Kozaczuk, JHEP **10**, 135 (2015), [1506.04741], 10.1007/JHEP10(2015)135.

[258] S. J. Huber and M. Sopena, 1302.1044.

[259] J. T. Giblin, Jr. and J. B. Mertens, JHEP **12**, 042 (2013), [1310.2948], 10.1007/JHEP12(2013)042.

[260] M. Hindmarsh, S. J. Huber, K. Rummukainen and D. J. Weir, Phys. Rev. Lett. **112**, 041301 (2014), [1304.2433], 10.1103/PhysRevLett.112.041301.

[261] M. Hindmarsh, S. J. Huber, K. Rummukainen and D. J. Weir, Phys. Rev. **D92**, 123009 (2015), [1504.03291], 10.1103/PhysRevD.92.123009.

[262] M. Hindmarsh, S. J. Huber, K. Rummukainen and D. J. Weir, Phys. Rev. **D96**, 103520 (2017), [1704.05871], 10.1103/PhysRevD.96.103520.

[263] J. Ahonen and K. Enqvist, Phys. Lett. **B382**, 40 (1996), [hep-ph/9602357], 10.1016/0370-2693(96)00633-8.

[264] G. Baym and H. Heiselberg, Phys. Rev. **D56**, 5254 (1997), [astro-ph/9704214], 10.1103/PhysRevD.56.5254.

[265] T. Stevens and M. B. Johnson, 1001.3694.

[266] U.-L. Pen and N. Turok, Phys. Rev. Lett. **117**, 131301 (2016), [1510.02985], 10.1103/PhysRevLett.117.131301.

[267] A. Kosowsky, A. Mack and T. Kahniashvili, Phys. Rev. **D66**, 024030 (2002), [astro-ph/0111483], 10.1103/PhysRevD.66.024030.

[268] A. D. Dolgov, D. Grasso and A. Nicolis, Phys. Rev. **D66**, 103505 (2002), [astro-ph/0206461], 10.1103/PhysRevD.66.103505.

[269] G. Gogoberidze, T. Kahniashvili and A. Kosowsky, Phys. Rev. **D76**, 083002 (2007), [0705.1733], 10.1103/PhysRevD.76.083002.

[270] T. Kahniashvili, L. Campanelli, G. Gogoberidze, Y. Maravin and B. Ratra, Phys. Rev. **D78**, 123006 (2008), [0809.1899], 10.1103/PhysRevD.78.123006, 10.1103/PhysRevD.79.109901.

[271] S. J. Huber and T. Konstandin, JCAP **0805**, 017 (2008), [0709.2091], 10.1088/1475-7516/2008/05/017.

[272] A. Klein *et al.*, Phys. Rev. **D93**, 024003 (2016), [1511.05581], 10.1103/PhysRevD.93.024003.

[273] LIGO Scientific, B. P. Abbott *et al.*, Class. Quant. Grav. **34**, 044001 (2017), [1607.08697], 10.1088/1361-6382/aa51f4.